DEVELOPMENT OF THE GAS PHASE LASER INDUCED PHOSPHORESCENCE TECHNIQUE AND SOOT MEASUREMENTS IN FLAMES USING LASER INDUCED INCANDESCENCE

A thesis submitted for the degree of

Doctor of Philosophy

by

Martin Lawrence

School of Engineering and Design

Brunel University

September 2013

Abstract

Thermometry measurements were carried out using planar laser induced phosphorescence in conjunction with thermographic phosphors in heated turbulent jets and laminar flames in order to further develop the technique for usage in flames. Two dimensional thermometry measurements are essential to improve the understanding of combustion processes, as temperature governs soot pyrolysis, leading to soot formation. Two particular thermographic phosphors, BAM and YAG:Dy were tested and compared and it was found that they were unsuitable for gas phase flame thermometry measurements. Soot volume fraction measurements were carried out using planar two colour laser induced incandescence in gaseous and liquid fuel flames. The gas fuel flames were diluted with nitrogen, carbon dioxide and hydrogen individually and then with nitrogen and hydrogen together, as well as carbon dioxide and hydrogen together, separately. Results revealed the dilution effects of the gases on the soot formation process, where increasing nitrogen percentage in the flow decreased SVF, carbon dioxide reduced it further and hydrogen showed no marked difference. Biodiesels were compared with each other and with diesel in a wick burner in order to analyse their compositional effects on soot. Biodiesel composition was measured using gas chromatography. The sooting tendencies of the biodiesels were as expected, fuels with a longer average carbon chain length and a higher degree of unsaturation were found to produce more soot than shorter, more saturated fuels. Diesel was sootier than all of the biofuels tested, due to containing aromatics and a lower oxygen content. A pilot study was also done, where the performance and emissions of biofuels and biofuel-diesel blends were tested in a gas turbine engine, in order to relate the investigation to real world situations.

Acknowledgements

First and foremost, I would like to thank my supervisor, Dr Lionel Ganippa for his guidance and continuous support throughout my PhD. His consistent advice has assisted me through numerous difficult situations and helped me grow in character, gaining confidence, knowledge and experience. Secondly, my wife Jade, whose love and support has got me through the last three years. My son, Ace and new born daughter, Charlotte for bringing me so much joy since they came into the world, during my PhD and my step children, Stefan, Haydn and Francesca for their love and support. I would like to express my gratitude to the Brunel laboratory technicians, Kenneth Anstiss, Costas Xanthos, Clive Barret, Keith Withers and Andrew Selway for their efforts and guidance towards equipment setup. Their helped has proven to be an invaluable contribution towards the success of this work. I would like to express my appreciation to the Thomas Gerald Gray Charitable Trust for funding me and making the project possible. The contributions from Phosphor Technology Ltd are also greatly appreciated, as well as the help and advice provided by Photonic Solutions, particularly from Dr Ben Agate who aided me on several occasions with laser maintenance and repairs over the phone. I would like to thank David Peirce, who worked with me on the biodiesel flame study. Last but not least, I would like to thank Professor Hua Zhao for allowing me to make use of lab space and equipment throughout my time at Brunel.

Publications

1. Martin Lawrence, Hua Zhao, and Lionel Ganippa, 2013. Gas phase thermometry of hot turbulent jets using laser induced phosphorescence. *Optics Express*, Volume 21, Issue 10, pp. 12260 – 12281.
2. Martin Lawrence and Lionel Ganippa. Limitations of YAG:Dy and BAM for temperature measurements in flames. *To be submitted to Combustion and Flame.*
3. Martin Lawrence and Lionel Ganippa. Nitrogen oxides, partially and unburned hydrocarbon emission and performance monitoring of biofuels in an SR-30 gas turbine engine. *Final preparations of manuscript.*
4. Martin Lawrence and Lionel Ganippa. Dilution and hydrogen addition effects on soot volume fraction in propane diffusion flames. *Work in progress.*
5. Martin Lawrence, David Peirce, and Lionel Ganippa. Biodiesel composition effects on soot volume fraction. *Work in progress.*

Nomenclature

Acronyms

2C	Two colour
2D	Two dimensional
BAM:Eu	Barium magnesium aluminate doped in Europium ($BaMgAl_{10}O_{17}$:Eu)
BNC	Bayonet Neill-Concelman
C	Carbon
CARS	Coherent anti-stokes Raman scattering
CME	Coconut methyl ester
EGT	Exhaust gas temperature
FEE	Fish ethyl ester
FID	Flame ionisation detector
FWHM	Full width half max
GC	Gas chromatography
H	Hydrogen
HAB	Height above burner
HC	Hydrocarbon
HACA	Hydrogen abstraction carbon addition
ICCD	Intensified charge coupled device
JME	Jatropha methyl ester
JO	Jatropha oil
LED	Light emitting diode
LIBS	Laser induced breakdown spectroscopy
LIF	Laser induced fluorescence
LII	Laser induced incandescence
LIP	Laser induced phosphorescence
N	Nitrogen
Nd:YAG	Neodymium doped yttrium aluminium garnet (Nd:$Y_3Al_5O_{12}$)

NOC	Nanoparticles of carbon
O	Oxygen
PAH	Polycyclic aromatic hydrocarbons
PC	Personal computer
Q	C_nH_m hydrocarbon chain
R	Alkyl or allyl chain
RME	Rapeseed methyl ester
RO	Rapeseed oil
RPM	Revolutions per minute
SME	Sunflower methyl ester
SNR	Signal to noise ratio
SVF	Soot volume fraction
TME	Tallow methyl ester
TEM	Transmission electron microscope
TIT	Turbine inlet temperature
TLAF	Two line atomic fluorescence
TP	Thermographc phosphor
TR	Time resolved
TSFC	Thrust specific fuel consumption
TTL	Transistor – transistor logic
UCOME	Used cooking oil methyl ester
UV	Ultraviolet
YAG:Dy	Yttrium aluminium garnet doped in dysprosium ($Y_3Al_5O_{12}$:Dy)

Subscripts

0	Initial conditions
1	Wavelength 1
2	Wavelength 2
λc	Centre wavelength
Cal	Calibration measurement
e	Exhaust gas
Exp	Experiment measurement
Fil	Lamp filament
g	Gas
j	Hot thermocouple junction
Lamp	Lamp measurement
m	Film
n	Fuel jet
p	Particle
s	Surroundings

Greek symbols

α	Thermal diffusivity		$[m^2s^{-1}]$
ε	Emissivity		
η	LII calibration factor		
η_t	Thermal efficiency		
$\theta(\lambda)$	Detector response		
κ	Thermal conductivity		$[Wm^{-1}K^{-1}]$
λ	Wavelength		[nm] or [m]
π	Pi	3.14159265359	
ρ	Density		$[kgm^{-3}]$
σ	Stefan-Boltzmann constant	5.670400×10^{-8}	$[Js^{-1}m^2K^{-4}]$
$\tau(\lambda)$	Filter transmission		
ϕ	Radiated power per unit volume		$[Wm^{-3}]$
Ω	Solid angle of detection		[steradian]
ω	Laser sheet thickness		[m]

Roman symbols

A_P	Area of aperture		$[m^2]$
(A_L/u^2)	Solid angle of collection		
c	Speed of light	299792458	$[ms^{-1}]$
c_p	Specific heat capacity		$[Jkg^{-1}K^{-1}]$
d	Diameter		[m]
D	Dark current		
E(m)	Soot absorption function		
f	Fuel to air ratio		
f_v	Soot volume fraction		
G	Gain		
h	Planck constant	$6.62606957 \times 10^{-34}$	$[m^2kgs^{-1}]$
h_c	Convective heat transfer coefficient		$[Wm^{-2}K^{-1}]$
I	Measured intensity		[counts]
j	Irradiance		$[Wm^{-2}]$
k	Boltzmann constant	$1.3806488 \times 10^{-23}$	$[m^2kgs^{-2}K^{-1}]$
M	Magnification		
m_f	Mass flow rate		$[kgs^{-1}]$
Nu	Nusselt number		
Q_R	Lower heating value of combustion		$[kJmol^{-1}]$
R_p	Radius		[m]
R_S	Spectral radiance		$[Wm^{-2}sr^{-1}nm^{-1}]$
T	Temperature		[K]
T	Thrust		[N]
t	Response time		[s]
v	Volume		$[m^3]$
V	Velocity		$[ms^{-1}]$

Contents

List of figures

List of tables

CHAPTER 1
INTRODUCTION

1.1 Introduction and motivation

Combustion is one of the oldest technological processes, dating back almost 800,000 years. It is widely used throughout modern society in many domestic and industrial applications, including transportation, manufacturing and power generation and is currently receiving a large amount of attention in scientific research due to worldwide environmental and sustainability conditions (Law, 2007). There is considerable interest in improving combustion efficiency and finding viable alternatives to energy production, such as renewable sources and biofuels (Agarwal, 2007).

There has been significant work and a great deal of debate put into fossil fuel depletion and global warming in recent years. Both economic and environmental issues are affected by the usage of fossil fuels and ideal solutions to the majority of problems involving them are still unresolved. A recent study (Shafiee & Topai,

2009) predicts fossil fuel supplies of oil, coal and gas could be depleted by 35, 107 and 37 years respectively. The fact that these fuels are diminishing leads to alternative fuel solutions, as many industrial and domestic applications involve them. Renewable energies such as wind, solar and hydroelectric power have the advantage of producing no emissions which is good for aiding in the fight against global warming. Their downsides are that with current technology, massive wind farms, huge hydroelectric dams or many acres of solar panels are required to provide a substantial amount of energy. Hydrogen and nuclear energy are slightly more developed and can be used for larger scale processes, but they have their own underlying issues to contend with, such as safety and application to transport. Therefore, another option is biofuels; fuels which are renewable, provide a large amount of return per litre used and produce a smaller amount of emissions than their fossil fuel counterparts.

Biofuels are becoming a formidable alternative to fossil fuels, with ever growing research interest and worldwide usage. Biodiesels are proving to be a viable route towards cleaner combustion, with more realistic usage goals, in terms of new technology and converting current designs, compared with other renewable sources. In particular transport, where current internal combustion engine designs can be modified to use biodiesel, whereas other renewable sources, which produce less power, would require a whole new infrastructure to function normally. Biodiesels are an achievable and sustainable option for near future solutions.

There have been many studies on biofuels, including looking into their efficiency, emissions and sustainability in practical devices, such as gas turbine engines (Borjesson & Tufvesson, 2011; Love, et al., 2009; Martin & Eklund, 2011). There are important factors to consider, including finding a replacement for fossil fuels such as oil. The burning efficiency of the fuels relates to the amount of work that can be done by burning them which is clearly of great importance. One way of measuring this is to look at the combustion process itself, especially the products of incomplete combustion. Equation (1.1) shows the ideal equation of combustion of hydrocarbons

with oxygen and Equation (1.2) is the equation of combustion with air (Flagan & Seinfeld, 1988).

$$C_nH_m + \left(n + \frac{m}{4}\right)O_2 \longrightarrow nCO_2 + \frac{m}{2}H_2O \qquad (1.1)$$

$$C_nH_m + \left(n + \frac{m}{4}\right)\left(O_2 + 3.78N_2\right) \longrightarrow nCO_2 + \frac{m}{2}H_2O + 3.78\left(n + \frac{m}{4}\right)N_2 \qquad (1.2)$$

In real life situations combustion occurs in air and is not ideal. The ideal equation assumes all of the reactant fuel reacts with air to produce carbon dioxide and water, with the nitrogen remaining unchanged. Real life combustion occurs at high temperatures, producing nitrogen oxide compounds and is almost always incomplete, leaving partially and unburned hydrocarbons in the exhaust gases, as well as soot. A measure of these particular emissions in conjunction with engine performance could help categorise biofuel efficiency and applicability. Nitrogen oxide compounds, referred to as NO_X, can form through either prompt or thermal mechanisms. Prompt reactions result from molecular nitrogen (N_2) reacting with radicals produced during fuel pyrolysis and thermal reactions are a result of N_2 decomposition and subsequent atomic nitrogen reactions. Nitrogen oxide compounds are toxic and can be lethal (Hartzell, 1996) and can be a problem within gas turbine engines, which are involved with high temperature combustion. Some biodiesels are blended with diesel or other fossil fuels in an attempt to reduce emissions, prolong oil reserves and improve biodiesel performance, as biodiesels alone may not be efficient or sustainable enough. However, if the biodiesel is blended with a fossil fuel such as diesel the performance could be improved and emissions may also decrease, resulting in an overall better solution.

It can be seen from Equation (1.1) that combustion produces CO_2, which is a greenhouse gas. So called greenhouse gases contribute to global warming by increasing the amount of infrared radiation that remains within the atmosphere. The energy absorbed by the earth from the sun therefore becomes greater than that which

can escape, causing an increase in temperature over time. Improving combustion efficiency in current technology is a good way to reduce CO_2 emissions, where increasing the amount of work done for a given amount of fuel will result in a lower amount of CO_2 produced.

The combustion process produces undesirable particulate emissions including soot and nanoparticles of organic carbon (NOC) which form from incomplete combustion of hydrocarbons. Epidemiology studies show that these pollutants are toxic, resulting in a decline in human health as well as increased mortality rates in certain areas (Dockery, et al., 1993; Osunsanya, et al., 2001; Oberdörster, et al., 2005; Kennedy, 2007). Environmental and sustainability reports indicate that issues such as global warming and depleting fossil fuel reserves are becoming more and more prevalent (Penner & Berlad, 1995). There has been a significant impact due to these findings, leading to increased pressures on westernised countries from governments to decrease particulate emissions, as well as other harmful by products of combustion, by progressively tightening legislation.

The ever increasing regulations have led to the need to reduce emissions and improve combustion efficiency to meet targets, as well as more efficiently utilising fossil fuel resources. This requires improved combustion equipment to be developed through a better understanding of the chemical and physical processes that occur during combustion, which can be achieved through advanced fundamental and applied research. Fundamental studies on laboratory flames can provide insights into the soot formation process without using large amounts of fuel and using relatively simple burner equipment, compared with engine studies (Love, et al., 2009).

1.2 Flow regimes

The properties of the working fluid in any combustion system will determine its efficiency. Physical properties such as density, temperature, viscosity and whether the flow is laminar or turbulent can be very important parameters when considering efficiency. When considering the flow regime, either laminar or turbulent flow can

be beneficial, depending on the application. For example, in flame studies it can be advantageous to keep the flame stable and laminar for consistency. Also, in practical applications turbulent mixing is often used, especially in combustion in order to increase the rate of reaction. Fluid flow is defined in terms of Reynolds number, which is a dimensionless ratio of the dynamic pressure and shearing stress of the flow, calculated using flow velocity, density, viscosity and a length which is characteristic to the particular problem. For flow within a pipe, the laminar region is defined as having a Reynolds number that is less than 2300, there is a transitional period between 2300 and 4000, above which the flow becomes fully turbulent. Laminar flow is smooth and steady, occurring in low flow rate applications. Turbulent flow is characteristic of unpredictability, conveying eddy structures and vortices, often occurring in high flow rate situations. Studying turbulent flow, either in fundamental or practical applications can lead to more efficient real world solutions such as better engine designs, enhanced gas turbine aerodynamics and cleaner combustion.

1.3 Flame types

There are two main types of combustion, namely premixed and non-premixed, or diffusion flames. Diffusion flames are not premixed with an oxidant to any extent and mix with an oxidant at the exit of the fuel feed pipe by means of molecular diffusion. The fuel and oxidant in partially premixed and premixed flames are allowed to mix together to some extent before ignition and the main mode of transport is mixing. Laboratory flames emanating from a pipe are considered to be fully premixed when the length/diameter (L/d) ratio of the mixing pipe is greater than 50. When the L/d ratio is less than 50 the flow is considered to be partially premixed and the behaviour of the flame can again, be different. Both flame types are common in practical combustion devices used throughout the world. For example in automotive transport, non-premixed combustion is used in diesel engines and premixed combustion in spark ignition engines.

Investigations into premixed and non-premixed combustion processes generally consist of either fundamental or practical applications, where fundamental studies are on flames and practical applications are carried out in engines. Both have advantages and disadvantages associated with them. Flame studies are done using burners which generally do not use much fuel, it is also easy to access the combustion process physically for sampling and optically, for laser diagnostics. Their main purpose is to gain insight into the fundamental physical and chemical processes which occur during combustion. Some types of burners include cylindrical flame burners, producing coflow and inverse diffusion flames, counterflow burners, flat flame and slot burners such as the Wolfhard-Parker burner, wick burners and vaporiser chambers for liquid fuels and shock tubes.

Engine studies can produce real world results, which can directly impact practical solutions, leading to improvements in design and technology. Often practical applications can build on the fundamental knowledge gained in flame investigations. The downside is that large amounts of fuel and time can be used during engine experiments. Types of internal combustion engines include spark ignition, direct injection compression ignition and homogeneous charge compression ignition. Gas turbine engines have also been used to test fuels.

1.4 Laser induced incandescence

In order to understand the soot formation and oxidation processes in combustion and hence to improve practical combustion systems in terms of efficiency and reducing soot, high fidelity quantitative diagnostics with precise spatial and temporal resolution detection capabilities are required. The combustion process involves fuel being oxidised to some extent which causes reactions to take place between the molecules until products and by-products of combustion are produced. Hydrocarbon fuel combustion produces carbonaceous nanoparticles and there are considered to be many intermediate reactions during combustion which are yet to all be found and categorised. Soot is a carbonaceous material that is produced during incomplete

combustion. The production of soot is affected by numerous factors, including temperature, equivalence ratio, fuel properties and oxidiser properties, among others.

Soot diagnostics consist of intrusive and non-invasive techniques. Intrusive techniques involve sampling soot directly from a flame or exhaust. These methods face challenges and limitations involved with preserving and transporting the particulates (Hofeldt, 1993). Non-invasive techniques have the advantage that they do not interfere with the sample. However, they often require the knowledge of many complex variables of which some may be unknown, or at least imprecisely defined.

Laser induced incandescence (LII) is a non-invasive, laser diagnostic technique which can be used for qualitative and quantitative soot volume fraction (SVF) and soot size measurements in laminar and turbulent flames (De Iuliis, et al., 1998; Köhler, et al., 2011; Snelling, et al., 2004), as well as in practical combustion systems, such as engines with combustion chamber optical access (Bougie, et al., 2007; Menkiel, et al., 2012; Labecki & Ganippa, 2012; Labecki, et al., 2013). The main principle is to use a high energy laser pulse to heat up the soot particles within the flame to approximately 4000 K, where they begin to sublimate. The temperature dependant properties of the consequent Planck radiation can be used to determine certain parameters of soot. In terms of radiation, soot can be treated as a black body, which means its radiation at a known temperature can be related to various soot properties, including initial laser heated soot temperature, soot volume fraction and diameter of primary particles. Other non-invasive techniques include LIF, PIV, CARS, TLAF and LIBS. These techniques can measure parameters including temperature, soot and velocity and some are briefly discussed in Chapter 5.

1.5 Laser induced phosphorescence

Temperature is closely linked with soot formation and pyrolysis mechanisms and is therefore a very important aspect of soot measurements. The formation and behaviour of soot precursors and particulates are governed by the temperature distribution of the environment they are in. Thermocouples are widely used to

measure the temperature of a system at specific points, however in small scale studies involving laboratory flames, intrusive techniques are undesirable, as they may cause a significant error due to relatively large perturbations in the flow.

Laser thermometry enables in-situ measurements to be carried out with minimal disturbances and with high spatial and temporal resolution, which is an advantage when measuring dynamic systems such as those in fluid flow and combustion. Improving the understanding of such systems will lead to more efficient real world solutions such as better engine designs, enhanced gas turbine aerodynamics and cleaner combustion. The particular technique used in this study is laser induced phosphorescence (LIP), which is a new for gas phase temperature measurement and has only been carried out successfully a small number of times.

LIP is a semi-invasive, thermometry technique that uses the temperature dependent properties of thermographic phosphors (TPs) to determine the temperature of a system. A phosphor is a microcrystalline solid luminescent material which appears transparent but comes in powder form and is usually white in appearance due to light scattering. Phosphors are thermographic if they display variations in their emission characteristics with a change in temperature. TPs are generally made up of ceramic materials doped in rare earth metals (Yen, et al., 2007). Each chemical exhibits different absorption and emission characteristics, with varying temperature sensitivity and survivability capabilities, making TPs suitable for thermometry measurements in environments from cryogenic to combustion temperatures (Allison & Gilles, 1997).

1.6 Aims and objectives

The main objective of the project was to gain a better understanding of the early soot formation process through increasing the knowledge of temperature distributions and soot measurements in flames, combined with the knowledge of how soot is produced, from pyrolysis and throughout its growth into its final form. Thermographic phosphor thermometry using LIP was used to produce temperature

distributions within turbulent flows and laminar flames, where the work focused on improving the knowledge of the particular thermometry technique.

Soot emissions tests were carried out on laboratory flames and in a gas turbine engine for practical applications. Soot volume fraction measurements using LII were carried out on two types of flames, namely gas and liquid fuel flames, with the purpose of improving the overall understanding of pyrolysis and soot formation. The gas fuel flames were diluted with nitrogen and carbon dioxide, as well as adding varying amounts of hydrogen, in order to analyse their effects singularly, as well as together. The liquid fuel burner was used to compare various biodiesels with each other and standard diesel, as well as diesel-biodiesel blends. A pilot study was carried out on a gas turbine engine, measuring unburned hydrocarbons and NO_X emissions of biodiesels and diesel-biodiesel blends. The investigation was split into several main tasks which are briefly discussed below.

1.6.1 Characterising the LIP technique for 2D temperature measurements in non-reacting jets

There is very limited work available in the literature regarding gas phase temperature measurements using LIP. It was therefore essential to become familiar with the technique before attempting to further develop it for usage in flames. Investigations into high temperature thermographic phosphors were carried out, in order to find TPs which could be used for combustion. The experimental setup was put together and optimised through experiment. Finally, spectral and image results were acquired. The performance of two particular, so called high temperature TPs, BAM and YAG:Dy were compared in detail in heated turbulent jets, using the gas phase LIP technique.

1.6.2 The suitability of LIP for flame thermometry

Characterising the technique in terms of seeding TPs and optical setup was an essential prerequisite to developing the technique for usage in flames. Crucial knowledge was gained which had to be applied and adapted for successful flame temperature measurements. Two dimensional temperature measurement techniques which can be carried out in combustion environments are essential to improving the

understanding of the combustion process. This part of the project utilised the first thermometry measurements carried out with TPs in a flame in this way, where LIP temperature profiles were compared with corresponding thermocouple measurements, with the purpose of determining the suitability of the technique, as well as the particular TPs used, for flame temperature measurement.

1.6.3 Effects of diluents on soot formation in gaseous fuels

A burner was built where gaseous fuel and diluents could be introduced into the flow before being ignited at the burner exit. The LII optical setup was put together and optimised based on information from the literature and preliminary experiments. Once the setup was established, LII measurements were carried out on a series of flames with different amounts of nitrogen, CO_2 and hydrogen, in order to find out how soot is affected by dilution and hydrogen enrichment singularly and together.

1.6.4 Effects of biodiesel composition on soot formation

For the liquid fuel flame experiments, the same LII optical setup was used as that in the gaseous fuel soot measurements. A wick burner was used which allowed the fuel to be ignited without any preheating or vaporisation. The flame size could be varied with wick height. The main purpose of these experiments was to compare the sootiness of flames for the various fuels in order to determine the compositional effects on soot formation. Gas chromatography was used to determine the fuel composition. The SVF results are complimented with thermophoretic sampling and a pilot study involving a gas turbine engine was carried out in order to relate the study to practical applications. All aspects of this investigation will lead to an improved understanding in combustion processes, ultimately resulting in cleaner combustion.

1.7 Thesis layout

This investigation is split into two main parts, firstly focusing on the temperature measurements using LIP and secondly, the soot measurements using LII and thermophoretic sampling, along with gaseous emission measurements using exhaust gas analysers. This thesis is organised as follows. Chapter 2 includes the scientific

background and literature review of LIP applied to gas phase thermometry. The LIP experimental setup and methodology are discussed in Chapter 3 and Chapter 4 presents the results from the heated turbulent jet and flame temperature experiments, of which the turbulent jet results have been published in Optics Express (Lawrence, et al., 2013). Chapter 5 introduces the scientific background of soot, including soot formation and oxidation, as well as how soot is influenced in relation to dilution and fuel composition. The soot experiments are discussed in detail in Chapter 6, with an introduction to LII and derivation of the key equations. Chapter 7 presents soot volume fraction results for both gas and liquid fuelled flames, as well as fuel composition results and TEM images for the diesel and biodiesel fuels. The gas turbine engine pilot study is discussed in Chapter 8. Finally, conclusions are presented in Chapter 9, along with recommendations for future work.

CHAPTER 2
GAS PHASE LASER INDUCED PHOSPHORESCENCE

2.1 Introduction

The scientific background of laser induced phosphorescence is covered in this chapter. Section 2.2 details the physical interactions occurring within molecules, with respect to absorbing and transmitting energy, explaining fluorescence and phosphorescence. The laser induced phosphorescence thermometry technique is introduced and outlined in Section 2.3. Section 2.4 describes two particular, so called high temperature TPs, BAM and YAG:Dy in detail, in terms of the physical mechanisms leading to their particular phosphorescence emission. Main issues with the gas phase LIP thermometry technique are described in section 2.5. Section 2.6 introduces thermocouple thermometry, which is used to determine the error of the LIP temperature distributions.

2.2 Fluorescence and phosphorescence

Every molecule has several electronic states that are a combination of different available electron orbits and spin orientations, which are further divided into vibrational and rotational energy levels. Each electronic energy state, whether ground or excited has a number of vibrational energy levels which can transfer small increments of energy corresponding to molecule vibrational modes, whilst the molecule retains its electronic energy level configuration. These electronic states are represented in Figure 2.1 as groups of horizontal lines which denote the vibrational energy levels.

A molecule can absorb energy and reach an excited energy state via several methods including electronic excitation, vibrational excitation and light absorption through physical, mechanical or chemical processes. Luminescence is defined as the radiative emission through the electronic de-excitation of a molecule from an excited energy state to a lower energy level. Photoluminescence is defined as the emission of visible light following excitation via the absorption of photons and is split into two types; fluorescence and phosphorescence. Fluorescence emission occurs throughout excitation and the fluorescent lifetime is governed by the decay lifetime of the emitting energy state which can range from 10^{-9} to 10^{-7} seconds (Pringsham, 1949; Valeur, 2001). Phosphorescence emission is also governed by the decay lifetime of the emitting energy state, which is several orders of magnitude longer than that of fluorescence, ranging from 10^{-6} to 10^{2} seconds. This longer decay lifetime is due to forbidden (less likely) electronic energy transitions occurring, either directly or indirectly. Radiative transitions are represented in Figure 2.1 as straight arrows.

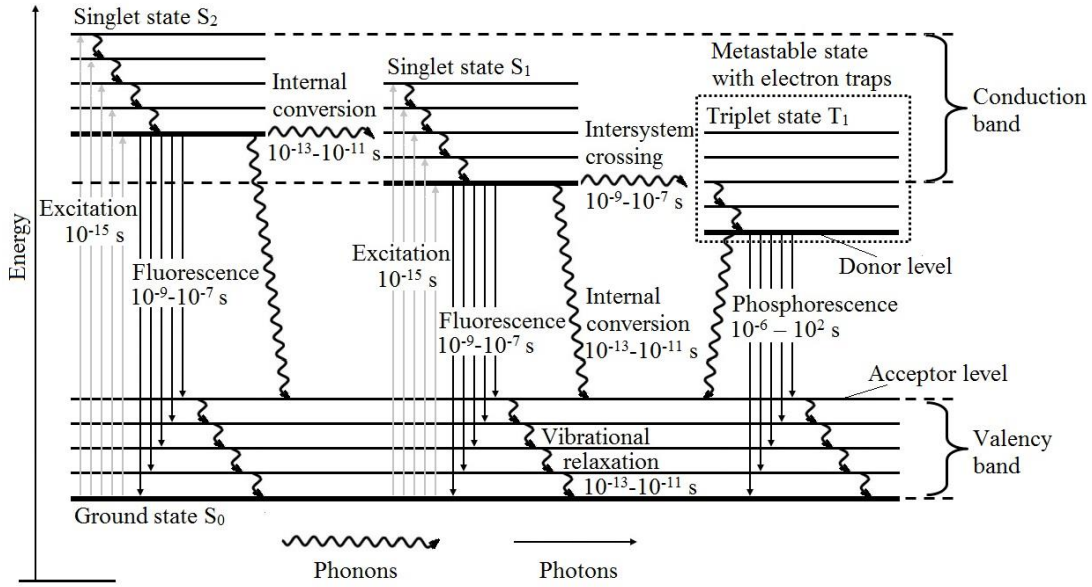

Figure 2.1. Energy level diagram conveying energy transfers within thermographic phosphors.

The difference in electronic energy levels is the photon energy. A certain range of photons can excite a molecule and another range will be emitted subsequent to electronic excitation. The difference between energy absorbed and energy emitted in the form of photons is called the Stokes shift. The Stokes shift is generally towards a longer wavelength due to the lower energy transitions involved and occurs due to other non-radiative energy transfer mechanisms, such as vibrational relaxation and internal conversion. These non-radiative energy transfer mechanisms are known as phonons and are represented in Figure 2.1 as wiggly arrows. Vibrational relaxation transfers energy between higher to lower vibrational energy levels, within an electronic energy state (10^{-13} to 10^{-11} s). Other internal conversion mechanisms can occur from the lowest vibrational energy level of an excited state to another excited state with the same multiplicity of lower energy (10^{-13} to 10^{-11} s). Intersystem crossing is a spin dependant internal conversion (10^{-9} to 10^{-7} s) (Valeur, 2001). Quenching is the non-radiative transition of energy to another atom or molecule. Internal conversions and quenching are processes which compete with radiative processes.

Fluorescence can be summarised as follows. A photon is absorbed (10^{-15} s), exciting the molecule to a higher energy state of similar multiplicity, where typically, some energy is transferred between higher to lower vibrational energy levels via

vibrational relaxation (10^{-13} to 10^{-11} s). Finally, energy is emitted from the molecule to the lowest vibrational level of the excited electronic singlet state to the ground state by releasing a photon (10^{-9} to 10^{-7} s). Phosphorescence follows the same excitation and vibrational relaxation mechanisms as that described for fluorescence, however instead of a photon being released from the molecule to the ground state, energy is transferred through intersystem crossing (10^{-9} to 10^{-7} s) via an electron spin flip occurring, from a singlet state to a triplet state (Valeur, 2001). A singlet state has all its electrons with their spins paired and a triplet state has one of the electrons with spin unpaired and is always lower in energy compared with its corresponding singlet state. Energy is then transferred down to the lowest vibrational level of the excited triplet state through vibrational relaxation (10^{-13} to 10^{-11} s). Finally, a photon is released from the molecule to the singlet ground state, typically with a relatively longer decay time, compared with fluorescence (10^{-6} to 10^{2} s), because it depends on the time it takes for the electron spin to flip back. The radiative emission is lower in energy compared with excitation and fluorescence due to the lower energy of the triplet state. Fluorescence and intersystem crossing, leading to phosphorescence are competing processes which can both occur following excitation.

An electron spin flip can occur if the correct conditions are present. For inorganic phosphors a transparent microcrystalline host material is doped with small amounts of impurities, usually rare earth ions or transition elements. Crystals are transparent when the incident light energy is lower than the difference between the electronic energy bands of the crystal (Nara & Ibuki, 2006). Dopants are used to reduce the energy gap between electronic levels, creating metastable states which can create traps for electrons, see Figure 2.1 for details. Excited electrons become trapped in the donor level of the conduction band (conveying triplet characteristics) and holes become present in the acceptor level of the valency band, producing red shifted light due to the lower energy gap. The radiative transition energy can correspond to the distance between donor and acceptor pairs in the molecule which can vary and hence, broadband excitation and emission can occur (Nara & Ibuki, 2006; Ozawa, 2007).

2.3 Laser induced phosphorescence

2.3.1 Background

LIP is a relatively simple technique with respect to the experimental setup and post processing methodology, compared to other laser-based thermometry techniques, such as CARS, LIF, LIBS and TLAF. The limitations in terms of speed and temperature of the technique depend on the specific TP and therefore LIP could be applied to a wide range of surface and flow situations. Challenges that occur when using thermographic phosphors include overcoming the stickiness of the particles and discovering an efficient seeding method. The particles must be seeded within the flow with a sufficient enough volume density that a significant phosphorescence signal can be detected. Low signal to noise ratio is one of the major concerns in gas phase LIP. These challenges are met and discussed in more detail later on.

Both the phosphorescence emission spectra and decay lifetime are affected by temperature variation (Fuhrmann, et al., 2013). Therefore it is possible to perform temperature measurements using two methods. The spectral method takes the ratio of two or more bands of the emission spectrum, compared with previously recorded calibration data, to convey the local temperature (Wade, et al., 2003). The temporal method records the time it takes for the phosphorescent emission to decay to 1/e or $1/e^2$ of the starting level (Someya, et al., 2009). The time constant of the decay rate is usually determined by fitting a mono-exponential curve to the data, through which the temperature can be found when compared with a calibration measurement. Both methods can be used for either point (Omrane, et al., 2003) or planar measurements (Sarner, et al., 2008), achieved by using a focused laser beam or laser sheet, respectively. Planar measurements are essential for surveying a flow field and are advantageous for combustion studies. TPs provide a high signal yield, where the intensity ratio is insensitive to oxygen quenching and is very negligibly affected by laser profile and TP concentration.

The LIP technique has been applied to surface temperature measurements, such as thermal barrier coatings (Eldridge, et al., 2004), optical access internal combustion

engines (Fuhrmann, et al., 2012) and gas turbine studies (Tobin, et al., 1990; Noel, et al., 1991; Feist, et al., 2002). In order to carry out surface temperature measurements the TPs have to be adhered to the surface in question. Specific adhesives are required for this, which are called binder materials, this is usually a liquid which can be easily mixed with the TP powder and then the mixture painted onto the surface. Surface measurements are well established and the work has been reviewed in the following review articles (Allison & Gilles, 1997; Aldén, et al., 2011; Brubach, et al., 2013). More recently thermometry techniques using TPs have advanced from surface measurement to droplet and spray applications (Omrane, et al., 2004; Omrane, et al., 2004; Brubach, et al., 2006), where instead of the TP powder being attached to a surface it is suspended within a droplet of solution. This led the way for non-surface measurements, leading to the capability of gas phase temperature measurement, where TPs are seeded within the flow in powder form. Examples of previous studies in the gas phase include fundamental studies of heated jet temperature distributions (Hasegawa, et al., 2007 a; Omrane, et al., 2008; Fond, et al., 2012; Rothamer & Jordan, 2012; Jovicic, et al., 2012; Abram, et al., 2013) and more practical applications of in-cylinder temperature measurements in engines and pressure vessels (Hasegawa, et al., 2007 a; Hasegawa, et al., 2007 b; van Lipzig, et al., 2012).

2.4 Thermographic phosphors

2.4.1 High temperature thermographic phosphors

As mentioned previously, specific thermographic phosphors produce phosphorescence emission sensitivity at different temperature ranges. The choice of TP will therefore reflect on the accuracy and reliability of the temperature measurement. Flame temperature measurements require TPs that must first of all survive in harsh, high temperature combustion environments and also convey phosphorescence emission sensitivity at these high temperatures. There has been a lot of research interest in high temperature thermometry using TPs. Possible TP candidates for combustion temperature measurements include Y_2O_3:Eu, $LuPO_4$:Dy, BAM:Eu, Y_2O_2S:Sm and various YAG based phosphors (Aldén, et al., 2011; Bosze, et al., 2011; Feist & Heyes, 2000; Cates, et al., 2003; Heyes, 2009). YAG:Dy and

BAM:Eu were chosen for this study for their particular attributes which are discussed below.

2.4.2 YAG:Dy

YAG is the acronym for yttrium aluminium garnet, with chemical formula $Y_3Al_5O_{12}$. The specific TP used in this study is $Y_3Al_5O_{12}$:Dy, which is YAG doped with trivalent dysprosium (Dy^{3+}) ions. In this work 2.5 and 10.2 µm median diameter YAG:Dy particles (QMK66/UF-X and QMK66/N-X respectively) were used, which were provided by Phosphor Technology Ltd. YAG crystals are widely used in solid state lasers, such as Neodymium doped YAG (Nd:YAG) lasers. The YAG:Dy crystal structure is described as body centred cubic, with Dy^{3+} ions replacing Y^{3+} ions at the dodecahedral Y^{3+} sites in the $Y_3Al_5O_{12}$ host lattice (Raju, et al., 2010). There are three emission bands in Dysprosium that occur from ^4I to ^6H transitions in the Dy^{3+} ion, see Figure 2.2 for details. The most energetic of which is an electric dipole around 453 nm, due to the transition from $^4I_{15/2}$ to $^6H_{15/2}$. This band is weak near room temperature, but intensifies significantly as temperature increases (Cates, et al., 2003). The remaining blue part of the spectrum between 460 and 500 nm is due to electronic transitions $^4F_{9/2}$ to $^6H_{15/2}$, corresponding to a magnetic dipole transition which is insensitive to crystal field symmetry around the Dy^{3+} ion. The yellow emission band from 555 - 610 nm is due to electronic transitions $^4F_{9/2}$ to $^6H_{13/2}$, relating to a forced electric dipole transition which is strongly influenced by the crystal field. At a local site without inversion symmetry, the yellow emission is dominant, however for YAG:Dy^{3+} there is inversion symmetry and the blue emission is prevalent (Raju, et al., 2010; Skinner, et al., 2009).

Increasing the temperature can affect the spectrum of rare earth ions in several ways. Broadening of linewidth due to lattice vibrations, or phonons, which also reduce the radiative transition lifetime via quenching, vibrational relaxation and internal conversions, represented in Figure 2.2 as wiggly arrows, where the increased vibration non-radiatively relaxes the excited electronic state. Thermal expansion of the lattice creates larger ion separation, which can lead to a frequency shift, reducing the crystal field and reducing Stark component separation (Goss, et al., 1989). An

increase in the population of upper energy levels of the system, according to Boltzmann's law, causes the intensity distribution of the spectrum to change with temperature. This thermalisation effect occurs when two rare earth energy levels are relatively close to one another. It can be seen from Figure 2.2 that YAG:Dy displays this in its F and G energy levels, which are separated by about 1000 cm^{-1}. Laser light can excite the Dy^{3+} ions into the F level, which undergoes fast thermal equilibrium and can pump some of its population to the G level and phosphorescence can then be observed from both states. At low temperatures, the G level will generally not emit phosphorescence due to very high multiphonon relaxation rates which quench the closely spaced levels. The population of the G level emission band rises with temperature, significantly increasing the amount of phosphorescence from this level. Above 1800 K the phosphorescence intensity diminishes below detectable limits due to large phonon quenching rates at such high temperatures (Goss, et al., 1989).

The melting point of the YAG crystal is approximately 2200 K (Caslavsky & Viechnicki, 1980). Phosphorescence decay time ranges from 1 ms at room temperature to an order of 1 μs at high temperatures (Cates, et al., 2003). The survivability of the YAG:Dy phosphorescence at high temperatures has been investigated, where the intensity ratio was found to be the same before and after the phosphor particles had passed through a flame front (Yu, et al., 2010).

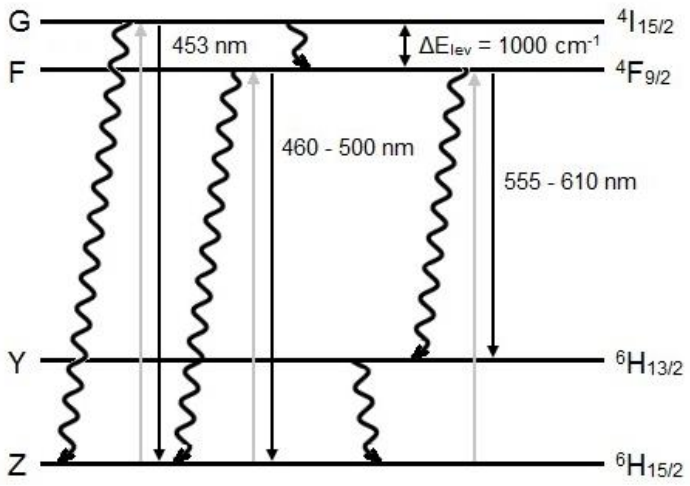

Figure 2.2. Simplified YAG:Dy^{3+} energy diagram, where grey arrows represent absorption of a photon and excitation to a higher energy level, black wiggly arrows represent non-radiative de-excitation mechanisms (phonons) and black straight arrows represent radiative de-excitation mechanisms (photons) i.e. phosphorescence.

2.4.3 BAM

BAM is the common name for barium magnesium aluminate, with chemical formula $BaMgAl_{10}O_{17}$. The specific TP used in this study is $BaMgAl_{10}O_{17}$:Eu, which is BAM doped in divalent europium (Eu^{2+}) ions of 2.9 µm median size BAM particles (KEMK63/UF-P1) which were provided by Phosphor Technology Ltd. BAM is widely used in display technology such as plasma display panels (Ronda, 1997; Justel, et al., 2003; Kim, et al., 2003). It has a β-alumina crystal structure which is made up of spinal blocks, spaced by conduction layers. The BAM:Eu has its barium ions in the conduction layer replaced with Eu^{2+} ions which activate it, producing a highly efficient broad band emission around 450 nm, due to the transition from $4f^6 5d^1$ to $4f^7$ of divalent europium ions (Kim, et al., 2003; Bizarri & Moine, 2005). As the temperature increases the emission band broadens and shifts towards the UV. The decay behaviour of BAM is governed by activator properties and defects in the crystal structure. Divalent europium shows quite a short decay time in the range of 1 – 10 µs due to the 5d – 4f transition. The decay time was shown to be 1.17 µs with a single exponential fit (Ronda, 1997). This short lifetime makes BAM an excellent candidate for turbulent flow visualisation. It also has a high melting point of approximately 2200 K (Ravichandran, et al., 1997).

It has been reported that BAM:Eu^{2+} undergoes a degradation mechanism which occurs when it is heated above a temperature of 500 ºC, in an air atmosphere (Kim, et al., 2003; Bizarri & Moine, 2005). Both emission and excitation efficiency are affected and studies show that the amount of degradation increases as temperature increases, up to approximately 900 K. Near and above this temperature the emission spectra changes. The blue peak around 450 nm diminishes whilst peaks between 580 and 700 nm, in the red region becomes more prominent, with a maximum around 610 nm. This emission is representative of the trivalent europium ion, consistent with the $4f^6$ intra-configurational transitions (Bizarri & Moine, 2005), which is not considered in this study. It has been shown that when the TP is heated in a non-oxidising atmosphere, the emission spectrum remains almost unchanged (Kim, et al., 2003). This evidence points to the degradation mechanism being caused by the divalent europium ion concentration decreasing due to oxidation effects, which results in an increase in trivalent europium ions. There also appears to be a structural variation contributing to the reduced emission around 450 nm, where the location structure of the trivalent ions changes from β-alumina to magnetoplumbite ($EuMgAl_{11}O_{19}$). The degradation mechanism has been reported when BAM is heated for long incubation times of greater than 1 hour (Kim, et al., 2003; Bizarri & Moine, 2005). Though, it is possible that no degradation effects will occur when BAM experiences an extreme temperature environment for a significantly shorter period of time (Fond, et al., 2012). The survivability of the BAM signal was proven in (van Lipzig, et al., 2012), where phosphorescence intensity is shown to be the same, prior and subsequent to a combustion event. However, the work in (van Lipzig, et al., 2012) also disregards results above 650 K due to weak signal. The diminishing signal with increasing temperature is probably due to similar thermal effects as YAG:Dy, such as increased phonon quenching rates at elevated temperatures.

2.5 Gas phase thermometry

2.5.1 Phosphorescence emission signal intensity

It is advantageous for gas phase temperature measurements in a flow to use TPs with a short lifetime and shorter camera exposure, in order to keep up with changes that occur with time. This is especially important in turbulent flows where the time resolution must match the characteristic time scales of the flow. Particle size also determines the quality of the results. Tracer particles must be large enough to produce a significant signal, whilst still small enough to follow the flow with sufficient accuracy (Melling, 1997; Tran, et al., 2009). The result is a trade-off between the two. Due to size limitations it is feasible to capture the global large scale details of the flow, rather than the small scale details. Gas phase measurements suffer from a relatively low signal, compared with surface measurements (Rothamer & Jordan, 2012; van Lipzig, et al., 2012). This is due to a low volume density of TPs seeded within the gas. The signal to noise ratio (SNR) can be improved in several ways, including using TPs with a higher signal yield and greater laser fluence. However the laser fluence must not exceed 1.5 J/cm^2 to prevent laser induced heating effects on the TPs (Lindén, et al., 2009). Laser induced breakdown spectroscopy must also be avoided at high laser fluences, which has been documented in (Lindén, et al., 2009) and was also experienced in the preliminary phases of this study. Blue emitting phosphors are favourable in high temperature studies as the phosphorescence avoids Planck radiation, which increases in the red region of the spectrum as the temperature of the system increases. TPs with a shorter lifetime can allow for time gating in favour of the phosphorescence signal, discriminating against background signals.

2.5.2 Flow to particle temperature equilibrium

The TP particles are required to reach thermal equilibrium with the surrounding flow quickly enough to correctly convey the local gas temperature. A recent study has shown via numerical simulation that smaller particles of around 2 μm diameter will adequately respond to a temperature change of 2000 K. However, a larger diameter leads to significantly increased heat capacity, resulting in longer response times and

therefore affecting accuracy (Fond, et al., 2012). The response time can be calculated analytically using the relationship in equation (2.1), refer to (van Lipzig, et al., 2012) for details:

$$t = \frac{\rho_p R_p^2 c_p}{3k_g} \ln \frac{T_p - T_\infty}{T_d - T_\infty}, \tag{2.1}$$

where t is the response time, ρ_p is the density of the TP particle, R_p is its radius, c_p is the specific heat capacity, κ_g is the thermal conductivity of the gas, T_p is the temperature of the particle, T_∞ is the gas temperature and T_d is 95% of the gas temperature. The heat capacity of BAM is not known and therefore that of aluminium oxide was used (777 J/kgK) (Ginnings & Furukawa, 1953), resulting in a response time of 145 µs for 2.6 µm diameter BAM particles, which was deemed adequate to capture the transients of the flow (van Lipzig, et al., 2012).

In this work, the temperature throughout the particle is considered to be homogeneous. This due to the thermal conductivities of both phosphors being several orders of magnitude higher than the surrounding medium (k_{BAM} = 24.2 W/mK, k_{YAG} = 14 W/mK, $k_{air,300\ K}$ = 0.026 W/mK $k_{air,800\ K}$ = 0.057 W/mK). The same procedure for calculating the response time of the phosphors was used as explained above. The values are set to k_g = 0.0415 W/mK (mid way between $k_{air,300\ K}$ and $k_{air,800\ K}$) with a maximum temperature T_∞ = 850 K. The densities of BAM and YAG:Dy are 3700 and 4550 kg/m^3 respectively and the c_p of undoped YAG crystal is known to be 590 J/kgK (Koechner, 2006). The c_p used for the BAM calculation was also that of aluminium oxide. The response time for the 2.9 µm BAM particles was 124 µs and the 2.5 µm YAG:Dy was 86 µs, which were deemed acceptable for conveying temperature with sufficient accuracy. The larger 10.2 µm YAG:Dy particles showed a 1.4 ms response time which means that they would produce less accurate results. The result is expected to be inexact due to the changing nature of c_p and k_g with temperature and the fact that the of c_p of BAM was unknown.

2.6 Thermocouple measurements

A common method for verifying temperature distributions that have been determined using the LIP method is to compare the results with temperatures derived from thermocouple measurements. A thermocouple is made by joining two wires made of different metals in order to create a 'hot' junction and a 'cold' junction, where the hot junction is placed into the region of interest. The consequent temperature difference between the two junctions creates a potential difference which can be related to the hot junction temperature very accurately. However, the hot thermocouple junction temperature often differs from the surrounding gas temperature due to heat losses. It is therefore necessary to correct thermocouple temperature measurements to account for this difference.

The main sources for the temperature differences in a steady state situation occur from radiative, conductive and convective heat transfer mechanisms, where radiative heat transfer is most prominent in flame measurements. The actual gas temperature in a steady state system can be calculated from an energy balance of these heat transfer mechanisms. However, the mathematics is significantly simplified when only the dominant mechanisms are taken into account. In the case of thermocouple flame temperature measurement it is reasonable to assume that the effects of conduction are negligible, therefore only considering the effects of radiation and convection. The energy balance for a thermocouple at thermal equilibrium in a non sooting flame is therefore (Brundage, et al., 2011)

$$h_c A_s \left(T_g - T_j\right) = \sigma \varepsilon A_s \left(T_j^4 - T_s^4\right), \tag{2.2}$$

where A_s is the surface area of the hot thermocouple junction, σ is the Stefan Boltzmann constant, ε is the probe emissivity, h_c is the convective heat transfer coefficient between the gas and the junction and T_s is the effective temperature of the surroundings for the hot junction. The difference between the surrounding gas temperature (T_g) and the thermocouple hot junction temperature (Tj) can be calculated using the following formula (Pitts, et al., 2002)

$$T_g - T_j = \frac{\sigma\varepsilon}{h_c}\left(T_j^4 - T_s^4\right). \tag{2.3}$$

Values for h_c can be calculated from heat transfer correlations with respect to the Nusselt number (Nu)

$$Nu = \frac{h_c d}{k}, \tag{2.4}$$

where d is the wire diameter and k is the gas thermal conductivity. The Nusselt number can be obtained using (Collis & Williams, 1959)

$$Nu\left(\frac{T_m}{T_j}\right)^a = A + B\,\mathrm{Re}^n = A + B\left(\frac{ud}{\nu}\right)^n, \tag{2.5}$$

where u is the local gas flow velocity, v is the kinematic viscosity, T_m is the film temperature, which is the fluid temperature within the convective boundary layer, which in this case is $T_m = 0.5\left(T_g - T_j\right)$ and a, A, B and n are constants. The thermocouple in a flame problem can be approximated by considering the heat transfer to a cylinder in a cross flow.

CHAPTER 3
JET AND GASEOUS FUEL FLAMES LIP EXPERIMENTAL METHODOLGY

3.1 Introduction

The experimental setup and methodology for the laser induced phosphorescence experiments are detailed in this chapter. Section 3.2 describes the experimental setup, including the heated jet, laminar flame and optical setups. The methodology behind the optimisation of the equipment and the laser induced phosphorescence technique is explained in Section 3.3, in terms of spatial and temporal alignment and equipment calibration. Section 3.4 details the analysis and the methods of the post processing of the data.

3.2 Experimental setup

3.2.1 Heated gas jet setup

The experimental setup involved feeding standard air through a custom built seeder via a controllable flow rotameter. The thermographic phosphors were seeded using vortex generation and mechanical vibration to disturb the powder, which was subsequently entrained into the flow. This seeding method was found to be considerably more effective for the low flow rates used in this study, compared with commercially available aerosol generators. The seeded air was heated with a controllable 2000 W inline heater, reaching a maximum temperature of about 850 K. A retractable type K thermocouple was positioned at the exit of the heater in order to verify the flow temperature. Figure 3.1 shows a diagram of the entire setup. The thermocouple was removed during phosphor thermometry measurements and replaced immediately after to verify flow temperature.

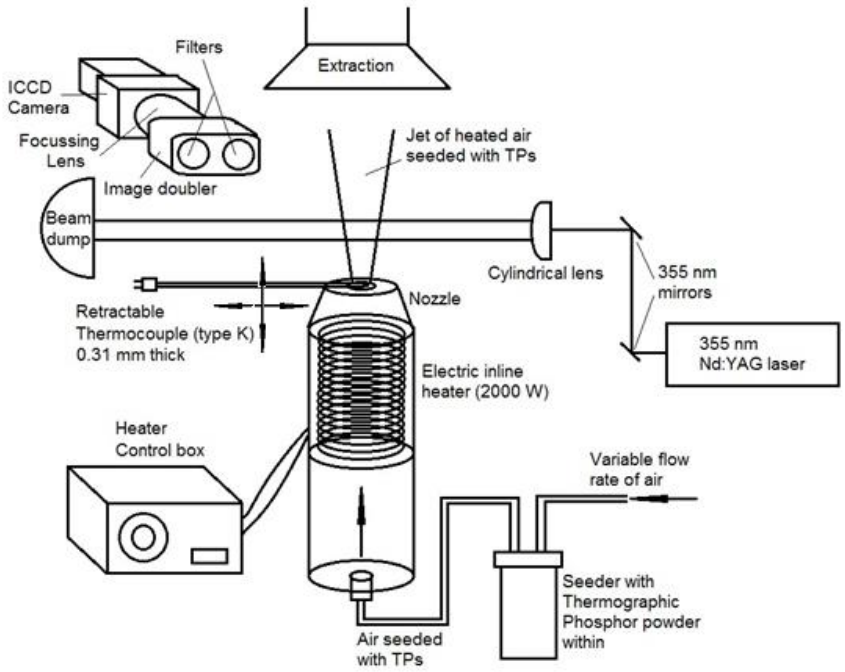

Figure 3.1. Diagram of the heated jet experimental setup.

A free turbulent jet issuing into quiescent air was produced, where the Reynolds number could be varied by changing the flow rate or altering the exit nozzle geometry. For time-averaged shots, steep gradient flow restrictors with 2.1, 4.2 and

8.4 mm sized diameters were used to generate turbulent jets, with Reynolds numbers of 10,000, 5,000 and 2,500 respectively at a flow rate of 15 l/min. For single shot measurements, the larger 8.4 mm diameter nozzle was used in an attempt to improve resolution (larger jet) and the Reynolds number was varied by changing the airflow rate. Flow rates of 10, 15 and 18 l/min were used, producing Reynolds numbers of 1,650, 2,500 and 3,000 respectively. Increasing the flow rate caused a higher phosphor seeding density within the flow, due to increased turbulence within the seeder. The seeding method produced relatively high density seeding at such low flow rates, compared with commercially available aerosol generators.

The stickiness of the particles has been addressed in previous studies (van Lipzig, et al., 2012; Lindén, et al., 2009). This property can become a problem in applied optical engine studies where the phosphors can coat the internal surfaces including the optical window and it is shown that using TPs with a transparent, anti-stick coating would reduce the degree of stickiness (van Lipzig, et al., 2012). The phosphors used herein were uncoated and the smaller 2.5 YAG:Dy and 2.9 µm BAM particles tended to stick significantly more than the larger 10.2 µm YAG:Dy particles. This was denoted by the difficulty of seeding of the smaller particles, compared with the larger ones. A higher seeding density could be achieved at lower flow rates using the larger YAG:Dy phosphors.

3.2.2 Laminar premixed flame setup

The laminar premixed flame experimental setup was very similar to the heated gas jet setup, where the heater was replaced with pipework encompassing the mixing of standard air seeded with TPs with consumer grade propane in order to produce laminar flames that were premixed to some degree. Figure 3.2 depicts a diagram of the setup. The air flow rate was kept constant and the fuel flow rate was changed to achieve the different flames shown in Figure 3.3. The optical setup and image processing techniques were almost identical to the gas jet experiment, where the only difference was that only the smaller 10 mm light sheet was used.

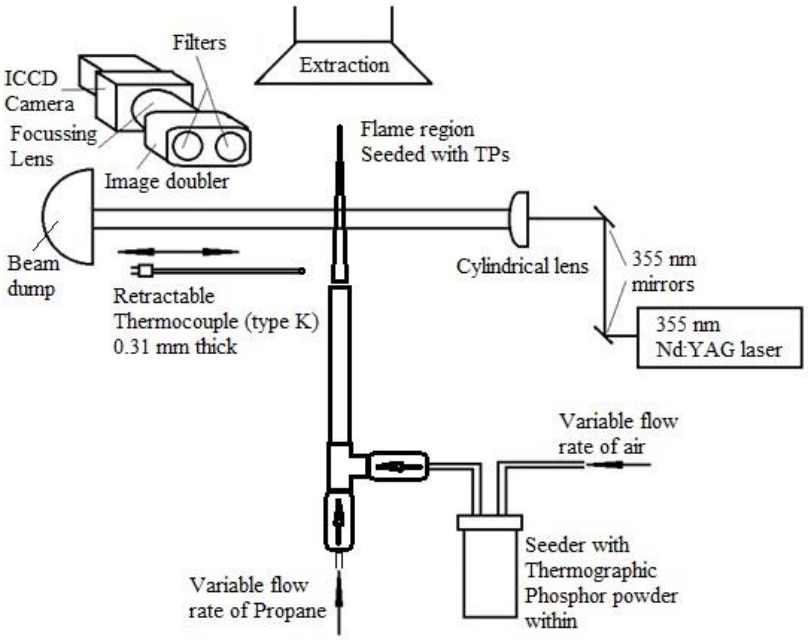

Figure 3.2. Diagram of the laminar flame setup.

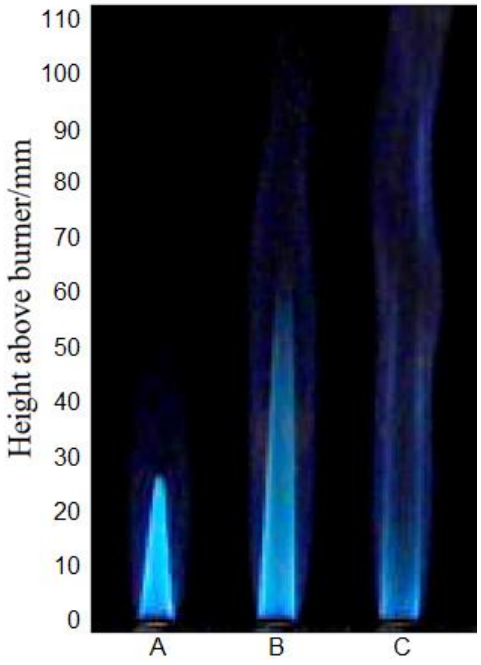

Figure 3.3. Photographs of the flames used in the LIP experiments, where air flow rate was kept constant and fuel flow rate was increased from flame A to B to C.

3.2.3 Optical setup

Both BAM and YAG:Dy were excited with the third harmonic of a Continuum Surelite II solid state, neodymium doped YAG (Nd:YAG) laser, operated at 10 Hz, using a pulse energy of 20 mJ, for phosphorescent excitation. The laser beam was guided using high reflectivity 355 nm mirrors (99.75 % at AOI 45º). Spectral measurements were acquired by focussing the laser beam with a spherical lens and two dimensional measurements were carried out by transforming the beam into a sheet with a cylindrical lens. The laser sheet was 0.5 mm wide and 12 mm high for the accumulated measurements and 0.5 mm wide and 32 mm high for single shot measurements, producing laser fluences of 0.333 and 0.125 J/cm^2 respectively. Both laser sheets were chopped at the extremities, leaving heights of 10 and 30 mm. The phosphorescence emission was focused by a 50 mm Nikkor lens and collected by an Andor Instaspec V ICCD camera through an image doubler from LaVision. High efficiency filters (>90%), corresponding to the individual TP, were placed over the image doubler. Great care was taken to ensure both parts of the image were the same, through alignment and flat fielding. The camera and laser pulse were synchronised using a Stanford Research DG645 delay generator and were controlled by image acquisition software. Spectra were measured at a maximum of 10 Hz and for 2d spectral filtered images, approximately 7 shots per min were acquired. A short delay had to be incurred due to fluorescence interference after laser excitation, which will be discussed in more detail later. Spectral measurements were taken using an imaging spectrograph, 1/8 m, Oriel MS127i, model 77480, with a single grating of 600 lines/mm, combined with the ICCD camera. The entrance slit width was 50 µm, providing a spectral resolution of less than 1 nm.

3.3 Equipment optimisation

The experimental and optical setups had to be linked and optimised in terms of both spatial and temporal alignment. This presented several challenges, including spatially aligning the laser beam and spectrograph with the flow region of interest, spectrograph calibration, temporal alignment of the ICCD camera and laser pulse and for imaging, spatial alignment of the camera and focussing onto the region of

interest. Optimising the setup allowed for the phosphorescence signal to be found and improved in terms of signal quality and intensity. The knowledge gained in this preliminary part of the investigation allowed for successful acquisition of gas phase flow temperature distributions, using the laser induced phosphorescence technique.

3.3.1 Optical alignment

The optical components of the laser induced phosphorescence setup had to be spatially aligned. As discussed in Section 3.2.3, 355 nm mirrors and a cylindrical lens combined with a spherical lens were used to guide and manipulate the laser beam. In order to ensure that the spectrograph was properly aligned a grid system was used, similar to that of a breadboard. A rectangular metal frame was built around the equipment which had holes drilled periodically throughout. This allowed for the spectrograph to be placed at the correct angle and in the exact position for alignment with the centre of the nozzle exit. The spectrograph could also be traversed up and down, while preserving the alignment. Figure 3.4 shows a sketch of the setup.

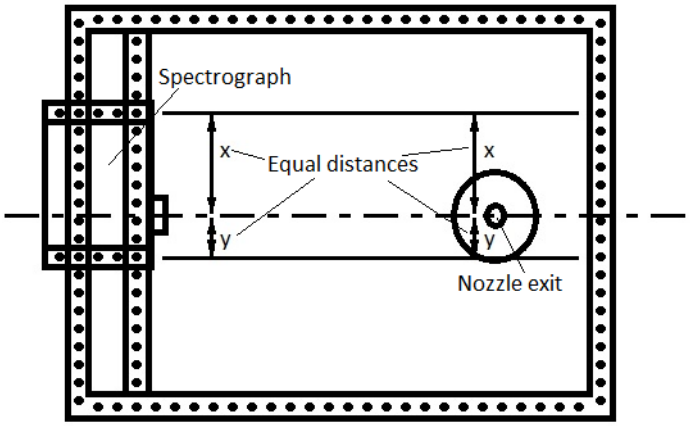

Figure 3.4. Spectrograph alignment setup.

3.3.2 Spectrograph calibration

The spectrograph needed to be calibrated prior to being used for the first time, as well as each time it was moved. The calibration was carried out using a light source with a known spectral emission. In this case a mercury lamp was used, as the spectral region of interest was in the near ultraviolet to visible region. A method similar to that stated in (Andor Technology Limited, 1999), combined with the specification for

the particular spectrograph, was used to identify the relevant spectral emission peaks and complete the calibration.

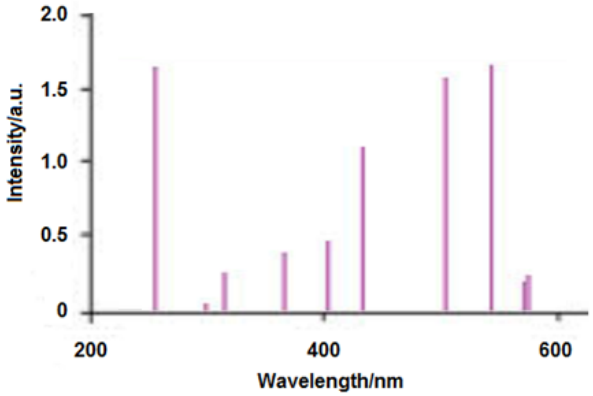

Figure 3.5. Mercury lamp spectrum (Ocean Optics, 1989 - 2012).

Figure 3.5 shows the emission spectrum produced by a mercury lamp. However, it should be noted that spectrographs with different gratings can pick up different spectral emission lines. Table 3.1 below lists the spectral lines produced by mercury vapour lamps (Ocean Optics, 1989 - 2012).

Table 3.1. Mercury lamp spectral emission lines in nanometres.

Ultraviolet	Visible
253.652	404.656
296.728	407.783
302.150	435.833
313.155	546.074
334.148	576.960
365.015	579.066

Contributions from higher order reflections of ultraviolet emission peaks interfered with the calibration (Lerner, 2006), however when placing a standard glass window between the lamp and the spectrograph entrance slit, these peaks disappeared. The remaining spectrum consisted of the following peaks, 404.656, 407.783, 435.833, 546.074, 576.960 and 579.066, as shown in Figure 3.6.

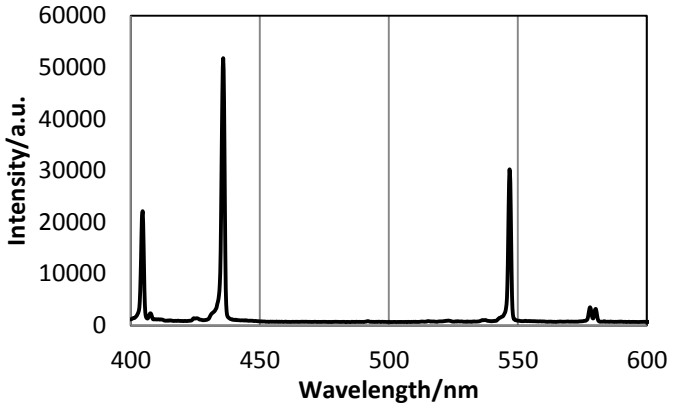

Figure 3.6. Mercury lamp spectrum measured using the spectrograph for calibration purposes.

3.3.3 Temporal alignment

The optical components of the laser induced phosphorescence setup had to be temporally aligned, as well as spatially in order to detect the phosphorescence emission, subsequent to laser excitation. In order to do this, the external triggering setup had to be determined, followed by finding the laser pulse and then finally, adjusting the ICCD camera settings in order to measure the phosphorescence signal. Figure 3.7 shows a diagram of the optical component setup. The system was controlled with a delay generator as the master, operated at 10 Hz which was set to coincide with the ideal laser operating speed. Three of the four output settings were used to trigger the laser and the camera. Output a) was set to trigger and control the camera and outputs b) and c) were used to trigger the laser flashlamp and Qswitch, respectively. The output signals could be set to vary the delay and pulsewidth of the transistor – transistor logic (TTL) pulses and both the camera and the laser were set to be triggered on the falling edge of the pulses.

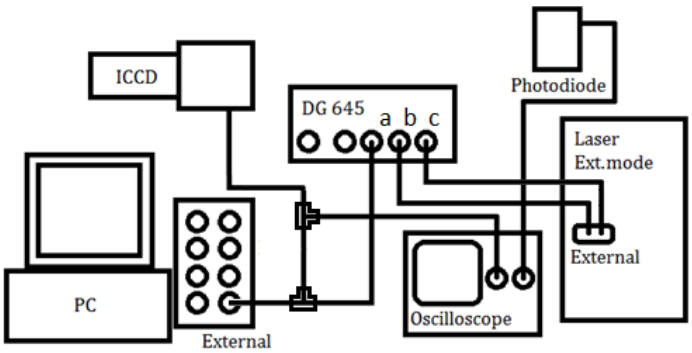

Figure 3.7. Temporal setup, including photodiode and oscilloscope for temporal alignment.

The laser had to be switched and set to external mode for external triggering. In order to trigger the laser, TTL pulses with a minimum of 10 µs pulsewidth had to be used in order for the system to recognise that a trigger signal had been received. Two separate triggers were used for the flashlamp and Qswitch for two reasons. To gain control over the Qswitch delay with respect to the flashlamp trigger and hence controlling the laser power output. Operating the system in this way also significantly reduced the amount of jitter produced by the laser system to +/- 1 ns, allowing for exact temporal positioning of the laser pulse.

The camera had to be set to external triggering mode and the TTL pulse had to be sent into the camera via the PC control system. This was done using a device with Bayonet Neill–Concelman (BNC) connections which was also connected to the PC, shown in Figure 3.7. The TTL pulse entered into the "fire" connection, triggering the system to open the camera gate. The same TTL pulse was also sent to the camera. The pulsewidth set on the delay generator determined the gatewidth of the camera and the delay of the pulse determined the delay between the flashlamp trigger and the camera gating trigger. The trigger timings are depicted in Figure 3.8 (upper).

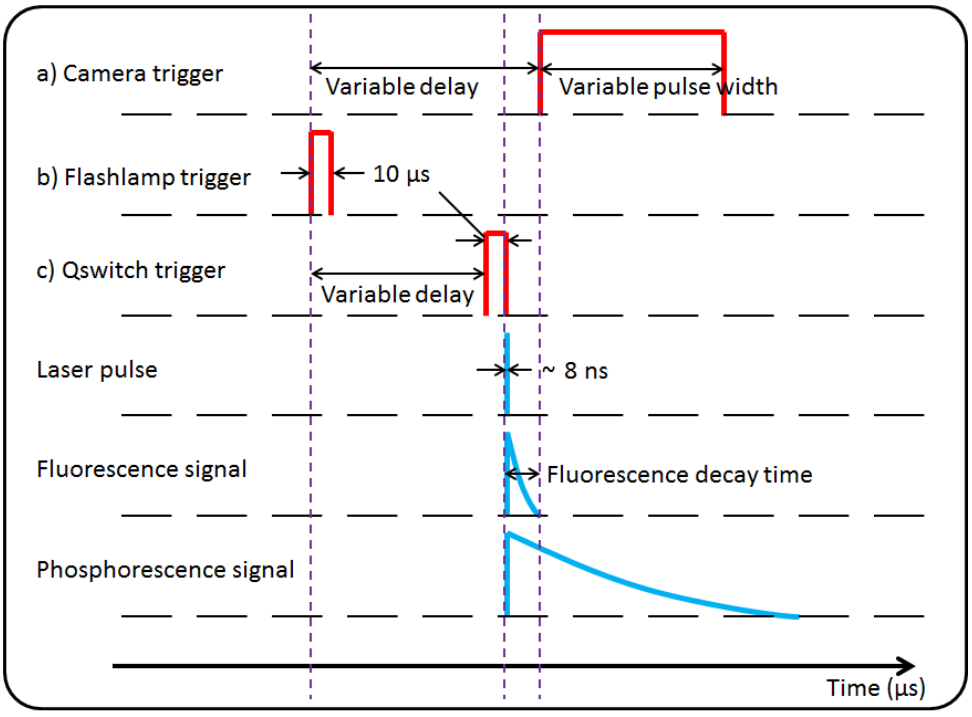

Figure 3.8. Laser induced phosphorescence timings diagram.

In order to find the laser pulse, a photodiode and oscilloscope were connected to the system. A piece of paper was placed in the path of the laser beam near the nozzle exit. The photodiode was connected to the oscilloscope, as well as the camera triggering signal. The laser beam was fired at 10 Hz and the photodiode was positioned facing the point in which the laser beam hit the paper. This allowed for the temporal position of the laser pulse to be determined, with respect to the camera gating times. The gatewidth of the camera was initially set to 10 μs and the camera delay was then varied until the laser pulse fell within the camera gatewidth.

The laser induced phosphorescence signal was identified using the spectrograph in conjunction with the ICCD camera. YAG:Dy thermographic phosphor powder was placed in the path of the laser beam and in front of the spectrograph entrance slit, so that the phosphorescence emission would be measured. On a trial and error basis, in conjunction with the data measured with the photodiode, the emission signals at various camera delay settings were recorded and it was found that a delay had to be set in order to avoid interfering laser and fluorescence signals. The temporal decay of the laser pulse and emission signals are depicted in Figure 3.8. A detailed analysis of the spectra measured at specific camera delay increments for BAM and YAG:Dy are presented in the next chapter.

3.3.4 Camera focussing

In order to acquire two dimensional images, the ICCD camera must be operated without the spectrograph and with a lens, which is used to image incoming light onto the ICCD chip. For laser induced phosphorescence measurements the camera had to be focussed onto the area of interest. This was done by placing a grid with symbols in place of the flow and focussing on the symbols. Figure 3.9 shows a picture of the grid taken using the ICCD camera. The grid squares were 10 x 10 mm. The thin line, striking through X, R, K and D was positioned along the centreline of the flow and the bottom row of the grid, with letters A – G was positioned from 0 – 10 mm height above the nozzle.

Figure 3.9. Image of a grid with symbols placed in position of the flow, captured using the ICCD camera.

For LIP measurements an image doubler was used which was placed over the lens. The same grid was captured with the image doubler in position. The position of the mirrors within the image doubler could be slightly adjusted to ensure each image was identical. The camera could also be traversed up and down whilst maintaining alignment with the centreline of the flow. A similar method was used to spatially align the camera for larger heights above the nozzle, where images of a ruler, placed in the position of the flow were captured. These alignment methods allowed for exact mapping of the data for analysis.

3.4 Data analysis

3.4.1 Spectrum processing

It was necessary to correct the phosphorescence emission spectra for background interferences prior to processing. This was done using the image acquisition software as part of the acquisition process. Preceding phosphorescence signal acquisition, images of the darkened room were taken, which were then subtracted from the signal. This would reduce excess noise signals, as well as the dark current produced by the ICCD camera itself. The spectra were analysed in MS Excel where they underwent further correction by reducing remaining background signals to zero.

A series of tests were carried out on both of the phosphors in order to find out how the emission spectra behave under different conditions. Significant efforts were put into analysing the spectra. The intensity of various regions of the spectra were

investigated in order to find the most sensitive intensity ratio for a given temperature range. As well as considering different wavelengths for the analysis, different FWHM were examined for those wavelengths, ranging from 1 to over 50 nm. The results are discussed in the next chapter.

3.4.2 Image processing

It was necessary to correct the phosphorescence images for background interferences prior to processing. This was done using the image acquisition software as part of the acquisition process. Preceding phosphorescence signal acquisition, images of the darkened room were taken, which were then subtracted from the signal on a pixel-by-pixel basis. This would reduce excess noise signals, as well as the dark current produced by the ICCD camera itself. The background corrected images underwent flat fielding using MATLAB to overlay the images for pixel-by-pixel division of the respective emission band intensities. A white light combined with a light box was used to create a uniformly illuminated field for pixel correction. A Gaussian filter of the same size as each image was applied to the images prior to division in order to smooth out fluctuations. As mentioned above, the spatial alignment of the images was achieved by capturing a reference image of a grid with symbols, which was positioned in place of the jet. This allowed for exact image mapping in both x and y directions using MATLAB.

CHAPTER 4
LIP SPECTRA AND 2D TEMPERATURE DISTRIBUTIONS IN JETS AND FLAMES

4.1 Introduction

This chapter consists of the results and discussion of the LIP turbulent gas jet and laminar flame experiments, where the gas jet measurements were published in Optics Express (Lawrence, et al., 2013). Section 4.2 discusses spectral measurements carried out on both the YAG:Dy and BAM thermographic phosphors, which were done in order to optimise the experimental setup and to calibrate the phosphors, relating phosphorescence intensity to temperature. The highest temperature heater available within budget reached up to approximately 1000 K, however in order to measure the complete calibration curves for each phosphor a novel method for carrying out the calibration was used. The spectral results acquired were in line with the literature. The results conveying jet and flame temperature distributions are presented in Sections 4.3 and 4.4 respectively. The gas phase jet temperature results contribute to a relatively new technique where only a handful of papers are available in the literature. The development of the gas phase technique for usage in flames is novel to this study.

4.2 Thermographic phosphor calibration

4.2.1 Setup and methodology

It was essential to carry out the calibration measurements for both phosphors in the same position and with the same optical equipment as the gas phase results, in order to minimise systematic errors which can occur from moving optical equipment (Lindén, et al., 2012). Calibrations were carried out for each TP individually. The calibration procedure involved heating a type K thermocouple with 0.31 mm diameter using two heating methods. The thermocouple was coated with the individual TP using an Omega CC high temperature binder. Care was taken to ensure TP-binder layer of minimal thickness was applied, ensuring that the thermocouple and TP temperature matched as closely as possible. A TP-binder layer thickness of 0.03 mm was measured by taking wire thickness measurements before and after application, using a micrometer.

For temperatures ranging from 300 to 850 K, the hot jet of air produced by the heater was used to heat the thermocouple and for higher temperatures a flame was used to heat the thermocouple from 500 to 1300 K. The thermocouple was moved to different locations within the flame in order to vary its temperature for the calibration measurements. The flame signal had to be subtracted from the phosphorescence signal and this was done in the same way as the background correction in other measurements. The phosphorescence signal was much stronger than the flame incandescence for surface measurements. The background image in this case was the thermocouple positioned within the flame. A stable, laminar premixed flame was used that remained consistent throughout the measurement process.

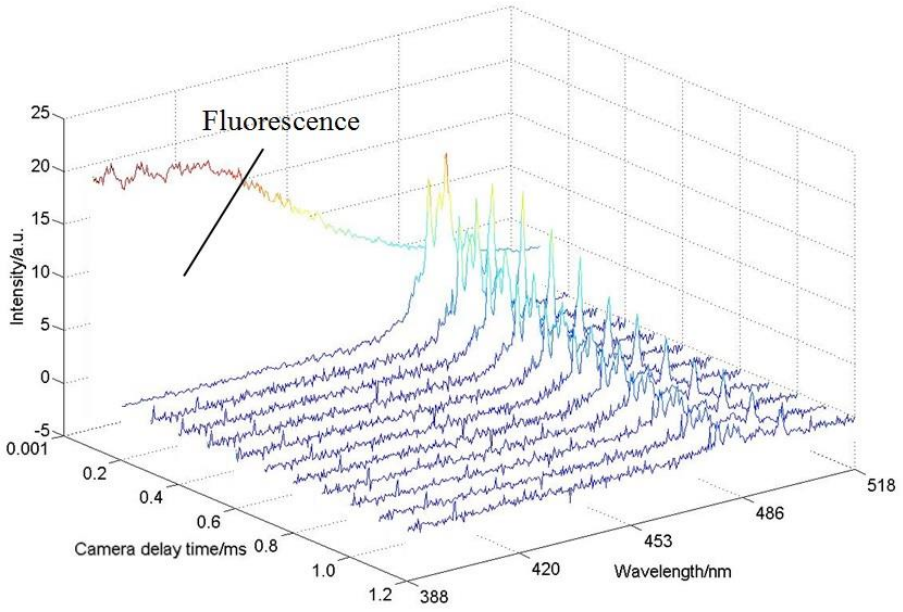

Figure 4.1. YAG:Dy phosphorescence signal intensity surface measurements at 300 K, taken at different time instances at selected delay increments after successive laser pulses.

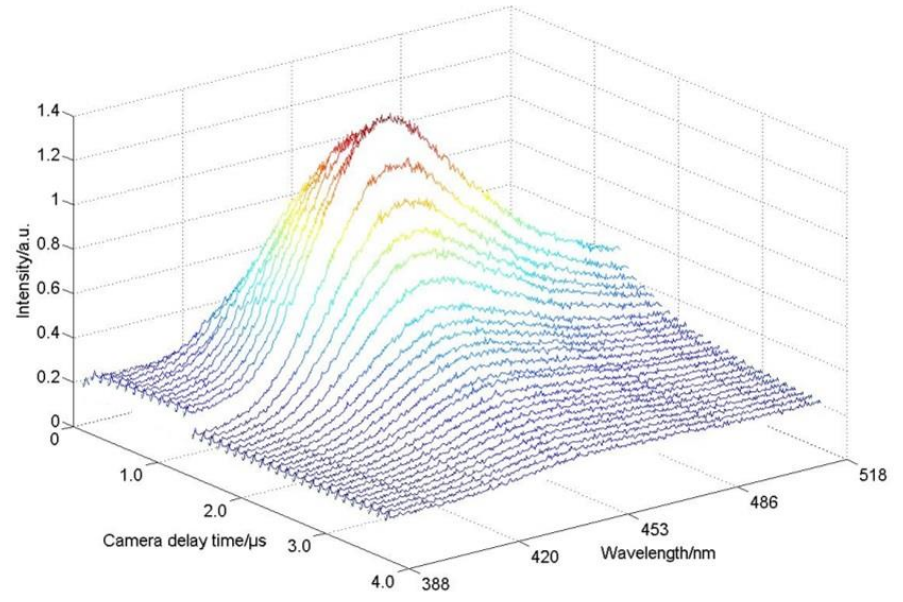

Figure 4.2. BAM phosphorescence signal intensity surface measurements at 300 K, taken at different time instances at selected delay increments after successive laser pulses.

4.2.2 Spectral signal variation with time

Both fluorescence and phosphorescence occur as competing de-excitation processes immediately after excitation for BAM and YAG:Dy and both of these emission signals can be seen in Figure 4.1, where the fluorescence is as a broadband emission.

As the BAM phosphor does not show this fluorescence signal, it is possible that it occurs due to a contaminant being present within the YAG:Dy phosphor. It is also possible that the signal may not be due to fluorescence, but could be due to light scattering or some other means. The aforementioned camera gating delay was introduced in order to avoid possible interference from this signal, which occurred in much shorter timeframes than phosphorescence. Figure 4.1 and Figure 4.2 show the entire emission spectra at different time instances, for YAG:Dy and BAM respectively, at selected delay increments of detection after successive laser pulses. The YAG:Dy timescale is in milliseconds, whilst the BAM timescale is in microseconds due to the phosphorescence lifetime variations. It was found that the interfering signal prevailed up to 1 µs after the laser pulse and therefore this timing was used for the camera gating delay. Phosphorescence emission lifetime reduces with an increase in temperature and no interfering signal was present at higher temperatures using these timings and therefore the interfering signal lifetime is expected to remain constant or reduce with an increase in temperature.

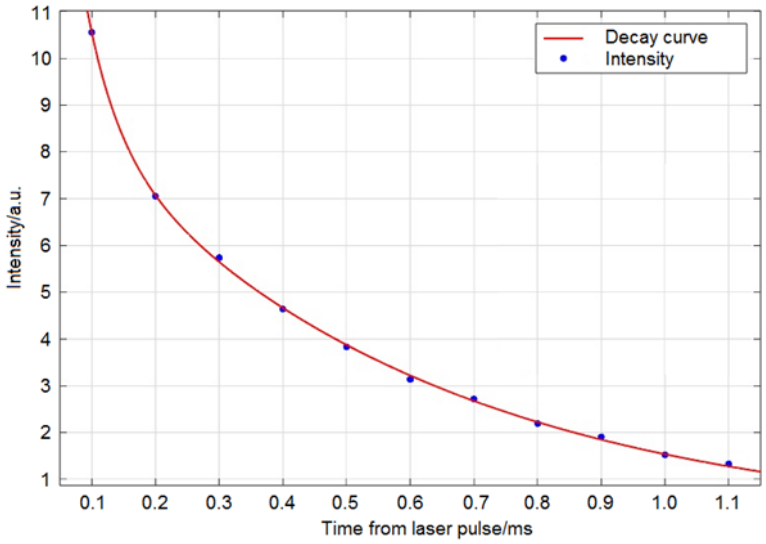

Figure 4.3. YAG:Dy phosphorescence signal decay curve at room temperature, determined from data points at different time instances from Figure 4.1 after the point fluorescence vanishes and phosphorescence is detectable, prevailing until the phosphorescence signal reaches the noise level. A double exponential fit was determined in MATLAB.

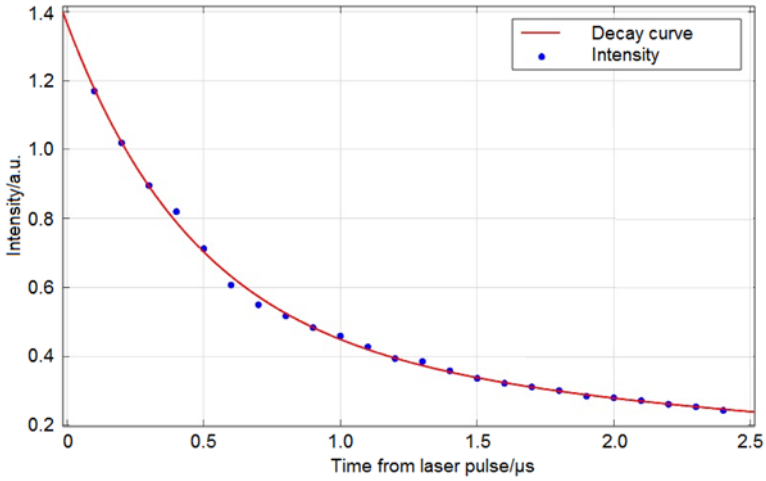

Figure 4.4. BAM phosphorescence signal decay curve at room temperature, determined from data points at different time instances from Figure 4.2 after the point fluorescence vanishes and phosphorescence is detectable, prevailing until the phosphorescence signal reaches the noise level. A double exponential fit was determined in MATLAB.

Figure 4.3 and Figure 4.4 show the phosphorescence decay lifetime at room temperature, translated from their respective emission histories, beginning after the fluorescence signal disappears, showing YAG:Dy to last for 1.1 ms and BAM approximately 2.5 μs. Both phosphors have double exponential curves fitted to their respective decay rate which confirmed the observations of (Justel, et al., 2003). Normally, for phosphorescence lifetime studies, a decay to 1/e or $1/e^2$ of the initial phosphorescence signal is used to determine the decay rate, however in this study the spectral method was used and the nature of the decay signal was not considered. The lifetime of BAM could be different to that shown in (Justel, et al., 2003) for this reason. In this work the phosphorescence lifetimes were used to determine the optimal camera gating times by comparing the spectral emission intensities measured with the spectrograph at various gatewidths.

4.2.3 Spectral signal variation with temperature

Figure 4.5 and Figure 4.6 show experimentally measured phosphorescence signals from YAG:Dy and BAM respectively, depicting how the signals vary with temperature. The shaded areas correspond to narrow band filters centred at 458 nm with a FWHM of 10 nm and 492 nm with a FWHM of 10 nm for YAG:Dy and 400 nm with a FWHM of 50 nm and 458 nm with a FWHM of 10 nm for BAM. In order to calculate the temperature using YAG:Dy, the signal intensity of the 458 nm band

is divided by that of the 492 nm band. Using BAM, the signal intensity of the 400 nm band is divided by that of the 458 nm band. The filtered spectral areas of each phosphor were chosen via experiment, after careful examination of their respective emission signal, in order to produce the highest temperature sensitivity. The intensity ratio for each phosphor is compared with a previously obtained calibration curve in order to express the local temperature. Optimal gating times were determined experimentally for both phosphors, in order to produce the best SNR, a gatewidth of 100 µs was used for YAG:Dy and a gatewidth of 1 µs was used for BAM. The short gating time which was used with BAM allowed for minimal background disturbances, producing a higher SNR than YAG:Dy.

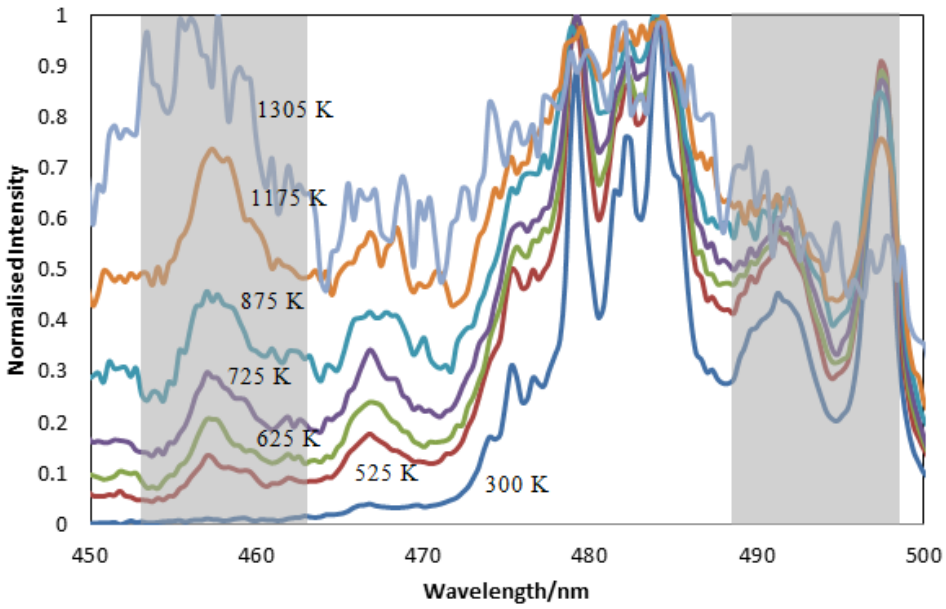

Figure 4.5. Normalised intensity YAG:Dy emission spectra at specified temperatures after 355 nm excitation, determined by surface measurements on a thermocouple coated in YAG:Dy using a high temperature binder, measured in the same position as the jet temperature measurements. The thermocouple was heated in two ways; in the hot air where temperature was varied by varying jet temperature and in a flame where temperature was measured by moving the thermocouple around the flame. The grey areas represent filters placed over the image doubler centred at 458 nm with a FWHM of 10 nm and centred at 492 nm with a FWHM of 10 nm.

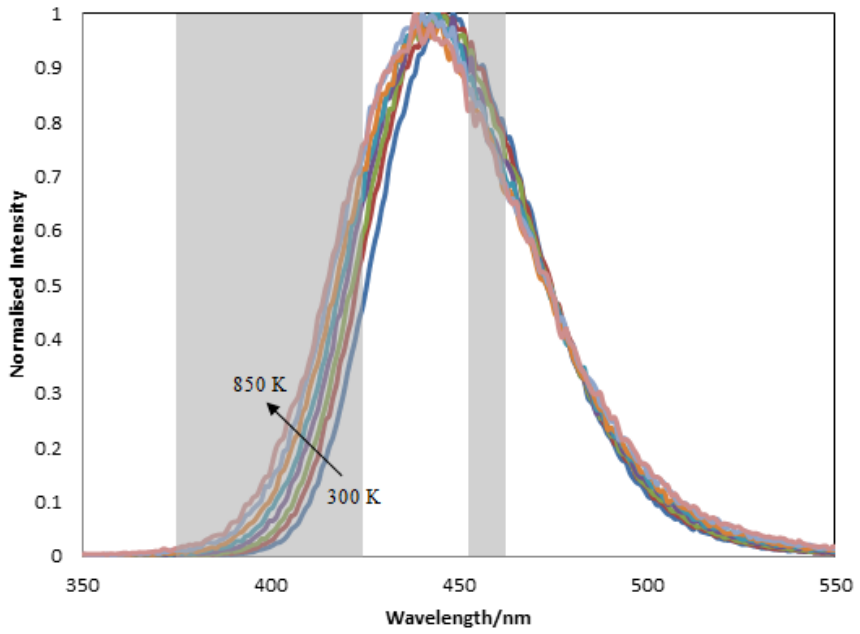

Figure 4.6. Normalised intensity BAM emission spectra at specified temperatures after 355 nm excitation, determined by surface measurements on a thermocouple coated in BAM using a high temperature binder, measured in the same position as the jet temperature measurements. The thermocouple was heated in two ways; in the hot air where temperature was varied by varying jet temperature and in a flame where temperature was measured by moving the thermocouple around the flame. The grey areas represent filters placed over the image doubler centred at 400 nm with a FWHM of 50 nm and centred at 458 nm with a FWHM of 10 nm.

Figure 4.7 and Figure 4.8 show the calibration curves for YAG:Dy and BAM respectively, as measured experimentally. The calibration was carried out with and without the spectrograph, conveying a very similar intensity ratio to temperature relation, fluctuating due to small differences induced by changing the optical equipment. The calibration curves presented are acquired from image acquisition for the corresponding phosphor. The calibration curves produced for the respective phosphors using both heating methods were almost identical within the overlapping temperature range, revealing that the flame method did not incur any significant errors due to flame incandescence background correction. The phosphorescence emission spectrum was found to be fluence independent within the fluence range tested in this study.

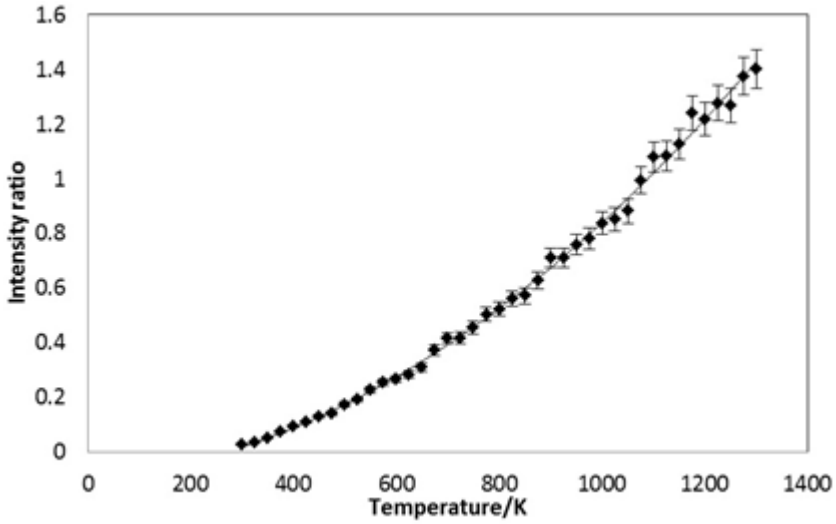

Figure 4.7. YAG:Dy calibration curve determined from surface measurements of a thermocouple heated to specified set temperatures by dividing the 458 nm filtered emission region by the 492 nm filtered emission region at each temperature.

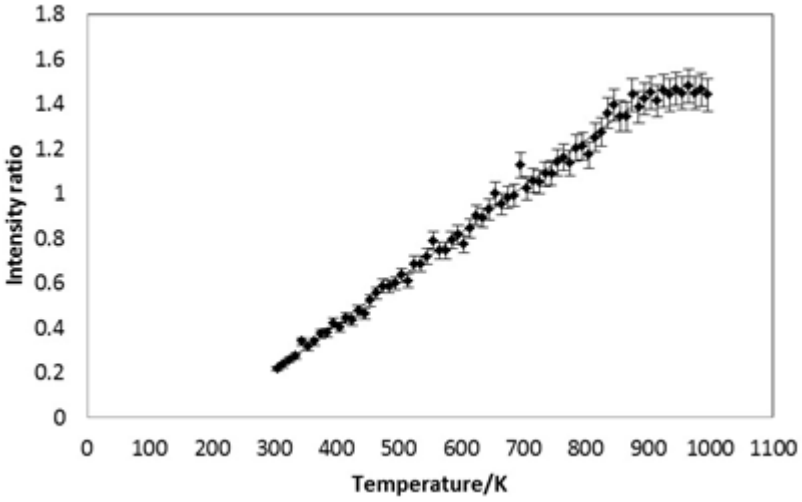

Figure 4.8. BAM calibration curve determined from surface measurements of a thermocouple heated to specified set temperatures by dividing the 400 nm filtered emission region by the 458 nm filtered emission region at each temperature.

4.2.4 Signal intensity variation with temperature

Figure 4.7 shows the YAG:Dy calibration curve up to 1300 K, where the phosphorescence signal starts to diminish. The upper limit of detection varies from study to study, from 1300 K (Yu, et al., 2010), to almost 1600 K (Hasegawa, et al., 2007 a; Hasegawa, et al., 2007 b), to 1800 K (Goss, et al., 1989), to around 2000 K (Cates, et al., 2003), where the discrepancies could be due to the differences in

experimental setup, such as optical equipment and calibration technique. Specifically, in (Yu, et al., 2010) a small particle diameter of 1.8 µm was used, which could have resulted in lower recorded phosphorescence intensity. The work in (Hasegawa, et al., 2007 a) and (Hasegawa, et al., 2007 b) uses the same calibration method, involving 4 µm sized particles, using fibres to focus the laser beam and for emission collection, along with an ICCD device coupled with a photomultiplier tube. These factors could all contribute to the high SNR. The study in (Goss, et al., 1989) specifies a doping concentration of 3%, which could be a factor contributing to relatively higher emission, along with the usage of relatively large particle sizes 10 – 100 µm. In (Cates, et al., 2003) the TPs were in powder form, therefore maximum volume density was used. The lifetime method was used with different percentage doping levels, which affected the phosphorescence signal intensity.

The maximum temperature of the heater used here was 850 K and therefore a calibration up to 2000 K was unnecessary. The curve shows an excellent fit, with an R^2 value of 0.9971. The spectral signal strength reduction, with an increase in temperature is shown in Figure 4.9. This is likely to be the cause of increasing error towards higher temperatures and explains why the data in Figure 4.1 appear noisier at elevated temperatures. The emission characteristics for both YAG:Dy particle sizes were identical for surface measurements.

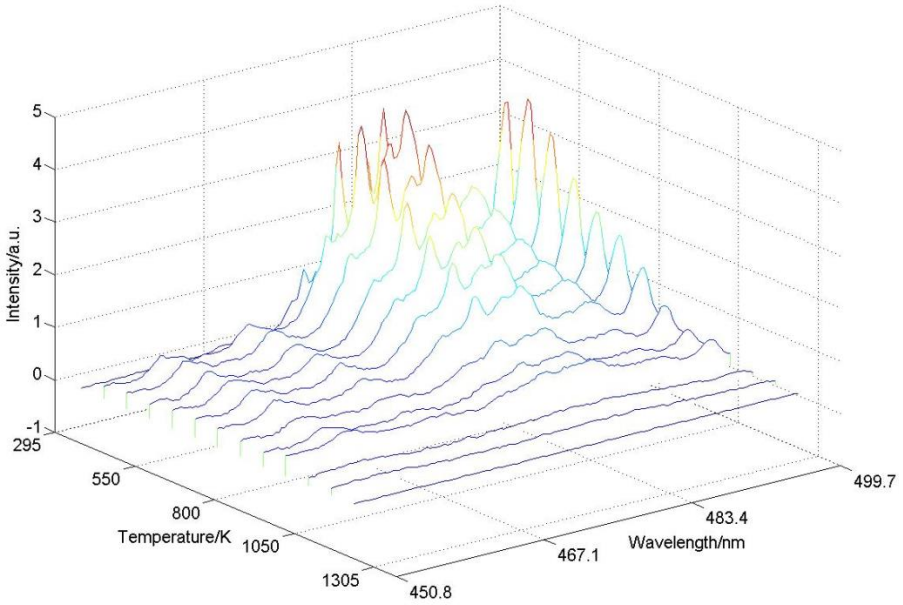

Figure 4.9. YAG:Dy spectral intensity variation with change in temperature determined from surface measurements of a thermocouple heated to specified set temperatures.

Figure 4.8 shows the BAM calibration curve up to 1000 K. The intensity ratio became insensitive to temperature change near 875 K, where the calibration curve began to flatten, reaching a maximum point. A curve was fitted to the linear part of the data, with a good fit, displaying an R^2 value of 0.9924. Other studies show temperature dependence up to 650 - 700 K (Fond, et al., 2012; van Lipzig, et al., 2012) and 1150 K (Lindén, et al., 2009) where again, inconsistencies could be due to experimental setup. Specifically, the study in (Fond, et al., 2012) does not investigate temperatures above 700 K and in (van Lipzig, et al., 2012) a relatively low laser fluence of 0.04 J/cm^2 was used and the phosphorescence emission intensity depends on the excitation energy, which could be why phosphorescence was only detected up 650 K. The work in (Lindén, et al., 2009) uses a longer exposure time of 8 µs, along with larger particles of 4.2 µm diameter and significantly higher laser fluences up to 1.5 J/ cm^2, which can all lead to producing a higher SNR, possibly revealing a phosphorescence emission up to higher temperatures than recorded herein.

The temperature dependence range exceeds that of the maximum temperature of the heater and therefore is sufficient in this case. Figure 4.10 depicts the spectral signal strength reduction, with increasing temperature, showing that the phosphorescence

signal vanishes around 1100 K. This signal reduction may account for the larger error at high temperatures. These results, along with other studies (Fond, et al., 2012; van Lipzig, et al., 2012; Lindén, et al., 2009) show that despite its high melting point, BAM shows a weakened signal at elevated temperatures and therefore may not be suitable for high temperature combustion measurements.

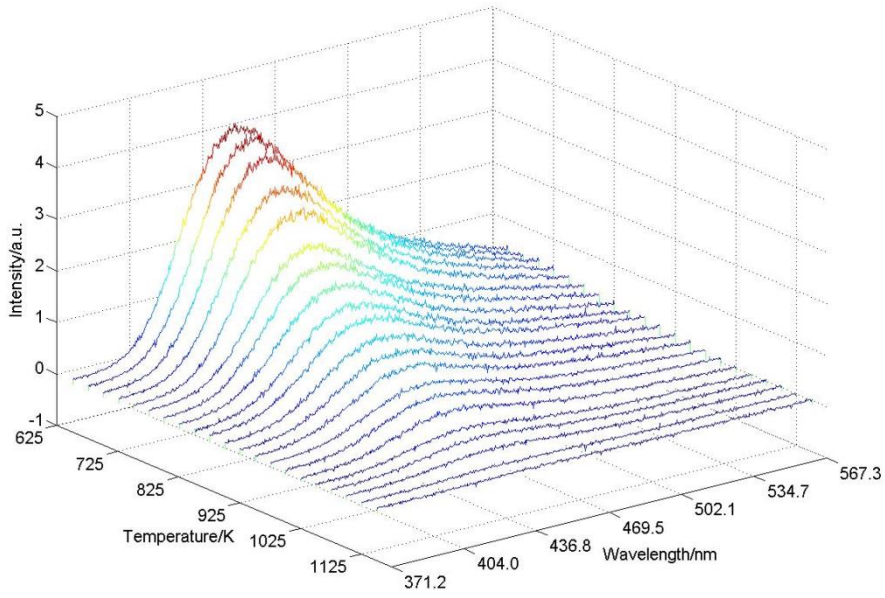

Figure 4.10. BAM spectral intensity variation with change in temperature determined from surface measurements of a thermocouple heated to specified set temperatures.

4.3 Jet temperature distributions using LIP

4.3.1 Jet temperature distributions using BAM

4.3.1.1 Single shot results using BAM

The 2.9 µm BAM particles produced a strong signal when seeded within the gas flow, which allowed for detailed single shot measurements to be made at various temperatures ranging from 500 – 850 K. Single shot measurements with BAM in heated jets were also achieved in (Fond, et al., 2012) up to 700 K. Herein, thermometry measurements were taken at heater temperature settings of 500, 600, 700 and 850 K. At each temperature and each position above the nozzle 50 background images and 50 phosphorescence images were taken and the average background signal was used for background correction. The laser sheet was 30 mm high and images were taken at various heights above the nozzle, covering a large

portion of the jet, with a maximum height of 90 mm. The jet was kept at constant temperature throughout each set of measurements, verified by the thermocouple.

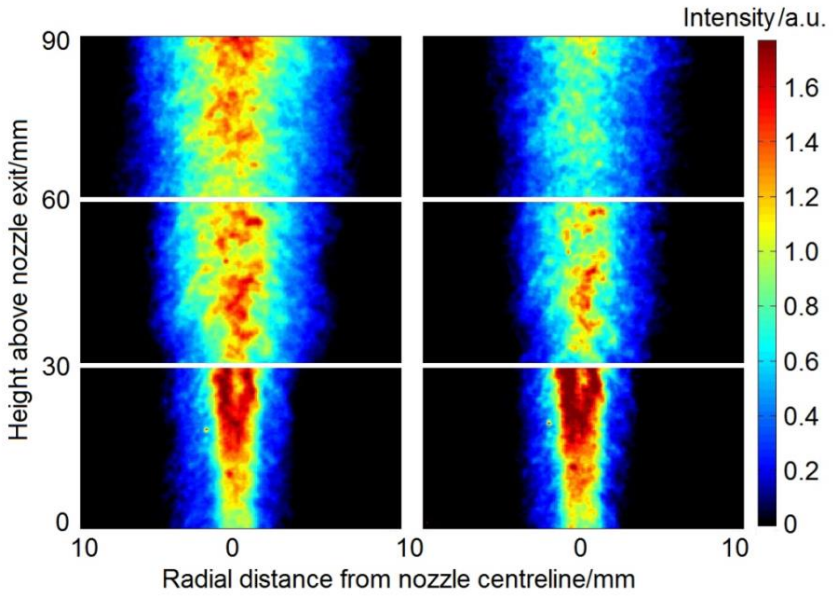

Figure 4.11. Gas phase single shot BAM phosphorescence emission intensity images of the 458 nm region (left) and the 400 nm region (right) from a jet at 850 K, where temperature was confirmed by a thermocouple inserted near the nozzle and centrally in the flow before and after measurements.

Figure 4.11 shows single shot phosphorescence intensity images of a jet at 850 K, filtered at the 458 nm (left) and 400 nm (right) emission bands. It can be seen that the phosphorescence signal is greater towards the middle of the jet, gradually reducing with radial distance, due to seeding density. Other studies based on heated jets produced similar results (Fond, et al., 2012; Rothamer & Jordan, 2012). The low signal towards the edges of the jet necessitated the use of conditional threshold filtering, which was applied to image intensities below a certain value, in order to prevent intensity ratio calculations in regions where there was little or no signal present. These regions would produce high noise and therefore inaccurate data due to the low SNR. This feature was also seen in (Rothamer & Jordan, 2012).

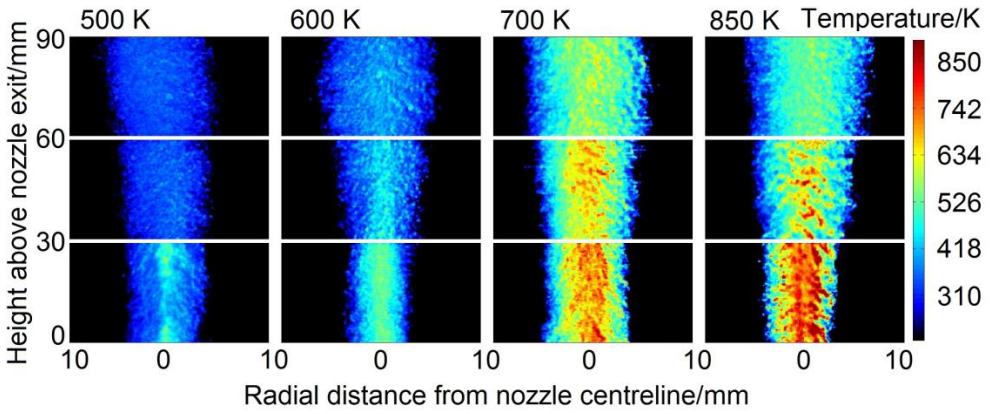

Figure 4.12. Gas phase single shot temperature distributions of jets with a Reynolds number of 2500 (8 mm diameter), conveyed with BAM phosphorescence, using the intensity ratio method by carrying out pixel to pixel divisions of the 400 nm region by the 458 nm region.

Figure 4.12 shows the stacked temperature distributions, conveying BAM phosphorescence emission ratio for jets at the specified set temperatures, with a Reynolds number of 2,500. The temperature does not exactly match up in corresponding stacked images due to the turbulent nature of the jets, different time instances of the image acquisition process and variations in the flow at a given experimental condition. The high signal yield produced by BAM at such short lifetimes and hence, short camera gating times, allows for shear layers be identified in each jet, along with the spatial temperature profile. Similar features can be seen in the results of (Fond, et al., 2012; Rothamer & Jordan, 2012). The temperature is higher in the central part of the jets, gradually dissipating radially outwards and upwards from the nozzle exit. The temperature profiles determined in this study match those found in the literature, for example (Fond, et al., 2012; Lemoine, et al., 1999; Agrawal, et al., 2004).

4.3.1.2 Time averaged results using BAM

Figure 4.13 (a) shows the phosphorescence images acquired at 458 nm (left) and 400 nm (right) for a 300 K jet at Re = 5000 and Figure 4.13 (b) shows the corresponding jet temperature distribution. It can be seen that the lower temperature jets appear smaller in diameter when compared with the equivalent jets at higher temperature. This is because the BAM phosphorescence signal intensity in the 400 nm region is much lower than that of the 458 nm region, which results in a low intensity ratio,

conveying a temperature close to the temperature scale minimum. This effect is minimised for images with an intensity ratio of 1. The temperature distribution shown in Figure 4.13 (b) is slightly skewed which could be an artefact of the image doubler. Another observation from Figure 4.13 (b) shows that despite the phosphorescence signal inhomogeneity, the phosphorescence intensity ratio for the jet at 300 K is still relatively homogeneous. This result is supported by the work presented in (Lindén, et al., 2012).

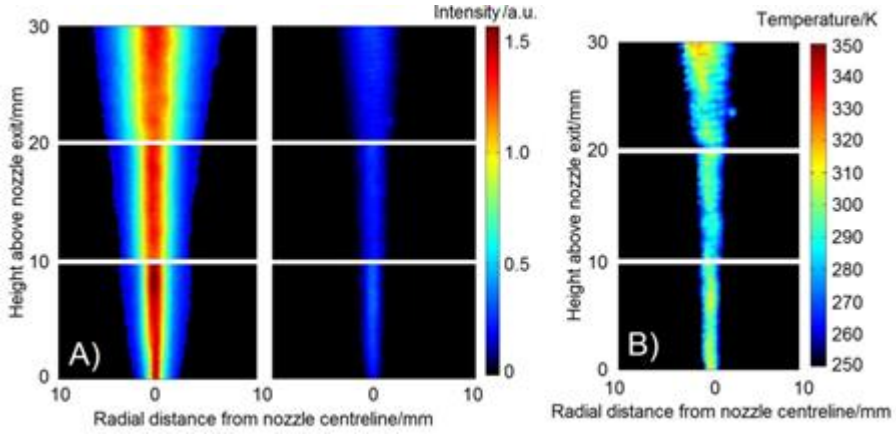

Figure 4.13. (a) Gas phase time averaged phosphorescence intensity images of the 458 nm band (left) and the 400 nm band (right) from the BAM phosphorescence emission at 300 K with a Reynolds number of 5,000. (b) 100 shot time averaged intensity ratio image found by carrying out pixel to pixel divisions of the 400 nm region by the 458 nm region of (a).

The time averaged temperature distributions produced by BAM phosphorescence intensity images at near nozzle positions of jets at various temperatures from 300 to 700 K at different Reynolds numbers are presented in Figure 4.14, where the Reynolds number was varied by changing the diameter of the nozzle exit. Thermometry measurements were taken at heater temperature settings of 300, 500, 600 and 700 K, for the three Reynolds numbers investigated. At each temperature and each position above the nozzle 100 background images and 100 phosphorescence images were taken. The laser sheet was 10 mm high and the images were taken up to 30 mm height above the nozzle exit, presented as stacked images. The jet temperatures throughout each set of measurements were verified by the thermocouple. The temperature profiles match up in corresponding stacked images, despite turbulence, due to the results being time averaged. The flow pattern cannot be

identified in the time averaged data, however the spatial temperature profiles are more prominent compared with the single shot results. These features are also seen in the time averaged results in (Fond, et al., 2012; Rothamer & Jordan, 2012). The flow appears to diverge more at higher Reynolds number.

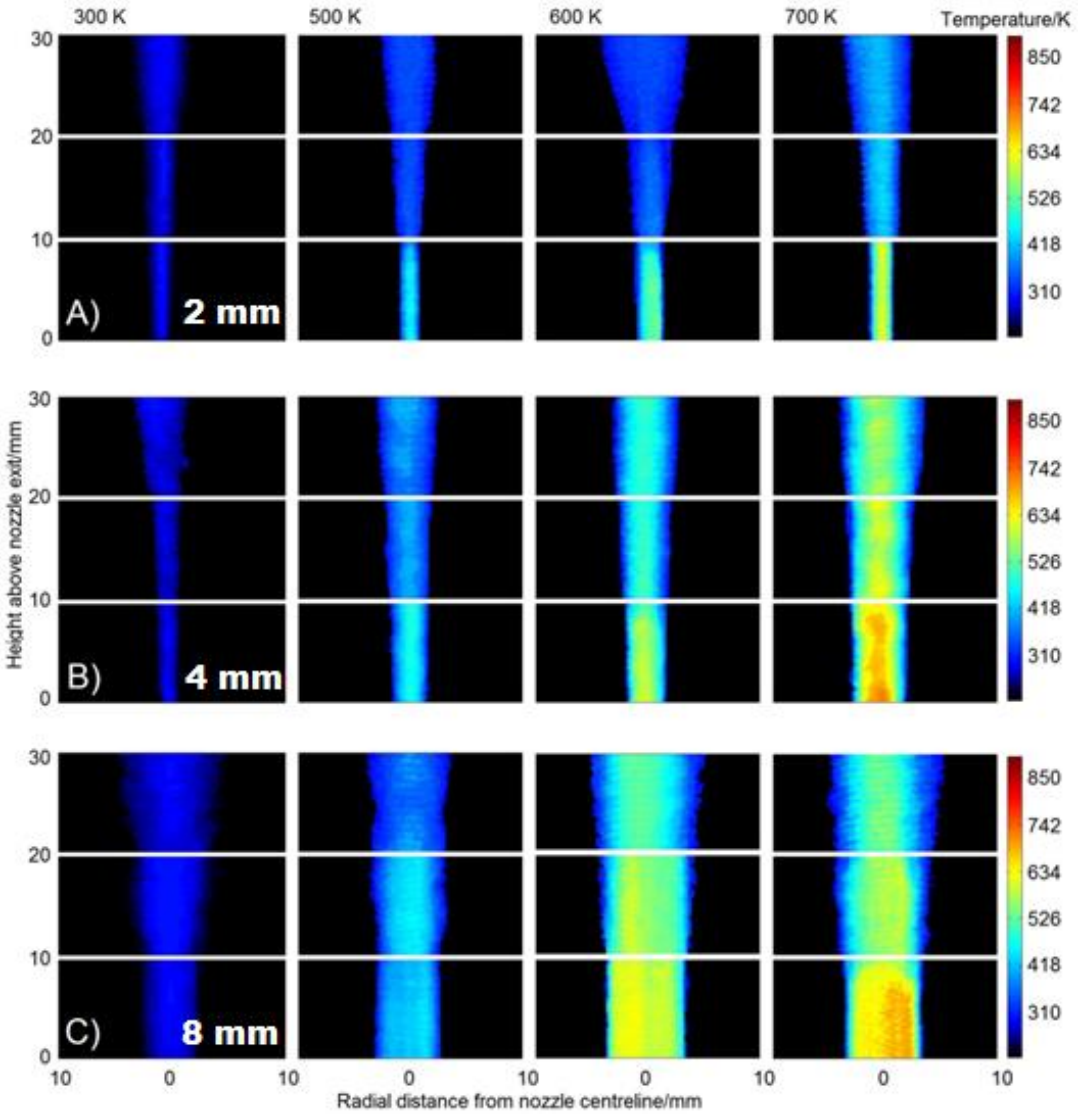

Figure 4.14. Gas phase 100 shot time averaged temperature distributions for various temperatures and Reynolds numbers, conveyed with BAM phosphorescence, using the intensity ratio method by carrying out pixel to pixel divisions of the 400 nm region by the 458 nm region. (a) shows jets with a Reynolds number of 10,000 achieved using a nozzle diameter of 2 mm (b) shows jets with a Reynolds number of 5,000 achieved using a nozzle diameter of 4 mm and (c) shows jets with a Reynolds number of 2,500 achieved using a nozzle diameter of 8 mm.

4.3.2 Jet temperature distributions using YAG:Dy

There was a very negligible amount of the phosphorescence signal produced by the 2.5 µm diameter YAG:Dy particles when seeded within the flow. This can be explained by the excitation and emission characteristics of the YAG:Dy phosphor becoming more transparent to visible light as it increases in size, reducing trapping efficiency caused by light scattering of particles (Tran, et al., 2009). Therefore at smaller sizes less luminescence is produced. This, combined with a relatively low seeding density, compared with surface measurements, resulted in little or no measured emission of phosphorescence for the jets both for single shot and time averaged measurements. This low signal effect was also mentioned in (van Lipzig, et al., 2012) where the authors mitigated the usage of BAM instead of YAG:Dy, in order to produce gas phase results.

The 10.2 µm YAG:Dy did produce relatively better phosphorescence signal than the 2.5 µm YAG:Dy particles, but still there was not a high enough phosphorescence signal yield for single shot measurements. However, accumulating a number of single shot images resulted in an average temperature distribution. It has also been documented in (Jovicic, et al., 2012) that the SNR of YAG:Dy is low, where the principle of superpixels is necessitated. Superpixels combine the intensities in regions consisting of multiple pixels, for example using 5x5 pixels to improve SNR. However, in this study it was sufficient to accumulate the data for an improved SNR. It was also beneficial not to use superpixels here, in the interest of comparing the results of the two phosphors, as well as preserving the spatial resolution of the images.

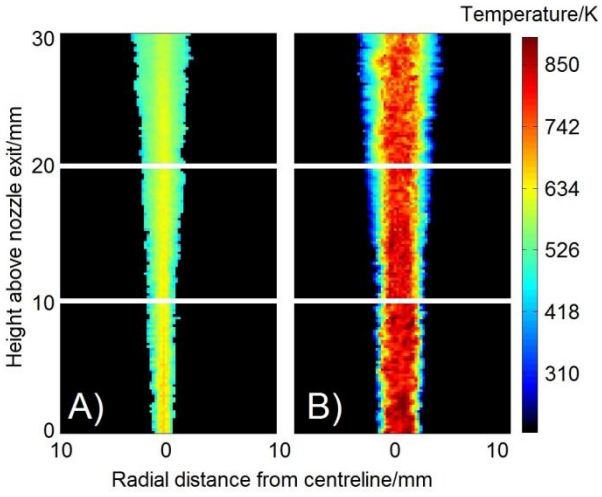

Figure 4.15. Gas phase 100 shot, time-averaged temperature distributions conveyed with YAG:Dy phosphorescence, using the intensity ratio method by carrying out pixel to pixel divisions of the 458 nm region by the 492 nm region for (a) A jet at 600 K with a Reynolds number of 5,000 achieved with a nozzle diameter of 4 mm and (b) a jet at 850 K with a Reynolds number of 2,500 achieved with a nozzle diameter of 8 mm.

The 458 nm emission band of the YAG:Dy conveyed no appreciable signal near room temperature and at low temperatures up to about 500 K, during gas phase measurements. This, combined with the application of conditional threshold filtering, mentioned above, meant that jets at temperatures below 550 K could not be accurately deduced using YAG:Dy. Figure 4.15 shows temperature distributions for two jets, where each image was an average of 100 shots. It can be seen from the less pronounced jet temperatures, that the signal strength is less than that of the BAM time-averaged shots. The figure shows a jet at 600 K with a Reynolds number of 5,000 (left) and a jet at 850 K with a Reynolds number of 2,500 (right). Only two jets of temperatures of 600 K and 850 K are presented using YAG:Dy. In Figure 4.15 (a) and (b) the jets appear thinner relative to the corresponding BAM measurements of jets taken at the same temperature and Reynolds number. This is again due to a low phosphorescence signal produced at low temperatures in the 458 nm region, for YAG:Dy, producing a low intensity ratio and hence conveying a temperature close to the temperature scale minimum. The YAG:Dy calibration curve in Figure 4.7 is steeper towards higher temperatures and the jet temperature distributions show only a small change over a variation of 250 K. This shows that YAG:Dy displays less sensitivity to temperature change, compared with BAM at this range.

4.3.3 Precision and uncertainty

The precision of the gas phase LIP thermometry technique was calculated using single shot BAM phosphorescence images from the near nozzle part of the gas jets, within the central region. Five matching pixels were compared from each of the 50 single shot images at every temperature increment presented in the results. Figure 4.16 depicts the number of pixels conveying specific temperatures for each temperature set. The standard deviation of the results at 300 K was 8.6 K (2.8 %), increasing up to 49.8 K (5.9 %) at 850 K, showing a decrease in precision and increase in uncertainty with an increase in temperature. The data for each temperature was corrected using conditional filtering in such a way that the temperature did not go below 280 K. The YAG:Dy phosphor could not be used for this analysis as its emission signal was not strong enough for single shot analysis. However there is expected to be a further inaccuracy induced when using the YAG:Dy due to the larger diameter and hence longer response times with change in temperature. This, combined with having to average data shows that YAG:Dy is more suited to steadier situations, such as laminar jets with low temperature and velocity gradients.

The amount of error induced by the thermocouple gas temperature measurement was approximately +/- 0.2 K at 300 K and about +/- 4.3 K at 850 K. The heater induced an error of up to +/- 5 K for temperatures below about 550 K, increasing to between 10 and 15 K at 850 K. The data is expected to convey a bias towards higher temperature as only the hot jet flow is seeded and therefore cooler entrained air is only represented by the amount the hot jet is cooled.

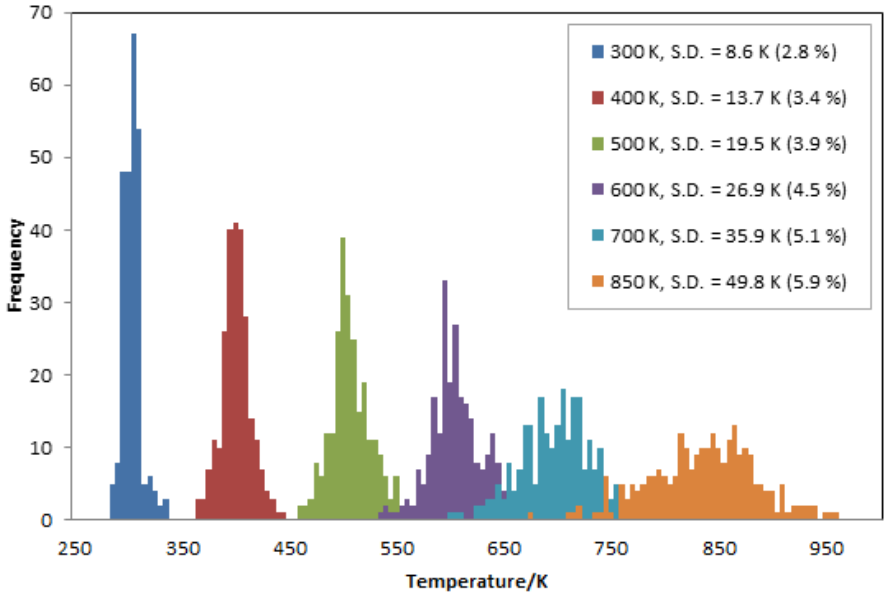

Figure 4.16. Histograms of gas phase LIP temperature measurements from 5 matching pixels in the same region of 50 individual BAM single shot images at each temperature used in this study.

Time averaged thermocouple data was compared against the time averaged temperature distribution from the BAM and YAG:Dy phosphorescence data to find the error induced by each individual phosphor. A thermocouple was placed at specific heights above the nozzle, centrally in the jet and pixels matching these areas in BAM and YAG:Dy time averaged temperature images were compared to the thermocouple measurements. The difference in temperature at each position was calculated and converted to a percentage of the thermocouple temperature reading. The analysis revealed that there was an error of up to 3.1 % for BAM, taken as an average over all of the positions measured. For YAG:Dy, the error increased as the height above nozzle increased, from 4.4 % at 5 mm above the nozzle exit, up to 10.1 % at 25 mm above the nozzle. It is possible that the greater error is because the larger diameter particles of YAG:Dy retain their heat for longer.

4.4 Laminar flame temperature distributions using LIP

4.4.1 Flame consistency

For flame thermometry, the flame luminescence had to be subtracted for background correction. This was also done during the calibration. A camera gatewidth of 100 µs was used for YAG:Dy and 1 µs was used for BAM. The short gating time used for the BAM measurements discriminated against a significant amount of the flame emission, detecting a relatively low interfering flame signal, compared with YAG:Dy. It was imperative that the flame remained as consistent as possible throughout the measurement process, in terms of position and radiative emission and great care was taken to ensure this was the case. This was done by ensuring there were no external flow perturbations and that fuel and air flow rates were kept constant, hence maintaining a constant seeding flow rate.

In order to show that the portion of the flames analysed was consistent, 100 shots of each flame were taken with a high speed camera and then pixel to pixel standard deviations were carried out and are presented as a percentage of the mean in Figure 4.17 (b). The figure shows that the central areas of the flames remain consistent within 1 % of the mean at each pixel, increasing to a maximum of 6 % at the very edge and tips of the flames, due to small flame perturbations which were unavoidable. Taking into account the steadiness of the flame, only the near burner region was considered for analysis, up to a maximum of 30 mm HAB. The same camera delay as in the previous study of 1 µs was used to minimise LIF and possible LII signals and none were measured. This was confirmed with spectrograph measurements.

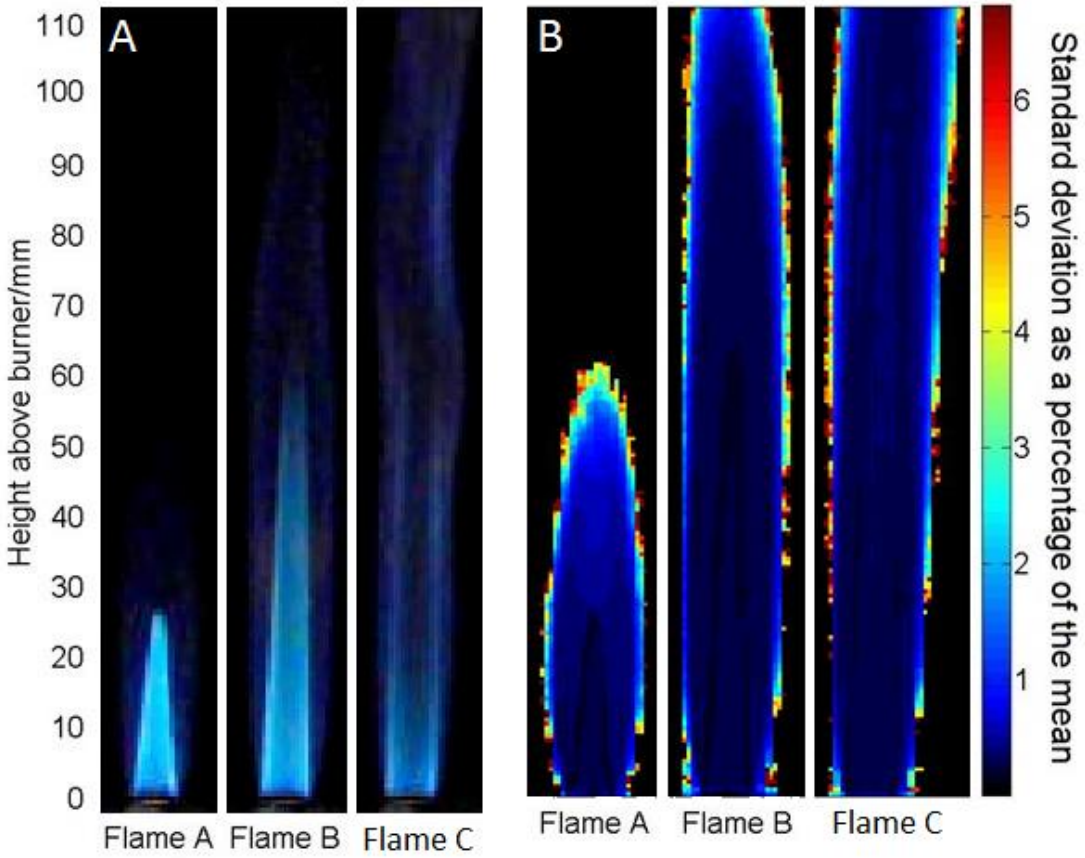

Figure 4.17. (a) Examples of photographs of flames A, B and C, taken using a high speed camera (1000 fps) (b) Pixel to pixel standard deviations calculated from 100 images of each flame, presented as a percentage of the mean at each pixel for each flame.

4.4.2 Flame temperature distributions

The radial temperature distributions obtained using the thermocouple show that the region where the fuel is unburned, within the premixed flame cone is the coolest. The gas temperature rises at an increasing rate as it approaches the flame front. Figures 4.18 – 4.20 show time averaged temperature distributions over 100 accumulations for flames A, B and C respectively. The images were produced by YAG:Dy (left) and BAM (middle) and radial temperature profiles for both phosphors are also presented at heights above the burner (HAB) of 5, 15 and 25 mm (right). The radial temperatures at the specified HAB were also superimposed onto the images. The thermocouple measurements were also included for comparison.

It is evident from the figures that neither phosphor produced a complete temperature distribution throughout an entire flame. When comparing the magnitude of the temperatures measured with that of the thermocouple, the temperatures in the relatively colder part of the flame matched up well, however as the temperature increased, the error of the LIP method increased, due to its limitations. The main aim of this section is to attempt to explain the processes and mechanisms that the TPs undergo as they are transported through the flame, thereby revealing the limitations of the LIP technique for flame thermometry.

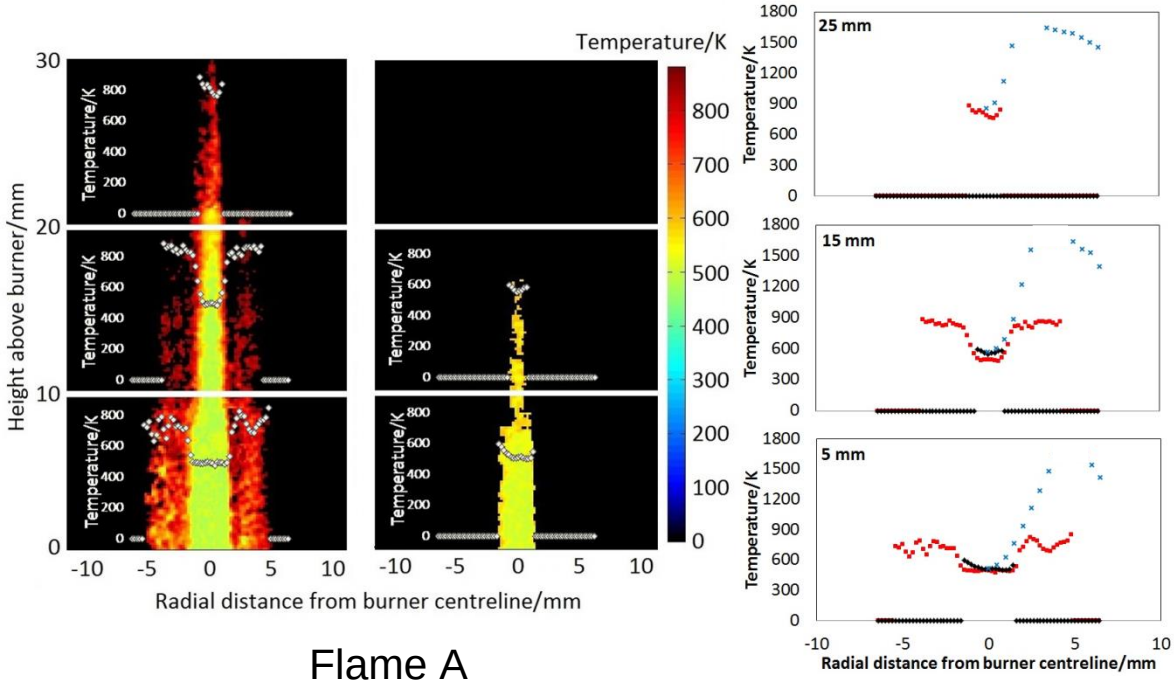

Figure 4.18. Temperature distribution images for YAG:Dy (left) and BAM (middle) conveying temperatures throughout Flame A, with radial temperatures at 5, 15 and 25 mm HAB, superimposed onto the images. A comparison of the temperatures measured by each phosphor at 5, 15 and 25 mm HAB against corrected thermocouple measurements are presented (right), where the red squares, black diamonds and blue crosses represent temperatures measured with YAG:Dy, BAM and the thermocouple respectively.

It can be seen in Figures 4.18 – 4.20 that the TPs conveyed a different local temperature throughout the high temperature regions in the flame, compared with the thermocouple measurements. This can be explained by the differences in the two thermometry methods. The thermocouple method is invasive and therefore perturbs the flame somewhat. The thermocouple is placed within the flame at each position

until it reaches thermal equilibrium. Conversely, the LIP method is a semi-invasive technique where the TPs remain in the flame for a fraction of a second. During this time, the particles heat up as they approach the premixed flame front, reaching a maximum temperature as they encounter the flame front and cool down progressively as they get further from the flame front. Ideally, the TP particles would follow the temperature gradients identically, reaching temperatures above 2000 K at the flame front in most flames. However certain factors cause the particles to heat up slower and reach a lower maximum temperature and hence, induce error.

Consider a single thermographic phosphor particle as it travels through the flame. Initially it is seeded within the premixed fuel/air flow within the pipe. As it leaves the pipe it enters the relatively cool premixed zone. The particle will increase in temperature as it approaches the flame front. The speed in which the particle heats up is a function of the particle size, density, heat capacity and thermal conductivity, described by the relation in Equation (2.1) in Chapter 2 (van Lipzig, et al., 2012). As the particle coincides with the flame front it receives maximum energy input along its specific path and therefore will reach a maximum temperature. The particle temperature up to and including this point will be lower than the ideal temperature due to parameters in Equation (2.1).

The LIP temperature distributions of flames A – C in Figures 4.18 – 4.20 convey a significantly lower maximum temperature, in the region of 880 K, compared with that of the thermocouple, which is over 1650 K for all of the flames. The differences occur due to short residence times and from effects due to longer response times deduced from Equation (2.1). It was found that the response time for YAG:Dy to heat up from room temperature to 850 K was 1.4 ms, compared with BAM which was 124 µs. The average velocity of the particles in the flames in this study was determined to be approximately 3 ms^{-1}. The distance that the particles travelled in 1.4 ms ranged from 4.25 to 4.5 mm in flames A - C. This meant that by the time the TP particles reached the flame front, BAM would have reached a higher temperature than YAG:Dy. Low phosphorescence intensity at high temperatures is another factor which affects the maximum measured temperature. The particles may not have

reached a temperature much higher than 880 K and even if they did, the phosphorescence signal may have been negligible.

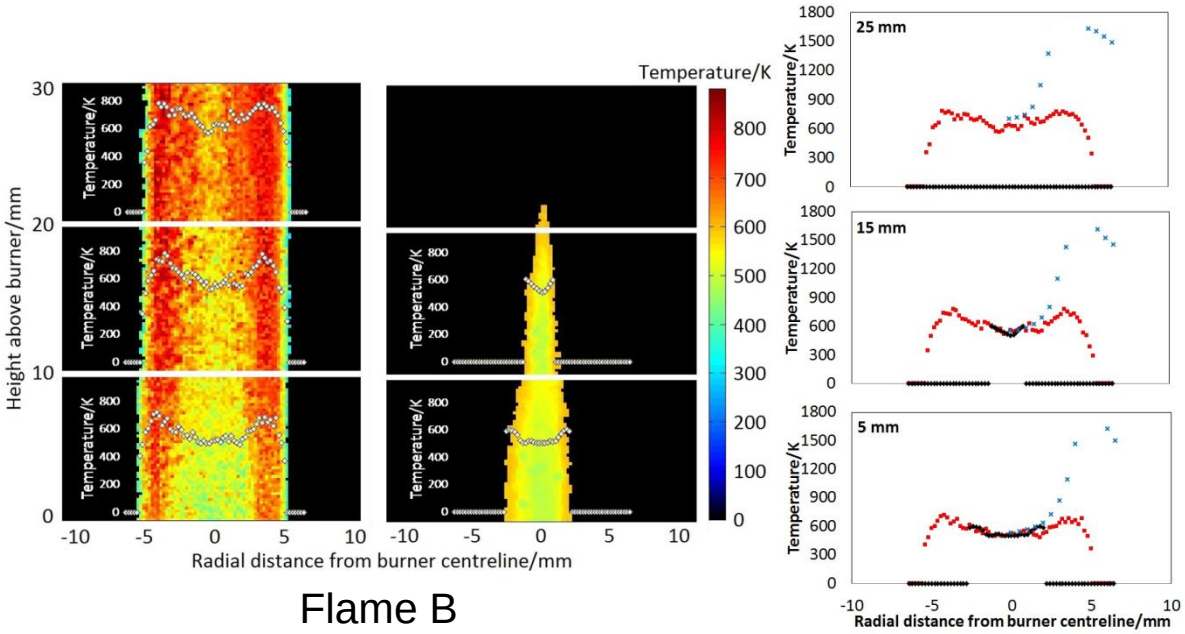

Figure 4.19. Temperature distribution images for YAG:Dy (left) and BAM (middle) conveying temperatures throughout Flame B, with radial temperatures at 5, 15 and 25 mm HAB, superimposed onto the images. A comparison of the temperatures measured by each phosphor at 5, 15 and 25 mm HAB against corrected thermocouple measurements are presented (right), where the red squares, black diamonds and blue crosses represent temperatures measured with YAG:Dy, BAM and the thermocouple respectively.

Figure 4.18 shows the time averaged temperature distribution over 100 accumulations for flame A, using both YAG:Dy and BAM, separately. For YAG:Dy (left) there is a reduced signal outside of the flame cone, similar to that seen in the BAM images in Figures 4.18 – 4.20. The detection of only a smaller flame cone in Figure 4.18 for flame A, is an indication that the TPs have experienced a longer residence time in the hotter part of the flame (outside the flame front), which allows the TPs to heat up passed the maximum phosphorescence detection temperature. The regions where no signal is present indicate where the phosphorescence signal is negligible. This is because the flame temperatures in these regions are too high to measure the low phosphorescence signal produced by the phosphors. This lack of phosphorescence signal shows that flame temperature cannot be effectively measured using these TPs combined with this methodology.

It can be seen from the figures that YAG:Dy can measure higher temperatures than BAM, shown by the temperature distributions of YAG:Dy conveying temperature throughout the measured parts of the flame in Figures 4.18 – 4.20, compared with BAM which only measured a small portion of the flame. Due to the added interferences from the flame, the highest temperature in which the phosphorescence could be measured was even lower than that of the non-reacting jets and therefore a reduced SNR was achieved for flame measurements. The maximum temperature measured in the flames using YAG:Dy was approximately 880 K and that of BAM was about 600 K. From the calibration measurements that were carried out, it could be seen that this was near the measureable limit of BAM, which was approximately 875 K, however YAG:Dy was expected to measure significantly higher, in the region of 1300 K. The significant reduction in the maximum measureable temperature for both phosphors can be explained by a reduction in phosphorescence intensity as temperature increases, along with the increased background signal produced by the flame. This effect is more significant for YAG:Dy because its phosphorescence signal yield is weaker than that of BAM (Jovicic, et al., 2012; van Lipzig, et al., 2012).

The radial temperature distributions obtained through YAG:Dy and BAM show good consistency between the two phosphors, within the cooler flame cone. Figure 4.20 shows YAG:Dy and BAM are in good agreement at 5 mm HAB within the flame cone, where the phosphorescence signal was strong for both phosphors. However, at positions of 15 and 25 mm HAB, BAM conveyed a lower temperature than YAG:Dy for some parts of the flame. This is due to the low signal that was produced by BAM at high temperatures, shown by the incomplete temperature distribution in Figure 4.20 (middle), causing erroneous results.

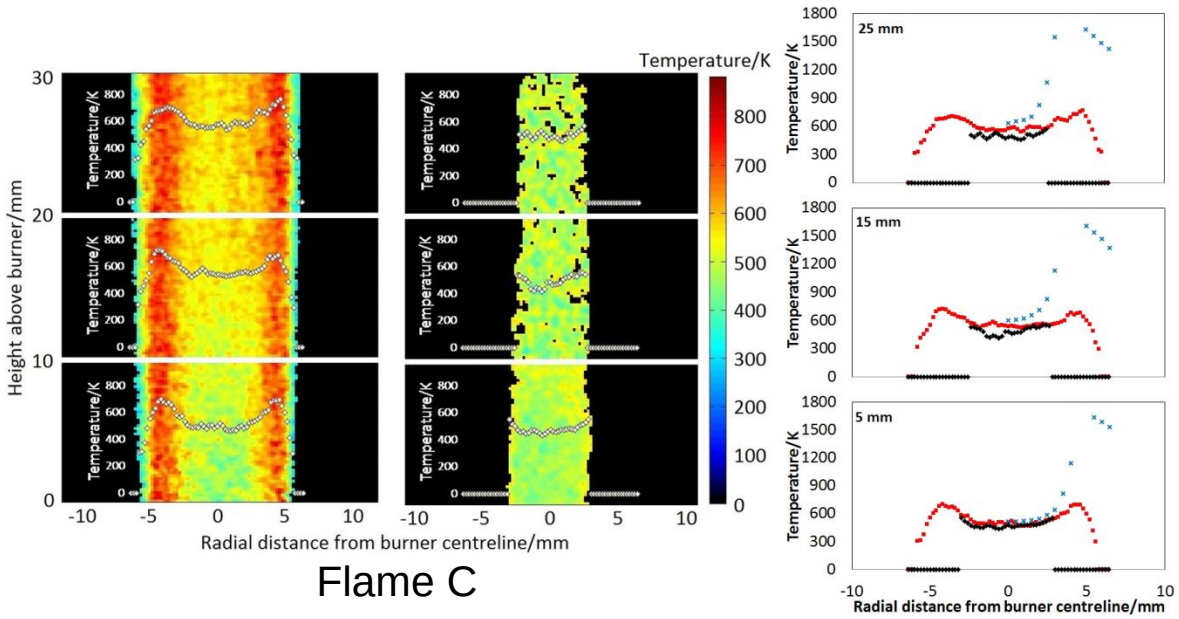

Figure 4.20. Temperature distribution images for YAG:Dy (left) and BAM (middle) conveying temperatures throughout Flame C, with radial temperatures at 5, 15 and 25 mm HAB, superimposed onto the images. A comparison of the temperatures measured by each phosphor at 5, 15 and 25 mm HAB against corrected thermocouple measurements are presented (right), where the red squares, black diamonds and blue crosses represent temperatures measured with YAG:Dy, BAM and the thermocouple respectively.

Inside the flame cone the premixed gases are significantly cooler than the rest of the flame and the temperatures measured within the flame cone using the TPs are close to the actual temperature, due to their small size and hence, low heat losses and fast temperature response times at these relatively low temperatures. The average temperature difference along the centreline of all of the flames was 41.4 K for both TPs, where the largest differences occurred in Flame C with BAM, compared with the thermocouple measurements, due to diminishing phosphorescence signal at higher temperatures.

CHAPTER 5
SOOT FORMATION, OXIDATION AND INFLUENCING FACTORS

5.1 Introduction

This chapter covers the scientific background of carbonaceous soot, including its formation, oxidation and factors which influence the soot formation process. The properties of soot and the soot formation process are detailed in Section 5.2. Section 5.3 describes the factors that influence soot formation, focusing on dilution effects. Pyrolysis mechanisms for long chain fuel molecule types, found in biodiesels are discussed in Section 5.4. Section 5.5 introduces biofuels, listing the biodiesels used in this investigation, as well as introducing the gas chromatography technique which was used to confirm the composition of the biodiesels in this study. Soot analysis techniques are described in Section 5.6, where LII is introduced, along with thermophoretic sampling, which are both used in this study and finally, some other laser soot diagnostics are briefly described.

5.2 Soot

There are considered to be two fundamental categories of particle that are produced in both premixed and non-premixed combustion, which are distinguished by size. The smaller particles that are less than 10 nm in size are considered precursors of soot and can be detected downstream of the luminous flame zone by ultraviolet (UV) light absorption using laser induced fluorescence (LIF). Polycyclic aromatic hydrocarbons (PAHs) and nanoparticles of organic carbon (NOC) are considered to be within this range. The larger particles that are more than 10 nm in size are referred to as soot and are detectable by visible light absorption using laser induced incandescence (LII) (D'Anna & Kent, 2008). The characteristics of soot have been described in (Glassman, 1996; Palmer, 1965), where the soot particles are roughly spherical in shape and joined together in a chain-like configuration. The particles consist of mainly carbon and hydrogen, with hydrogen making up approximately 1 % by weight, corresponding to an empirical formula of C_8H. The structure of soot resembles that of graphite, with particle sizes ranging between 10 and 200 nm. Smaller particles are found in the luminous zone of flames and larger particles are can be seen to break through the luminous envelope in heavily sooting flames, producing visible black smoke.

Carbon can be formed in a number of ways, including through gas or vapour phase reactions, deposition onto a solid surface that is positioned near the reaction zone and through liquid fuel pyrolysis. The amount of soot that is formed depends on the particular combustion process and a number of physical and chemical factors from the types of fuel and oxidiser used. The main concern is the rate in which soot is formed, which can vary significantly with these influencing factors, unlike the soot properties, which remain more or less invariant (Palmer, 1965; Haynes & Wagner, 1981). The soot formation rate determines the SVF of soot that is formed for a particular combustion system.

There are many theories behind possible reaction pathways leading to the formation of soot and some have been discussed in the following reviews (Richter & Howard, 2000; McEnally, et al., 2006; D'Anna, 2009; Haynes & Wagner, 1981). Initially,

PAHs are formed through various molecular reactions from component molecules in the fuel. These PAHs consist of benzene rings which are ‘stacked’ together and are smaller than 1 nm in size. It is thought that the rate of soot formation and hence, the amount of soot produced, depends on the formation of the first benzene ring or rings. This process depends on the type of fuel used, where aliphatic compounds undergo cyclisation to form the first benzene ring and aromatic compounds are broken down in order to allow for the first benzene ring to be created (Miller & Melius, 1992; Westmoreland, et al., 1989). These ring structures develop into PAHs from the addition of alkyl groups and other intermediate reactants.

PAHs can be as small as 2 – 3 rings and can grow larger and larger, forming the molecular precursors of soot, which are thought to be heavy PAHs. The hydrogen abstraction/carbon addition (HACA) mechanism is thought to be one of the main reaction pathways for this soot mass growth. The HACA mechanism involves the abstraction of hydrogen from the reacting fuel, via a reaction with hydrogen atoms. The newly formed radical site in the fuel then undergoes acetylene addition (Pandey, et al., 2007). It has also been found that the HACA mechanism cannot solely account for PAH concentrations found in experimental results (D'Anna & Violi, 1998). The PAH molecular reaction pathways suggested by (D'Anna & Violi, 1998) also takes into account reaction of intermediate reactants containing cyclic structures with five carbons, which can lead to the production of multiple benzene ring structures or small PAHs, such as naphthalene (two rings) and phenanthrene (three rings), as well as the reaction of larger radicals such as benzyl and propargyl. Nascent soot particle inception occurs when these small molecular PAHs become large enough to become particle nuclei. These nascent soot particles are known as NOC and have a diameter in the region of 1.5 nm. The hydrogen rich particles undergo dehydrogenation and absorb gas phase molecules, such as acetylene and PAHs, thereby continuing to increase in mass (Richter & Howard, 2000). There are thought to be many thousands of chain reactions taking place via radicals during these early stages of soot formation.

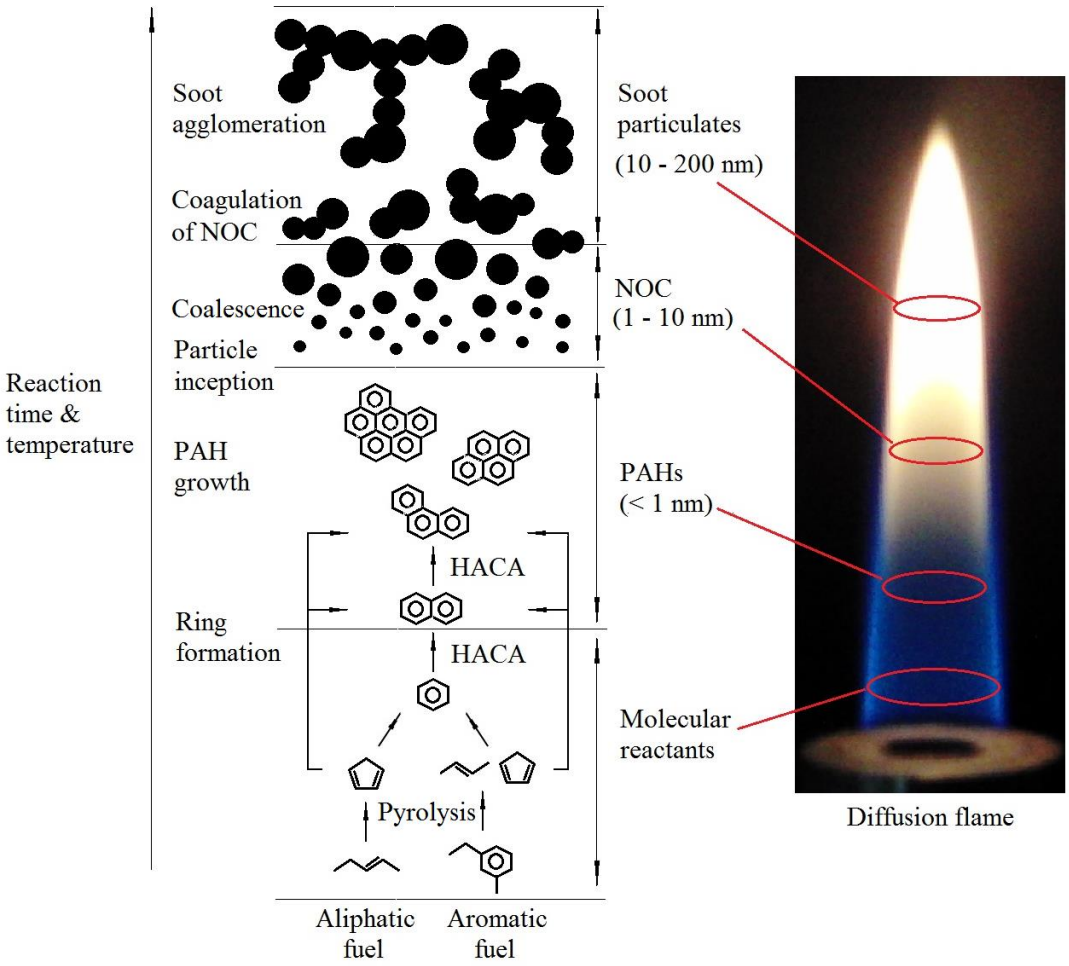

Figure 5.1. The soot formation process, including a photograph of a diffusion flame from this work.

Experimental results from a study (D'Anna, et al., 2005) show that NOC are formed largely in the central region, towards the lower part of the flame. The larger soot particles are formed in the upper part of the flame, with a similar concentration to the NOC, suggesting that soot formation is caused by coagulation of NOC particles. The particles undergo coalescence and coagulation through reactive particle to particle collisions where they agglomerate together, producing larger soot particles. As the process continues, the particulate material becomes progressively more homogeneous, through dehydrogenisation and growth. Oxidation occurs as a competing process to soot formation and happens simultaneously during premixed combustion and subsequently during non-premixed combustion (Richter & Howard, 2000). The soot formation process is summarised in Figure 5.1.

5.3 Factors influencing soot formation

5.3.1 Physical factors

5.3.1.1 Temperature and pressure

Early studies into soot revealed that there was a temperature dependence on the amount of soot that was produced in a given flame, where increasing temperature increases reaction rates. The SVF produced during premixed combustion decreases with an increasing temperature (Milliken, 1962). This can be explained by two competing processes within flames, namely the rate of fuel pyrolysis, leading to molecular precursors which then form PAHs and the rate of oxidation of these molecular precursors. The rates of both processes increase with an increase in temperature, however the oxidation rate increases more, resulting in less soot being produced at higher temperatures during premixed combustion. In diffusion flames there is no oxidation until after the soot formation process, therefore SVF increases with temperature (Glassman & Yaccarino, 1981). Changes in pressure can also affect flame behaviour by altering its structure and temperature, as well as the flow velocity and gas thermal diffusivity. As pressure is increased, the soot volume fraction increases due to higher reaction rates, arising from more molecular collisions (Tree & Svensson, 2007). A study showed that soot volume fraction increases with the square of the pressure in diffusion flames and higher pressures also increased primary particle size (Flower, 1985).

5.3.1.2 Fuel composition and structure

It is believed that in diffusion flames the fuel composition affects the soot, whereas in premixed flames compositional effects on soot are minimal. The chain length of the fuel and type of bonds within the chain affect the amount of soot produced during non-premixed combustion. For aliphatic fuels, alkanes increase in sootiness as chain length increases, whereas alkenes and alkynes show negligible change (Ladommatos, et al., 1996). However, the double and triple carbon bonds cause a significant increase in soot and an increase in the number of double bonds substantially increases the amount of soot. Fuels with chain lengths of four carbons or more soot more easily than shorter chains, due to the faster rate of reaction of the formation of the butadienyl radical (C_4H_5) from butene, compared with that of acetylene

(Glassman, 1988). It was also found in (Ladommatos, et al., 1996) that alkyl branches increase soot and aliphatic ring structures are sootier than open chain fuel structures. Aromatic fuels are fuels with benzene ring structures and produce more soot than aliphatics.

5.3.1.3 Oxygen content and Stoichiometry

When the fuel is composed of larger amounts of oxygen, there is more oxygen available to partake in oxidation reactions, reducing soot. The particular structure of the fuel and how the oxygen is bonded within the fuel molecules will determine how pronounced the effect of oxygen content within the fuel is in terms of reducing the amount of soot formed. Effects of fuel composition, structure and oxygen content on pyrolysis and oxidation reactions is discussed further in Section 5.4.

Stoichiometric combustion is an ideal situation where the reactants burn completely, as stated in Equations 1.1 and 1.2, in Chapter 1. The oxygen content can be increased by changing the oxygen content of the fuel or by increasing the amount of oxygen available in the oxidiser flow. Premixing the fuel and oxidiser will also increase the available oxygen, reducing soot. The oxygen content is also linked with temperature, which as mentioned previously, affects the amount of soot produced. Increasing the amount of oxygen increases the rate of reaction of oxidation due to increased oxygen concentration, increasing the amount of collisions. This, in turn, increases the temperature. Initially, the addition of oxygen enables radical attack on relatively stable fuel molecules, increasing soot formation rates. Further addition of oxygen increases the temperature of the reaction zone which increases soot formation in diffusion flames. Eventually, enough oxygen is added for oxidation to overcome the increase in soot formation due to higher temperature, which decreases the amount of soot formed (Tree & Svensson, 2007).

5.3.2 Dilution effects

5.3.2.1 Inert, thermal and diffusion effects

The edge of the luminous envelope of a diffusion flame defines where the small soot particles become completely burned. Above a certain fuel flow rate the luminous

flame front opens and visible black soot begins to break through. This is called the sooting flow rate and distinguishes when there is a sufficient amount of time for the soot particles become large enough to overcome the subsequent competing oxidation processes. The flame height associated with the sooting flow rate is known as the sooting height, which varies with fuel structure and is often used as a measure to compare the sooting tendency of different fuels (Olson & Pickens, 1984; Olson, et al., 1985; Ladommatos, et al., 1996). The flow rate of the coflowing air can also have an effect on the sooting height of a particular fuel, where increasing the coflowing air reduces the amount of soot produced. Subsequently increasing the fuel flow will cause the flame to soot once again at an increased sooting height. This process can be repeated until the sooting height remains constant regardless of the fuel or air flow rates. This is known as the ultimate sooting height (Ladommatos, et al., 1996).

Investigations have shown that nascent soot particles occur within a small temperature range and therefore soot particle formation can be assumed to occur along an isotherm, which overlaps certain flow streamlines within a diffusion flame. There is some discrepancy between the exact temperature range, where some studies (Glassman, 1998) show soot beginning to form at temperatures near 1600 K and others (Kobayashi, et al., 2008) suggest a lower temperature of around 1200 K. The discrepancy could be due to the point in which the particles detected were considered to be soot, or due to differences in experiment. The high temperatures suggest that the soot inception process requires a large amount of energy. Regardless of the magnitude of this value, a qualitative analysis of the addition of inert gases to a diffusion flame can be inferred. A diffusion flame has a sooting height at a given fuel flow rate, where the isotherm defines the point of nascent soot formation. There is consequently sufficient soot growth between the isotherm and the maximum flame temperature isotherm for the soot particles to become large enough to break through the luminous envelope. The sooting height is therefore determined by the growth in mass of the soot, which is in turn influenced by the rate of particle inception (Glassman, 1996).

Table 5.1. Some relevant gas properties under standard conditions.

Gas	Symbol	Molecular weight [$gmol^{-1}$]	Density [kgm^{-3}]	Specific heat capacity [$kJkg^{-1}K^{-1}$]	Diffusivity (in air) [cm^2s^{-1}]	Thermal conductivity [$Wm^{-1}K^{-1}$]	Heat of combustion [$kJkg^{-1}$]	Thermal diffusivity
Air		29	1.205	1.005	1	0.024		
Carbon monoxide	CO	28.01	1.165	1.04	0.1807	0.024	10100	0.02
Carbon dioxide	CO_2	44.01	1.842	0.846	0.1381	0.0146		0.01
Hydrogen	H_2	2.016	0.0899	14.31	0.61	0.168	141900	0.13
Nitrogen	N_2	28.0134	1.165	1.04	0.1788	0.024		0.02
Oxygen	O_2	32	1.331	0.918	0.182	0.024		0.02
Propane	C_3H_8	44.097	1.882	0.163	0.1	0.017	50340	0.06
Water	H_2O	18.016		4.181	0.2178	0.58		

The addition of an inert gas to the fuel stream causes a temperature drop by means of inert, thermal and diffusion effects (Shih & Hsu, 2013), depending on the properties of the gas. Some gas properties are listed in Table 5.1. Inert effects decrease the reaction rate through a reduction in the reactive species concentration, thereby reducing the overall energy released during the exothermic reaction, thermal effects are brought about by the variation in thermal properties of the mixture and diffusion effects change the species distribution because of the alteration in the transport properties of the mixture. These factors can result in the soot inception isotherm moving closer to the maximum flame temperature isotherm. There is consequently less time for soot particles to increase in mass and therefore the SVF is reduced. Furthermore, soot growth is slower due to the reduced reaction rate. Above a certain flow rate of inert diluent gas, the soot particles are all consumed by the flame, therefore no longer breaking through the luminous flame envelope. The flame temperature rises again when the fuel flow rate is increased due to the effects of the inert gas being decreased and a greater sooting height is reached at a certain fuel flow rate. This is because the soot inception isotherm has increased in distance from the maximum flame temperature isotherm, resulting in an increased SVF due to a longer residence time. Upon increasing the flow rate of inert gas again, its effects will once again become prevalent, reducing the amount of soot and adding more fuel will thereby increase the sooting height further.

It has been hypothesised that the distance z between the soot formation isotherm and the flame temperature isotherm along a streamline for one dimensional flow depends on the following relation (Glassman, 1998)

$$Ln\left(\frac{T_f - T_0}{T_n - T_0}\right) = \frac{v}{\alpha} z, \tag{5.1}$$

where T_f, T_n and T_0 are the flame, soot formation and initial fuel jet temperatures respectively, v is the gas velocity and α is the thermal diffusivity, which is defined by

$$\alpha = \frac{\kappa}{\rho c_p}, \tag{5.2}$$

where κ is the thermal conductivity of the mixture and ρc_p is the volumetric heat capacity, which is the product of the mixture density (ρ) and specific heat capacity (c_p). Thermal diffusivity is a measure of how quickly a substance can adjust its temperature, where a high thermal diffusivity relates to a fast change in temperature.

From equation (5.1) it can be seen that the thermal diffusivity is clearly a major contributor to the SVF. Diluting the flow with an inert gas that has a thermal diffusivity greater than that of the fuel, causes the isotherms to be spaced further apart, compared with an inert gas with a lower thermal diffusivity. Therefore different inert diluents will affect the SVF to a different degree. Where the inert effect, reducing rate of reaction and hence soot growth, competes with the thermal diffusivity effect, in the case of the diluent having a larger thermal diffusivity than the fuel. This reduces the decrease in soot growth to some extent. For a diluent gas with a thermal diffusivity lower than that of the fuel, soot growth is further reduced.

It was noted in (Glassman, 1998) that the number of atoms in an inert gas diluent at a given volumetric flow rate affected the SVF, where triatomic molecules reduced the SVF more than diatomic molecules, which reduced SVF more than monoatomic molecules. When taking into account thermal diffusivity of the diluent for identical

or similar temperature flames, it was found that higher thermal diffusivity diluents reduce soot growth less, producing more soot, which supports the above hypothesis. When comparing the SVF of the diatomic diluent nitrogen with the monoatomic diluent argon, which burned at a significantly hotter temperature than the nitrogen flame, there was no significant difference. This was due to the *ln* relation with temperature in equation (5.2), which dampens the effect of temperature on the distance between the two isotherms and hence, the SVF. This confirmed the idea that the thermal diffusivity of the diluent affected the soot growth rate more than the flame temperature, which was supported with data from other studies (Axelbaum & Law, 1990).

Diffusion processes govern the amount of soot produced in diffusion flames. There are many particles and hence many collisions within flames. The interaction of intermolecular forces controls the amount of collisions and therefore controls the overall mass transport into and out of flame zones. Under standard conditions gas molecules travel near to the speed of sound, however diffusion speeds are much less, in the region of 1 cms^{-1}, due to molecular collisions. The actual path of a molecule is expected to be about 10,000 times the total distance travelled (Marrero & Mason, 1972). Different atoms, molecules and radicals have varying degrees of diffusivity, where H_2 molecules and H• radicals have a high diffusivity and can there diffuse more easily into fuel rich zones and accelerate normal pyrolysis. Therefore the amount of hydrogen in a fuel, along with how easily it is abstracted during pyrolysis and oxidation, has a significant effect on the soot formation process.

5.3.2.2 Chemical effects

The addition of diluent gases is often not chemically inert and therefore the gases become involved in the chemical reaction. This is referred to as the chemical effect of diluent gases. For example, water (H_2O) dissociates, contributing to the amount of H and OH radicals present within the flame, carbon dioxide (CO_2) can also dissociate at flame temperatures and nitrogen (N_2) produces NO_X emissions at these high temperatures (Shih & Hsu, 2013). The dissociation of CO_2 occurs at high

temperatures above 1000 K, in which the main reaction sequence is (Liu, et al., 2001; Ladommatos, et al., 1996)

$$CO_2 + H \leftrightharpoons CO + OH$$

where the hydroxyl radicals enhance the oxidation of soot precursors and soot, resulting in the production of less soot. CO_2 can also affect fuel pyrolysis in a similar way, whereby the main reaction is (Liu, et al., 2001; Abián, et al., 2012)

$$CO_2 + H_2 \leftrightharpoons CO + H_2O$$

This reaction reduces the amount of hydrogen molecules, which increases the H•/H_2 ratio, resulting in increased hydrogen abstraction from the fuel (Pandey, et al., 2007). This promotes fuel pyrolysis and early oxidation reactions, leading to the production of precursors, increasing soot formation. In contrast, the reaction with atomic hydrogen will have the opposite effect. The dominant reaction will determine the net soot formation due to CO_2 dissociation from these reactions.

5.4 Pyrolysis and early oxidation mechanisms

The initial stages of combustion are known as fuel pyrolysis, which involves the fuel decomposing in some way, due to elevated temperature and surrounding environment. The structure of the fuel will affect the reaction pathways that occur during pyrolysis, which lead to the formation of soot precursors and finally, into soot. The effects of fuel structure on these early pyrolysis reactions can be used to determine the fuel oxidation and soot formation rate and hence, the amount of soot produced by a combustion system. There are considered to be two stages of combustion, involving low temperature (up to about 900K) and high temperature pyrolysis and early oxidation mechanisms, which both consist of many types of subsequent reactions, leading to the formation of soot. The rates of early stage

reactions for both low and high temperature pyrolysis and early stage oxidation are highly dependent on the fuel structure.

The dominant types of reaction which take place during the early low temperature stages of combustion for long chain molecules, such as biodiesels have been explained in detail in (Curran, et al., 1998; Naik, et al., 2011) and are summarised as follows. Initially, a hydrogen atom is abstracted from a relatively weak carbon-hydrogen bond. An alkyl radical is formed which reacts with an oxygen molecule to form an alkylperoxy radical (RO_2•), where R represents an alkyl or allyl chain. These RO_2• species then undergo isomerisation RO_2•↔•QOOH (where Q represents a C_nH_{2n} structure), along with undergoing attack from various smaller radicals, forming various species including RO_2H, RO•, •OH and O_2. RO• will subsequently decompose and the •OH radical concentration is important to the overall reaction rate. The hydroperoxyalkyl radicals (•QOOH) can then undergo several decomposition processes, including the formation of cyclic ether compounds after breaking of the O-O bond and the formation of alkenes through β radical sites and β-scission. β-scission is the process in which a free radical causes a carbon-carbon bond to break, forming a new carbon=carbon double bond, plus a new free radical. The hydroperoxyalkyl radicals can also undergo O_2 addition and subsequent isomerisation to ketohydroperoxide, which then decompose forming oxygenated radical species.

The main types of initial high temperature pyrolysis and early oxidation reactions are also described in detail in (Curran, et al., 1998) and have been summarised here. Hydrogen abstraction also occurs in high temperature pyrolysis, producing alkyl radicals. The alkyl radicals can then undergo several reactions, including decomposition via β-scission, isomerisation and O_2 addition, where O_2 addition produces alkenes through β-scission. The alkene then undergoes hydrogen abstraction due to small radicals such as H•, O•, •OH and •CH_3. Radicals then get added to the alkene, which then finally decomposes.

5.4.1.1 Alkanes

Biodiesel molecular structure contains a relatively long alkyl chain and an ester group, where the alkyl chain can be saturated. In the case of alkane pyrolysis, hydrogen abstraction is the principle mechanism. Long chain alkanes have two types of carbon-hydrogen bonds, namely primary and secondary, where primary hydrogen atoms are bonded to the end carbons and secondary hydrogen atoms are part of the CH_2 groups, as shown below for pentadecane.

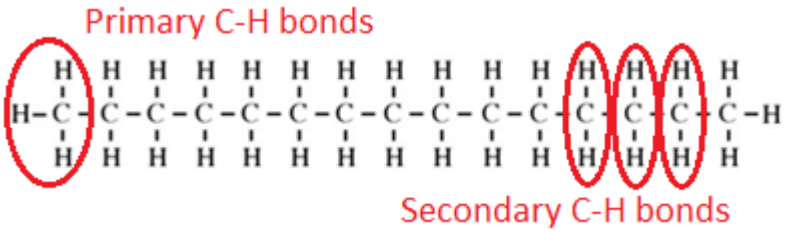

The bond dissociation energy of secondary carbon-hydrogen bonds is less than that of primary bonds, where secondary bonds are approximately 98 kcal/mol and primary are about 101 kcal/mol. Therefore hydrogen abstraction occurs mainly from secondary bonds (Westbrook, et al., 2013).

5.4.1.2 Alkenes

The alkyl chain part of biodiesel molecules can often be unsaturated, containing carbon=carbon double bonds. Alkene chains have at least one double bond, which changes how pyrolysis processes proceed. The carbon atoms that are double bonded have a single hydrogen bonded to each of them, which are vinylic carbon-hydrogen bonds. These vinylic bonds are stronger than primary and secondary bonds, with a bond dissociation energy of approximately 108 kcal/mol. The carbon-hydrogen bonds adjacent to the double bonded carbons are allylic bonds (illustrated below), which are relatively weaker than primary, secondary and vinylic bonds, with a bond dissociation energy of approximately 87.7 kcal/mol.

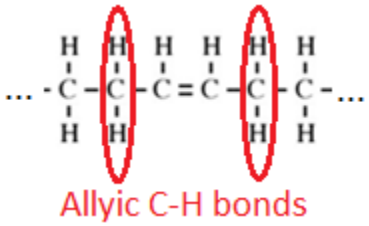

Therefore in alkenes and any fuel that contains allylic bonds, these hydrogen atoms are abstracted most easily (Westbrook, et al., 2013). Carbon-hydrogen bonds that are adjacent to two carbon=carbon double bonds (bisallylic) are even weaker.

The chemistry of an alkene is determined by its chain length, where longer chain alkenes of 5 carbons or more can undergo several processes that smaller chains cannot. Large alkenes can partake in six-centre elimination reactions and can decompose directly into benzene precursors, 4 or 5 carbons in length. This is much faster than the addition reactions that are required to produce these precursors from smaller chain alkenes. Larger alkenes also have allylic carbon-carbon bonds, which are relatively weak compared with non-allylic carbon-carbon bonds. An allylic carbon-carbon bond is positioned but one away from the double carbon=carbon bond in an alkene chain, for example in 2-hexene:

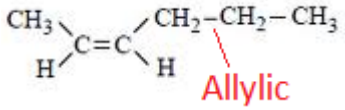

1-butene is the only short chain alkene that has an allylic bond. Allylic bond fission is a unimolecular bond breaking process, where a relatively weaker carbon-carbon or carbon-hydrogen allylic bond is broken to form an allylic radical and an alkyl radical (McEnally & Pfefferle, 2005). Allylic carbon-carbon bonds are approximately 50 kJ/mol weaker than allylic carbon-hydrogen bonds and therefore are more likely to undergo fission and allylic hydrogen atoms are the most abstractable hydrogen atoms in alkenes.

Hydrocarbons mainly decompose by either bimolecular hydrogen abstraction or unimolecular dissociation and it has been shown that unimolecular processes are dominant for most hydrocarbons (McEnally & Pfefferle, 2005; McEnally & Pfefferle, 2004; McEnally & Pfefferle, 2005). The possible unimolecular decomposition reactions for large alkenes are six-centre elimination, isomerisation and allylic bond fission, where that latter was shown to be the fastest reaction in the pyrolysis zone and hence most dominant, over 400 times faster than the fastest bimolecular reaction.

Radical sites that are formed from allylic hydrogen abstraction next to a carbon=carbon double bond, undergo oxidative attack from O_2 molecules, resulting in the formation of RO_2• radicals. These RO_2• radicals have very weak carbon-oxygen bonds and readily turn back into the original R• and O_2 species. The presence of a double bond therefore reduces the RO_2• concentration which inhibits alkylperoxy radical isomerisation leading to •QOOH and subsequent reactions. Furthermore, the weak allylic carbon-hydrogen bonds due to the presence of a double bond reduce the number of smaller radical species because more are participating in hydrogen abstraction reactions (Westbrook, et al., 2013).

5.4.1.3 Esters and biodiesels

Biodiesel molecular structure contains an ester group and a relatively long alkyl chain, which is either saturated or contains varying degrees of unsaturation. The amount of acetylene produced during pyrolysis is proportional to the number of carbon=carbon double bonds (Garner, et al., 2009), where more double bonds result in more acetylene, leading to more soot due to increased amounts of precursors. This is because the double bond is more likely to remain intact during pyrolysis due to its relatively high stability over carbon-carbon single bonds. The reactivity of esters increases with chain length and large methyl esters and alkanes have similar reactivities (Lai, et al., 2011; Hakka, et al., 2009). This is due to an increase in the number of possible six centre reactions. Reactions that are able to form six membered transition states are also preferred and longer chains will provide more possibilities. The presence of a carbon=carbon double bond inhibits six centre

reactions and certain isomerisation reactions involving hydrogen atom transport, due to the higher stability of the double bond. This reduces the reactivity at low temperatures and therefore saturated esters are more reactive than unsaturated esters (Lai, et al., 2011; Kohse-Höinghaus, et al., 2010). The position of the double bond in the molecule is also important, as it dictates how and what pyrolysis processes can take place.

The weakest carbon-hydrogen bonds in an ester molecule can determine the oxidation rate. For saturated molecules, these are the carbon-hydrogen bonds adjacent to the carbon bonded to the carbonyl group. For unsaturated molecules, the carbon-hydrogen bonds which are the weakest are those adjacent to the carbons which are double bonded, i.e.

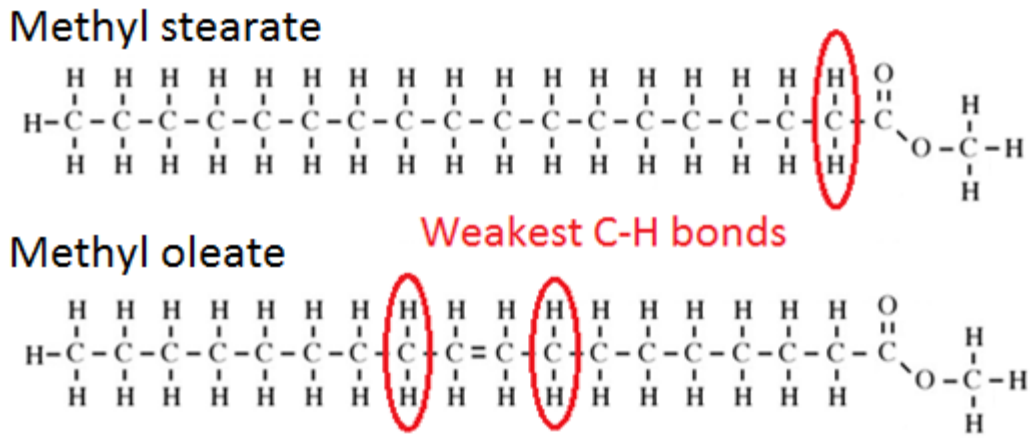

Carbon-carbon bonds are more easily broken than carbon-oxygen bonds in an ester. The oxidation of an ester can result in the early formation of carbon dioxide, which is caused by the two oxygen atoms remaining attached to the carbon atom. Methyl esters can decompose into either two carbon monoxide molecules, or a single carbon dioxide molecule. Carbon monoxide and carbon dioxide form as a result of the relatively stronger carbon-oxygen bonds. The oxidation of carbon to form CO and CO_2 decreases the mass of the soot, where the formation of CO has a larger effect on soot reduction, as a single oxygen atom sequesters a carbon atom and the formation of CO_2 requires two oxygen atoms per carbon atom (Lai, et al., 2011; Kohse-Höinghaus, et al., 2010). (Kohse-Höinghaus, et al., 2010) also mentions some

important radicals in biodiesel combustion, including $\bullet OCH_3$ and $CH_3OCO\bullet$, where $CH_3OCO\bullet$ decomposes to $\bullet CH_3$ and CO_2. These radicals are postulated to be the reason that biodiesel is highly reactive.

The significance of the alkyl ester part of the methyl ester molecule reduces as the chain length of the alkyl part of the molecule increases. Hydrogen abstraction from methyl esters produces formaldehyde (HCOH) and that of ethyl esters produces acetaldehyde (CH_3COH). Unimolecular decomposition of methyl esters produces $\bullet CH_3$ and $CH_3O\bullet$ radicals and that of ethyl esters produces ethylene through a six membered ring transition state. More C_2 is produced from ethyl esters, compared with methyl esters, due to direct formation from the ethyl group, which may lead to more soot production (Kohse-Höinghaus, et al., 2010).

5.5 Biofuels

5.5.1 Biodiesels

Biodiesels are fuels that mainly consist of alkyl esters made from long chain fatty acids which originate from plant oils or animal fats. The plant or animal based fatty acids are in the form of triacylglycerides (triglycerides) and have to undergo transesterification in order to become biodiesel. The transesterification process involves the triglycerides and an alcohol reacting together in the presence of a catalyst, resulting in fatty acid alkyl esters and glycerine (glycerol). The type of alcohol used determines the type of ester and the most common alcohol used in this process is methanol which produces methyl esters. The process is outlined in reaction 1 below.

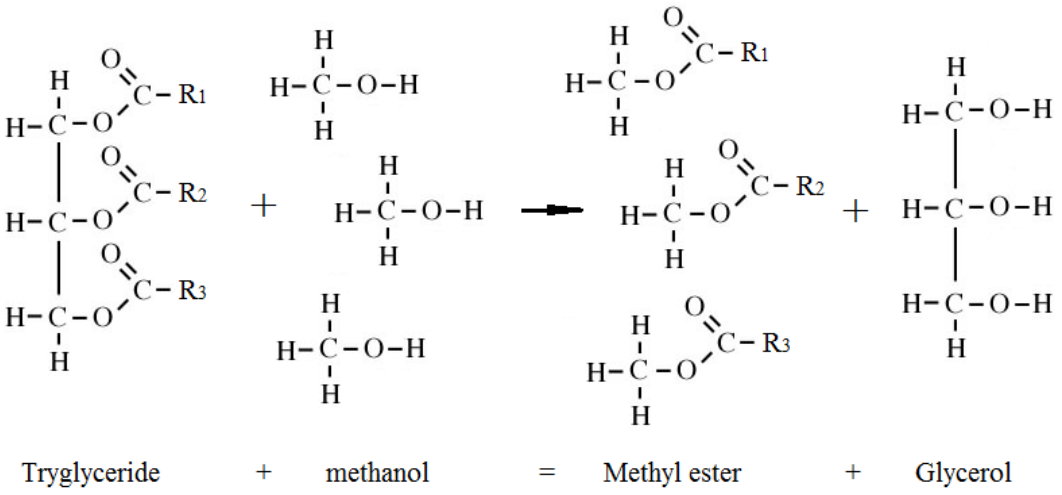

Reaction 1. Transesterification of a tryglyceride with methanol to produce a methyl ester and glycerol.

5.5.2 Biodiesel composition

Biodiesel can be made from almost all feedstock containing triglycerides. The most popular sources used globally at present are Soybean, Rapeseed and Palm oils. Other plant and vegetable oils including canola, coconut, jatropha, safflower and sunflower are also good potential biodiesel producers. Other sources include algae, fish oil and animal fats, such as tallow. Some of the most common fatty acids present within these feedstocks are included in Table 5.2 (Hoekman, et al., 2012). The first number in the abbreviation represents the number of carbons present in the fatty acid chain and the second number denotes the number of carbon=carbon double bonds.

The fuels used in this study are coconut methyl ester (CME), rapeseed methyl ester (RME), sunflower methyl ester (SME), tallow methyl ester (TME), fish ethyl ester (FEE) and a methyl ester produced from used cooking oil (UCOME). Jatropha methyl ester (JME) was used in the gas turbine engine study, but not in the flame study. The composition of the fuels have been included in Table 5.3. Values for all fuels apart from FEE were taken from a recent biodiesel composition review paper, taking into account a large number of references (Hoekman, et al., 2012). Composition of the feedstock can change through region to region, as well as through other factors, such as production techniques and genetic modification,

however the percentages shown in the table are considered to be good enough for a comparative analysis of the fuels in this work. It is worth noting that the UCOME is likely to vary more notably that the other fuels, due to the fact that it is likely to comprise of any number of other biodiesels, hence it may resemble particular fuels for different regions.

Table 5.2. Common fatty acid components in biodiesel sources.

Common name	Formal name	Abbrev.	Molecular formula	Molecular weight	Molecular structure
Lauric acid	Dodecanoic acid	12:0	$C_{12}H_{24}O_2$	200.32	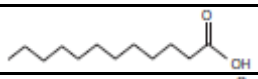
Myristic acid	Tetradecanoic acid	14:0	$C_{14}H_{28}O_2$	228.38	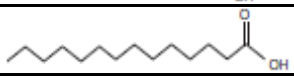
Palmitic acid	Hexadecanoic acid	16:0	$C_{16}H_{32}O_2$	256.43	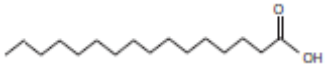
Palmitoleic acid	*cis*-9-Hexadecenoic acid	16:1	$C_{16}H_{30}O_2$	254.42	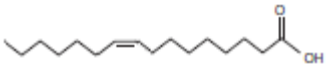
Stearic acid	Octadecanoic acid	18:0	$C_{18}H_{36}O_2$	284.48	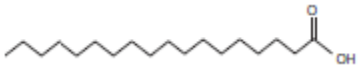
Oleic acid	*cis*-9-Octadecenoic acid	18:1	$C_{18}H_{34}O_2$	282.47	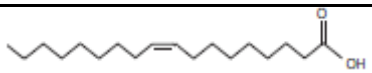
Linoleic acid	*cis*-9,12-Octadecenoic acid	18:2	$C_{18}H_{32}O_2$	280.46	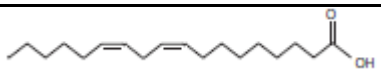
Linolenic acid	*cis*-9,12,15-Octadecenoic acid	18:3	$C_{18}H_{30}O_2$	278.44	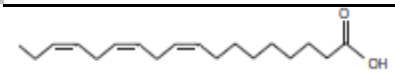
Gondoic acid	*cis*-11-Eicosenoic acid	20:1	$C_{20}H_{38}O_2$	310.53	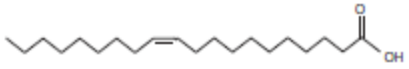
Erucic acid	*cis*-13-Docosenoic acid	22:1	$C_{22}H_{42}O_2$	338.58	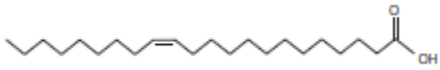

The FEE was acquired from waste anchovy oil, after it had been harvested for its omega 3 fatty acids. The original composition of anchovy oil was acquired from (Ackman, 2005), where the fatty acid chains for the Peruvian anchovy was listed. It is unknown from what area that the anchovies used to produce the FEE in this study originated, however it was assumed that the composition of anchovies worldwide is at least similar, to a reasonable degree of accuracy. The omega 3 fatty acids were listed to include 16:3, 18:3, 18:4, 20:3, 20:4, 20:5, 22:3, 22:4, 22:5 and 22:6, constituting approximately one third of the oil. The omega 3 extraction from the fish

oil mainly removed the relatively longer chain fatty acids which do not appear in significant numbers in the other oils discussed in this study. The FEE composition was then calculated from the fatty acid chains remaining and is presented in Table 5.3.

Table 5.3. Main fatty acid components of biodiesels used in this study, taken from the literature.

Fatty acid	Abbrev.	CME		RME		SME		TME		FEE		UCOME		JME	
		mean	dev	mean	dev	mean	dev	mean	dev	mean	dev	mean	dev	mean	dev
Caprylic acid	8:0	6.8	1.9												
Capric acid	10:0	5.4	1.1												
Lauric acid	12:0	47.7	5.4	0.1	0.1	0.1	0.3	0.2	0.1	0.15		0.2	0.6	0.1	0.2
Myristic acid	14:0	18.5	1.3	0.0	0.0	0.1	0.1	2.6	0.7	11.30		0.8	0.6	0.3	0.5
Palmitic acid	16:0	9.1	1.7	4.2	1.1	6.4	1.8	24.3	2.8	26.46		16.5	5.6	14.9	2.1
Palmitoleic acid	16:1	0.1	0.2	0.1	0.1	0.1	0.1	2.6	1.0	13.65		0.9	1.1	1.0	0.5
Stearic acid	18:0	2.7	0.7	1.6	0.7	3.6	1.1	18.2	4.5	6.07		7.1	3.9	6.1	1.7
Oleic acid	18:1	6.8	2.1	59.5	7.8	21.7	5.3	42.2	4.1	17.51		44.6	9.3	40.4	6.7
Linoleic acid	18:2	2.1	1.4	21.5	2.8	66.3	7.6	4.4	2.9	2.88		25.1	10.3	36.2	6.1
Linolenic acid	18:3	0.1	0.1	8.4	1.3	1.5	2.6	0.9	0.7	0.76		1.1	1.1	0.3	0.2
Gondoic acid	20:1	0.0	0.0	2.1	3.0	0.2	0.2	0.6	0.2	2.35		0.5	0.1	0.1	0.0
Erucic acid	22:1	0.0	0.0	0.5	0.5	0.1	0.1	0.1	0.0	1.74		0.1	0.1	0.1	0.1

None of the plant or animal fats contained a significant number of relatively longer chain molecules (20 or above), unlike the original fish oil, before omega 3 extraction. The maximum chain length with a significant proportion of the fuel found in the other fuels was 18. As a comparison, CME mainly consists of saturated short chain fatty acid ester chain lengths, RME of mono and polyunsaturated long chain lengths, SME similarly has long of mono and polyunsaturated chains with a small amount of mid-range saturated parts, TME consists of mainly longer chains, both saturated and monounsaturated, with some mid-range saturated portions, FEE contains chain lengths ranging from short to long, both saturated and monounsaturated and JME contains mainly long mono and polyunsaturated chains, as well as mid-range saturated chains. The UCOME appears to resemble JME somewhat. Table 5.4

includes some of the physical properties of the biodiesels used in this study, apart from FEE which is unknown due to the omega 3 fatty acid removal prior to transesterfication. For a comparison, although diesel composition varies, generally diesel is composed of a significant amount of linear and cyclic saturated hydorcarbons, in the region of 65 %, a small percentage of unsaturated hydrocarbons and about 30 % aromatics, with carbon chains ranging from 10 – 22 averaging near 14 – 15 (Pitz & Mueller, 2011).

Table 5.4. Some properties of biodiesels used in this study (Hoekman, et al., 2012).

Property	CME	RME	SME	TME	UCOME	JME
Kinematic viscosity	2.75	4.50	4.42	4.69	4.80	4.75
Iodine value	18.5	116.1	128.7	65.9	88.9	109.5
Specific gravity	0.874	0.879	0.878	0.878	0.879	0.876
Average chain length	13.40	17.90	18.10	17.30	18.50	18.30
Average unsaturation	0.12	1.31	1.59	0.59	1.06	1.15

5.5.3 Gas chromatography

As mentioned, the composition of biodiesels can vary from region to region, depending on the source. It is therefore advantageous to this investigation that the composition of the specific biodiesels used in this study is measured, in order to eliminate any discrepancies. The individual emissions characteristics of each fuel can then be related to its composition and perhaps, other attributes. There are a wide range of chemical and physical measurement techniques available for determining the composition of a material, such as photometric analysis, including spectroscopy, electrometric techniques, including electrical conductivity cells and chromatography, including gas chromatography, which uses physical factors. For the analysis of long chain fatty acid esters within the range of 6 to 26 carbons in length, gas chromatography was deemed the most suitable for this work (Hakka, et al., 2009; Kim, et al., 2004).

Gas chromatography is a widely used technique for identifying the composition of various compounds. Generally, the process is involves a mobile phase and a stationary phase, where the mobile phase is a carrier gas and the stationary phase is a liquid with a high boiling point. The methodology behind the technique is summarised as follows. A small sample of the liquid being analysed is put into the injector, which is heated above the boiling point of the sample, causing it to vaporise. The vaporised sample is then transported into a chromatographic column by the flow of the gaseous mobile phase. There are two types of injection, namely split or splitless, where in split mode the gas flow can exit through 3 routes, either into the main column, split outlet or the septum purge. The column is heated within an oven in order to keep the sample in its gaseous phase. The liquid stationary phase is adsorbed onto the inner surface of the column. There are two types of column, namely packed and capillary, where packed columns contain a finely divided solid support material with the stationary phase adsorbed onto the surface, with an internal diameter between 2 and 4 mm. Capillary columns have much smaller internal diameters, in the region of 0.1 mm, where the stationary phase is either directly coated onto the supporting walls, or adsorbed onto a thin layer of supporting material, which is attached to the walls

The speed in which a particular compound travels through the column, depends on how long it is retained within the stationary phase, before it reaches the detectors. There are several types of detectors that can be used in gas chromatography, including flame ionisation, thermal conductivity, electron capture, nitrogen-phosphorus, flame photometric, photo-ionisation and hall electrolytic conductivity detectors. The flame ionisation detector is used for the analysis of organic compounds, such as those within the biodiesels used in this study. The material exiting the column is mixed with hydrogen and air and ignited to produce a flame. A voltage is applied to the burner tip and an electrode is positioned above the flame tip. The ions and electrons produced by the pyrolysis of the fuel compounds cause a current to flow between the electrode and the burner tip which is recorded for each type of compounds as it passes through flame. As each fuel component is detected in

the flame its retention time within the column is recorded, along with the amount of each particular compound, providing a percentage composition for each component.

5.6 Soot analysis techniques

5.6.1 Thermophoretic sampling

Thermophoretic sampling is an ex-situ soot diagnostic technique that involves the extraction of soot particles from a combustion environment for subsequent analysis in a transmission electron microscope (TEM). Soot particles are usually deposited onto a carbon coated TEM grid that is attached to a probe which is inserted into the combustion environment for a short amount of time. The residence time within the combustion environment should be long enough to allow for a reasonable amount of soot to become deposited onto the TEM grid, but also short enough to prevent the grid from heated up significantly. The principle behind the technique is that the particles within the hot combustion environment are attracted to the relatively cold TEM grid through thermophoresis, which occurs due to the temperature gradient. The cooling effect of the cold probe surface also causes the soot aggregates to stop reacting, as their temperature becomes lower than the soot formation temperature, preserving the soot as it is sampled (Dobbins & Megaridis, 1987).

5.6.2 Laser induced incandescence

5.6.2.1 Background

The LII technique uses high energy laser light to heat soot particles to the point of sublimation. The soot particles absorb the laser energy and reach a temperature that is determined by the energy balance between the rate of laser energy absorption, conductive heat transfer from the soot particle to the surrounding gases, radiative heat loss and the latent heat of sublimation. The laser energy absorption is much higher than the radiative and conductive heat losses for sufficiently high fluences and therefore the soot particles heat up during the laser pulse (Will, et al., 1996). Near 4000 K, where the soot particles begin to sublimate their temperature reaches a plateau region due to the large amounts of energy expended during sublimation. The

temperature of the soot particles gradually reduces subsequent to the laser pulse due various heat transfer mechanisms, including radiative and conductive heat losses.

The LII signal is the Planck radiation emitted from the laser heated soot particles which is called incandescence. Incandescence is the emission of light by a hot body and is in the form of a continuous spectrum. The measured intensity of the LII signal is dependent on the laser fluence, detection wavelength and particle temperature, where the temperature relation is described by the Stefan-Boltzmann law

$$j = \varepsilon \sigma T^4 , \tag{5.3}$$

where j is the irradiance of the soot particle, ε is the emissivity soot, T is the soot temperature and σ is the Stefan-Boltzmann constant, which is

$$\sigma = \frac{2\pi^5 k^4}{15c^2 h^3} = 5.670400 \times 10^{-8}\, Js^{-1} m^{-2} K^{-4} , \tag{5.4}$$

where k is the Boltzmann constant, c is the speed of light and h is the Planck constant. The emission spectrum of the LII signal is described by Planck's law

$$R_s(\lambda, T) = \frac{2c^2 h}{\lambda^5}\left[\exp\left(\frac{hc}{\lambda k T}\right) - 1\right]^{-1} , \tag{5.5}$$

where R_s is the spectral radiance and λ is the wavelength. The LII signal increases with an increase in laser fluence up to a threshold of around 0.2 J/cm^2 (Hofmann, et al., 2003), where the intensity levels off, due to the soot temperature remaining constant throughout the phase change process. At relatively higher laser fluences above approximately 0.5 J/cm^2 (Wal, et al., 1998), effects due to sublimation are no longer negligible and therefore this fluence independent plateau region, between 0.2 and 0.5 J/cm^2, should be used for LII measurements.

5.6.2.2 LII methods

The initial intensity of the LII signal, due to laser heating can be related to the SVF of soot within the flame. The LII signal has also been shown to be dependent on soot particle size, where larger particles heat up to higher temperatures than smaller particles and therefore a larger portion of the LII signal is produced by the larger particles. The temporal decay of the LII signal, which is shown in Figure 5.2 is also dependant on soot particle size, where larger soot particles cool slower than smaller particles due to increased heat capacity. These two factors contribute to a bias in the LII signal towards larger soot particles. Detecting the LII signal within the first 100 ns of the laser pulse will reduce this bias (Will, et al., 1995).

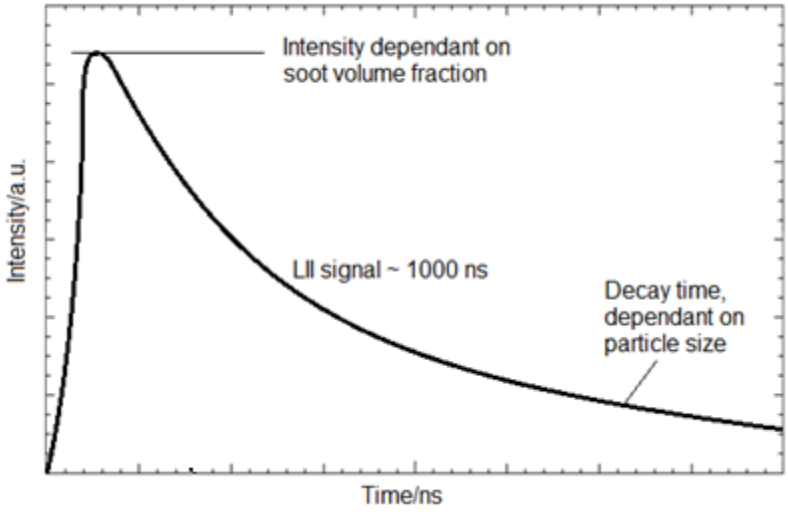

Figure 5.2. Sketch of the temporal lifespan of the LII signal.

A number of detection schemes can be used for LII measurements, depending on the particular parameter being measured. Several LII detection schemes were analysed in (Wal & L., 1996) and have been summarised as follows. Detection within the first 25 ns of the laser pulse will provide the highest signal to flame background ratio, however detection within the first 100 ns still provides a high signal, compared with flame background. This is because the LII signal intensity is considerably higher than the flame luminosity. The point in which the LII signal is of greatest intensity coincides with the laser pulse. Therefore, if LII detection is delayed then the signal to

flame background ratio is reduced. If the detection regime is any longer than 100 ns there will be an error due to the signal bias towards larger particles.

The decay rate of the LII signal after the laser pulse varies depending on the particle size. The decay time of the LII signal increases with increasing particle size (Will, et al., 1995). Time resolved LII determines the soot particle size at a given location within the flame by detecting the LII signal at two or more points along the decay curve after the laser pulse. The initial 10 ns of the LII signal are not characteristic of particle size and therefore the laser pulse should be avoided during detection. It is ideal to choose a detection time of 100 ns for the first detection window, as the signal depends on the rate of soot sublimation.

5.6.3 Laser induced fluorescence

Laser induced fluorescence (LIF) takes advantage of the fluorescence of early stage combustion species. The fundamental frequency of an Nd:YAG laser (1064 nm) is the ideal wavelength for LII measurements, but 1064 nm light is unable to excite fluorescence from PAHs via multiphoton excitation (Vander Wal, et al., 1997). LII can also be carried out using the second harmonic of an Nd:YAG laser (532 nm) as soot particles are broadband absorbers and can absorb light from UV to infrared (IR). However, nanoparticles of organic carbon (NOC) are transparent to visible light and so 532 nm light would also be ineffective. NOC can be detected by UV light absorption and LIF. The third and fourth harmonic of an Nd:YAG laser (355 nm and 266 nm respectively) are both in the UV region which means that both wavelengths could be suitable for NOC measurements. Some studies (Harrington & C. Smyth, 1993; Brackmann, et al., 2003) have shown that formaldehyde combustion intermediates can be excited with 355 nm light. Formaldehydes have been found in methane/air flames and can be used for instantaneous flame front detection. However, the absorption spectrum of a preinception region of a slightly sooting flame shows a strong absorption coefficient in the UV at 200 nm which sharply decreases for longer wavelengths and is below the detection limit at 350 nm (Basile, et al., 2002). This absorption characteristic is representative of NOC particles and shows that 355 nm is not preferable for their detection. 266 nm is more suitable as it

is closer to the peak absorption wavelength and as soot particles are broadband absorbers, this wavelength could also be used to follow kinetics of clusters of PAHs to larger soot particles.

A study (D'Anna, et al., 2001) has shown that UV absorption at 266 nm is linked to PAHs of 2 -3 benzene rings. (Basile, et al., 2002) states that the yellow luminous region of a slightly sooting flame has a large absorption peak at 200 nm which also extends towards the visible due to soot particles. In fully sooting conditions the absorption region extends from UV to visible and exhibits a broad maximum at 230 nm. The paper goes onto explain how the soot volume fractions of both the NOC and the soot can be found if the volume attenuation coefficients, specific cross sections and refractive index of the particles are known, for a fixed wavelength. So, knowing these properties at 266 nm and using a 266 nm laser to find the spectrum could lead to finding NOC and Soot volume fractions in a flame. The results in the study show that soot particles are less than 50% of the total particulate fraction in the flame, even in the sooting region. It can be seen that UV absorption is used to find out the amount of particulate matter there is, UV scattering is also employed in other studies (D'Anna, et al., 2009; D'Alessio, et al., 2000) which is used to find the size distribution of particulates in flames. Scattering signals can be affected by gas phase molecules such as CO_2 and H_2O and so these signals need to be known, so that they can be subtracted from the overall signal. Light scattering is related to the real part of the refractive index, whereas the absorption is related to the imaginary part (Sgro, et al., 2003).

5.6.4 Other laser soot diagnostic techniques

Other laser diagnostics for detecting combustion species include light extinction, Rayleigh scattering, laser induced breakdown spectroscopy (LIBS) and coherent anti-Stokes Raman spectroscopy (CARS). Light extinction is one of the first non-intrusive soot measurement techniques to be used. When light is passed through a flow that is laden with particles, the particles will absorb a certain amount of the light and the amount of absorption can be related to the concentration of particles. Rayleigh scattering is based on the elastic scattering of photons from gas molecules.

The energy of the scattered light is proportional to the number density of the gas molecules and can therefore be used to determine certain parameters of the gas. LIBS involves heating a sampling of solid, liquid or gas to upwards of 20,000 K by means of an intense light source, such as a laser, so that it becomes a plasma. In doing so, a small amount of the sample is destroyed. The constituent elements of the high temperature plasma then give off individual spectral lines and the technique can therefore be used to identify substances. The CARS technique is a non-linear laser diagnostics technique that induces Raman coherence in the target. The technique uses two lasers to induce the Raman coherence and then a third to probe the signal.

CHAPTER 6
EXPERIMENTAL METHODOLGY FOR SOOT MEASUREMENTS IN FLAMES

6.1 Introduction

The experimental setup and methodology for the emissions experiments are detailed in this chapter, focusing on the laser induced incandescence (LII). LII was used on gas and liquid fuel laboratory flames in order to investigate into dilution, hydrogen addition and fuel composition effects on soot volume fraction and hence the soot formation process. Section 6.2 details the gas and liquid fuel burners, along with the LII optical setup and temporal alignment. The gas chromatography equipment that was used to identify the main components of the fuels is described in Section 6.3. Section 6.4 introduces thermophoretic sampling, details the experiment and outlines post processing methods. The derivation of the key LII equations and how the soot volume fraction was determined from the raw data is outlined in Section 6.5, including a description of the calibration procedure.

6.2 Experimental setup

6.2.1 Gas fuel burner

An axisymmetric burner with 2 concentric ports was used for the gas fuel flame dilution and hydrogen addition experiments. The burner consisted of a network of pressurised gas bottles, regulators, controllable flow rotameters, single way valves and pipework. The inner port had an internal diameter of 6 mm and the outer port has an internal diameter of 10 mm and outer diameter of 100 mm. The setup produced laminar non-premixed, coflowing flames. The laminar coflowing air and the flame guard kept the flame from experiencing external perturbations. Controllable flowmeters allowed for precise control of the amounts of fuel and additives. The burner was properly mounted to produce stable laminar flames and the flame guard was designed with borosilicate windows for laser diagnostics. The transmission curves for the borosilicate glass windows were acquired from the manufacturer and are presented in Figure 6.2. The transmission wavelengths encompass all wavelengths used in the experiments and more.

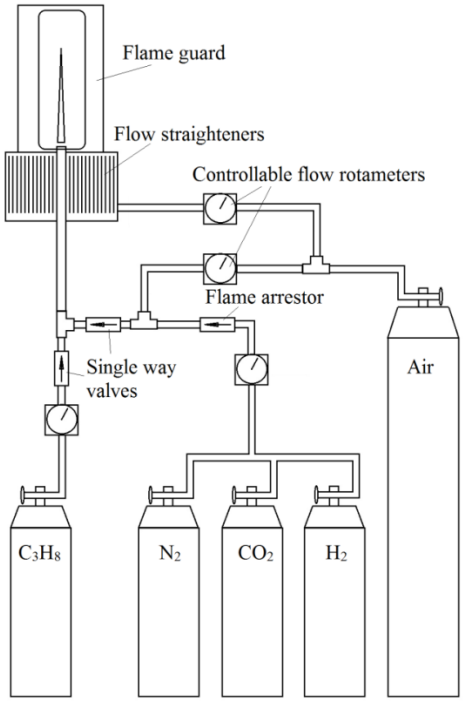

Figure 6.1. Gas fuel experimental setup.

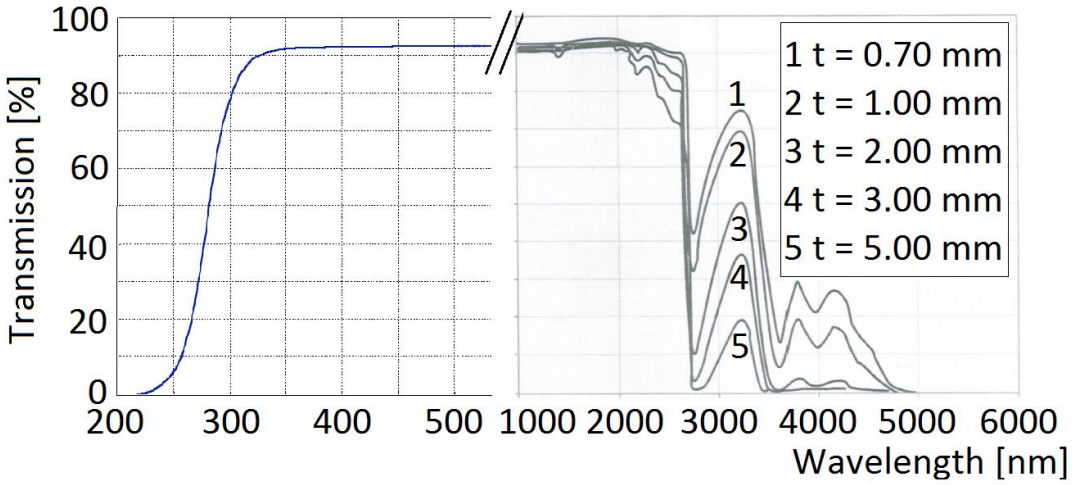

Figure 6.2. Borosilicate transmission curves, provided by Multilab.

6.2.2 Liquid fuel burner

A wick burner, shown in Figure 6.3, with a nozzle diameter of 3 mm was used to produce a laminar diffusion flame using CME, RME, SME, TME, FEE and diesel. The wick material was a short fibre ceramic wool (calcium magnesium silicate) which was not consumed within the flame and therefore did not take part in the combustion process. The supporting nozzle was drilled and placed within a bath of fuel which travelled up the wick due to capillary flow. The nozzle exit was made to stand 5 mm above the fuel surface in order to avoid pool burning which would occur if the fuel reached its vaporisation temperature. The UCOME and JME did not produce a flame in this burner due to their high viscosity. The viscosity of the fuel determined the speed in which it travelled up the wick. The same flame guard was placed over the flame during experiments which was used to prevent flame perturbations. The wick and fuel reservoir was placed over the gas fuel pipe in the same position as the gas fuel flame.

It was found that the flame height could be controlled by the height and shape of the wick and great care was taken to keep the wick constant for a particular set of measurements. Although the wick did not take part in the combustion process, carbon did gradually get deposited onto its surface when the flame was blown out after taking measurements, therefore the same wick could not be used throughout all of the measurements.

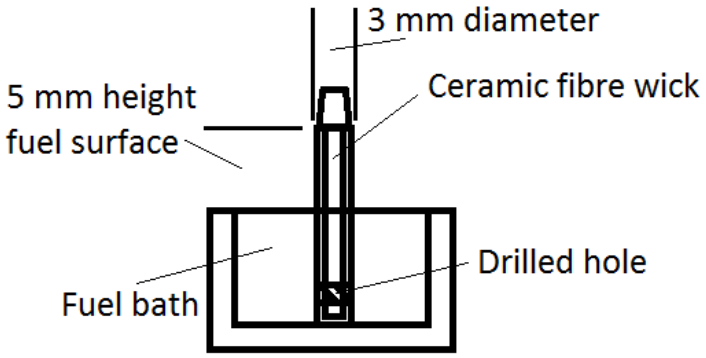

Figure 6.3. Wick burner diagram.

6.2.3 Optical setup

Figure 6.4 shows a diagram of the optical setup, with respect to the gas burner. The fundamental wavelength (1064 nm) of a Continuum Surelite solid state, neodymium doped Nd:YAG laser, operated at 10 Hz, using a pulse energy of 10 mJ, was used to heat the soot particles, in order to ensure that no interfering fluorescence signals from PAHs would be detected. The laser beam had a top hat profile and was guided using 1064 nm mirrors and was transformed into a laser sheet with a combination of spherical and cylindrical lenses. The size of the sheet was determined by placing a piece of burn paper at the burner exit and firing the laser. The burn mark left on the paper by the laser sheet was 12 mm high and 0.5 mm wide, producing a laser fluence of 0.25 J/cm^2, taking into account the optics used. The laser sheet was chopped at the extremities, leaving a laser sheet height of 10 mm. The LII signal was focused by a 50 mm Nikkor lens and collected by an Andor Instaspec V ICCD camera through an image doubler from LaVision. Great care was taken to ensure both parts of the image were the same, through alignment and flat fielding. Bandpass filters centred at 415 nm and 632 nm, with FWHM of 25 nm and 11 nm respectively were placed over the image doubler apertures, for specific wavelength detection. The camera and laser pulse were synchronised using a Stanford Research DG645 delay generator and were controlled by image acquisition software. Prompt LII signals were recorded with no delay and synchronisation is discussed in more detail later on.

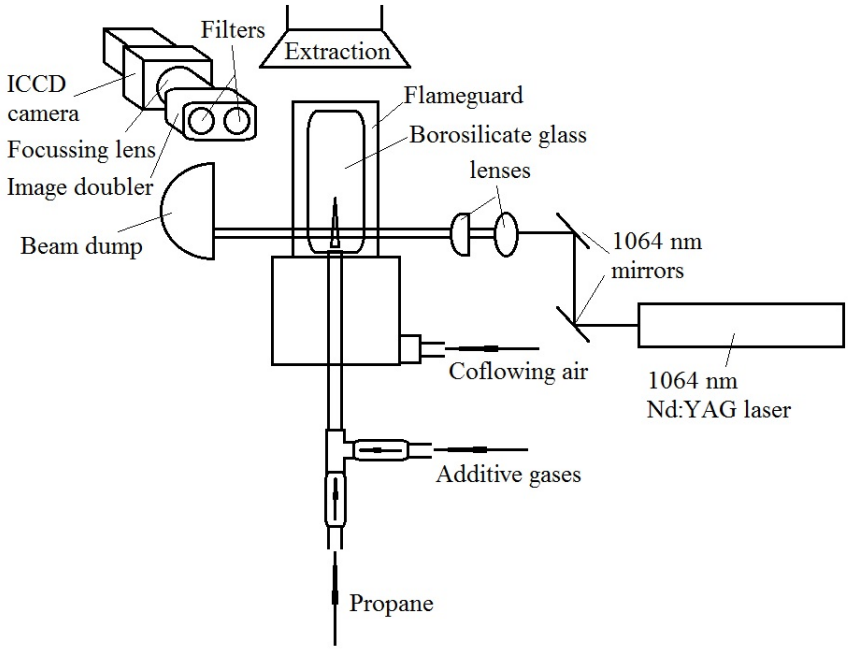

Figure 6.4. Optical setup.

It was necessary to correct the LII images for background interferences prior to processing. This was done by capturing a background image of the flame without the laser present, using the exact optical setup and camera settings as with the LII images. The background image was subsequently subtracted from the LII images on a pixel by pixel basis, reducing any excess noise signals, as well as eliminating the dark current produced by the ICCD camera itself. The background corrected images underwent flat fielding using MATLAB, ensuring that like-for-like pixel intensity values were used in the calculations. A white light combined with a light box was used to create a uniformly illuminated field for pixel correction. Spatial alignment of the images was achieved by capturing a reference image of a grid with symbols, which was positioned in place of the jet. This allowed for exact image mapping in both x and y directions.

6.2.4 Synchronisation

The experimental setup was optimised in the same way as was done for the LIP experiments, in terms of optical alignment and with the same temporal alignment setup. The LII signal does however, differ from phosphorescence and therefore a slightly different temporal arrangement was used. Other considerations also had to be included, such as identification of the plateau region in which the LII signal is independent of laser fluence.

Figure 6.5 shows a schematic of the triggering setup. A delay generator produced a 10 Hz signal that sent out signals to the laser and ICCD camera. The laser was set to external trigger mode and two triggers were used for minimal laser jitter (in the order of 1 ns). The Q-switch and flashlamp were triggered separately, where the Q-switch delay was initially set to 180 µs, with respect to the flashlamp trigger, as suggested in the laser manual. In order to trigger the laser, a 10 ms TTL pulse was sent by the delay generator to the flashlamp. The Q-switch trigger was also a 10 ms TTL pulse, delayed by 180 µs and the falling edge of the pulse caused the system to lase. The camera was triggered with the rising edge of another TTL pulse, where the pulsewidth and delay determined the camera gating time and delay with respect to the laser trigger, respectively. The minimum camera gatewidth that could be achieved by this setup was 200 ns because the camera trigger could not detect any shorter pulses.

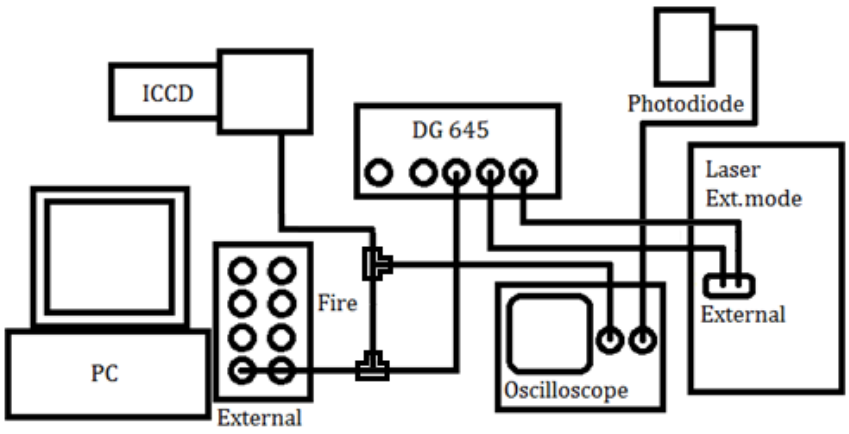

Figure 6.5. Camera and laser triggering setup.

Temporal alignment of the camera and laser was determined experimentally using a photodiode and an oscilloscope. The camera trigger signal was also sent to the oscilloscope and the photodiode was positioned facing a surface in which the laser was aimed at. The two signals were displayed on the oscilloscope with nanosecond precision. The camera delay was altered with respect to the laser pulse until the beginning of each signal matched. The camera delay was then further reduced by 100 ns for Prompt LII detection. A diagram of the experimental timings is included in Figure 3.8.

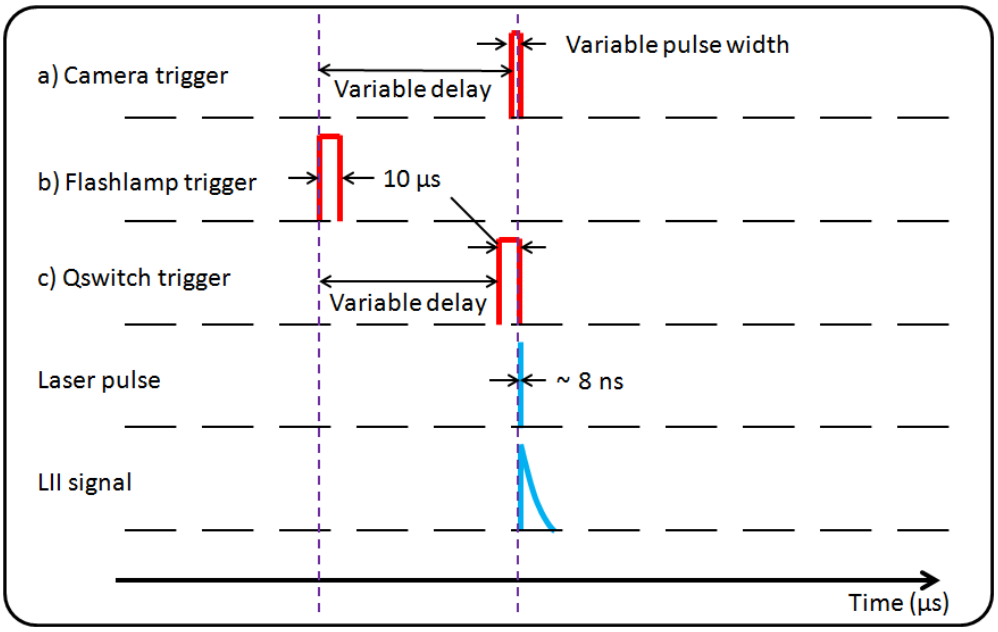

Figure 6.6. Laser induced incandescence timings diagram.

6.3 Fuel composition using gas chromatography

Fuel samples were analysed using an Agilent Technologies 6890N gas chromatograph in order to determine the individual biodiesel composition. 1.0 µL of fuel was injected into the inlet, which was operated in split mode at 300 ºC, with hydrogen as the carrier gas. The gas mixture was passed through a polyethylene glycol capillary column and retention times were measured using a flame ionisation detector. The oven was initially heated to 60 ºC, then set to 200 ºC for 10 mins, then 240 ºC for 5 mins and then 260 ºC for 20 mins. Retention times of up to almost 27 minutes were measured, relating to alkyl ester carbon chain lengths between 8 and

22. In order to relate the retention times and peak area with the composition of the individual biodiesel fuels, possible carbon chains were matched to the composition stated in the literature. This could be done with some fuels that matched well with the literature, within a few percent for each constituent. Other fuels varied slightly more, but could still be worked out, taking into account the scale of the retention times, with respect to the known peaks. Finally, the fuels that matched the least were determined in a similar way.

6.4 Thermophoretic sampling

6.4.1 Sampling setup

Thermophoretic sampling was carried out in diesel and biodiesel flames, where samples were subsequently analysed in a Jeol 2100F transmission electron microscope (TEM). A sampling probe was designed and constructed in order to minimise the amount in which the flame is perturbed during the sampling process. A 3.05 mm diameter copper TEM grid coated in a carbon film, provided by Agar Scientific was held at the tip of the probe, with the carbon film facing down into the flame. The probe was attached to a pneumatic cylinder that was controlled by a solenoid valve. The sampling equipment could be traversed up and down the flame with 0.5 mm precision and the experimental setup is shown in Figure 6.7. The probe residence time within the flame could be varied by changing the air pressure and it had to be aligned prior to the experiments such that its furthest reach coincided with the flame centreline. High speed camera footage at 1000 fps, of the probe in operation with a grid in the background was used to calculate the residence time, which was approximately 25 ms. The footage was also used to spatially align the probe. Soot aggregates were thermophoretically deposited onto the carbon film side of the TEM grids during probe insertion into the flame.

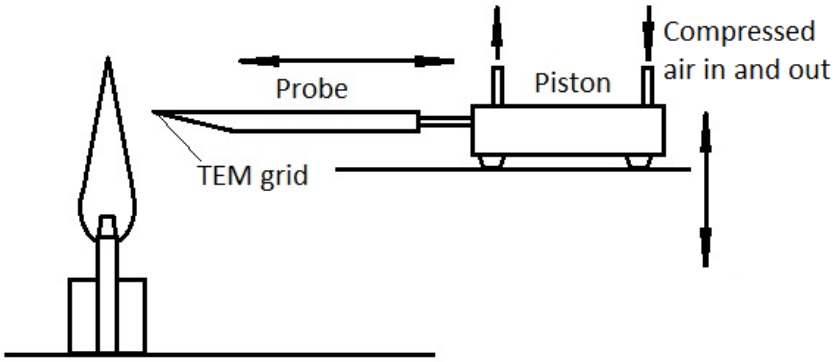

Figure 6.7. Thermophoretic sampling setup.

6.4.2 TEM Analysis

TEM images were acquired from the centre of the TEM grids, which avoided any errors that can occur from boundary effects (Pandey, et al., 2007). The TEM was capable of detecting down to a 0.5 nm probe volume, allowing for ultra-high resolution image quality. Images were acquired at three positions within each flame, at 5, 10 and 15 mm height above burner. Sampling measurements were carried out using TEM grids for diesel, FEE and TME. A number of different magnifications were used for each flame, where most were represented by 20,000 and 50,000 times, in order to convey an overall picture of how soot size and formation varies throughout the fuels. Some larger soot agglomerates were also presented at 10,000 times magnification and 1500 times magnification was used to convey the order of sampled soot concentration in the diesel flame, which was the sootiest.

6.5 LII Methodology

6.5.1 Two colour LII derivation

The two colour LII (2C-LII) method is used in this study, combined with prompt detection for investigating the SVF in diffusion flames and using a camera for planar measurements. The 2D-2C-LII technique used in this work produces images of the LII signal intensity through optical bandpass filters, centred at specified wavelengths (λ_c). It has been shown that it is beneficial to use detection wavelengths within the visible range. This is because the rate of change of spectral radiance with a change in

temperature is greater for two visible wavelengths and hence, there is a greater difference between the measurements at the two wavelengths (Ladommatos & Zhao, 1994; Ladommatos & Zhao, 1994; Zhao & Ladommatos, 1998).

In order to calculate the soot volume fraction (SVF), relations for both temperature and SVF were derived, as explained in this section. In order to relate the pixel intensity of the images to soot volume fraction, a calibration procedure must also be carried out using a light source of known intensity. This is usually done with a calibrated tungsten lamp. The spectral radiance of the calibration lamp can be expressed as Planck's law for black body radiation, as well as taking into account the emissivity of the lamp filament (Snelling, et al., 2005)

$$R_s\left(\lambda_c, T_{Fil}\right) = \frac{2c^2 h\varepsilon\left(\lambda_c, T_{Fil}\right)}{\lambda_c^5}\left[\exp\left(\frac{hc}{k\lambda_c T_{Fil}}\right) - 1\right]^{-1}, \tag{6.1}$$

where c is the speed of light, h is the Planck constant, λ_c is the centre wavelength of the bandpass filter, k is the Boltzmann constant, T_{Fil} is the filament temperature and $\varepsilon(\lambda_c,T_{Fil})$ is the emissivity of the lamp filament at a specific wavelength, which is a ratio of the spectral emissive power of a grey body (non-black body) to that of a black body, which has a value between 0 and 1

$$\varepsilon\left(\lambda, T\right) = \frac{I_g\left(\lambda, T\right)}{I_b\left(\lambda, T\right)}, \tag{6.2}$$

where the subscripts g and b are representative of a grey body and a black body respectively.

The measured total spectral radiance (over 4π steradians) emitted from the lamp at a specific wavelength and temperature, can be related to the LII signal, which can be expressed as the total radiated power per unit volume for a particulate of diameter d, where the volume of the particle is $v_p = \frac{\pi d_p^3}{6}$ (Snelling, et al., 2005)

$$\phi_p\left(\lambda_c, T_p\right) = \frac{48\pi^2 c^2 h}{\lambda_c^6}\left[\exp\left(\frac{hc}{k\lambda_c T_p}\right) - 1\right]^{-1} E\left(m_{\lambda c}\right), \tag{6.3}$$

where T_p is the temperature of the soot and $E(m_{\lambda c})$ is the soot absorption function at a specific wavelength and is related to the soot refractive index. The following relation can be used to calculate the soot absorption function (Snelling, 2000)

$$E\left(m_{\lambda c}\right) = 0.232 + 1.254 \times 10^{-4}\lambda, \tag{6.4}$$

where λ is in nm.

The calibration consists of two parts: firstly, recording a spectrum of absolute light intensity using the ICCD camera coupled with a spectrometer where the lamp is placed within an integrating sphere and secondly, recording the light emission from the lamp placed in the same position as the flame with the exact same optical setup as the LII measurements. The signal measured by the ICCD during calibration is (Snelling, et al., 2005; Crosland, et al., 2011)

$$I_{lamp} = G_{cal} M^2 A_p \left(\frac{A_L}{u^2}\right) 4\pi R_s\left(\lambda_c, T_{Fil}\right) \int_{\lambda} \tau(\lambda)\theta(\lambda)\, d\lambda + D_{lamp}, \tag{6.5}$$

where G_{cal} is the gain used when measuring the light emission from the lamp in the same position as the flame, M is the magnification, A_p is the area of the aperture, A_L/u^2 is the solid angle of collection, $\tau(\lambda)$ is the filter transmission, $\theta(\lambda)$ is the detector response and D_{lamp} is the dark current measured by the ICCD camera. The dark current that can be corrected during or after the image acquisition process, which gives the corrected lamp signal

$$I_{lamp} = G_{cal} M^2 A_p \left(\frac{A_L}{u^2}\right) 4\pi R_s\left(\lambda_c, T_{Fil}\right) \int_{\lambda} \tau(\lambda)\theta(\lambda)\, d\lambda, \tag{6.6}$$

The LII signal measured by the ICCD camera during the experiment is given by (Snelling, et al., 2005; Crosland, et al., 2011)

$$I_{exp} = f_v G_{exp} M^2 A_p \omega_b \left(\frac{A_L}{u^2}\right) \phi_p\left(\lambda_c, T_p\right) \int_{\lambda} \tau(\lambda)\theta(\lambda)\, d\lambda + D_{\exp}\,, \tag{6.7}$$

where f_v is the soot volume fraction, ω_b is the laser sheet thickness, G_{exp} is the gain used during the LII measurements and D_{exp} is the dark current measured by the ICCD camera. Where correcting for the dark current will result in the corrected LII signal

$$I_{exp} = f_v G_{exp} M^2 A_p \omega_b \left(\frac{A_L}{u^2}\right) \phi_p\left(\lambda_c, T_p\right) \int_{\lambda} \tau(\lambda)\theta(\lambda)\, d\lambda\,. \tag{6.8}$$

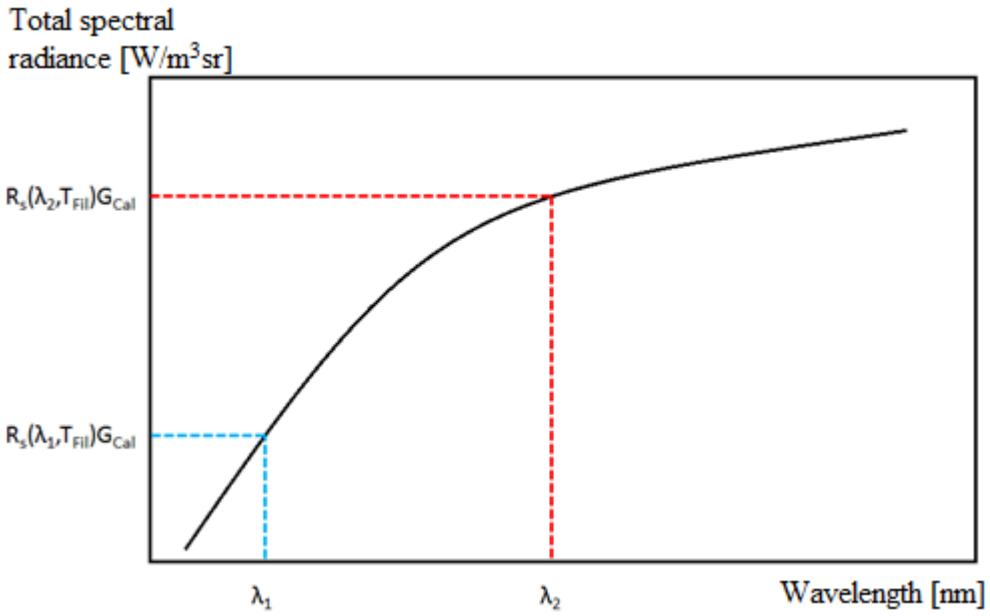

Figure 6.8. Sketch of the spectral radiance curve produced by the calibration lamp.

Figure 6.8 shows a sketch of a spectral radiance curve produced by a calibration lamp when used in conjunction with an integrating sphere. The curve shows the total spectral radiance of the lamp, multiplied by the gain for a selected range of wavelengths. The signal recorded by the camera from the lamp placed in the position of the flame is $I_{lamp,\lambda}$. The $I_{lamp,\lambda}$ signal can be related to the total measured output $R_s(\lambda_c, T_{Fil})$ by some calibration factor η

$$\frac{I_{lamp}}{\eta} = R_s\left(\lambda_c, T_{Fil}\right) G_{cal}\,, \tag{6.9}$$

where the calibration factor is

$$\eta = \frac{I_{lamp}}{R_s\left(\lambda_c, T_{Fil}\right) G_{cal}} = M^2 A_p \left(\frac{A_L}{u^2}\right) 4\pi \int_{\lambda} \tau(\lambda)\theta(\lambda)\, d\lambda\,. \tag{6.10}$$

The corrected LII signal can then be converted to soot spectral radiance similarly, by dividing equation (6.8) by the calibration factor, giving

$$\frac{I_{exp}}{\eta} = f_v G_{exp} \omega_b \frac{1}{4\pi} \phi_p\left(\lambda_c, T_p\right). \tag{6.11}$$

By rearranging equation (6.11) and replacing the term for total radiated power per unit volume for a particulate of soot with equation (6.3), the following expression for soot volume fraction (SVF) can be obtained

$$f_v = \frac{I_{exp}}{\eta G_{exp} \omega_b \dfrac{12\pi c^2 h}{\lambda_c^6} E\left(m_{\lambda c}\right)\left[\exp\left(\dfrac{hc}{k\lambda_c T_p}\right) - 1\right]^{-1}}. \tag{6.12}$$

The initial laser heated soot temperature (T_p) is the only unknown in equation (6.12).

In this work, it holds that $hc \gg k\lambda_c T$ and therefore the Wein approximation can be used, where

$$\left[\exp\left(\frac{hc}{k\lambda_c T}\right) - 1\right]^{-1} \approx \exp\left(-\frac{hc}{k\lambda_c T}\right). \tag{6.13}$$

Using this approximation and by taking a ratio of the LII intensities (I_{exp}) at two different wavelengths, the initial laser heated soot temperature can be obtained, which is given by

$$T_p = \frac{hc}{k}\left(\frac{1}{\lambda_2}-\frac{1}{\lambda_1}\right)\left\{\ln\left[\frac{I_{exp,\lambda_1}}{I_{exp,\lambda_2}}\frac{\eta_2}{\eta_1}\frac{\lambda_1^6}{\lambda_2^6}\frac{E\left(m_{\lambda_2}\right)}{E\left(m_{\lambda_1}\right)}\right]\right\}^{-1}, \tag{6.14}$$

where the subscripts *1* and *2* represent the different bandpass filter centre wavelengths (λ_c) used.

6.5.2 Calibration

The LII calibration measurements were carried out using an Ocean Optics Tungsten Light Source (HL-2000) of known spectral output, from 300 to 1050 nm. The corresponding Ocean Optics fibre optic cable was used to place the light emission in the correct position. The calibration was done in two parts, for the first part the light was directed into an integrating sphere in order to measure the total spectral power of the lamp. The spectrum is included in Figure 6.9. In order to calibrate the LII results, the spectral radiance of the lamp must be compared with that of the LII measurements, as mentioned previously in the two colour LII derivation.

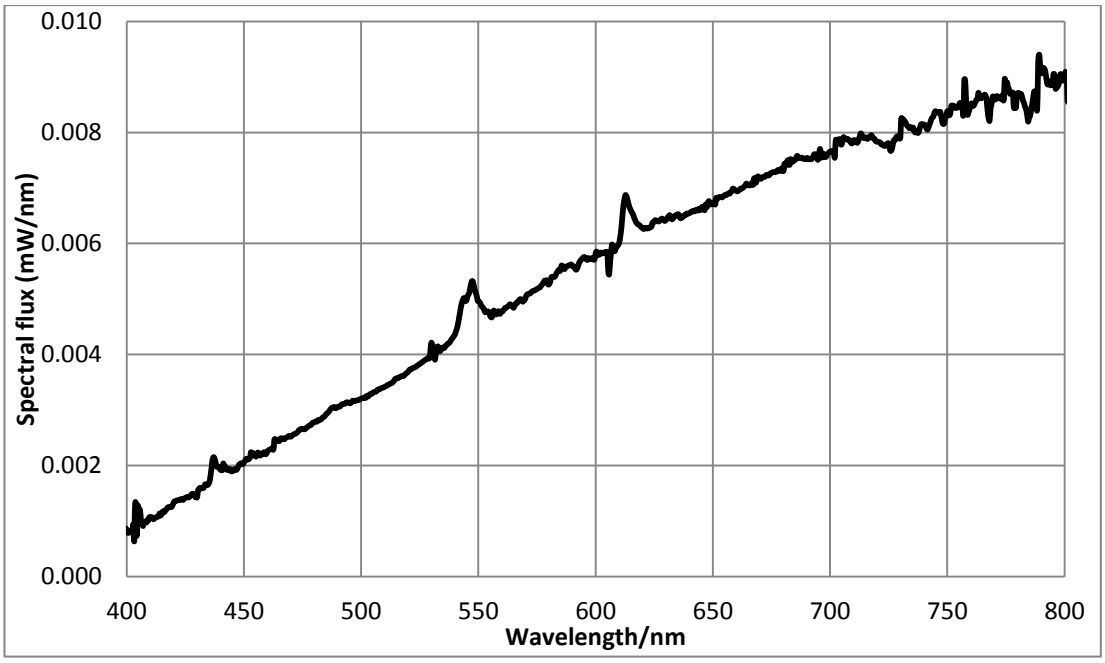

Figure 6.9. Spectrum showing total spectral power of the calibration lamp.

For the second part of the calibration, the fibre optic cable directed the lamp emission to the position where the flame would be. A diagram of the calibration setup has been included in Figure 6.10. The ICCD camera measures the spectral radiance R_S of the lamp at a solid angle Ω which depends on the distance from the camera to the source d and the detection area A according to

$$\Omega = \frac{A}{d^2}. \tag{6.15}$$

For a direct comparison, the measured spectral radiance of the lamp needs to be converted to spectral power P_S. These two parameters are related as follows

$$P_S = R_S A \Omega. \tag{6.16}$$

The distance between the camera and the fibre optic is known and the detection area is related to the image output, in terms of pixel size. For example, if the value of the lamp spectral radiance is calculated as an average over 5x5 pixels, then the detection area would be that of 5x5 pixels. The pixel size is known from the camera manual.

The spectral radiance measured at 415 nm and 632 nm, with the lamp in place of the flame, was converted to spectral power using equations (6.15) and (6.16). The values could then be directly compared with the total spectral power measured within the integrating sphere at the corresponding wavelengths (taken as an average across the bandwidth FWHM). Calibration constants were calculated for both wavelengths at various positions throughout the region where the flame would be and it was found that there was very little difference in the individual values of η_1 and η_2. The values of η_2/η_1 were also found to be quite consistent.

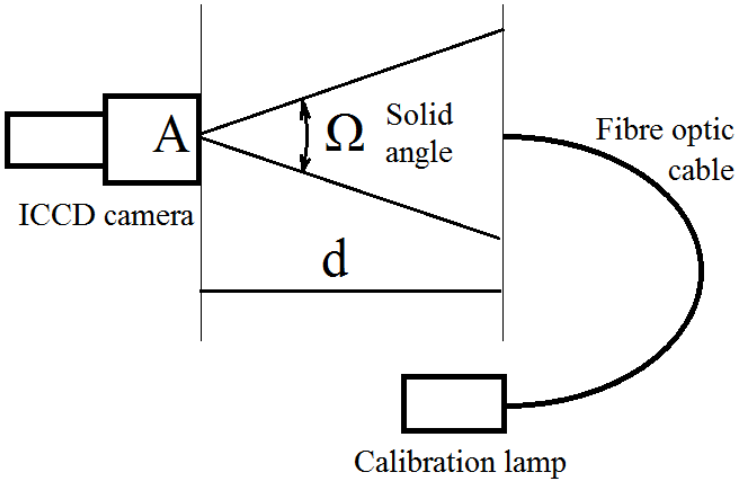

Figure 6.10. Diagram of the LII calibration setup.

6.5.3 Plateau region

Preliminary work was carried out on an undiluted diffusion flame using the gas fuel burner in order to optimise the optical setup. For the camera, a short pixel readout time of 2 μs had to be used in order to eliminate the vertical smear effect, which occurred due to the intense brightness of the flame. In order to ensure a high signal to noise ratio, the camera was set to maximum gain and each image is a single shot acquisition which was subsequently background corrected. LII signals were recorded at various Q-switch delays in order to determine the ideal laser power and hence fluence level. Above a laser fluence of around 0.2 J/cm^2 the LII signal is independent of the fluence level (Hofmann, et al., 2003; Wal, et al., 1998). This is known as the plateau region and the purpose of the preliminary experiments was to identify what range of laser power that the plateau region occurred. The Q-switch delay was

initially set to 70 µs, significantly reducing the laser power output, which was measured in the exact position of the flame with a laser power meter. The delay was increased, increasing the laser power until the LII signal had clearly levelled off. The results are presented in Figure 6.11 and show the plateau region beginning after about 0.15 J/cm^2.

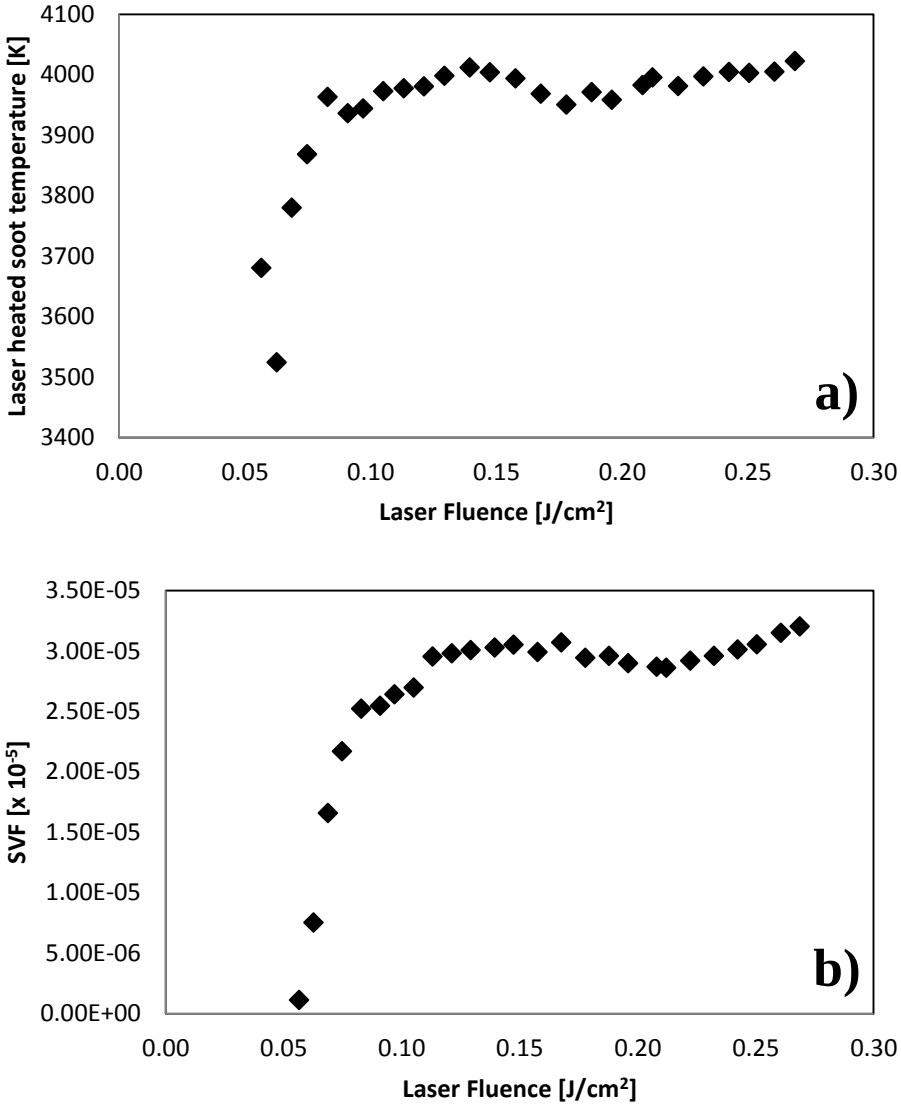

Figure 6.11. Plateau region for a) Laser heated soot temperature and b) soot volume fraction.

Measurements were taken at a laser fluence of around 0.25 J/cm^2 in order to ensure that the soot underwent complete sublimation. Using a laser fluence level that was too high would cause excessive soot sublimation, resulting in significant mass

reduction, which in turn would produce unreliable data. The fluence level used here should provide accurate and reliable soot volume fraction results.

6.5.4 Temperature and soot volume fraction

The laser heated soot temperature was calculated using equation (6.14), where the values for the constants *h*, *c* and *k* are listed in the nomenclature, λ_1 and λ_2 are 415 nm and 632 nm respectively, $E(m_{\lambda c})$ was calculated for each wavelength using equation (6.4) following the work of (Snelling, 2000; Snelling, et al., 2005), the η_2/η_1 ratio was determined from the calibration and the $I_{exp,\lambda 1}/ I_{exp,\lambda 2}$ ratio was found by dividing corrected LII intensities for the respective wavelengths on a pixel to pixel basis, after flat fielding. For soot volume fraction measurements, equation (6.12) was used, where the gain was known, the laser width (ω_b) was measured to be 0.5 mm and η_1 and η_2 were determined from the calibration.

CHAPTER 7
SOOT DISTRIBUTIONS IN GASEOUS AND BIODIESEL FLAMES

7.1 Introduction

Laser induced incandescence (LII), Gas chromatography (GC) and transmission electron microscopy (TEM) results are presented and discussed in this chapter. Dilution and hydrogen addition effects on soot, in terms of soot volume fraction are examined in Section 7.2, where nitrogen and carbon dioxide (CO_2) are used to dilute a propane diffusion flame, both with and without varying amounts of hydrogen being added to the flow. Section 7.3 compares emissions from various biodiesels and diesel-biodiesel blends in laboratory diffusion flames, in terms of fuel composition. Soot volume fraction results and TEM images are discussed for a range of biodiesels.

7.2 Dilution and hydrogen addition effects on soot emissions

The soot volume fraction (SVF) of propane diffusion flames individually diluted with varying amounts of nitrogen and carbon dioxide (CO_2) was investigated using laser induced incandescence (LII). The LII technique was also used to investigate the SVF in propane flames with varying amounts of hydrogen added, as well as those flames being diluted with nitrogen and CO_2. The purities of the gases used in the experiments were 99.95%, 99.9999%, 99.9995% and 99.999% for propane, nitrogen, CO_2 and hydrogen, respectively. Overall, 45 flames were tested, each with different amounts of the additive gases included within the flow. The gas flow rates in cm^3/min for the flames are listed in Table 7.1. Flame 1 is the base flame with just propane. Flames 2 to 15 are propane which has been mixed with only one other gas, where flames 2 to 6 have nitrogen added, CO_2 was added to flames 7 to 11 and hydrogen to flames 12 to 15. Flames 16 to 30 are propane mixed with hydrogen and nitrogen and flames 31 to 45 are propane, hydrogen and CO_2.

Table 7.1. Gas flow rates for flames in cm^3/min.

Flame	Propane	Nitrogen	CO_2	Hydrogen	Flame	Propane	Nitrogen	CO_2	Hydrogen
1	20	0	0	0	24	15	125	0	5
2	20	25	0	0	25	15	150	0	5
3	20	50	0	0	26	12.5	25	0	7.5
4	20	100	0	0	27	12.5	50	0	7.5
5	20	125	0	0	28	12.5	100	0	7.5
6	20	150	0	0	29	12.5	125	0	7.5
7	20	0	25	0	30	12.5	150	0	7.5
8	20	0	50	0	31	17.5	0	25	2.5
9	20	0	100	0	32	17.5	0	50	2.5
10	20	0	125	0	33	17.5	0	100	2.5
11	20	0	150	0	34	17.5	0	125	2.5
12	17.5	0	0	2.5	35	17.5	0	150	2.5
13	15	0	0	5	36	15	0	25	5
14	12.5	0	0	7.5	37	15	0	50	5
15	10	0	0	10	38	15	0	100	5
16	17.5	25	0	2.5	39	15	0	125	5
17	17.5	50	0	2.5	40	15	0	150	5
18	17.5	100	0	2.5	41	12.5	0	25	7.5
19	17.5	125	0	2.5	42	12.5	0	50	7.5
20	17.5	150	0	2.5	43	12.5	0	100	7.5
21	15	25	0	5	44	12.5	0	125	7.5
22	15	50	0	5	45	12.5	0	150	7.5
23	15	100	0	5					

Figure 7.1. Photographs of the propane diffusion flamed diluted with increasing amounts of nitrogen from left to right.

7.2.1 Nitrogen and CO_2 dilution

7.2.1.1 Nitrogen

Two dimensional laser heated soot temperature and SVF distributions were determined for all of the flames. Photographs of the propane diffusion flames with varying amounts of nitrogen dilution are shown in Figure 7.1. Two dimensional distributions for flames 1 to 6 are included in Figure 7.2, where the blue part of the flame is not visible due to the LII technique not being able to detect soot precursors, such as PAHs and NOC. The main SVF analysis is carried out using averages determined from the two dimensional distributions. Addition of nitrogen causes the luminous yellow envelope to progressively decrease in size and move upwards as more nitrogen is added, as shown in Figure 7.1 and Figure 7.2. As a result, the lower blue part of the flame becomes larger and the SVF decreases. Similar behaviour was observed with increasing amounts of other additives in the mixtures. The increase in height before the luminous zone begins is due to the reaction rates of soot formation reducing due to inert and dilution effects, which delays soot inception.

Figure 7.2 b) and c) show SVF distributions using η values calculated for both wavelengths (λ_1 = 415 nm and λ_2 = 632 nm) and it can be seen that the values are in good agreement with each other. The values matched, within the experimental error for all flames and therefore only SVFs calculated from η_2 are shown here in this chapter. The SVF images showed a small amount of laser attenuation due to soot particles within the flame for the relatively sootier flames, such as the non-diluted propane diffusion flame. However this effect was considered to be minimal in the gaseous fuel flames as it did not affect the results more than the experimental error.

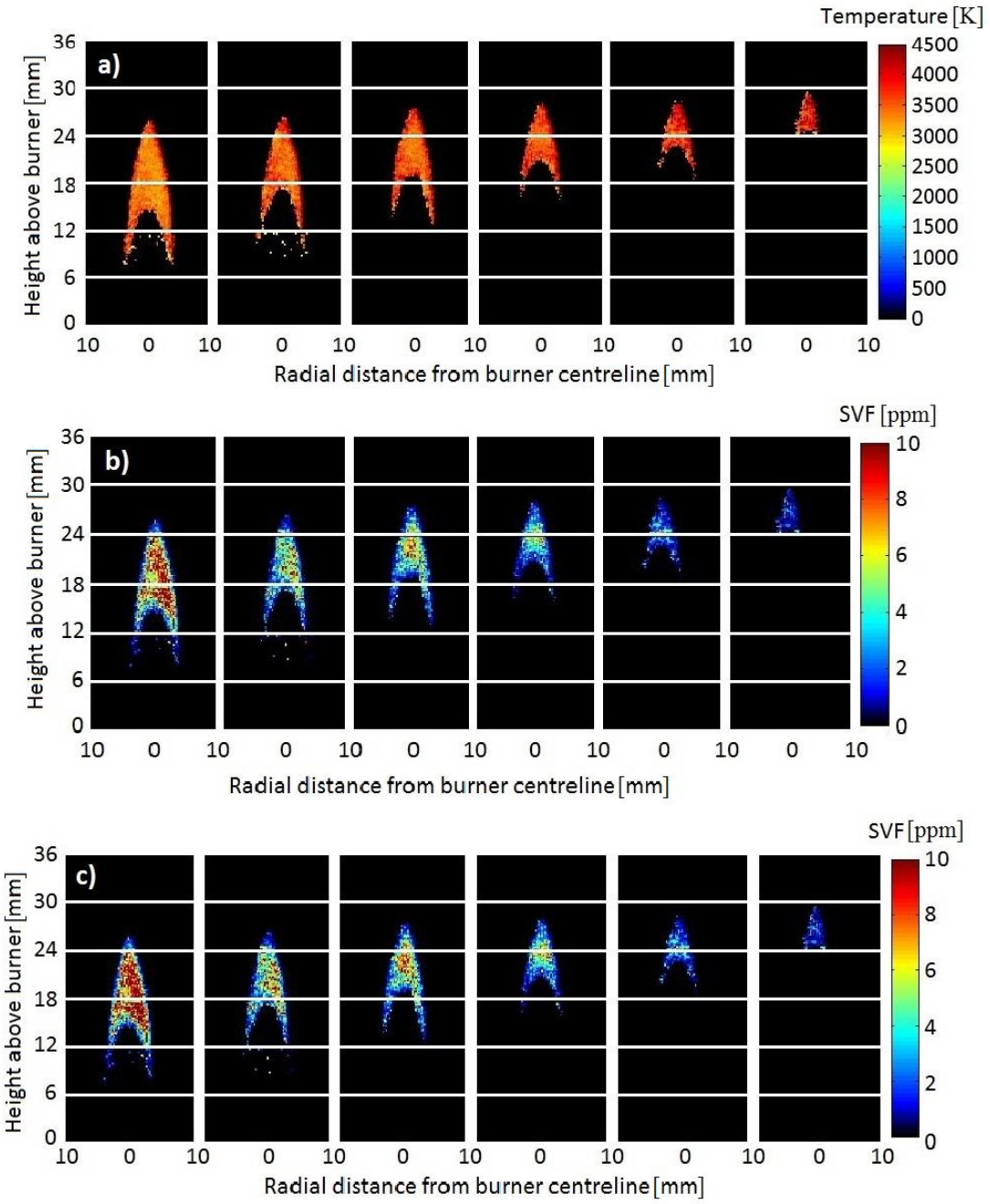

Figure 7.2. Flames 1 to 6 (left to right) a) Laser heated soot temperature distributions, b) SVF distributions calculated with η_1 (using λ_1) and c) SVF distributions calculated with η_2 (using λ_2).

Quantitative analysis could be carried out using averaged temperature and SVF data determined for each flame. Figure 7.3 shows average laser heated soot temperature (upper) and average SVF (lower) for flames 1 to 6. The average SVF was calculated over the whole laser heated soot area. The edge of the soot area was determined by only considering the LII intensity values above more than 1 % of the maximum LII

intensity, where values below this were of the same order of magnitude as the background noise.

As increasing amounts of nitrogen is added to the propane diffusion flame the SVF decreases significantly, from 5.0 ppm with zero nitrogen down to 1.4 ppm at a nitrogen flow rate of 150 cm^3/min. The decrease in SVF allows the soot within the flame to reach slightly higher temperatures; however all laser heated soot temperatures fall within the early sublimation range (3400 - 4000 K). Similar behaviour was shown for all of the flames. It is expected that the reasoning behind the reduction in SVF with addition of nitrogen is mainly due to inert dilution effects. The addition of the nitrogen reduces the soot formation rate of reaction by effectively decreasing the reactant concentration, thereby reducing successful radical collisions leading to soot precursor formation, hence lowering SVF. As combustion is an exothermic reaction, the reduced reaction rate results in a lower flame temperature and as a result of the lower temperature, the isotherm initiating soot formation is relatively closer to the maximum flame temperature isotherm. Soot therefore has less time to form and hence a lower SVF can be seen.

However, there are also chemical and thermal effects to consider. At high temperatures the nitrogen also partakes in the combustion reaction, forming NO_X species. These reactions will use up a percentage of the oxidising radicals, which could reduce the rate of reaction of soot oxidation, which could lead to a higher soot yield. The thermal diffusivity of nitrogen is less than that of propane, as shown in Table 5.1 and therefore the isotherms get closer together, producing less soot. The results show that there is a reduction in soot yield, which suggests that the effects of soot oxidation reduction due to the production of NO_X are less than the soot reduction effects due to inert and thermal effects. Moreover, the addition of nitrogen reduces the flame temperature, due to decreased reaction rates, which will reduce the amount of NO and NO_X that is formed, reducing their effects.

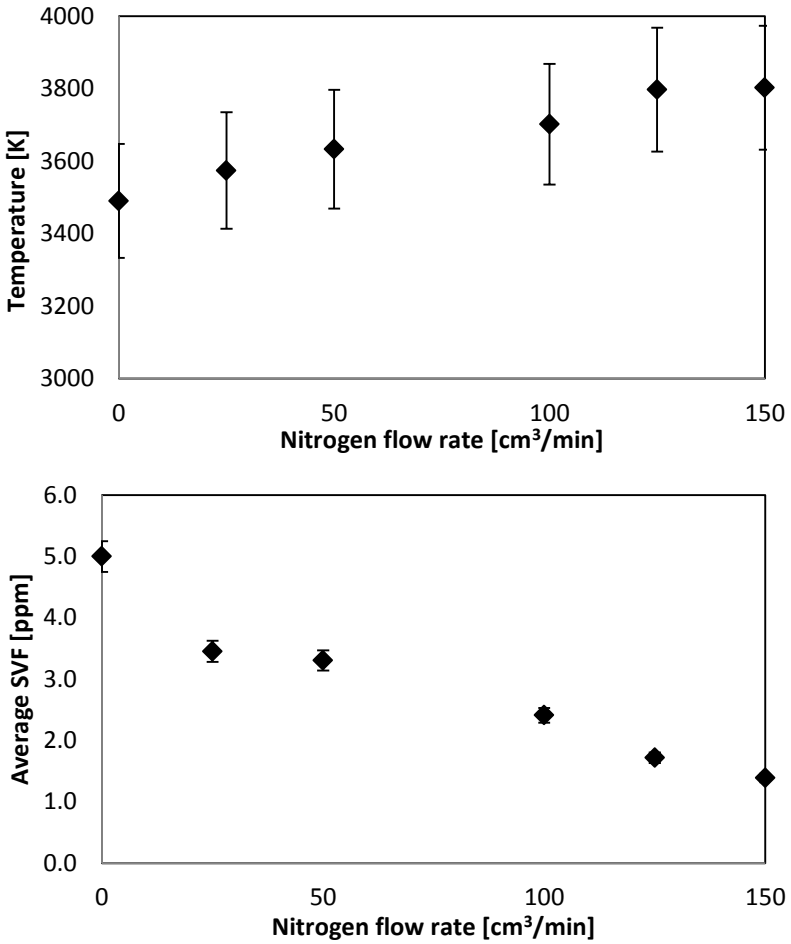

Figure 7.3. Graphs showing temperature (upper) and average SVF (lower) for flames 1 to 6, where propane is diluted with increasing amounts of nitrogen.

7.2.1.2 CO_2

Two dimensional SVF and average SVF for flames 7 to 11 are shown in Figure 7.4 upper and lower, respectively. Diluting the propane flame with CO_2 reduces the SVF markedly more than diluting the propane flame with nitrogen, when comparing the addition of an equal volume of each diluent, to the propane diffusion flame. For example, the addition of 50 cm^3/min of nitrogen to the propane flame produces a SVF of 3.3 ppm, whereas when 50 cm^3/min of carbon dioxide is added to the propane diffusion flame a SVF of only 0.7 ppm is formed. No soot at all was detected in flame 11, with 150 cm^3/min of carbon dioxide. These differences are due to the different dilution effects that dominate CO_2 dilution, compared with nitrogen addition. Introducing CO_2 into the propane flame affects the SVF in a number of ways. Similar to the addition of nitrogen, the CO_2 has inert effects on soot formation, where combustion reactant concentration is reduced, reducing the overall reaction

rate. The reduced exothermic reaction rate reduces flame temperature. The flame temperature is also decreased due to the thermal properties of CO_2. The thermal diffusivity of CO_2 is half that of nitrogen, increasing the impact of this particular thermal property on soot formation, where the lower the thermal diffusivity of the mixture, the less soot is produced. The chemical effects of CO_2 addition are also thought to be another main contributing factor towards soot reduction. Adding CO_2 provides more molecular oxygen and hence, the mixture has more oxidising potential. CO_2 dissociates at high temperatures that are encountered in flames, reacting with either molecular or atomic hydrogen, producing water and hydroxyl radicals which enhances oxidation of soot precursors and soot, reducing the amount of soot produced by eliminating carbon and preventing precursors from forming into soot.

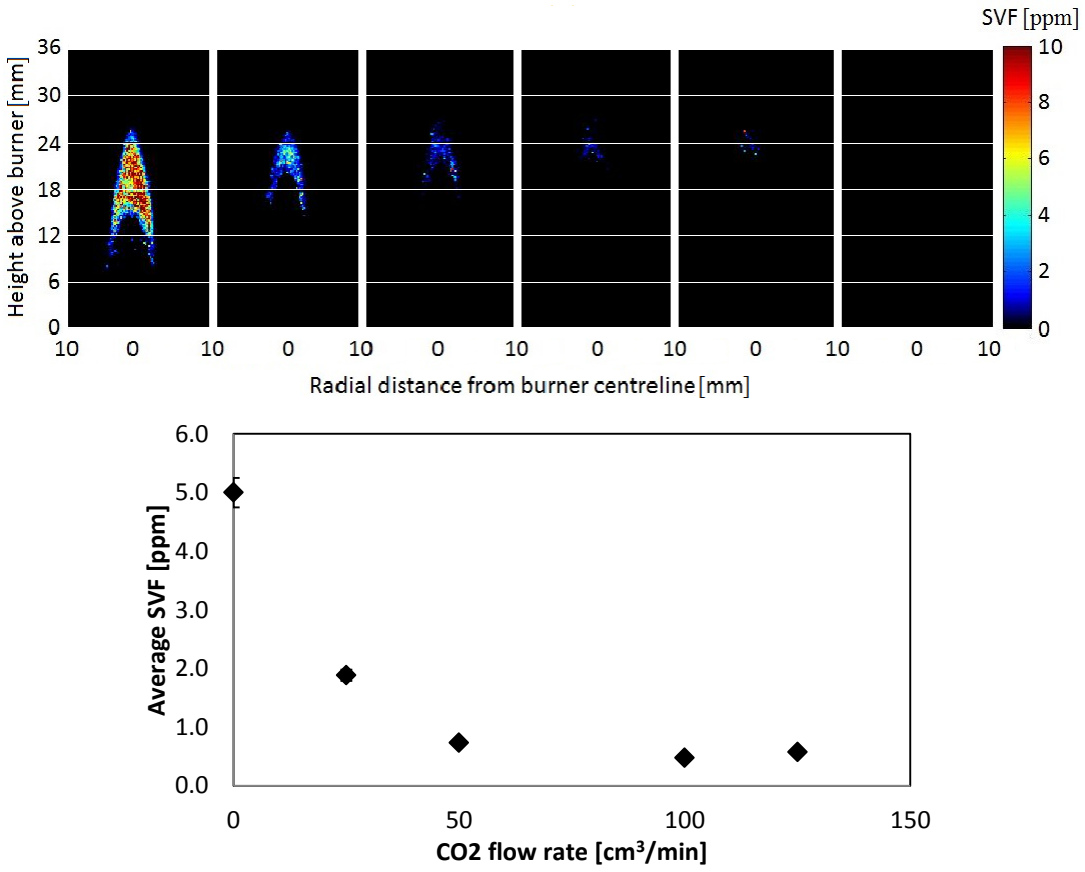

Figure 7.4. 2D SVF (upper) and average SVF taken over the whole LII luminous cross sectional area (lower) for flames 7 to 11, where propane is diluted with increasing amounts of CO_2 from left to right.

7.2.2 Hydrogen addition

7.2.2.1 Hydrogen

The addition of hydrogen to a gaseous fuel will also have similar effects to that of the diluents discussed above; the effects will be inert, chemical, and thermal. Adding hydrogen will have different effects for fuels with different characteristics. For example, an investigation on the effects of hydrogen addition to two alkanes, propane and butane and an alkene, ethylene was carried out (Gulder, et al., 1996). There was found to be a negligible change in flame temperature, however the soot production in the alkane and alkene flames differed. Both types of fuel were affected by inert dilution effects due to a lower concentration of reactants. The relatively high diffusivity of hydrogen is expected to cause a lesser reduction in soot, compared with a diluent with a low diffusivity. However, the chemical effects vary somewhat depending on fuel type. For ethylene, the soot reduction due to chemical effects as a result of the addition of hydrogen was attributed to an increase in the molecular hydrogen concentration, effecting the $H\bullet/H_2$ ratio, which is believed to be one of the main parameters governing PAH growth. However, for propane and butane, which are saturated, there is already a relatively large amount of hydrogen present and therefore the increase in hydrogen concentration has no marked effect on soot formation. For propane and butane, the reduction in soot formation is therefore only due to inert dilution and thermal effects.

Another study (Pandey, et al., 2007) involved the addition of hydrogen to acetylene. When hydrogen was added to the fuel flow the flame temperature increased, where the increase in temperature could be due to the higher diffusivity of hydrogen in the combustion zone. The addition of hydrogen substantially increases the number of •OH radicals, which are the main species that partake in soot oxidation reactions in fuel rich zones of the flame, inhibiting soot formation. The primary particle size was found to remain unaffected with the addition of hydrogen; however the agglomeration of soot particles is reduced with an increase in hydrogen. Hydrogen addition decreases the $H\bullet/H_2$ ratio by increasing H_2, which results in the hydrogen abstraction process becoming inhibited (Pandey, et al., 2007).

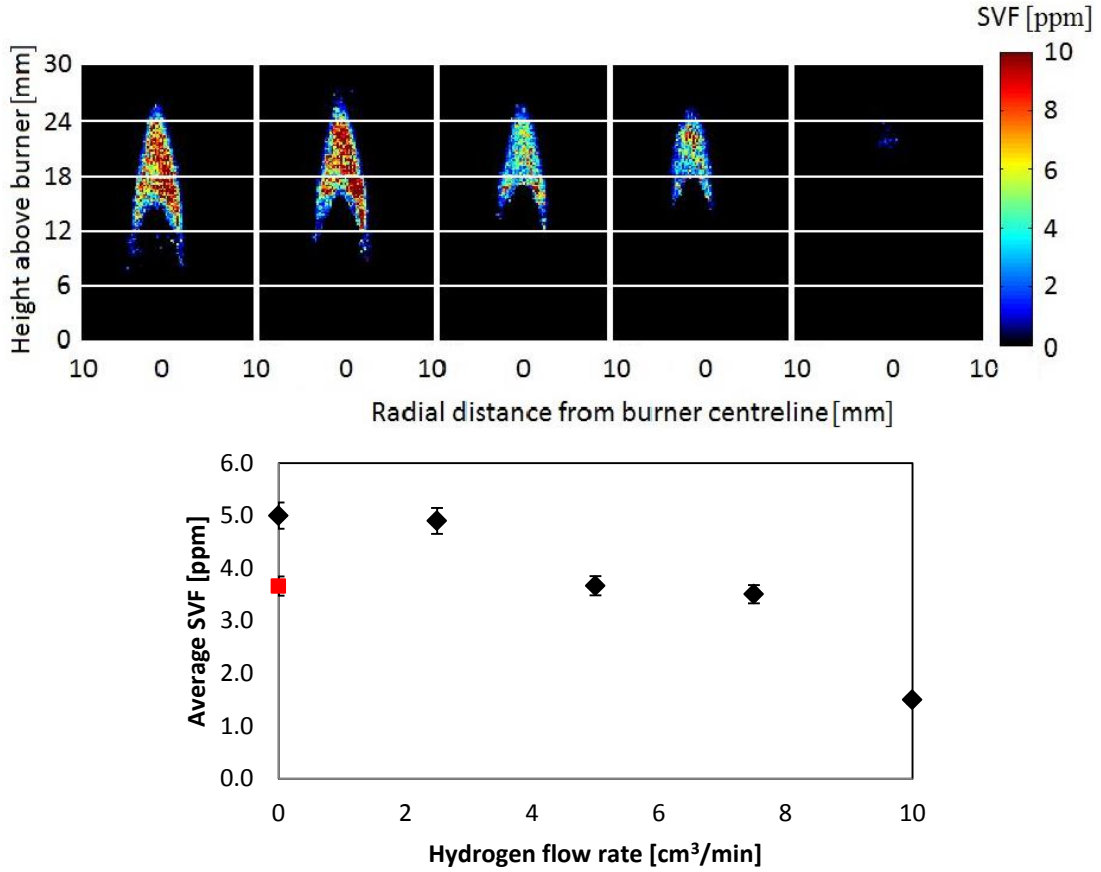

Figure 7.5. 2D SVF (upper) and average SVF taken over the whole LII luminous cross sectional area (lower) for flames 12 to 15 (black diamonds), consisting of propane diluted with varying amounts of hydrogen. The red square in the lower part of the figure represents a diffusion flame with 15 cm^3/min of propane with no hydrogen dilution.

The addition of hydrogen was accompanied by an equal decrease in propane, in terms of volumetric flow rate. The effects of hydrogen addition to the propane flame are depicted in Figure 7.5, where SVF images are presented for flames 1, 12 ,13, 14 and 15 (upper). The flames are presented as black diamonds in the lower part of the figure. The reduction in SVF could be due to hydrogen addition effects as well as the reduction in propane flow rate. In order to determine the effects of a reduction in propane flow rate alone, the SVF in a propane flame with a flow rate of 15 $cm^{3/}$min was also carried out and are presented in Figure 7.5 as a red square. The SVF of the 15 cm^3/min propane is in the same region as that of flame 13, with hydrogen added, within the experimental error. Flame 13 has a propane flow rate of 15 cm^3/min and a hydrogen flow rate of 5 cm^3/min. This shows that a small amount of hydrogen addition has little or no effect on the soot volume fraction. The results therefore

match that of the study carried out in (Gulder, et al., 1996), showing that hydrogen addition to propane has a negligible effect on soot formation due to the concentration of molecular hydrogen already being high before hydrogen addition in an alkane. Any inert or thermal effects on soot reduction are counteracted by the increase in soot formation reaction rate due to the increase in temperature that arises due to the addition of hydrogen. The flame temperature increases due to the addition of hydrogen because of the increase in pyrolysis reactions due to the relatively high diffusivity of hydrogen.

7.2.2.2 Hydrogen and nitrogen or carbon dioxide

The effects of the addition of nitrogen, carbon dioxide and hydrogen to propane have been discussed, individually. The combined effects of hydrogen and either nitrogen or CO_2 have also been analysed, with respect to the SVF and are discussed here. Figure 7.6 (upper) shows the SVF for flames 16 to 30, which were all diluted with varying amounts of hydrogen and nitrogen. Flame 1 is shown for comparison. The average SVF for the flames are shown in the lower part of the figure. Flames 16 to 20, which were diluted with 2.5 cm^3/min of hydrogen, are represented by red squares, flames 21 to 25 were diluted with 5.0 cm^3/min of hydrogen and are represented by green triangles and flames 26 to 30, which were diluted with 7.5 cm^3/min hydrogen, are represented by black diamonds. Figure 7.6 shows that as the flow rate of nitrogen increases, for all conditions, the SVF decreases. This is in line with the nitrogen dilution results earlier in this chapter. The results also show that as the amount of hydrogen is increased, the SVF decreases, which is also in line with the results in the previous section. The SVF results suggest that the hydrogen and nitrogen inert and dilution effects on soot occur separately despite them being in a mixture. The individual properties of the mixture of diluents have a cumulative effect on soot reduction.

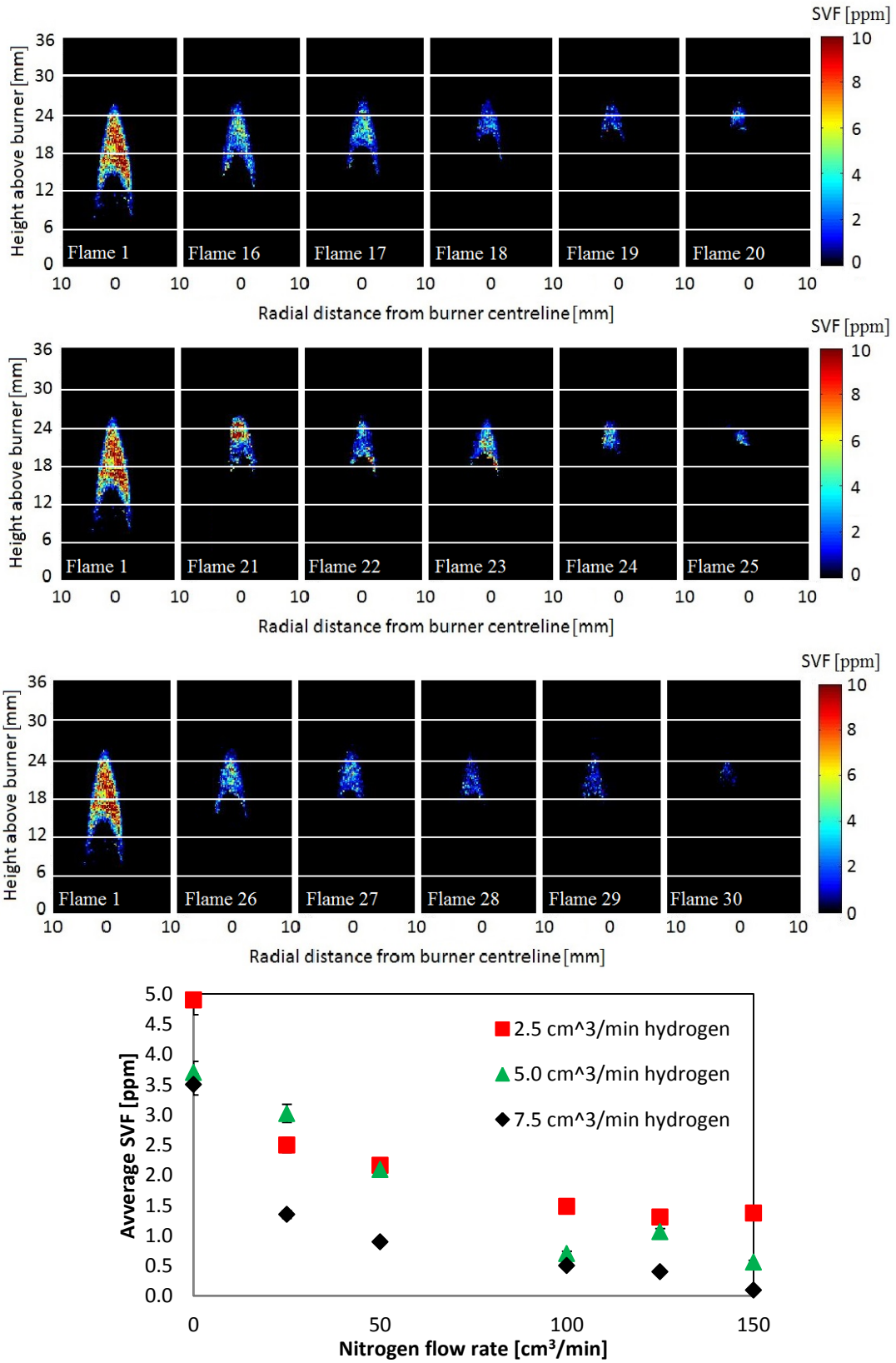

Figure 7.6. 2D SVF (upper) and average SVF taken over the whole LII luminous cross sectional area (lower) for flames 16 to 30, where propane was diluted with 2.5 (red square), 5 (green triangle) and 7.5 (black diamond) cm^3/min of hydrogen and varying amounts of nitrogen. Flame 1 is included in the SVF images for comparison.

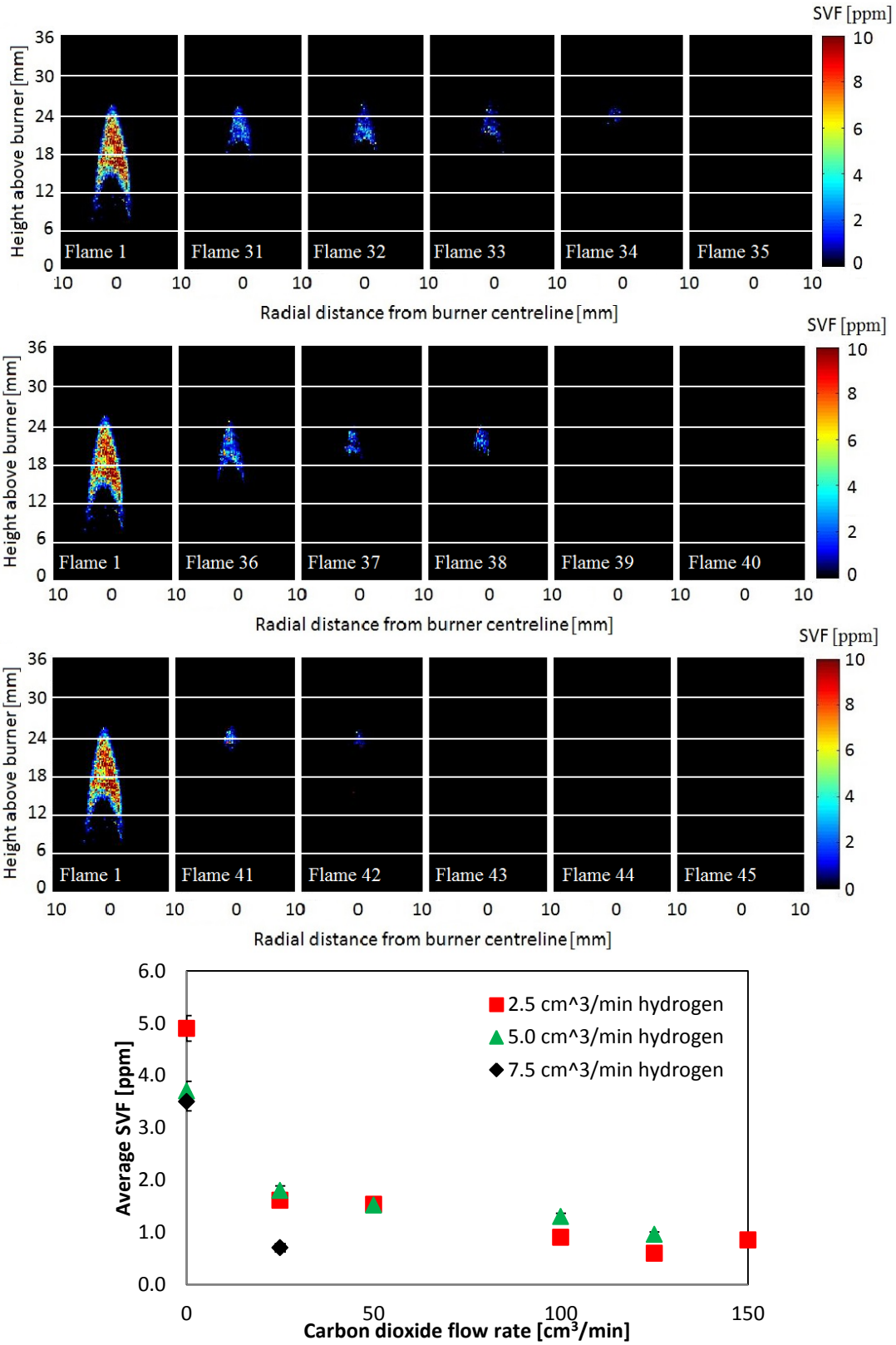

Figure 7.7. 2D SVF (upper) and average SVF taken over the whole LII luminous cross sectional area (lower) for flames 31 to 45, where propane was diluted with 2.5 (red square), 5 (green triangle) and 7.5 (black diamond) cm^3/min of hydrogen and varying amounts of nitrogen.

The addition of hydrogen, combined with the addition of carbon dioxide was also investigated in a similar way. Figure 7.7 shows the SVF for flame 1 and flames 31 to 45 (upper) and the average SVF for flames 31 to 45 (lower), where flames 31 to 35 were diluted with 2.5 cm^3/min of hydrogen (red squares), flames 36 to 40 were diluted with 5.0 cm^3/min of hydrogen (green triangles) and flames 41 to 45 were diluted with 7.5 cm^3/min of hydrogen (black diamonds). The average SVF results in Figure 7.7 reveal the same pattern as the addition of hydrogen and nitrogen. The reduction in SVF is more pronounced, due to the effects of CO_2. Flames 43 – 45 showed a negligible amount of soot due to the high soot reduction effects of the hydrogen and CO_2 mixture.

7.3 Biodiesel composition effects on emissions

Emissions measurements were carried out on diesel and biodiesel fuels using a wick burner. LII measurements were used to measure SVF and thermophoretic sampling, combined with transmission electron microscopy (TEM) was used to measure particle size. In order to relate the results to the individual fuel composition, gas chromatography was carried out on each of the fuels. SVF measurements were carried out on oxygenated diesel, as well as RME-diesel blends in order to compare effects of oxygenation, as well as other possible composition effects on soot. Individual biodiesels were also tested, in order to compare their compositional effects on SVF. The biodiesels tested were RME, CME, SME, TME and FEE.

7.3.1 Fuel composition using gas chromatography

Gas chromatography (GC) was carried out on the biodiesel fuels in order to ensure that the emissions measurements could be related to the fuel composition correctly. A chromatogram, such as those presented in Figures 7.8 to 7.13 was produced for each fuel and repeat tests were carried out in order to ensure that there were no erroneous results. The most significant peaks at various retention times were identified by comparing the composition to that of the literature. The fuels that matched the percentage composition for all of the peaks were identified first and then less well matched ones were identified subsequently, according to retention time.

The retention times for matching compounds in different biodiesels were very consistent throughout the analysis, apart from with FEE. This was attributed to the fact that this fuel contained ethyl esters and there was therefore some amount of shift in retention times for matching alkyl chain lengths, along with number and position of carbon=carbon double bonds. Peaks that showed less than approximately 1 % composition of the fuel were neglected from the analysis as the main constituents of the fuel will have a significantly more pronounced effect on the soot and emissions.

Figure 7.8 shows a chromatogram for RME, with the main peaks labelled with the most likely carbon chain length and number of carbon=carbon double bonds. Retention times of 17.634, 20.273, 20.648, 21.218, 22.097 and 23.332 mins were identified as the methyl ester chains of 16:0, 18:0, 18:1, 18:2, 18:3 and 20:1, respectively. The corresponding percentages of these molecules were consistent with that of the literature, listed in Table 5.3, which showed that the peaks were identified correctly. Percentages for 16:0, 18:0, 18:1, 18:2, 18:3 and 20:1 were shown in the GC analysis to be 4.3, 2.0, 64.4, 18.3, 9.8 and 1 %, respectively, compared with 4.2, 1.6, 59.5, 21.5, 8.4 and 2.1 %, respectively from the literature.

CME, shown in Figure 7.9, also matched with the literature quite well. Retention times of 7.341, 10.245, 12.961, 15.339, 17.654, 20.316, 20.502 and 21.137 mins were identified to be 8:0, 10:0, 12:0, 14:0, 16:0, 18:0, 18:1 and 18:2, respectively. Percentages for the components determined by the GC technique were 7.5, 6.0, 46.5, 18.2, 9.7, 1.8, 8.0 and 1.8 %, compared with 6.8, 5.4, 47.7, 18.5, 9.1, 2.7, 6.8 and 2.1 for 8:0, 10:0, 12:0, 14:0, 16:0, 18:0, 18:1 and 18:2, respectively. Comparative retention times for common compounds within the RME and CME fuels were 17.634 and 17.654 mins respectively for 16:0. 18:0 had times of 20.273 mins for RME and 20.316 mins for CME. For RME, retention times of 18:1 and 18:2 were 21.218 and 22.097 mins respectively and for CME, retention times were 20.502 and 21.317 mins respectively. These values showed good consistency, allowing for the identification of these compounds in the other fuels.

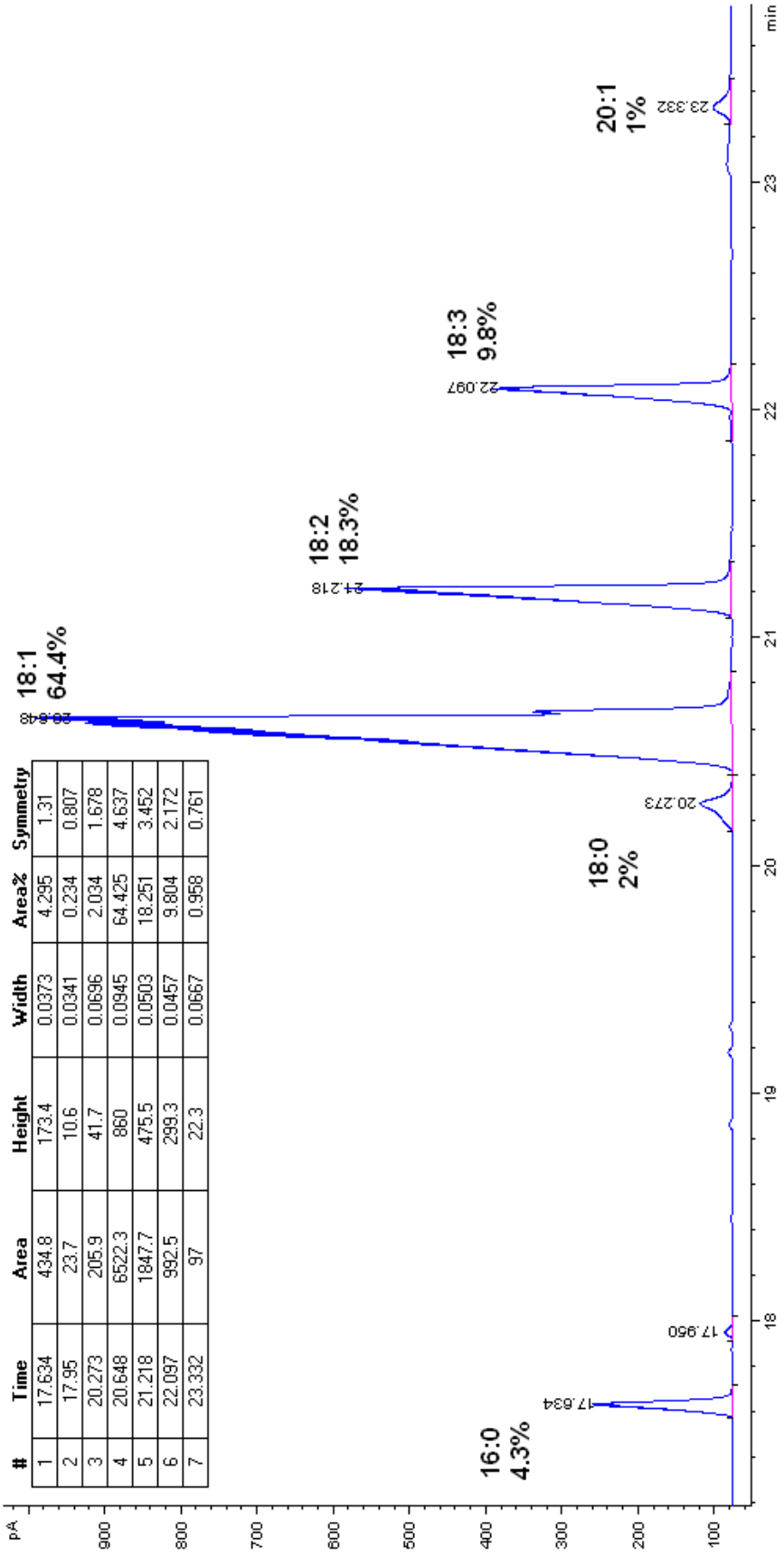

#	Time	Area	Height	Width	Area%	Symmetry
1	17.634	434.8	173.4	0.0373	4.295	1.31
2	17.95	23.7	10.6	0.0341	0.234	0.807
3	20.273	205.9	41.7	0.0696	2.034	1.678
4	20.648	6522.3	860	0.0945	64.425	4.637
5	21.218	1847.7	475.5	0.0503	18.251	3.452
6	22.097	992.5	299.3	0.0457	9.804	2.172
7	23.332	97	22.3	0.0667	0.958	0.761

Figure 7.8. Chromatogram for RME with main peaks labelled.

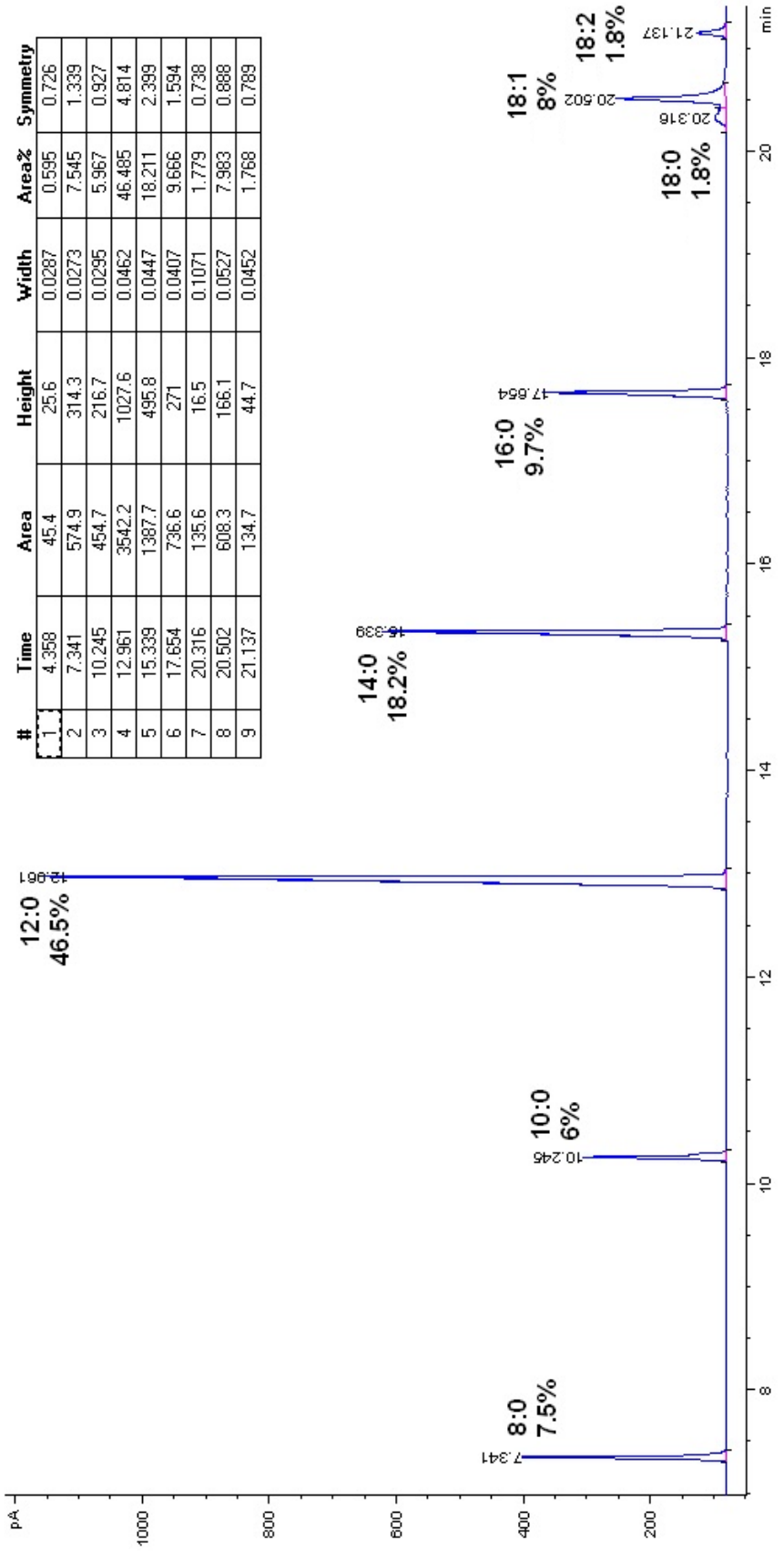

#	Time	Area	Height	Width	Area%	Symmetry
1	4.358	45.4	25.6	0.0287	0.595	0.726
2	7.341	574.9	314.3	0.0273	7.545	1.339
3	10.245	454.7	216.7	0.0295	5.967	0.927
4	12.961	3542.2	1027.6	0.0462	46.485	4.814
5	15.339	1387.7	495.8	0.0447	18.211	2.399
6	17.654	736.6	271	0.0407	9.666	1.594
7	20.316	135.6	16.5	0.1071	1.779	0.738
8	20.502	608.3	166.1	0.0527	7.983	0.888
9	21.137	134.7	44.7	0.0452	1.768	0.789

Figure 7.9. Chromatogram for CME with main peaks labelled.

#	Time	Area	Height	Width	Area%	Symmetry
1	17.634	434.4	170.6	0.0377	6.571	1.242
2	18.064	23.1	11.3	0.0317	0.349	0.865
3	20.209	239.7	47.2	0.0722	3.627	0.555
4	20.548	1764.4	442.6	0.0525	26.691	3.015
5	21.26	4107.7	711.2	0.0714	62.139	6.301
6	21.32	41.3	17	0.0353	0.624	0.443

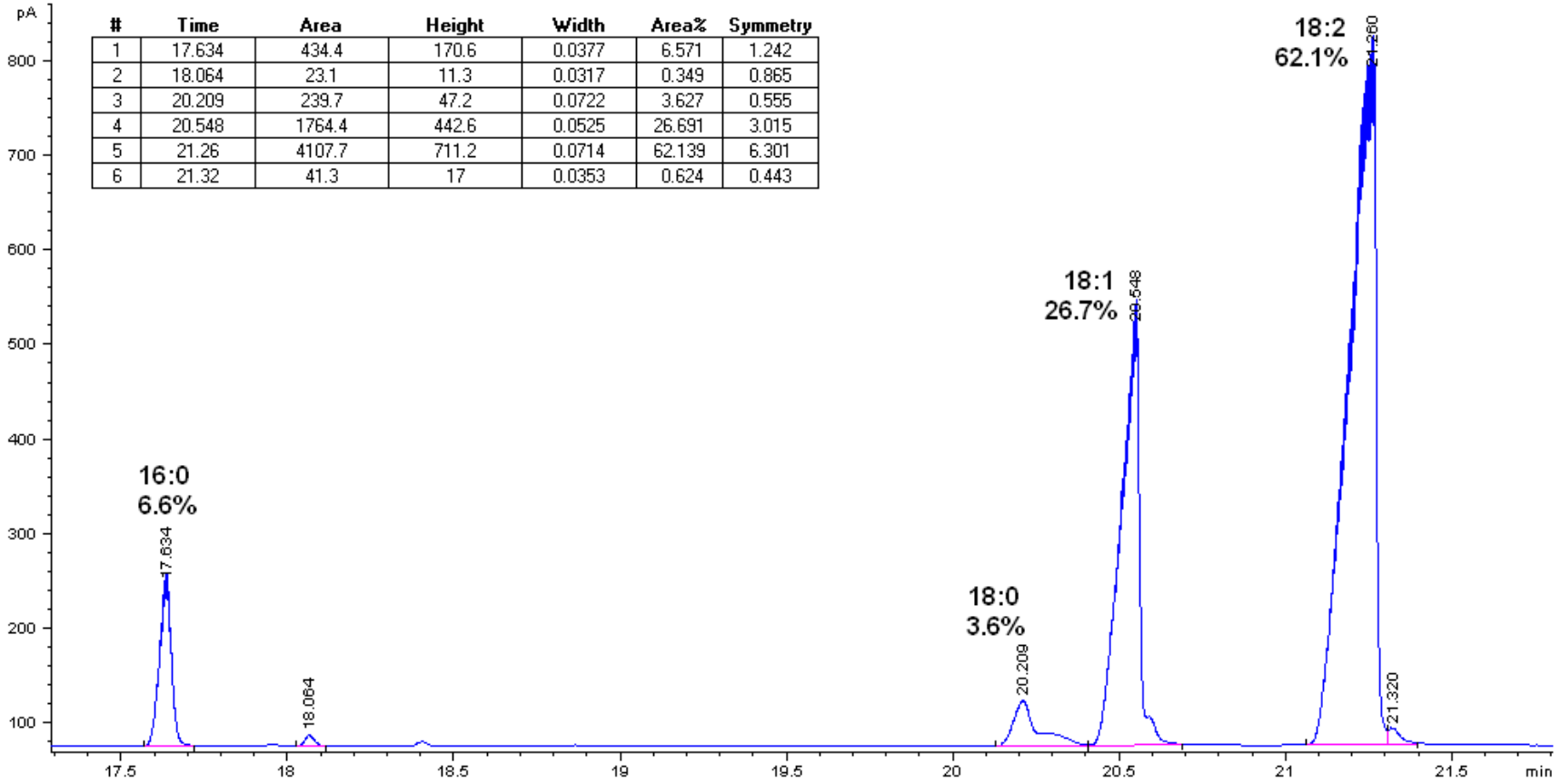

Figure 7.10. Chromatogram for SME with main peaks labelled.

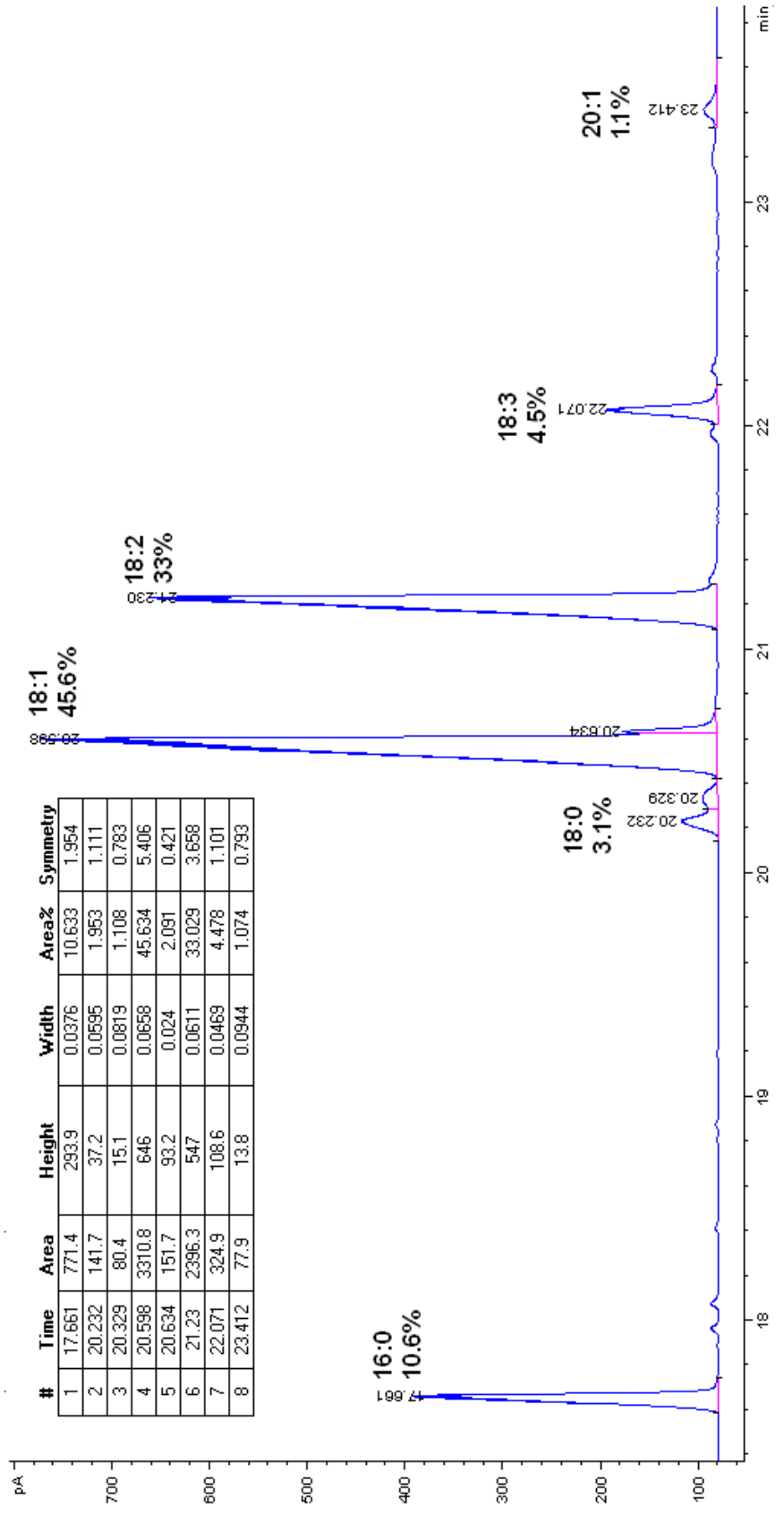

#	Time	Area	Height	Width	Area%	Symmetry
1	17.661	771.4	293.9	0.0376	10.633	1.954
2	20.232	141.7	37.2	0.0595	1.953	1.111
3	20.329	80.4	15.1	0.0819	1.108	0.783
4	20.598	3310.8	646	0.0658	45.634	5.406
5	20.634	151.7	93.2	0.024	2.091	0.421
6	21.23	2396.3	547	0.0611	33.029	3.658
7	22.071	324.9	108.6	0.0469	4.478	1.101
8	23.412	77.9	13.8	0.0944	1.074	0.793

Figure 7.11. Chromatogram for UCOME with main peaks labelled.

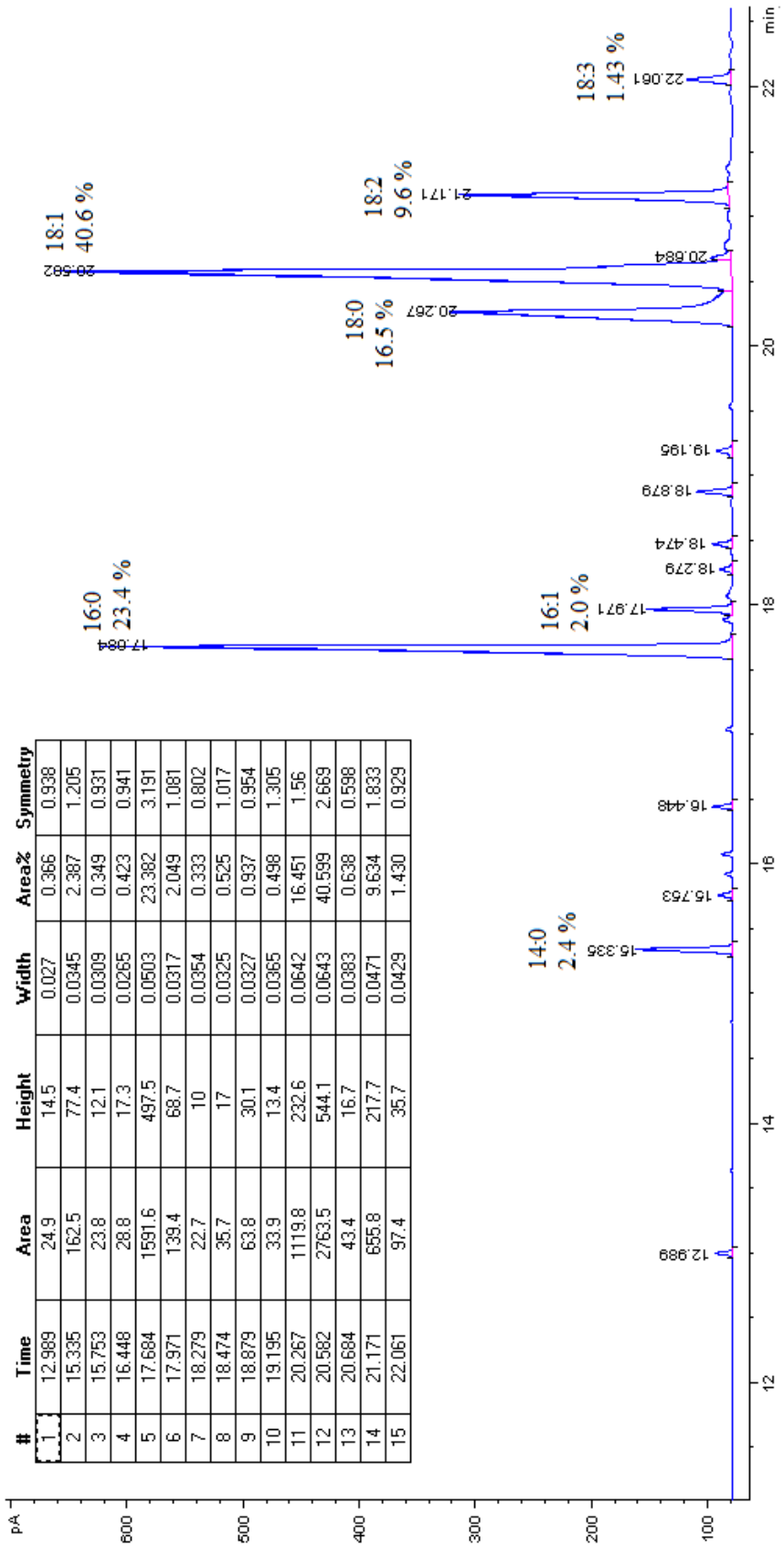

#	Time	Area	Height	Width	Area%	Symmetry
1	12.989	24.9	14.5	0.027	0.366	0.938
2	15.335	162.5	77.4	0.0345	2.387	1.205
3	15.753	23.8	12.1	0.0309	0.349	0.931
4	16.448	28.8	17.3	0.0265	0.423	0.941
5	17.684	1591.6	497.5	0.0503	23.382	3.191
6	17.971	139.4	68.7	0.0317	2.049	1.081
7	18.279	22.7	10	0.0354	0.333	0.802
8	18.474	35.7	17	0.0325	0.525	1.017
9	18.879	63.8	30.1	0.0327	0.937	0.954
10	19.195	33.9	13.4	0.0365	0.498	1.305
11	20.267	1119.8	232.6	0.0642	16.451	1.56
12	20.582	2763.5	544.1	0.0643	40.599	2.669
13	20.684	43.4	16.7	0.0383	0.638	0.598
14	21.171	655.8	217.7	0.0471	9.634	1.833
15	22.061	97.4	35.7	0.0429	1.430	0.929

Figure 7.12. Chromatogram for TME with main peaks labelled.

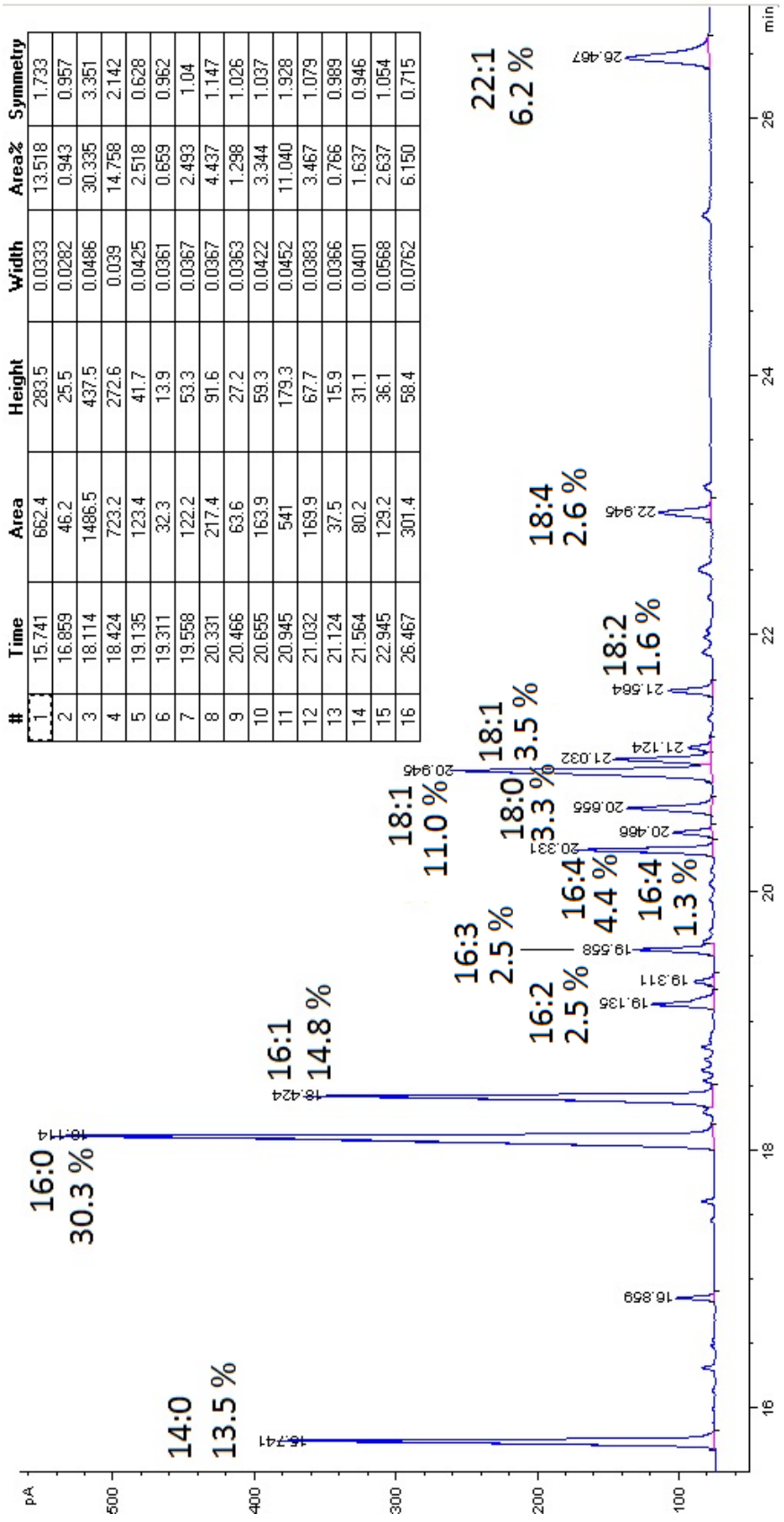

#	Time	Area	Height	Width	Area%	Symmetry
1	15.741	662.4	283.5	0.0333	13.518	1.733
2	16.859	46.2	25.5	0.0282	0.943	0.957
3	18.114	1486.5	437.5	0.0486	30.335	3.351
4	18.424	723.2	272.6	0.039	14.758	2.142
5	19.135	123.4	41.7	0.0425	2.518	0.628
6	19.311	32.3	13.9	0.0361	0.659	0.962
7	19.558	122.2	53.3	0.0367	2.493	1.04
8	20.331	217.4	91.6	0.0367	4.437	1.147
9	20.466	63.6	27.2	0.0363	1.298	1.026
10	20.655	163.9	59.3	0.0422	3.344	1.037
11	20.945	541	179.3	0.0452	11.040	1.928
12	21.032	169.9	67.7	0.0383	3.467	1.079
13	21.124	37.5	15.9	0.0366	0.766	0.989
14	21.564	80.2	31.1	0.0401	1.637	0.946
15	22.945	129.2	36.1	0.0568	2.637	1.054
16	26.467	301.4	58.4	0.0762	6.150	0.715

Figure 7.13. Chromatogram for FEE with main peaks labelled.

The chromatogram for SME is shown in Figure 7.10. SME had the least amount of peaks, with retention times of 17.634, 20.209, 20.548 and 21.26 mins, which correspond to 16:0, 18:0, 18:1 and 18:2, where the 16:0 peak constitutes 6.6 %, compared with 6.4 % in the literature. The results show that the 18:0 peak matches exactly with that in the literature, the 18:1 peak makes up 26.7 %, compared with 21.7 % in the literature and the 18:2 peak showed 62.1 %, with 66.3 % composition in the literature.

Figure 7.11 shows the results for UCOME which shared retention times with the previous fuels at 17.661 mins, corresponding to 16:0, 20.232 and 20.329 mins, consistent with 18:0, 20.598 and 20.634 mins, relating to 18:1, 21.23 mins pointing to 18:2, 22.071 mins matching 18:3 and 23.412 mins in line with 20:1. Percentage composition for each peak was determined to be 10.6, 2.0, 1.1, 45.6, 2.1, 33.0, 4.5 and 1.1 % respectively. The proportions of the compounds in the UCOME were similar to that of the literature, however as expected, the UCOME did not match as well as the previous fuels, which is thought to be due to the fact that it could be a mixture of various other oils prior to esterification. In Table 5.2 the composition of UCOME is 16.5 % 16:0, 7.1 % 18:0, 44.6 % 18:1, 25.1 % 18:2 and 1.1 % 18:3.

TME results are shown in Figure 7.12, where retention times of 15.335, 17.684, 17.971, 20.267, 20.582, 21.171 and 22.061 mins, correspond to 14:0, 16:0, 16:1, 18:0, 18:1, 18:2 and 18:3, respectively. The percentage composition of each compound respectively, was determined as 2.4, 23.4, 2.0, 16.5, 40.6, 9.6 and 1.43 %, compared with that of the literature, 2.6, 24.3, 2.6, 18.2, 42.2, 4.4 and 0.9 %.

FEE was the most difficult to determine due to it containing ethyl esters instead of methyl esters, which is thought to have caused the main peaks to shift to have a longer retention time of approximately 24 seconds. The FEE chromatogram is shown in Figure 7.13. The main peaks matching the compounds found within the other fuels were 14:0, 16:0, 16:1, 18:0, 18:1, 18:2, 22:1, with retention times of 15.741, 18.114, 18.424, 20.655, 20.945 and 26.467 mins, where 21.032 is thought to be an isomer of 18:1. There were a large number of additional, relatively smaller peaks among the

known peaks. These peaks were identified to be polyunsaturated chains of 16:2, 16:3, 16:4, an isomer of 16:4 and 18:4 for retention times of 19.135, 19.558, 20.331, 20.466 and 22.945 mins, respectively by comparing the results to that of the literature for anchovy oil, as well as taking into account the removal of omega 3 chains. The most significant peaks showed that FEE contained 13.5 % 14:0, 30.3 % 16:0 and 14.8 % 16:1, making up about 58.6 % of the fuel, with the remainder consisting of a large amount of smaller peaks, with 2.5 % 16:2, 2.5 % 16:3, 5.7 % 16:4, 3.3 % 18:0, 14.5 % 18:1, 1.6 % 18:2, 2.6 % 18:4 and 6.2 % 22:1.

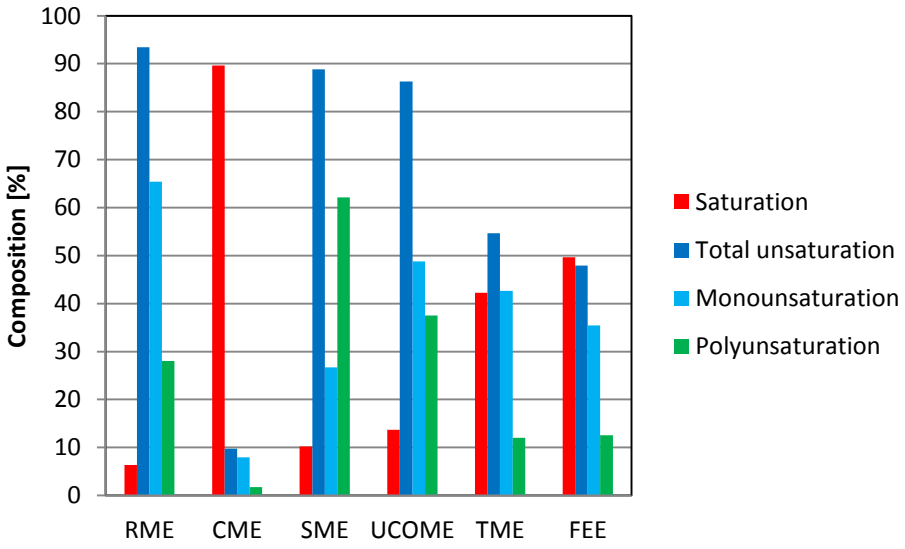

Figure 7.14. Fuel composition in terms of saturation.

Figure 7.14 shows the percentage saturation determined by comparing the saturated C:0 chains with the unsaturated C:>0 chains within each fuel. Red bars represent the percentage saturation in each fuel, dark blue bars show percentage of total unsaturation, encompassing both mono and polyunsaturated molecules. The percentage of monounsaturated and polyunsaturated molecules are then distinguished with light blue and green bars respectively. Figure 7.15 shows the average carbon chain length calculated from the GC analysis, by taking into account the percentage of each ester molecule within the fuel. It can be seen from the figures that CME was almost completely saturated, with approximately 10 % unsaturation, of which the molecules were mainly monounsaturated. CME also had the shortest average chain length of about 13, due to being composed of a large amount of shorter chains. This

is in line with the literature and should produce the least soot out of all of the fuels in this study, when considering fuel composition effects alone.

FEE had almost a 1:1 ratio of saturated and unsaturated molecules, where about 75 % of the unsaturated molecules were monounsaturated, however some of the polyunsaturated chains had relatively higher numbers of carbon=carbon double bonds, up to C:4, which was not seen in the other fuels. FEE had the second lowest percentage unsaturation, after CME, with just less than 50 %. The average chain length of FEE was about 16.5, which was also the second shortest chain length out of all of the fuels considered in this investigation. The composition and percentage saturation suggested that FEE would be one of the lesser sooting fuels, when considering fuel composition alone, however as its components were ethyl esters, this should cause an overall increase in sooting tendency, as discussed in Chapter 5.

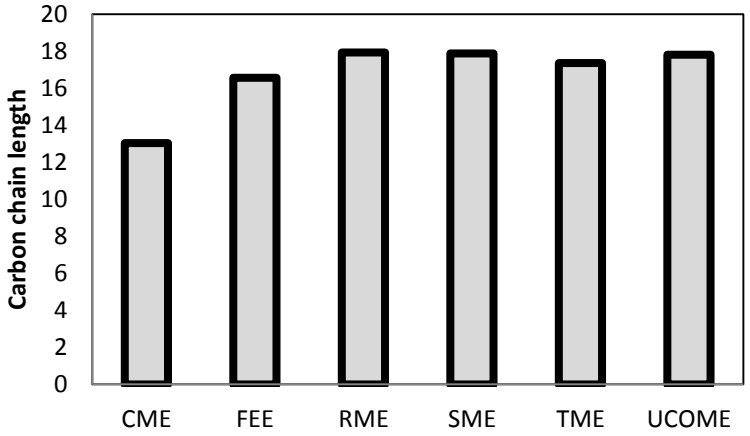

Figure 7.15. Average carbon chain length for fuels.

TME had a slightly lower percentage saturation than FEE. The remaining 58 % were saturated, of which about 70 % are monounsaturated. TME also had the next lowest average carbon chain length, of 17.4. RME and UCOME showed similar composition characteristics, with just over 90 % unsaturation and almost 90 % unsaturation for RME and UCOME, respectively. However, RME had just less than half of its unsaturated molecules consisting of polyunsaturates and UCOME had about 75 % polyunsaturates. SME showed about 10 % saturation, where about 65 % of the unsaturated molecules were polyunsaturated. Average chain lengths of RME,

UCOME and SME were very similar and were in the region of 17.9 %. The composition results determined here for RME, SME and UCOME should place them as the sootier of the biodiesels.

7.3.2 Soot volume fraction

LII was used to measure the SVF in biodiesel and diesel flames in conjunction with the wick burner, described in the previous chapter. The burner produced flames such as those presented in Figure 7.16, where both non-sooting (left) and sooting (right) flames are shown. The distinct luminous envelope can be seen to be closed in the non-sooting flame and is clearly open in the sooting flame, where the intensity of the soot luminosity diminishes as the sooting particles get further from the combustion zone and hence, decrease in temperature. A plume of visible black soot can be seen to be released from the sooting flame (out of shot in Figure 7.16). The definition of how the flame height was determined for the two types of flames is also shown in the figure, as where the brightest part of the luminous zone ends.

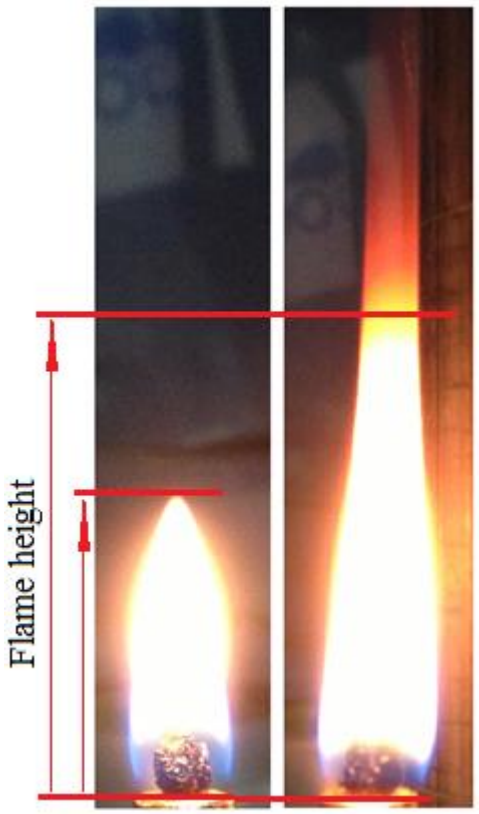

Figure 7.16. Examples of flames produced by the wick burner.

The wick caused a considerable amount of laser attenuation in the lower parts of the flame. The flame shape, shown in the gaseous fuel LII results, in Figure 7.2, shows the “wings” which are produced at the base of the flame, when the blue part of the flame merges into the luminous zone. The wing effect is created due to the external regions of the laminar flow being lower in velocity than the central regions. An example of some raw images conveying LII intensity through 415 and 632 nm optical filters are shown in Figure 7.17 a), along with the laser heated soot temperature distribution in b) and SVF distribution in c), which were calculated from the 415 nm filter wavelength for an RME flame at a height of 13 mm. The liquid fuel flame was a similar same shape as the gas fuel flame due to the wick protruding out of the nozzle, as shown in Figure 7.17. At flame heights matching up to the height of the wick, the LII results conveyed a SVF that was erroneous due to the laser being highly attenuated by the wick. There were also added flame perturbations due to the laser coming into contact with the wick at this height, which can be seen in the figure. The wings of the flame were therefore excluded from the analysis for the liquid fuel results. There was also found to be a slight difference in the SVF from one side of the flame to the other, which caused a noticeable amount of error to be produced in the SVF results. In order to reduce the error caused by the laser attenuation, the average soot volume fraction was calculated from the side of the flame in which the laser entered for the liquid fuel results, which has been highlighted in Figure 7.17 a) by red boxes.

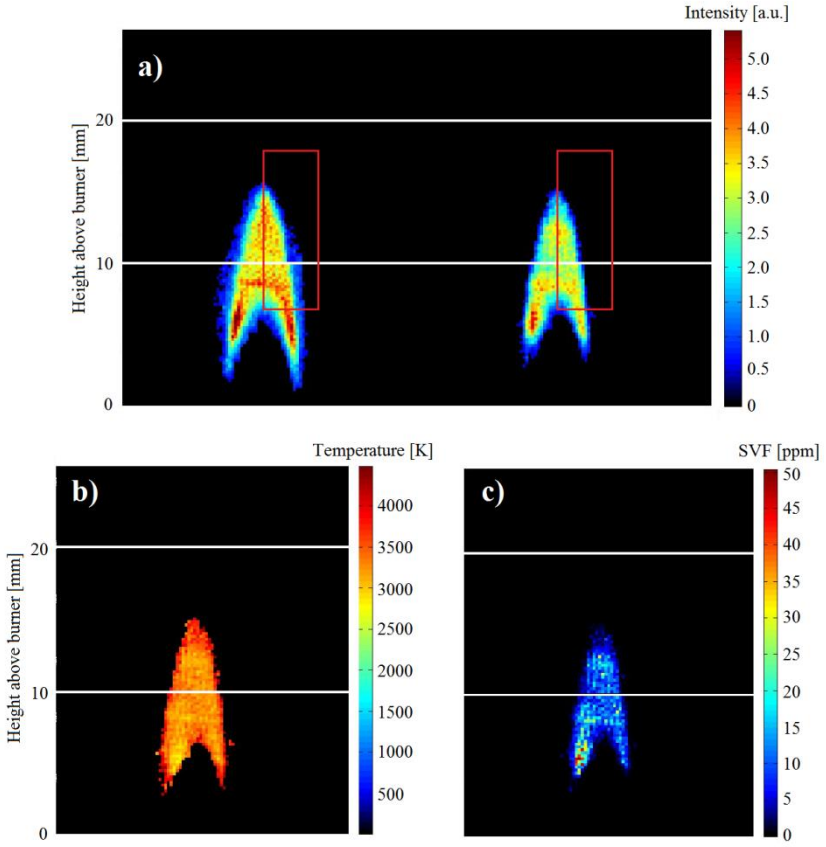

Figure 7.17. a) Raw images of LII intensity through 415 and 632 nm optical filters, b) laser heated soot temperature distribution and c) SVF distribution for an RME flame of 13 mm in height.

7.3.2.1 Oxygen content

The effects of the oxygen content in the fuel was investigated by oxygenating diesel, by mixing varying amounts of oxygenate with diesel, by weight. The particular oxygenate used in this study was diethylene glycol diethyl ether, which is 30 % oxygen by weight, shown below with the chemical formula:

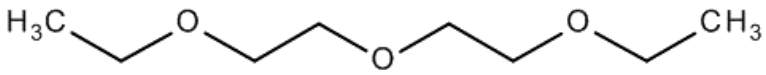

Diethylene glycol diethyl ether was mixed with diesel at 20, 30, 50 and 75 % by weight, providing oxygen percentages of 6, 9, 15 and 22.5 % respectively. Neat diesel was also tested, providing a baseline fuel of zero percentage oxygen content. LII was carried out in flames of the same height, which was set at 15 mm. This height was chosen as it was just below the sooting height for diesel, which was 16

mm with the wick burner used in this study. The planar SVF results for the oxygenated diesel flames are shown in Figure 7.18. As the diesel became more oxygenated, the flame appeared progressively dimmer, with a smaller luminous envelope, showing a reduction in soot. It can also be seen from the LII intensity and SVF distribution in Figure 7.18 a) and c) that SVF produced by diesel, biodiesel and diesel blends is higher than that of the propane flames that were discussed earlier. This is to be expected, as the fuel composition of diesel and biodiesels has significantly longer molecular chain lengths, as well as varying degrees of unsaturation and in the case of diesel, aromatic and cyclic hydrocarbon content, which all results in the production of more soot.

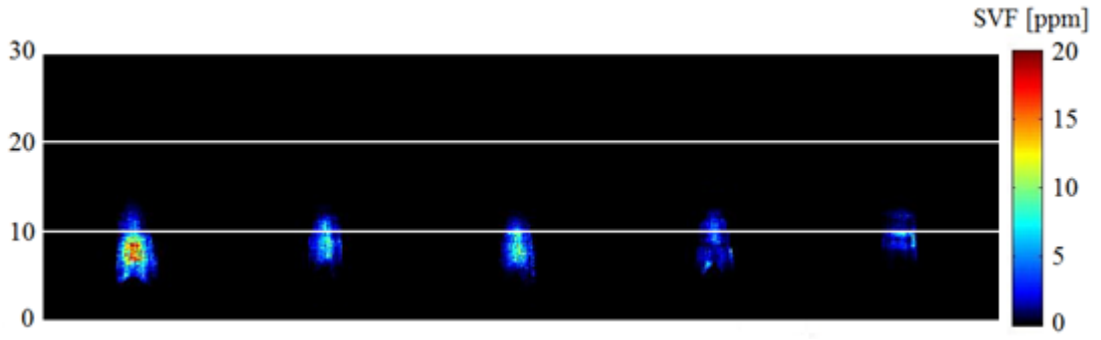

Figure 7.18. Planar SVF results for oxygenated diesel for neat diesel, 6, 9, 15 and 22.5 % oxygen by weight (left to right).

Figure 7.19 shows the average SVF for the diesel-oxygenate blends, calculated as the mean of the side of the flame in which the laser sheet enters. It can be seen that the SVF decreases with an increasing amount of oxygen content within the fuel molecule. The decrease appears exponential, decreasing by a smaller amount as more oxygen is added to the fuel composition. This is because there is more oxygen available during pyrolysis and the soot formation process. The higher oxygen content will result in there being more oxygen available for oxidation reactions to take place and hence increase the rate of reaction of soot oxidation, reducing soot. During pyrolysis, the rate of reaction of isomerisation and oxygenation of combustion intermediates will be increased, due to higher oxygen availability. The amount of carbon sequestered by oxygen to form CO and CO2 will also increase due to the presence of more oxygen. The overall effect is shown in Figure 7.19 and therefore the biodiesel fuels are expected to soot less than diesel, as they are oxygenated.

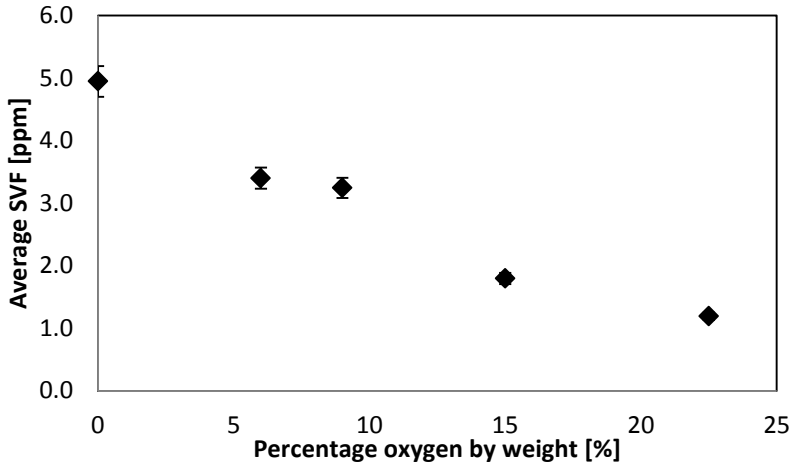

Figure 7.19. Average SVF for oxygenated diesel blends.

7.3.2.2 RME-diesel blends

RME is a widely used biodiesel and was mixed with diesel in order to analyse the amount of soot produced. In terms of oxygenation, the RME used in this study was calculated to be 11.4 % oxygenated by weight, taking into account the GC composition results. The oxygen content by weight, for each individual methyl ester molecule within the fuel was calculated from its molecular structure. This was then multiplied by the percentage of each individual molecule as determined by the GC analysis, providing the total molecular weight of oxygen in RME, which was then converted to a percentage of the overall RME composition by dividing by the total molecular weight of RME and multiplying by 100. RME was mixed with diesel at 20, 25, 45, 50, 60 and 75 %, by weight, providing oxygen percentages of 2.3, 2.9, 5.1, 5.7, 6.8 and 8.6 % respectively. Neat RME and neat diesel were also tested, with oxygen percentages of zero and 11.4 % respectively. The percentage oxygen in diesel may be higher than zero, however for the purpose of this comparison, diesel was used as a baseline fuel of minimal oxygenation.

Figure 7.20 shows the planar SVF results for the RME-diesel blends, where the percentage oxygen varies from left to right (upper) and then left to right (lower) as 0, 2.3, 2.9, 5.1, 5.7 6.8, 8.6 and 11.4 %. The average SVF was calculated for each flame in the same way as with the oxygenated blends and are presented in Figure 7.21. The results show a decrease in SVF with an increase in oxygen percentage. The decrease in SVF is much more pronounced in the RME-diesel blends, compared with the

oxygenated diesel blends. This could be due to not only oxygenating the fuel, but also due to the changes in the fuel blends molecular structure.

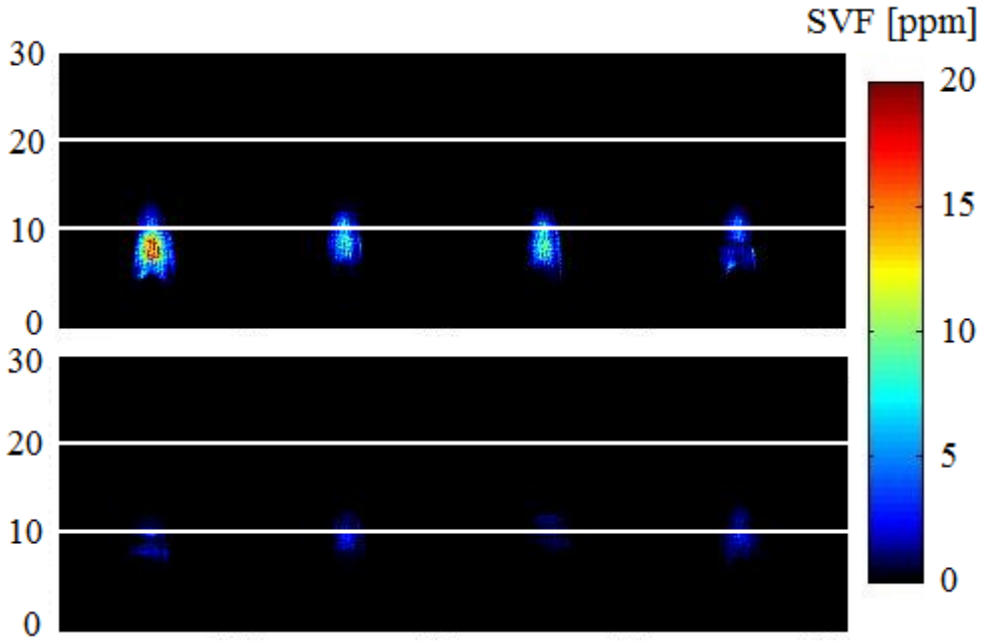

Figure 7.20. Planar SVF results for RME-diesel blends for neat diesel, 2.3, 2.9 and 5.1 % oxygen by weight (left to right, upper) and 5.7, 6.8, 8.6 and 11.4 % by weight (left to right, lower).

Assuming that diesel is made up of 65 % linear and cyclic saturated hydrocarbons, 30 % aromatics and 5 % olefins, with carbon chain lengths ranging from 10 – 22 and averaging at 15, then addition of RME will change the mixture molecular structure as follows. Considering that RME has an average chain length of 18 and is mainly composed of olefins with varying degrees of unsaturation, it can be deduced that the RME- diesel mixture will constitute increasing amounts of olefins as RME is added and relatively smaller amounts of aromatic and saturated hydrocarbons. The average chain length of the mixture will increase slightly throughout RME addition in the mixtures used here, from 15 to 18 as RME composition reaches 100 %. This is likely to cause a slight rise in SVF. It was found in (Ladommatos, et al., 1996) among others, that aromatics produce sootier flames than aliphatic fuels and that cyclic aliphatics are sootier than straight chain aliphatics, thereby effectively reducing their concentration within the mixture, should result in less soot. There is also the olefin concentration to consider. This will increase by virtually the same amount in which the aromatics and aliphatics decrease. According to (Ladommatos, et al., 1996), the

effect of cyclic aliphatics and the double bond on soot is of a similar magnitude, however aromatics soot much more heavily than aliphatic fuels. Therefore, for the SVF in Figure 7.21 to reduce by such an increased amount, compared with that in Figure 7.19, then the replacement of aromatics with olefins must be that cause. The olefins produce less soot than the aromatics, causing a reduction in SVF. This combined with the oxygenation of diesel due to the methyl ester component of the biodiesel molecules, reduces SVF significantly in the RME-diesel blends. These effects are more pronounced than the increase in SVF which is likely to occur from the increase in average chain length caused by adding RME.

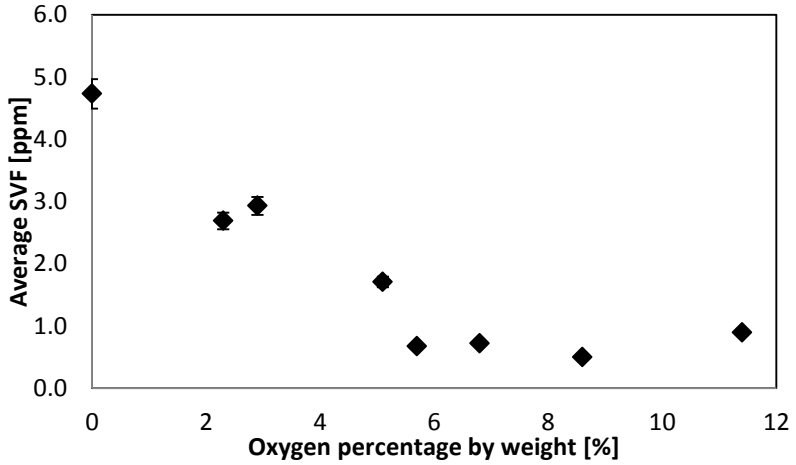

Figure 7.21. Average SVF for RME-diesel blends.

7.3.2.3 Biodiesel comparison

The effects of different biodiesel composition on SVF were investigated using the LII technique, in a similar way as described above for the diesel blends. The knowledge of the individual fuel composition gained using GC, combined with SVF results in a number of sized flames for each fuel, allowed for conclusions to be made on how SVF is affected by fuel composition. The fuel consumption of each fuel was also measured by weighing the burner before and after each set of measurements. For this reason there was no coflowing air used during the experiments, as it would have been considerably difficult to measure the fuel consumption with coflowing air in the same way. The fuel consumption rate has been plotted against flame height for each fuel in Figure 7.22. The figure shows diesel (orange circles), RME (blue diamonds),

SME (red squares), FEE (purple crosses), TME (blue crosses with a vertical line) and CME (green triangles).

It can be seen from the Figure 7.22 that CME required the most amount of fuel to produce a particular sized flame and diesel required the least. RME, FEE and SME were all very similar in between, with TME requiring slightly more in comparison. This could reflect on the quality of the fuels, where a lower fuel consumption rate per flame height conveys a more efficient fuel. This makes sense as diesel is a widely used fuel, producing better efficiency and performance in real life processes, such as that of engines. According to Figure 7.22, CME would be the least efficient fuel, however the CME caused the flame to flicker at times which was put down to the manufacturing process of the particular CME fuel. It was thought that the fuel may not have been filtered properly, meaning that by-products of the transesterification process may have remained within the fuel (Van Gerpen, 2005). The flickering could have been caused by water which can become trapped by these by-products.

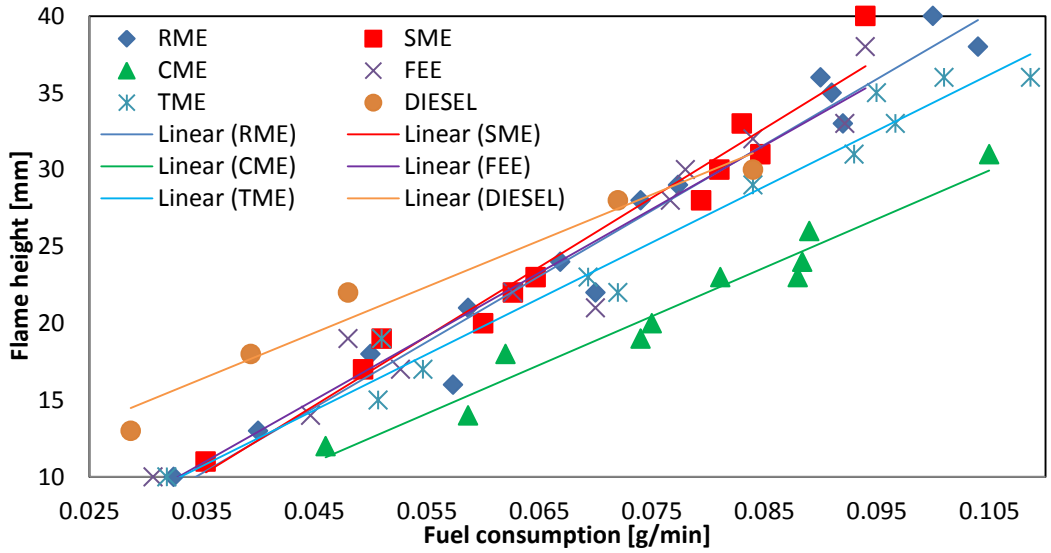

Figure 7.22. Fuel consumption rate for various flame heights for each fuel.

For diesel, the flames that were 28 and 30 mm in height were highly sooting ,which made it difficult to determine the exact flame height, as there was no defined edge to the luminous envelope. The values of 28 and 30 mm were nominal and could be determined differently at the discretion of the experimenter and therefore may not

accurately display the flame height for the particular fuel consumptions in the figure. It is expected that the flame heights were actually significantly higher than shown in Figure 7.22, resulting in the diesel line of best fit being markedly higher than the other fuels, as it is for smaller flame heights. However, even when considering this difference in height, the line is still expected to converge towards the biodiesels to some degree, as the production of more soot could mean that the efficiency of the fuel in the diesel flames becomes reduced.

Planar SVF results for diesel and biodiesel flames of different heights are shown in Figures 7.23 to 7.28, for RME, FEE, TME, SME, CME and diesel respectively. Flame heights of 8, 15 and 19 mm were investigated for RME, 8, 10 and 16 mm for FEE, 7, 10 and 16 for TME, 11, 15 and 20 for SME, 7, 8 and 9 for CME and 8, 10, 15, 19, 28 and 30 for diesel. The images show an increase in SVF with flame height, which is to be expected, as a bigger flame requires a larger wick and therefore there is a higher capillary flow rate, leading to more fuel being consumed, therefore producing more combustion products, including soot. The SVF results are distributed similar to that of the gaseous flame, where a relatively high amount of soot was found in the central region of the flame, directly above the wick, corresponding to the hottest parts of the flame and lesser amounts of soot can be found near the edges and wings of the flame, for non-sooting flames.

The three CME flames at similar heights show that the SVF is consistent at particular flame heights. The three larger flames of diesel (19, 28 and 30 mm) were all sooting flames, where the 19 mm flame was only beginning to soot, where the luminous zone could be seen to open slightly at the top, but with minimal black carbon emanating from it. The 28 and 30 mm flames were highly sooting, producing a significant plume of black carbon from the open luminous zone and can be seen to have a different SVF distribution to the other flames. There is a high amount of soot in the wings of the flame, where the flow is relatively slower compared with that of the middle of the flame, due to the fuel flow interacting with the quiescent air. Furthermore, there is a larger distance for the soot particles to travel along the streamlines of the flame wings, compared with the central parts of the flame.

Therefore the soot particles have a longer residence time within the combustion zone, where the soot formation process is taking place, hence more soot particles can form and mature to a greater extent, compared with the middle part of the flame.

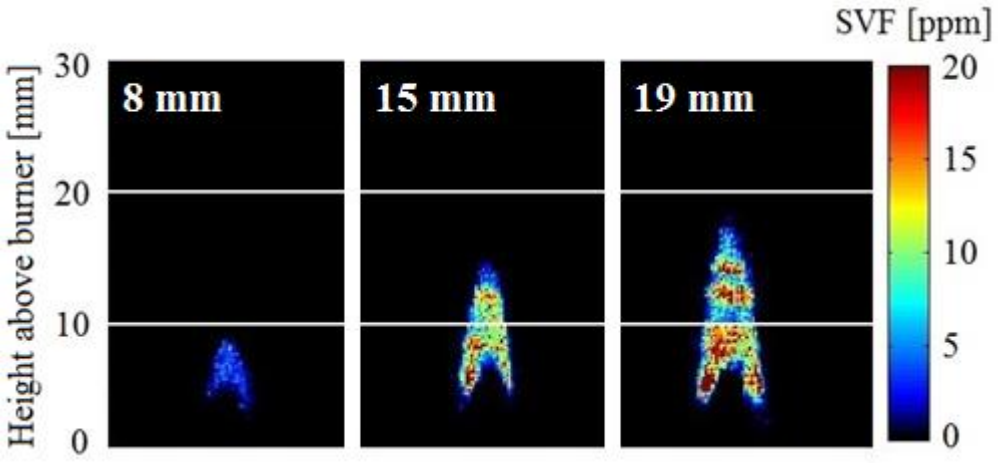

Figure 7.23. Planar SVF results for RME flames of heights 8, 15 and 19 mm (left to right) include how flame height varies.

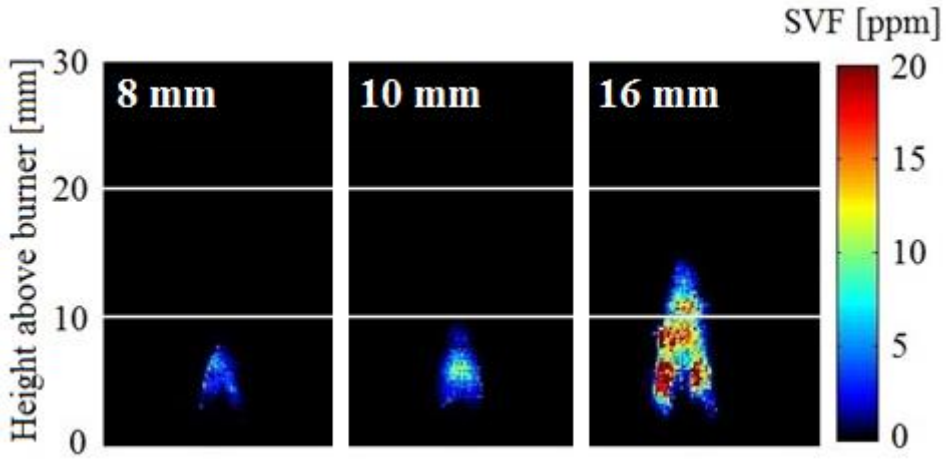

Figure 7.24. Planar SVF results for FEE flames of heights 8, 10 and 16 mm (left to right).

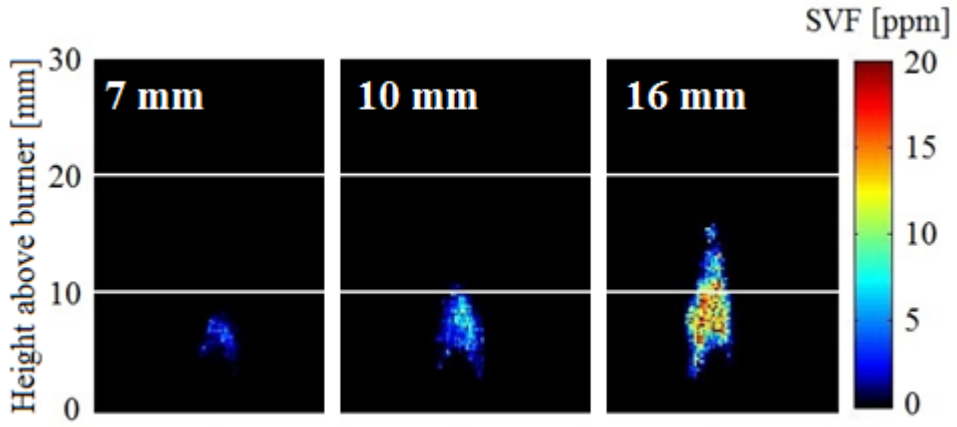

Figure 7.25. Planar SVF results for TME flames of heights 7, 10 and 16 mm (left to right).

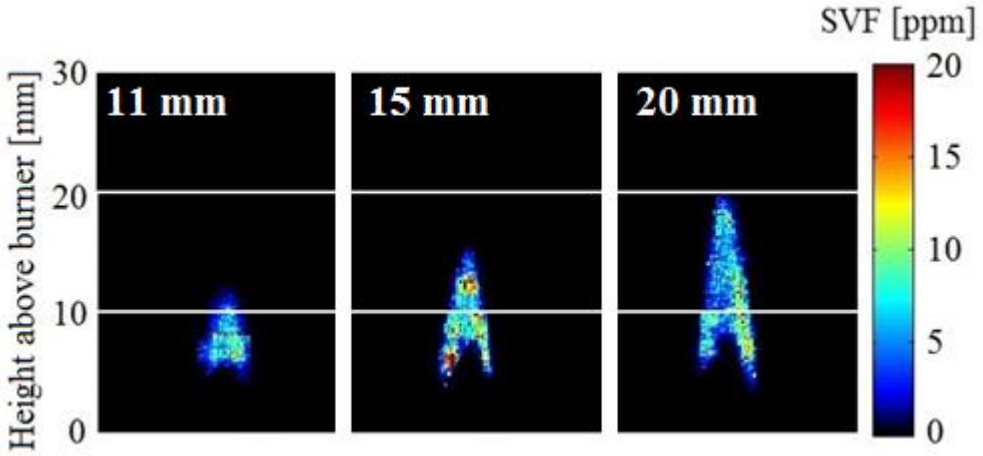

Figure 7.26. Planar SVF results for SME flames of heights 11, 15 and 20 mm (left to right).

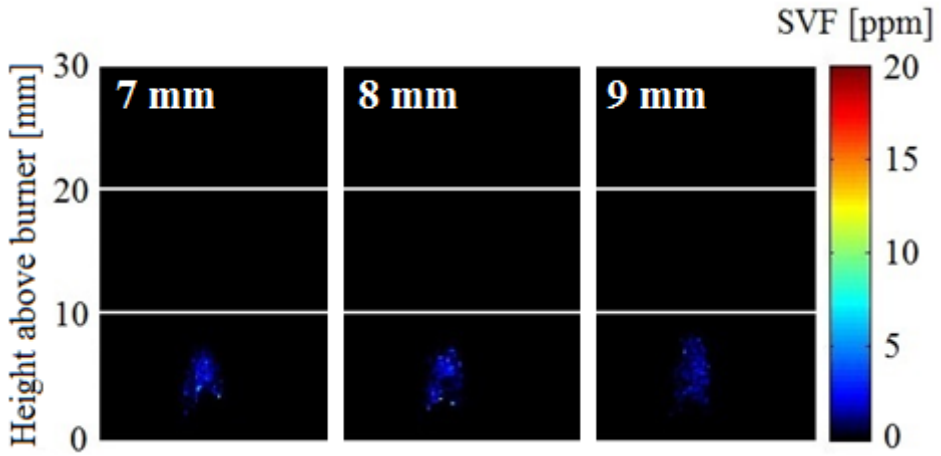

Figure 7.27. Planar SVF results for CME flames of heights 7, 8 and 9 mm (left to right).

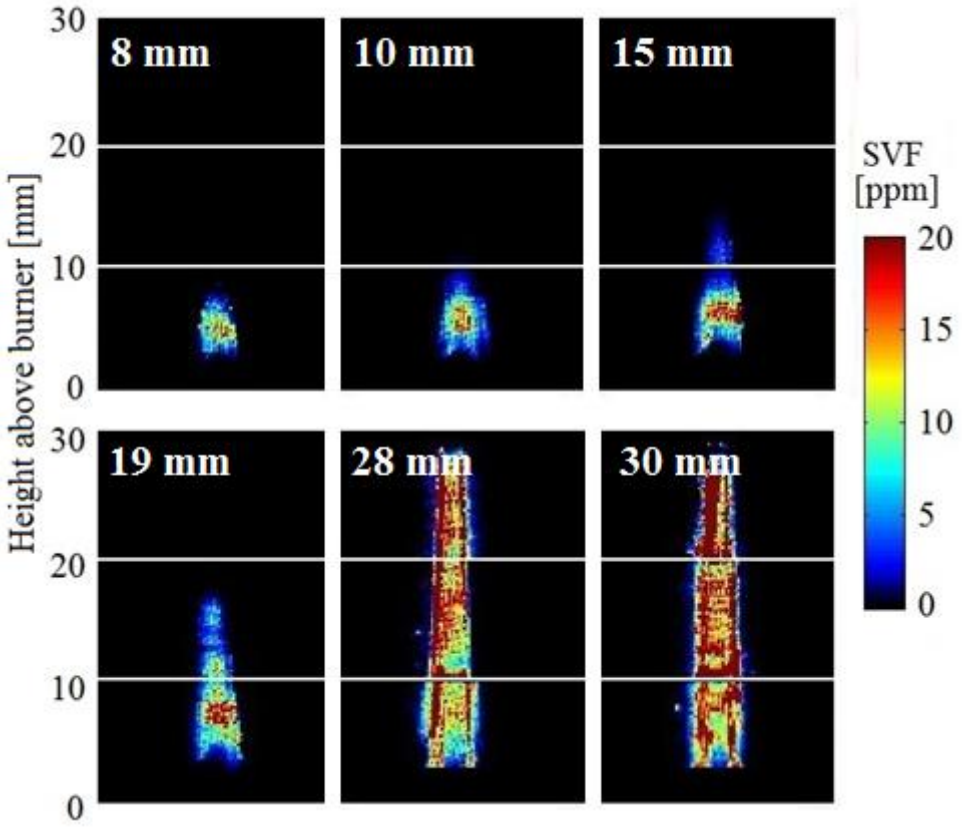

Figure 7.28. Planar SVF results for Diesel flames of heights 8, 10 and 15 mm (left to right, upper) and 19, 28 and 30 mm (left to right, lower), where the larger flames are sooting.

The average SVF results at different heights above burner for most of the flames have been included in Figure 7.29. Flames of similar heights have been grouped together into subfigures, where 8, 10, 15 and 20 mm flames are presented from top to bottom, respectively. For each fuel, a steep rise in SVF can be seen as the HAB increased to a certain point, followed by a relatively shorter reduction in SVF as HAB further increased. A general increase in SVF can be seen for each fuel, as flame height was increased, which can be more easily seen in the larger flames. From Figure 7.29 it can be seen that diesel was the sootiest fuel, which was due to its aromatic content and less percentage oxygen. The results show that RME, FEE and SME all produce a similar amount of soot, where RME was the most prolific sooting biodiesel, followed by FEE, then SME closely behind. TME was next in terms of sooting tendency and CME was the least sooty biodiesel fuel tested. Figure 7.30 shows the average SVF for a highly sooting diesel flame at a height of 28 mm. The SVF can be seen to increase throughout the flame, due to soot formation reaction rates overcoming oxidation reaction rates, producing a net increase in SVF.

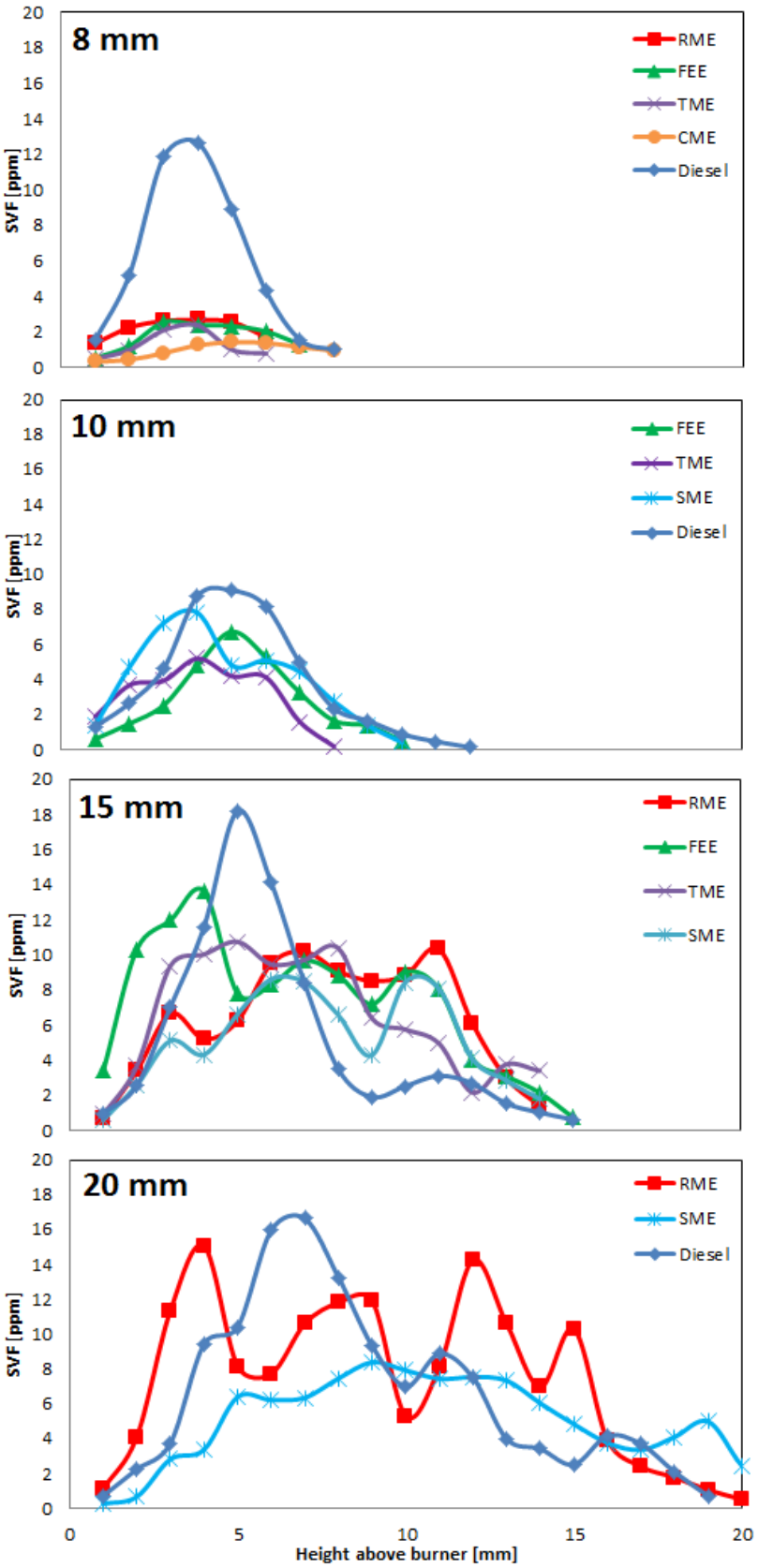

Figure 7.29. SVF at various HAB for each fuel in flames of different heights, varying from 8mm (top) to 20 mm (bottom), obtained from averaging SVF over 1 mm increments along the flame height axis for each flame.

The gas chromatography results show that RME had the longest average carbon chain length, as well as the highest percentage of total unsaturation, out of all of the biodiesels. This resulted in RME to being the sootiest biodiesel, as shown in the SVF results. FEE and SME followed closely behind for different reasons. FEE is an ethyl ester, instead of a methyl ester, which caused it to soot more readily than other methyl esters with similar ester alkyl chain composition. If the FEE was a methyl ester, i.e. fish methyl ester (FME), then its carbon chain length and degree of unsaturation should place it as a fuel which soots much less, possibly second to last out of all of the fuels tested in this study, after CME. In terms of composition, SME had the second highest amount of unsaturation and average carbon chain length after RME, which would have put it as the second most prolific sooting biodiesel in this work. However this was not the case as the effects of the ethyl ester constituents in the FEE outweighed that of the alkyl chain composition for FEE compared with SME. TME had the second from lowest average carbon chain length and second from highest percentage saturation out of all of the methyl esters. The LII results confirmed that it had the second lowest SVF out of all of the fuels tested, as expected from the composition results. Finally, CME had the lowest average carbon chain length, as well as the highest degree of saturation, where almost all of the molecules were saturated. The SVF results confirmed that CME was the least sooty fuel in this study.

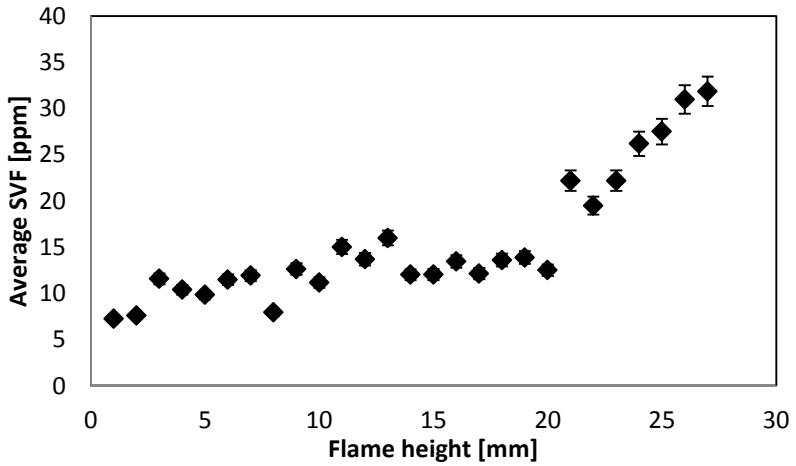

Figure 7.30. SVF at various HAB for diesel in a flame of 28 mm in height.

7.3.2.4 Uncertainty and error

The uncertainty and error of the LII technique and hence for the SVF results was calculated using single shot SVF images from each flame tested in this study. Pixel to pixel standard deviations, taken as a percentage of the mean were carried out in order find the shot to shot variation in SVF for each pixel in the flame images. 50 single shot images were taken for each HAB in each flame. An example of the analysis is shown in Figure 7.31 for a TME flame at a height of 10 mm. The figure shows that the SVF results are consistent within about 4 % in the central parts of the flame, increasing to between 6 and 10 % near the flame edges, particularly at the HAB coinciding with the wick, due to added flame perturbations that were induced by the laser interacting with the wick. There was expected to be a larger error in these regions, as discussed earlier in this chapter. The edges of the flame are likely to experience some perturbations due to small disturbances in the flow. Great care was taken to minimise flame perturbations, however small disturbances were unavoidable. The average SVF error for each flame was calculated by averaging the pixel to pixel standard deviation within the region of the flame considered for the SVF analysis, which is illustrated in Figure 7.17 a) with a red box. The maximum average SVF error calculated out of all of the flames was determined as 4.5 % and this was determined as the error of the LII technique used in the SVF investigations.

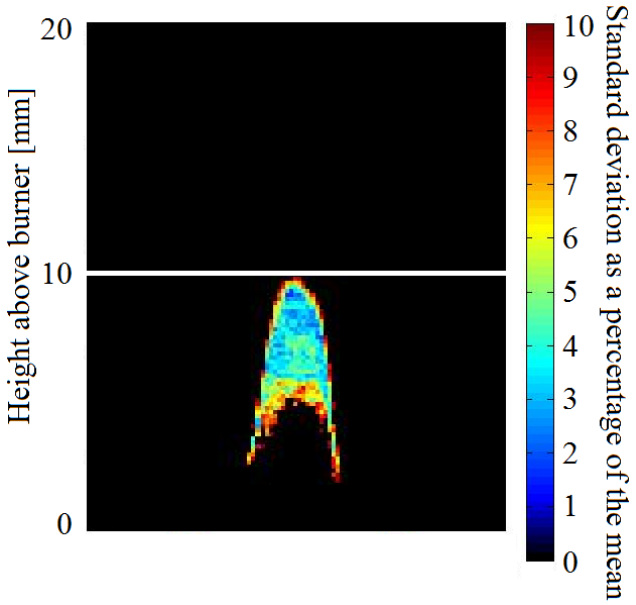

Figure 7.31. Pixel to pixel standard deviations calculated from 50 SVF images of a TME flame of 10 mm in height, presented as a percentage of the mean at each pixel for each flame.

7.3.3 TEM images

Thermophoretic sampling was carried out in some flames of particular fuels in order to show the difference between soot particles, due to composition. TEM images are presented for diesel, FEE and TME to represent the differences in soot size and distribution due to the different types of fuel. No statistical analyses of the images were carried out and any trends identified in the following are only representative of a limited number of images. These results are merely shown to supplement the LII data. The flame heights for the diesel, FEE and TME flames were 23, 21 and 22 mm respectively. Figure 7.32 conveys an idea of the distribution of soot particles deposited onto the TEM grids for diesel at 1,500 times magnification. It can be seen that the number of aggregates deposited is quite low due to the short residence times involved in the sampling process, combined with the relatively small flames used in this investigation, compared with that of other studies (Pandey, et al., 2007; Merchan-Merchan, et al., 2012). This is reflected throughout the results.

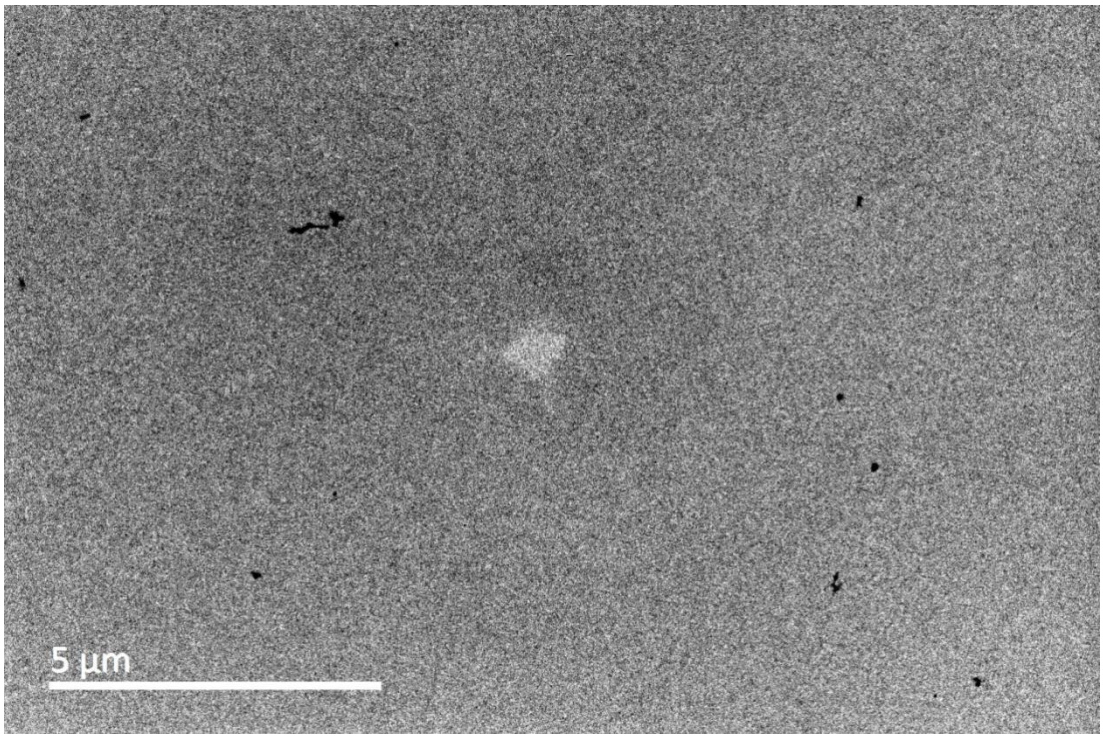

Figure 7.32. TEM image of diesel soot at 15 mm HAB and 1,500 X magnification.

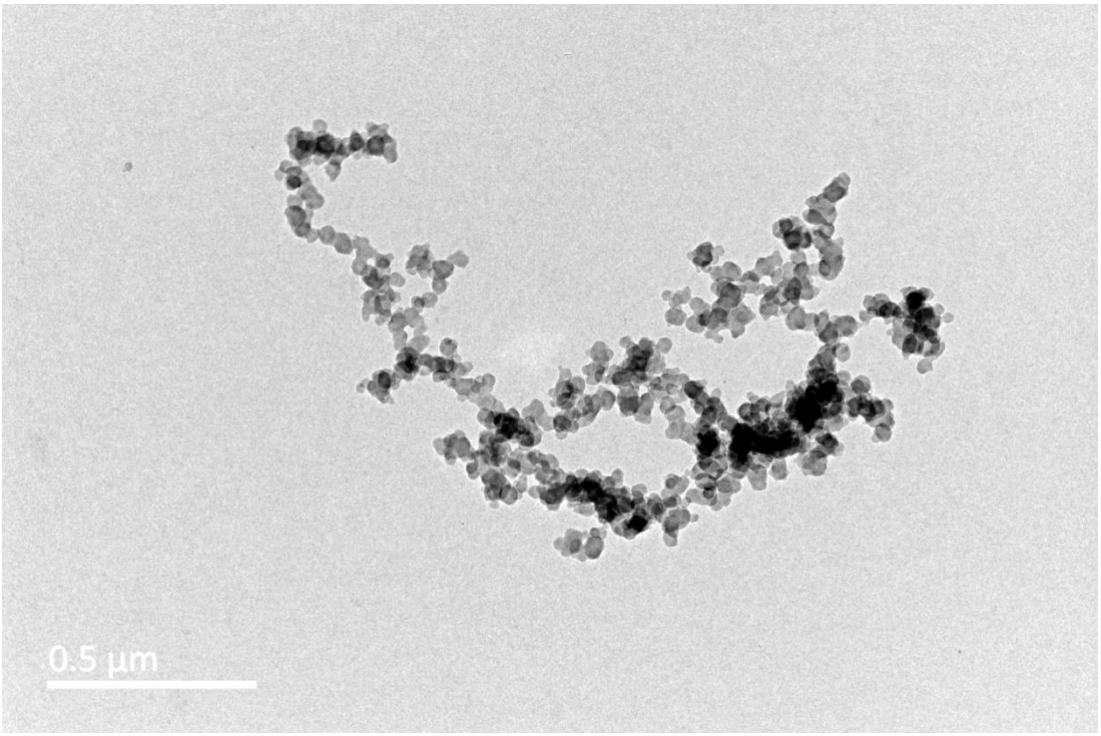

Figure 7.33. TEM image of diesel soot at 5 mm HAB and 10,000 X magnification.

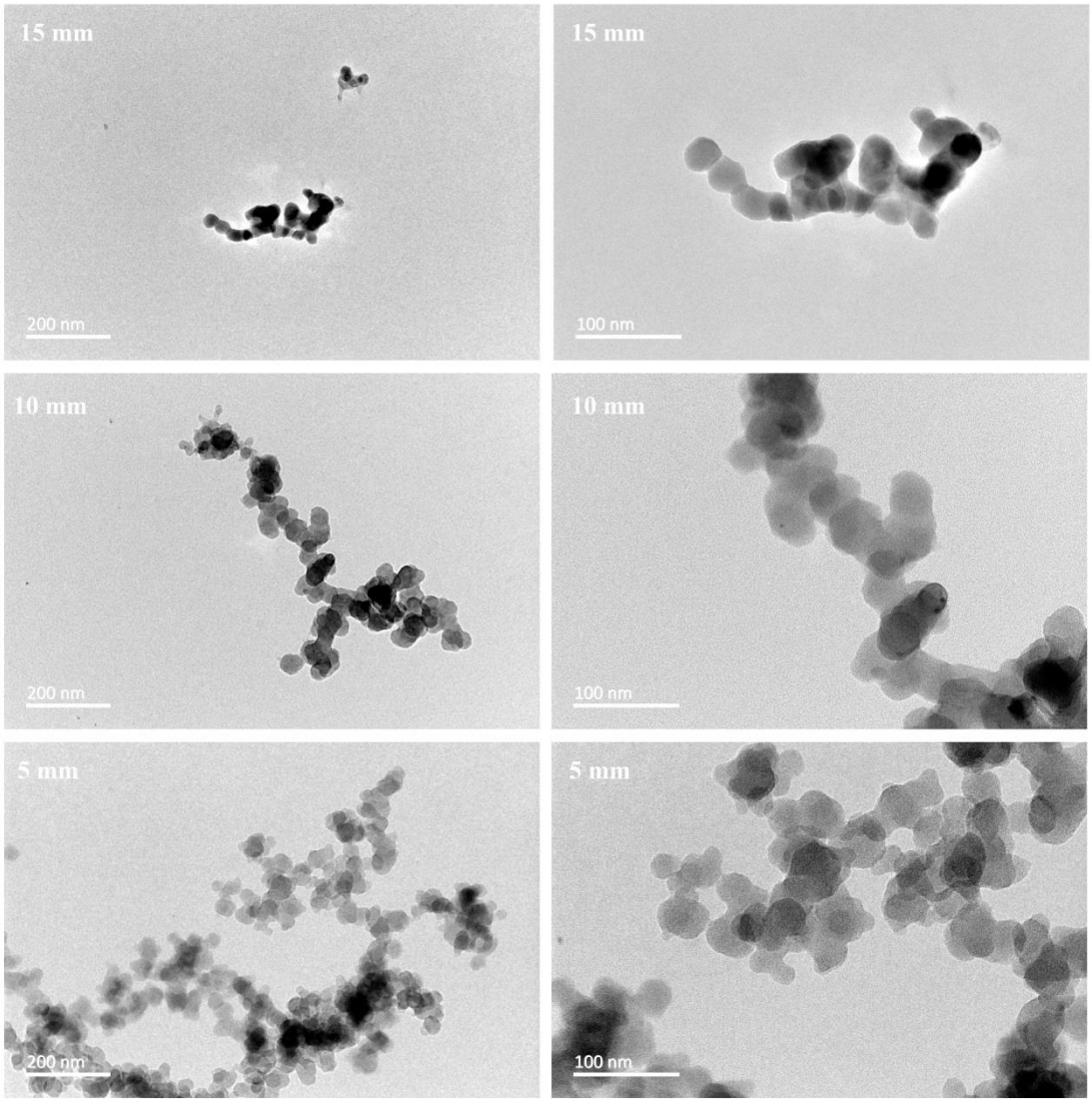

Figure 7.34. TEM images of diesel soot at 20,000 (left) and 50,000 (right) X magnification at HAB of 5 mm (bottom), 10 mm (middle) and 15 mm (top).

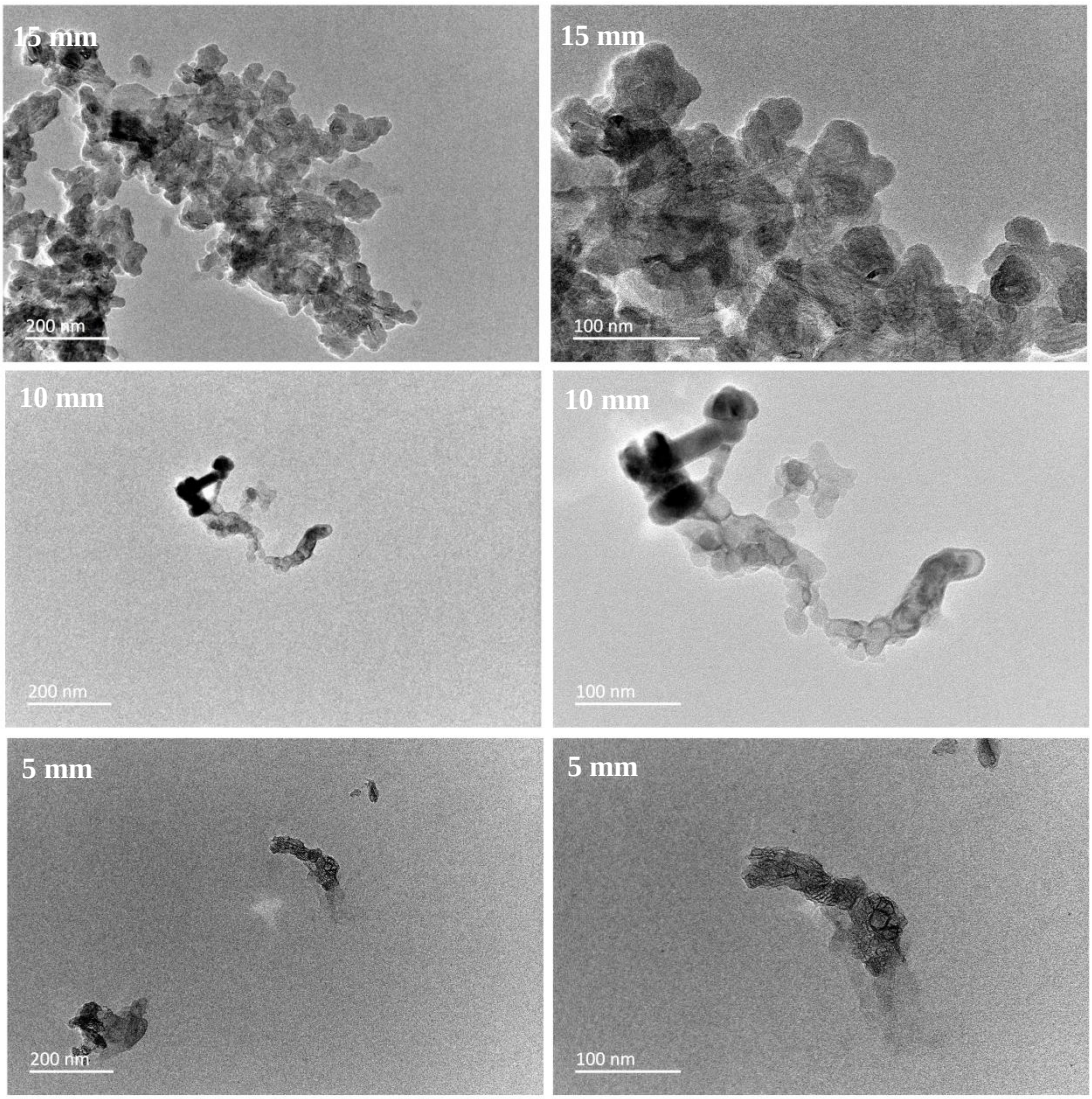

Figure 7.35. TEM images of FEE soot at 20,000 (left) and 50,000 (right) X magnification at HAB of 5 mm (bottom), 10 mm (middle) and 15 mm (top).

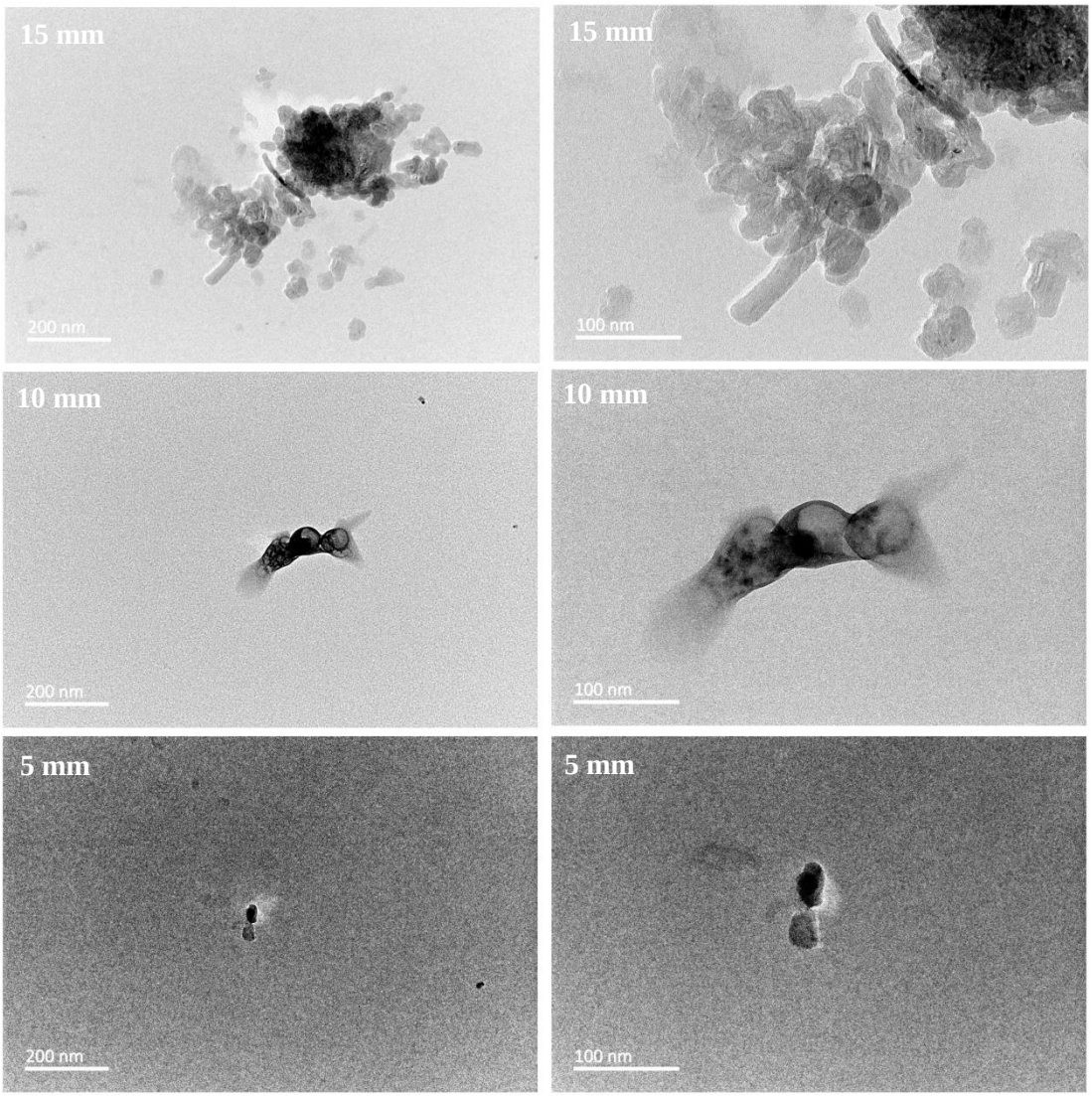

Figure 7.36. TEM images of TME soot at 20,000 (left) and 50,000 (right) X magnification at HAB of 5 mm (bottom), 10 mm (middle) and 15 mm (top).

Figure 7.33 shows a large diesel soot aggregate at 5 mm HAB and 10,000 times magnification. The soot can be seen to be made up of a large number of particles of a similar size. These particles are the soot primary particles whose size is dependent on the particular conditions of combustion in which they occur in. The particles can be seen to be in a chain like configuration. The aggregate shown in Figure 7.33 is shown at greater magnifications, of 20,000 and 50,000 times in Figure 7.34, as well as soot agglomerates at 10 mm and 15 mm HAB. Figure 7.35 and Figure 7.36 show TEM images for soot aggregates in FEE and TME flames at the same flame heights (5, 10 and 15 mm) and magnifications as the diesel TEM images in Figure 7.34.

The size of the soot aggregates can be seen to decrease as the HAB increases for diesel, in Figure 7.34. This shows that the soot aggregates for diesel reach their largest size near to the burner. This is reflected in the LII results, showing that the highest SVF for diesel is near to the burner. The opposite is true for the biodiesel flames, where the soot agglomerates increase in size with sampling height, according to the TEM images. The biodiesel soot aggregates in Figures 7.35 and 7.36 appear different to that of the diesel flame, where some of the primary particles look elongated and the aggregate morphology is more clumped together, than chain-like. This could be due to the difference in composition between the diesel and biodiesel fuels, where for example, variations in percentage oxygen in the combustion zone can reduce soot particle size (Lahaye, et al., 1996). Soot morphology and the amount of soot formed are associated with several parameters, including flame temperature, oxygen content and percentage aromatics.

CHAPTER 8
BIODIESEL PERFORMANCE AND EMISSIONS IN A GAS TURBINE ENGINE

8.1 Introduction

A pilot study was carried out in order to analyse the effects of biofuel and biofuel-diesel blends on a gas turbine engine, to further this study and provide an insight into the practical application of biofuels. Similar work to that of this pilot study (Habib, et al., 2010) uses jet A fuel blends with some biofuels and has shown that some characteristics of pure biofuels and blended fuels are generally comparable to that of jet A. Parameters such as turbine inlet temperature (TIT) and exhaust gas temperature (EGT) remained almost the same with static thrust not showing any significant drop. The study also showed that pure biofuels actually have a higher thermal efficiency than jet A and jet A blends and that some emissions were reduced with the usage of biofuels, illustrating that there is a potential to reduce emissions by using biofuel-jet A blends.

This pilot study focuses on the measurement of nitrogen oxide compounds (NO_X) and the amount of partially and unburned hydrocarbons (HC) produced by some biofuels and how they relate to each other and to the performance of the SR-30 gas turbine engine. The biofuels are blended with standard diesel in specific percentages by volume in order to directly measure the amount of NO/NOx and partially/unburned hydrocarbons in the gas turbine exhaust. This leads to the performance of each fuel and fuel mixture being discussed and compared with that of standard diesel.

8.2 Gas turbine setup

8.2.1 SR-30 gas turbine engine

Emissions and performance parameters were measured from an SR-30 gas turbine engine, provided by Turbine Technologies Limited. The main specifications of the SR-30 are listed in Table 8.1 and detailed information about the gas turbine engine is provided in the literature available from Turbine Technologies Ltd (Turbine Technologies, Ltd., 2006; Turbine Technologies, Ltd., 2006; Turbine Technologies, Ltd, 2006). The gas turbine system itself was contained within a protective casing with viewing windows. A Hushkit noise suppression system was placed several centimetres in front of the inlet nozzle. Metal ducting was placed behind the outlet of the engine in order to direct the exhaust gases safely out of the laboratory. A probe was positioned near the entrance of the metal duct in its centre, pointing into the exhaust gas flow, which led to a port at the side of the ducting for exhaust gas sampling. The controls for the gas turbine engine were positioned at the front on a small panel which also provided information on various operating conditions via digital LED readouts. A USB connection port from this front panel could connect further operating information to a computer using data acquisition software. Figure 8.1 shows a schematic of the setup.

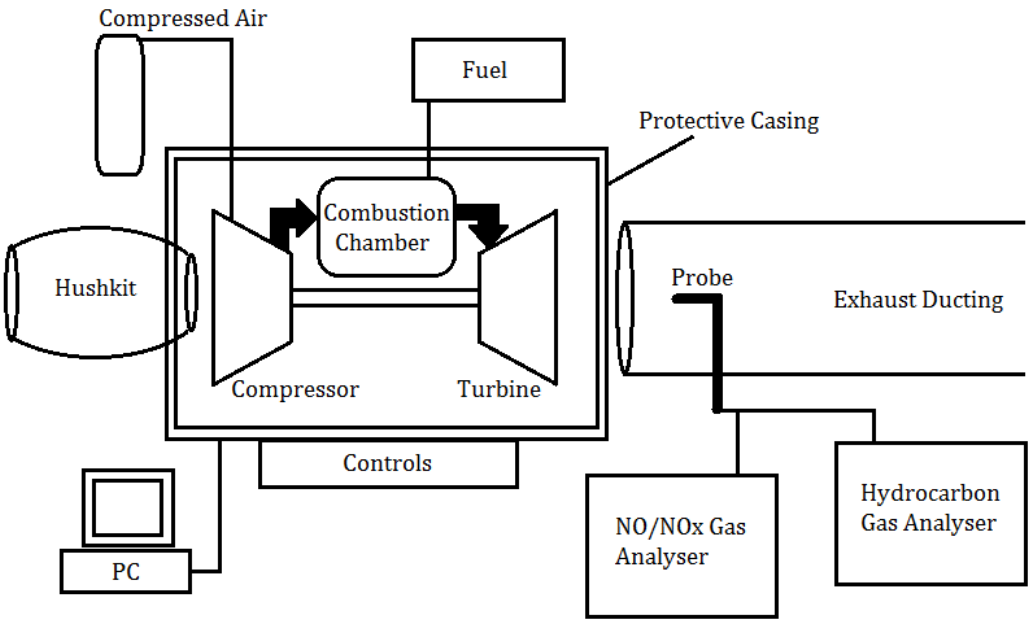

Figure 8.1. Schematic of the gas turbine setup with gas analysers.

8.2.2 Exhaust gas measurement

The exhaust gases were measured using two separate gas analysers provided by Analysis Automation Limited (AAL); AAL model 443 NO/NO_X Chemiluminescent analyser and AAL model 523 FID Hydrocarbon analyser. Both gas analysers can be used to measure emissions from combustion processes and both have detection ranges from 0 – 10,000 ppm. The ranges on the machines can be set to different precisions within the 0 – 10,000 ppm scope. The NO/NO_X analyser was set to 0 – 10 ppm which was accurate to the nearest 0.01 ppm and the HC analyser was set to 0 – 1000 ppm which was accurate to the nearest 1 ppm. These ranges were comparable to the order of magnitude of the results.

Table 8.1. SR-30 gas turbine engine specifications.

Engine diameter	17 cm
Engine length	27 cm
Compressor type	Single stage centrifugal
Turbine type	Single stage axial
Compression ratio	2.5:1
Specific fuel consumption	1.2 (mid thrust)
Mass flow rate	0.5 kg/s
Design maximum thrust	178 N
Design maximum RPM	87,000 RPM
Maximum turbine inlet temperature (TIT)	870 deg C
Maximum exhaust gas temperature (EGT)	720 deg C

The NO/NO_X gas analyser is capable of measuring the amount of nitric oxide (NO) within the gas phase of a sample. When NO reacts with ozone (O_3) it produces nitrogen dioxide (NO_2), of which some molecules are in the ground state, whilst others are in the excited state. Molecules in their excited state decay back to the ground state either by emission of a photon of a specific frequency, or by energy transfer by collision. The collision can be either with another molecule of gas or the walls of the container. If the concentration of ozone is high enough for its effective concentration to remain the same after the reaction, the intensity of the light is proportional to the amount of NO. The intensity of the emitted light is detected by a photomultiplier tube and can then be used to calculate the amount of nitric oxide in the sample. The analyser also has a catalytic converter which can be included in the

gas stream and is used to convert NO_2, allowing the determination of NO_X by finding the sum of the concentrations of nitrogen and NO. The analyser can therefore be used to measure either NO or NO_X depending on whether the catalytic converter is included within the sample gas stream (Analysis Automation Limited, 1990).

The HC analyser measures the total number of organic molecules in the sample by detecting carbon-hydrogen bonds. The analyser does this by using the flame ionisation detector (FID) method. The sample is continuously burnt in a polarised hydrogen flame which causes C – H bonds to form ions. A voltage is also applied to an electrode causing a potential difference between that and the flame. The ions then move towards the electrode creating a current which is proportional to the amount of HC in the sample. In order for this method to work the sample must be kept hot in order to prevent hydrocarbons condensing within the analyser. The detector is set up so that it is not affected by oxygen concentration (Analysis Automation Limited, 1990).

Table 8.2. Some properties of fuels used in SR-30 experiments (Britaine & Lutalado, 2010; Rabé, 2006; Graboski & McCormick, 1998; Knothe, et al., 1997).

Fuel	Density (g/cm^3)	Kinematic viscosity 40 deg C (mm^2/s)	Lower heating value of combustion (MJ/kg)	Solidifying Point (deg C)	Cetane number	Flashpoint (deg C)
Diesel	0.83	2 – 4.5	42	-14	51	56
JME	0.8378	4.2	36.5		51	191
RME	0.8374	6	37.3	2	52.9	84
JO	0.8434	43	39.2	-2	37.8	236
RO	0.8435	37	39.709	-3.9	37.6	246

8.2.3 Fuels

The fuels used in this study were standard diesel, jatropha methyl ester (JME), jatropha oil (JO), rapeseed methyl ester (RME) and rapeseed oil (RO) and some of the properties of these fuels are listed in Table 8.2. The biofuels were blended with standard diesel as 15%, 30% and 50% blends for most experiment runs. JO and RO blends could only be used as 15% blends due to its high viscosity and for the safety of the equipment. Standard diesel and the methyl ester fuels were also used as single

component fuels whereas the oils could not be used unblended in the SR-30. Table 8.3 lists the blends used in this study.

Table 8.3. Fuel mixtures used in SR-30 experiments.

Fuel	Description
D100	100% diesel
J15	85% diesel, 15% JME blend
J30	70% diesel, 30% JME blend
J50	50% diesel, 50% JME blend
J100	100% JME
R15	85% diesel, 15% RME blend
R30	70% diesel, 30% RME blend
R50	50% diesel, 50% RME blend
R100	100% RME
JO15	85% diesel, 15% JO blend
RO15	85% diesel, 15% RO blend

8.2.4 Experimental procedure

Both gas analysers were calibrated using zero grade air and a gas with known particulate concentrations. The probe from within the exhaust duct was connected to both analysers via a heated pipe which led to a t-piece connecting it to the two adjacent analysers. Preliminary tests showed that the readouts would take several minutes to stabilise and would vary within a certain amount after that point, due to the perturbations in the conditions of the engine. The amount of variation related to the overall accuracy of each measurement, which is discussed later. Measurements were taken after the emissions readout stabilised for both gas analysers.

Biodiesel blends were mixed in a container by volume before inserting into the SR-30 fuel tank. All blends could be used to start the engine, but the engine would not start on 100% RME, therefore for this run the engine was started up on diesel reserves within the fuel pipes, then RME put into the fuel tank. Biodiesels could possibly cause certain parts of the gas turbine engine to deteriorate if left in, therefore after each experimental run, the system was drained then flushed with standard diesel and the gas turbine engine was ran at mid power for several minutes. Another concern was the RO and JO fuels damaging the gas turbine engine, therefore these

runs were only carried out for 15% blends, as these fuels are more corrosive than biodiesel..

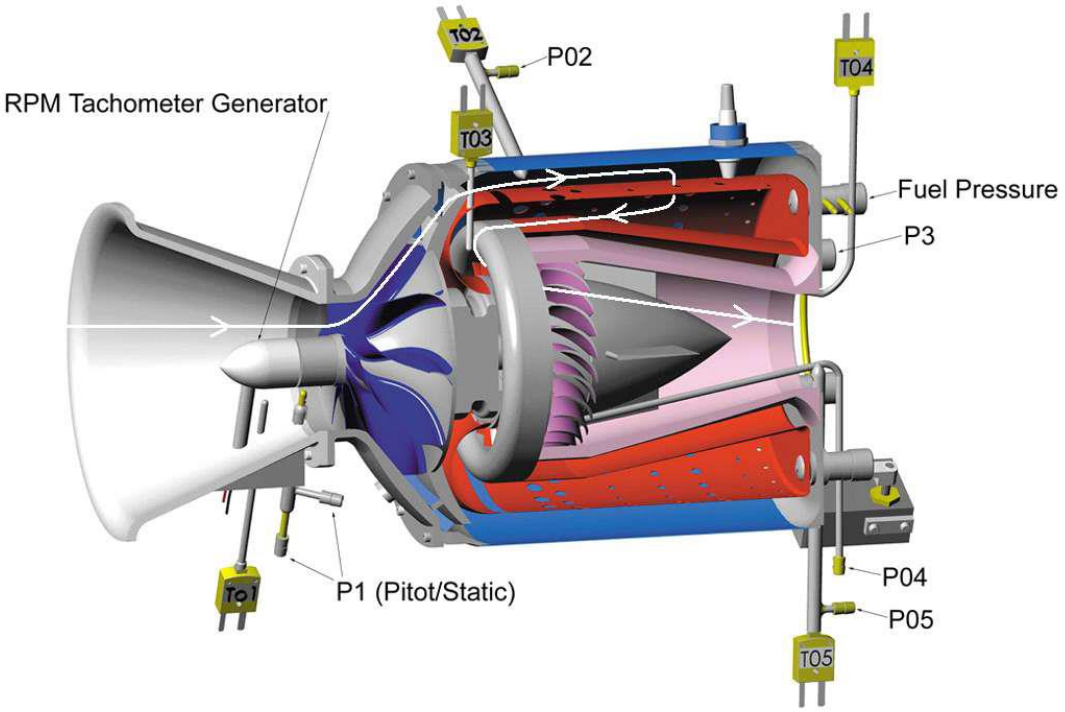

Figure 8.2. Gas turbine engine cut-away showing sensors.

The SR-30 gas turbine engine provides data on engine performance acquired via a USB port. A diagram of the gas turbine engine is shown in Figure 8.2 and it includes the sensors and data provided to the computer. The data mainly consists of temperatures and pressures of the various stages within the engine. These readings were later used to calculate important performance parameters of the gas turbine engine for the various fuels used. Simple mathematical relations were used in conjunction with the temperatures and pressures at key stages within the gas turbine engine to calculate air and gas velocities, mass flow rates of fuel and air, Mach number and fuel-to-air ratio. The thrust specific fuel consumption (TSFC) was calculated using the relation in Equation (8.1) and thermal efficiency calculated using Equation (8.2) (Habib, et al., 2010). Thermal efficiency accounts for combustion efficiency and thermodynamic cycle efficiency, providing a good indication of chemical to kinetic energy conversion.

$$TSFC = \frac{\dot{m}_f}{T} \times 10^6 \left[\frac{g}{kNs} \right] \quad (8.1)$$

$$\eta_t = \frac{(1+f)V_e^2}{2fQ_R} \quad (8.2)$$

Where $\dot{m}_f$ is mass flow rate of fuel in kg/s, T is thrust in N, f is fuel-to-air ratio, V_e is exhaust velocity and Q_R is lower heating value of combustion for the fuel.

8.2.5 Error and uncertainty

Each datapoint gathered was an average of 20 readings taken at 30 second intervals after the emissions readouts stabilised. The standard deviation of the digital readouts varied for each emission measurement. The maximum deviation for NO, NO_X and HC emissions was used respectively to calculate the error in the measurements for each type of emission. All recorded values would then fall within the error determined. The maximum deviation for NO measurements was rounded up to ±10%, for NO_X it was ±12% and for HC emissions it was also ±12%. The performance parameters were recorded on a computer which was plugged into the jet engine control panel, the readings also varied within a certain range, once the system was steady and so an error for these measurements was also calculated in a similar way. The percentage error for most of the performance readings was less than 1% and in other cases, mostly did not exceed 5%, apart from several outliers which were considered anomalous results and discarded from this analysis. The error for the performance readings was therefore ±5%.

8.3 Results and discussion

8.3.1 Individual unblended fuel comparison

Results of engine parameters are presented against engine speed and the emissions are plotted against TSFC. The results for comparison of unblended neat fuels are shown in Figure 8.3 which shows thrust, thrust specific fuel consumption (TSFC),

TIT, EGT, thermal efficiency (η_t), HC and NO/NO_X data. All unblended neat fuels have a range of thrust of 50 – 85 N over the engine speeds used, with an almost linear increase with higher engine speeds, which is due to more fuel being sent to the engine as the throttle is opened further. There is no discernible difference in thrust produced for each fuel used. TSFC for diesel has a range of 44 – 68 g/kNs and all fuels show a linear increase in TSFC with engine speed. Pure RME produces almost the same TSFC as diesel, whereas pure JME has a lower calorific value compared to the other fuels, noticeable by its higher TSFC at all engine speeds. The overall trend for the temperature of combusted gases entering the turbine stage shows an increase with engine speed which is due to an increasing heat release in the combustor. The neat biodiesels both show a higher TIT than diesel with a considerable difference at lower engine speeds, with the difference trailing off at higher speeds. The EGT on the other hand, remained approximately the same value regardless of engine speed and was almost the same for all unblended fuels. Thermal efficiency showed an increase with engine speed for all unblended fuels. Both pure RME and JME fuels showed a markedly higher thermal efficiency than diesel. This could be because the biofuels have more oxygen present within them, resulting in improved oxidation.

The HC, NO and NO_X emissions were also measured using the gas analysers discussed previously. Figure 8.4 shows the NO and NO_X emissions increasing as TSFC increases and hence as engine speed increases. As discussed above, an increase in engine speed is followed by an increase in temperature of combusted gases about to enter the turbine. As NO and NO_X are produced in high temperature environments, it would make sense that higher amounts of NO_X could be produced if combustion is occurring at higher temperatures and the results agree with this. It can be seen that the pure JME starts off with similar NO and NO_X emissions to diesel, at lower TSFC values and rapidly extends above diesel NO and NO_X emissions at higher TSFC values. Conversely, the pure RME shows lower NO and NO_X emissions than diesel for higher TSFC values. The steep rise in NO and NO_X emissions from the JME could be due to a larger TSFC than the other two fuels, resulting in more fuel being burned to achieve a particular amount of thrust,

increasing combustion temperature at an equal thrust value and therefore causing a higher NO and NO_X emissions count.

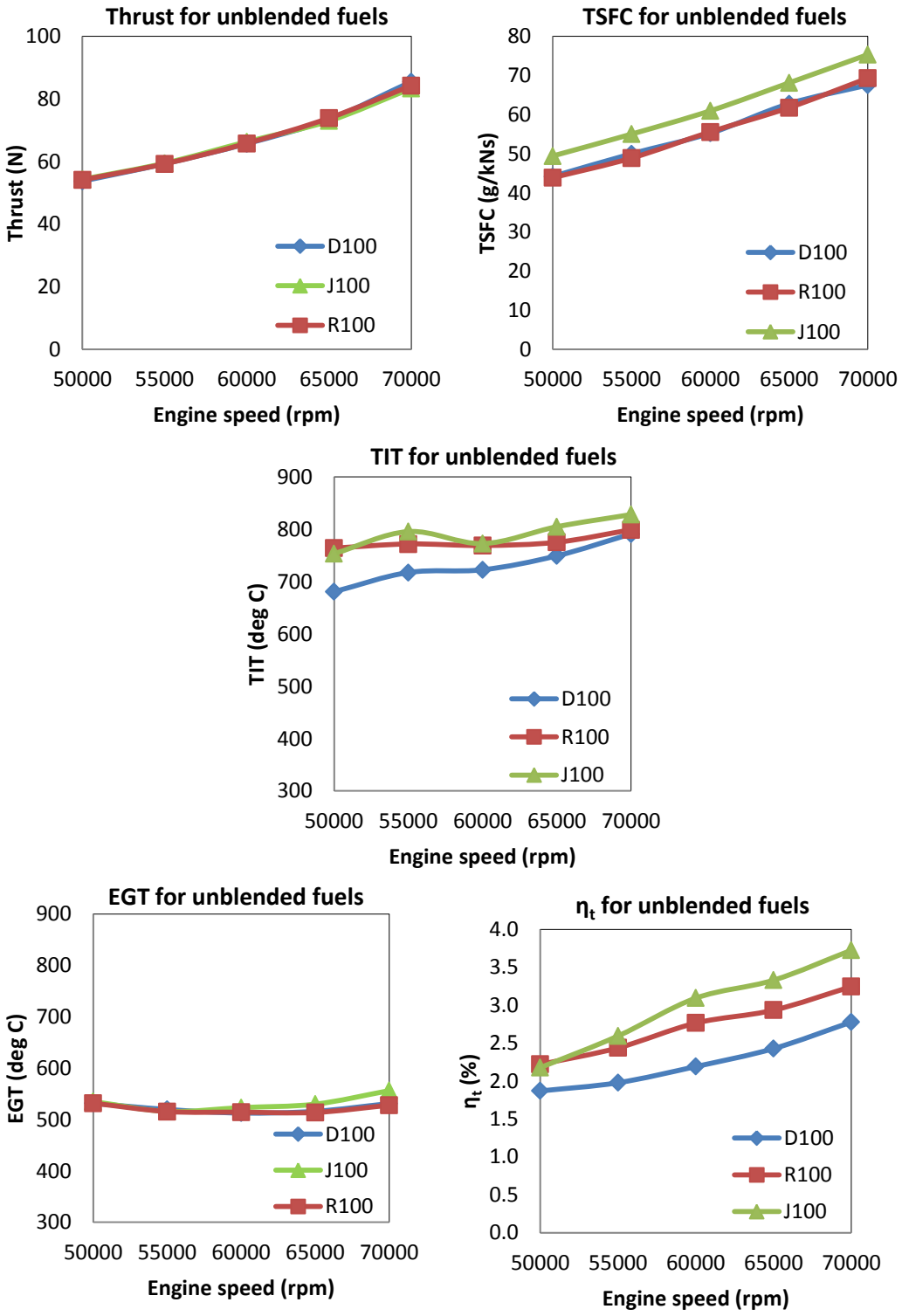

Figure 8.3. Comparison of gas turbine engine performance parameters for unblended fuels.

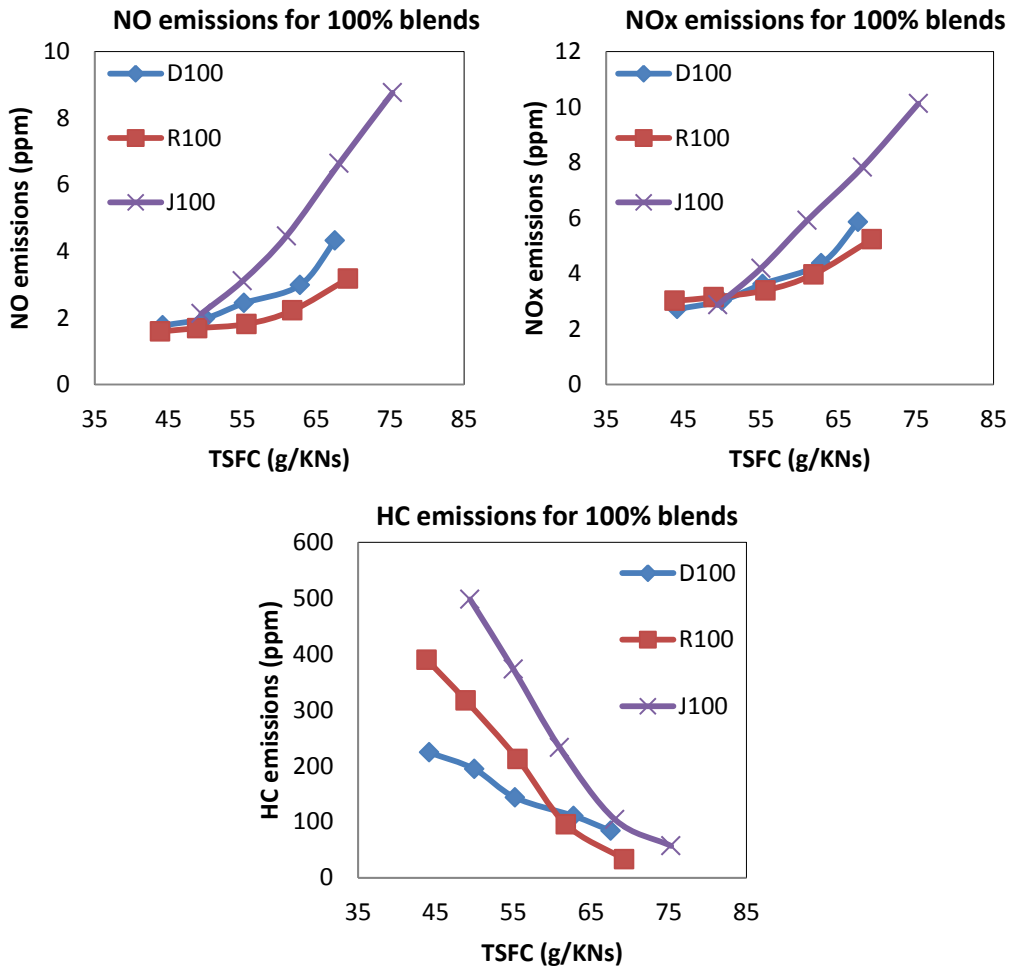

Figure 8.4. Comparison of some emissions from unblended fuels.

The HC emissions show an opposite trend with decreasing HC emissions as TSFC increases. This is as expected, as fuels will be burning more efficiently, allowing a more complete combustion process to occur. This will leave less partial and unburned hydrocarbons in the exhaust. Both pure biofuels show a larger amount of HC emission than diesel at lower TSFC values indicating that they do not burn as efficiently as diesel at lower engine speeds. At higher TSFC values however, the HC emissions drop right off to below that of diesel which shows that they actually burn better than diesel at higher engine speeds. This could be due to the higher temperatures, providing better evaporation of the injected fuel, as well as the higher oxygen content within the fuels, improving combustion. The pure JME fuel produces considerably more HC emissions than both diesel and RME, whilst the RME produces noticeably more than diesel at lower TSFC values.

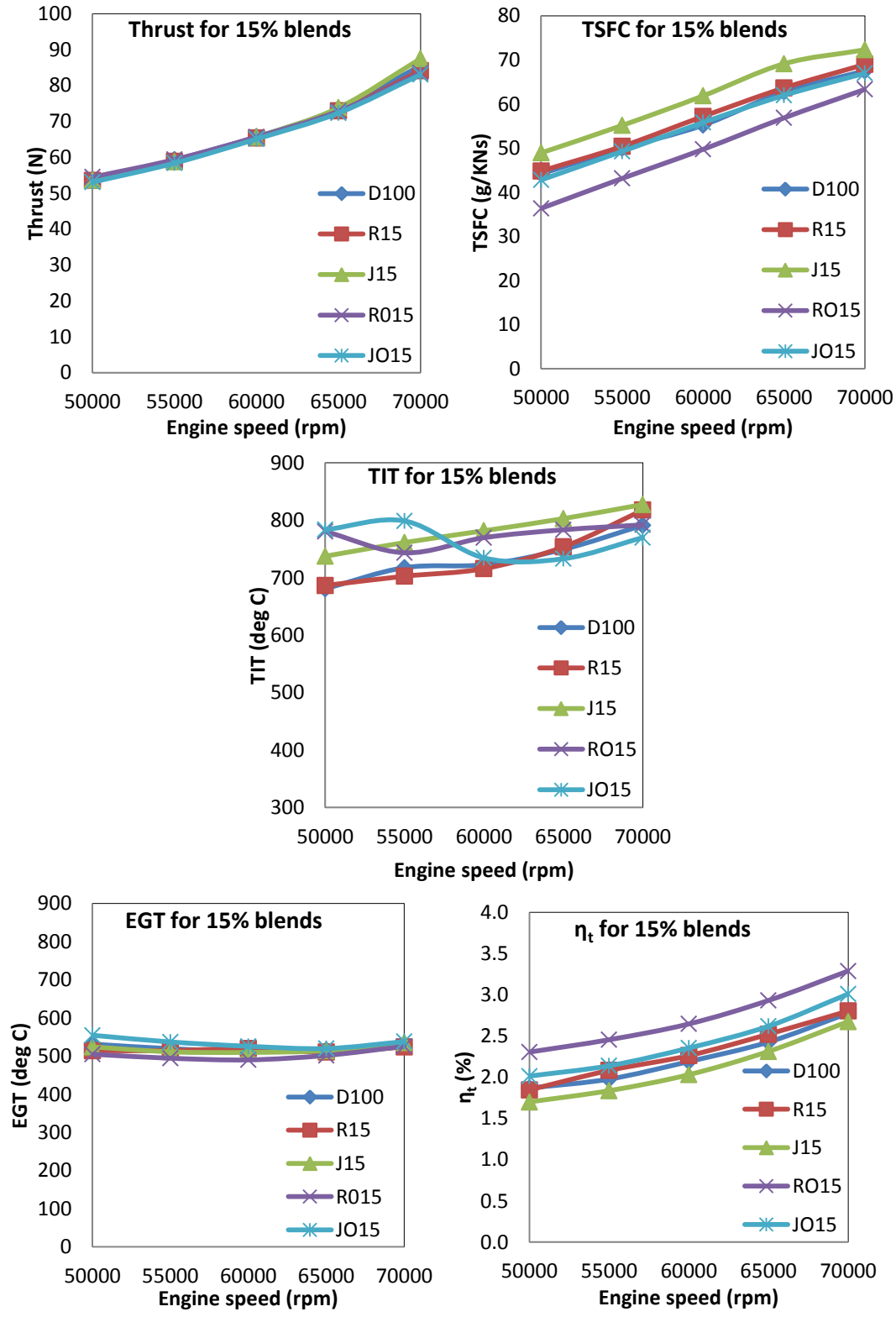

Figure 8.5. Comparison of gas turbine engine performance parameters for 15% blends.

8.3.2 15% biofuel-diesel blends

The results for comparison of 15% biofuel/85% diesel fuels are shown in Figure 8.5 and are again compared with neat diesel. There is no distinct change in thrust for any of the 15% fuel blends. R15 and JO15 are almost the same as diesel in TSFC, whereas J15 has a higher TSFC value. In contrast, RO15 has a lower TSFC value, showing that it requires less fuel to achieve a particular thrust, compared with diesel. Most 15% blends show the same correlation for TIT as discussed before apart from JO15 which appears to remain more or less constant with an increase in engine speed. R15 almost follows the same line as diesel, whereas J15 and RO15 have a higher TIT than diesel. There is no noticeable difference between EGT in the 15% blends. The thermal efficiency of diesel is, again followed closely by R15, JO15 is slightly higher than diesel and J15 is slightly lower. RO15 shows an obviously higher thermal efficiency than diesel, along with several other parameters, conveying a distinctly superior performance to diesel. This could be due to the differences between the fuels, such as composition, viscosity and calorific value.

The NO and NO_X emissions are shown in Figure 8.6 and are almost the same for diesel and all 15% blended fuels which is to be expected due to the relatively small fraction of biofuel content in them. The small difference that can be seen indicate that the biofuels have less NO and NO_X emissions than that of diesel at lower TSFC values. The HC emissions from diesel are also very similar to most of the biofuels; however a significant difference can be seen with RO15 producing somewhat less HC which means it undergoes more complete combustion than diesel.

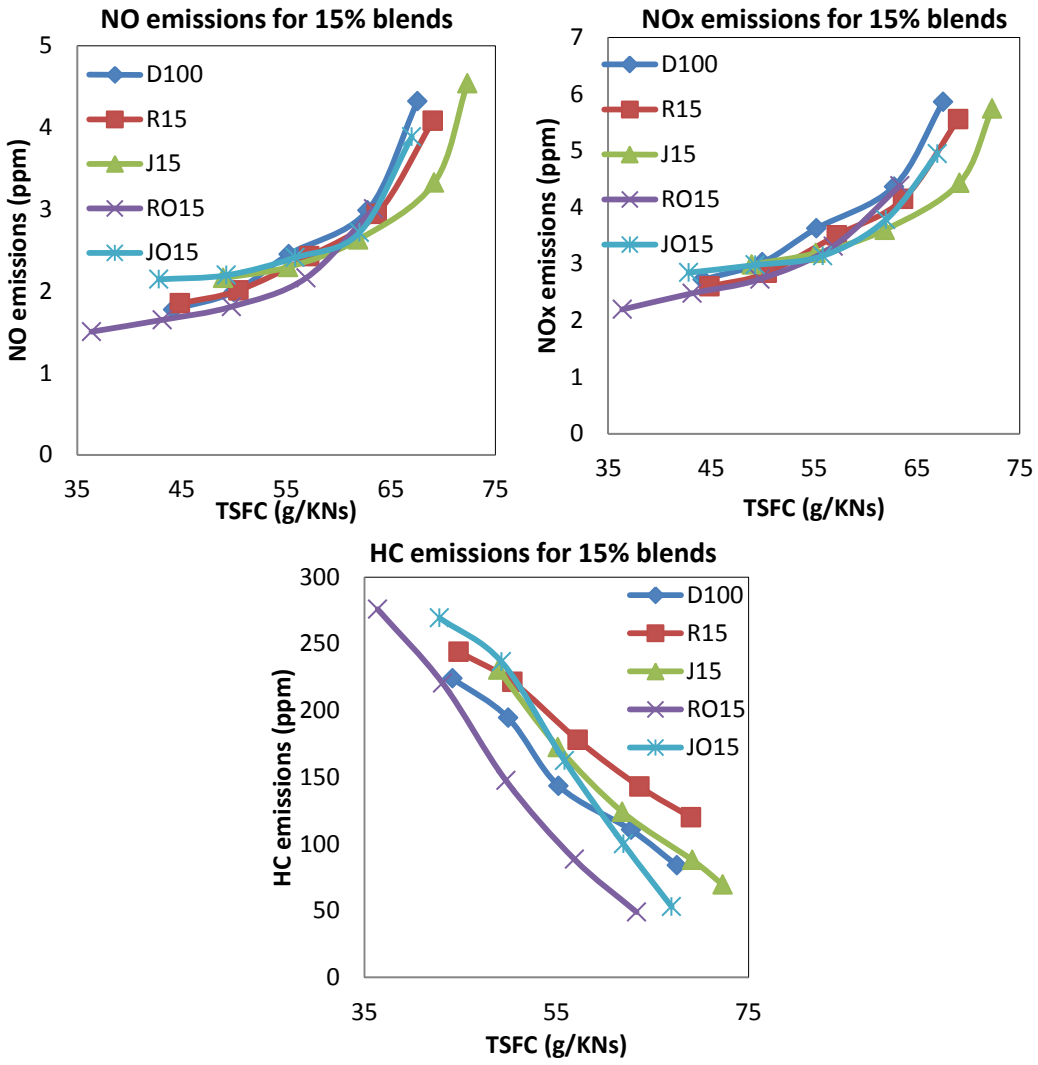

Figure 8.6. Comparison of some emissions from 15% blends.

8.3.3 RME-diesel blends

The results for comparison of RME/diesel blended fuels are shown in Figure 8.7 and are compared with neat diesel. The fuels are 100% diesel, 15% RME/85% diesel, 30% RME/70% diesel, 50% RME/50% diesel and 100% RME. Thrust and EGT remain the same for all RME blends and TSFC almost the same with no distinct differences between the fuels. As mentioned previously, R100 shows a markedly higher TIT and thermal efficiency than diesel. This does not occur for TIT over RME blends. This shows that there must have to be a considerable amount of RME in the mixture before any effects on TIT can be seen. It can be seen that the thermal

efficiency gradually increases with an increase in percentage RME in the fuels over all engine speeds.

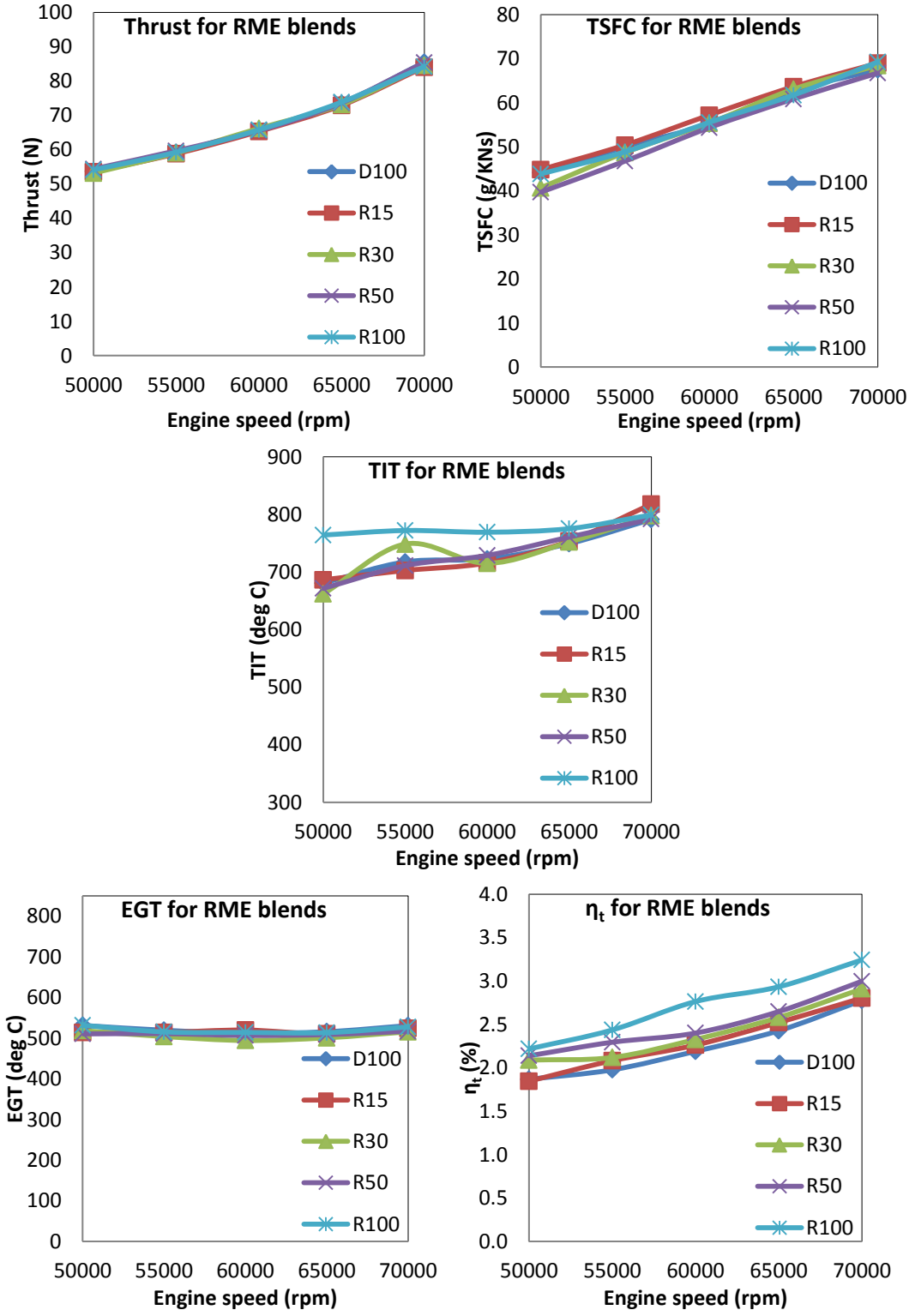

Figure 8.7. Comparison of gas turbine engine performance parameters for RME blends.

Figure 8.8 shows the emissions from RME blends. There is a noticeable difference between the NO and NO_x emissions of the different RME blends. R15 shows slightly lower NO and NO_x emissions than diesel, with somewhat less from R30 and R50. R30 appears to have less NO and NO_x emissions than R50 which cannot be explained at present, however the overall trend does suggest that RME blends are less offending polluters than diesel and the effect of RME may not become pertinent until a large fraction of RME makes up the total fuel content. The RME blends generally show higher HC emissions than diesel.

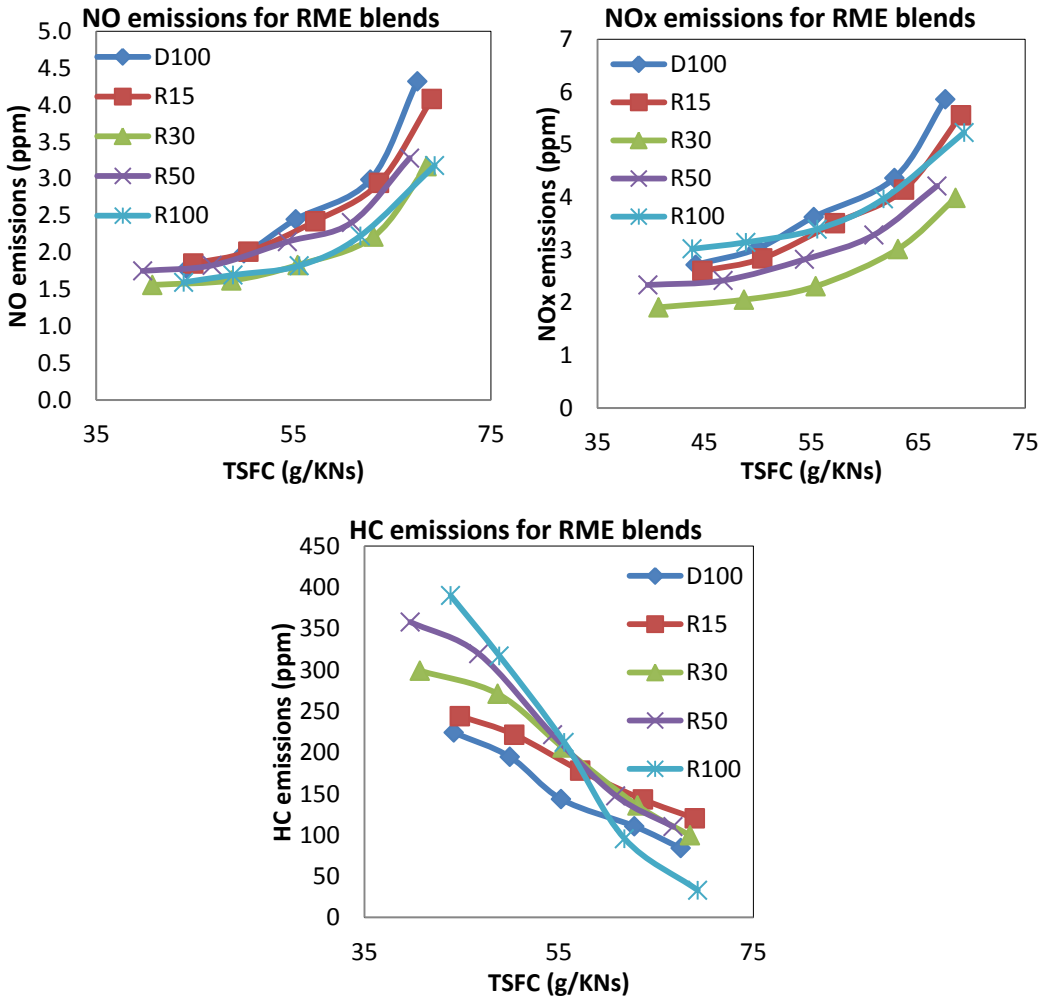

Figure 8.8. Comparison of some emissions from RME blends.

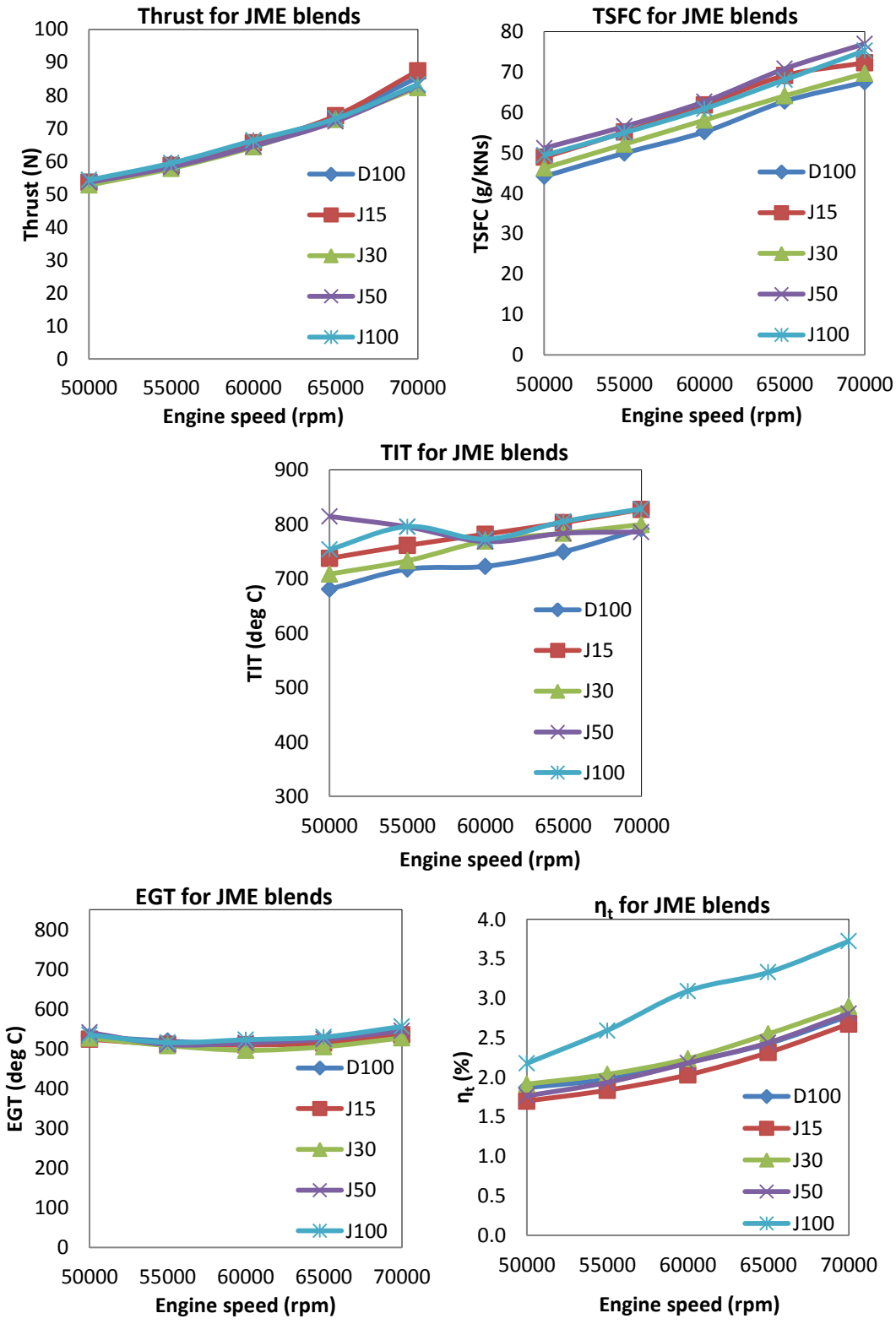

Figure 8.9. Comparison of gas turbine engine performance parameters for JME blends.

8.3.4 JME-diesel blends

The results for comparison of JME/diesel blended fuels are shown in Figure 8.9 and are compared with unblended diesel. The fuels are 100% diesel, 15% JME/85% diesel, 30% JME/70% diesel, 50% JME/50% diesel and 100% JME. The thrust and EGT remain the same regardless of the amount of JME in the fuel mixture. The TSFC does show some difference but no definite pattern; the JME blends have a slightly higher TSFC than diesel. The TIT also shows this. In contrast to the RME blends, the JME blends do not show a discernible difference in thermal efficiency until the 100% JME fuel, suggesting that a large fraction of the fuel mixture needs to be JME before the thermal efficiency is changed significantly.

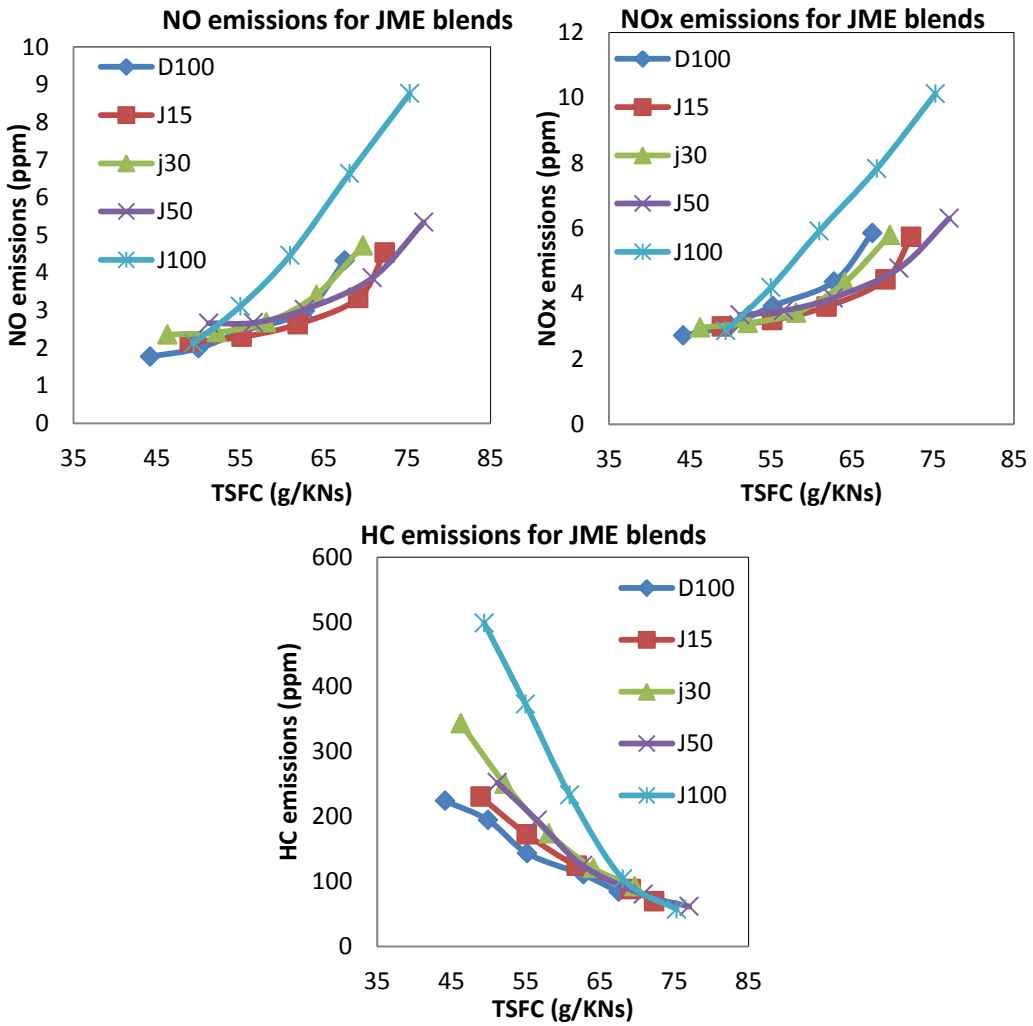

Figure 8.10. Comparison of some emissions from JME blends.

NO and NO_x emissions are almost equal for JME blends and diesel, as shown in Figure 8.10. Pure JME shows a dramatic increase towards higher TSFC values, as discussed previously which suggests a large amount of JME content is necessary to increase emissions a significant amount. The HC emissions show similar HC emissions at high TSFC values, but significantly different values at lower TSFC values. This suggests that the combustion process of JME mixtures becomes less and less complete at low engine speeds, as more JME is added to the mixture.

8.4 Conclusions

An increase in engine speed appears to increase TSFC, combusted gas temperature and thermal efficiency which, in turn produces more NO and NO_x emissions and less HC emissions, meaning a more complete combustion process is occurring. R100 performs equal to, or better than diesel in most parameters tested, especially at high engine speeds. J100 is better in some areas than others compared with diesel, it has higher thermal efficiency and more complete combustion at higher engine speeds, but is less fuel efficient and it produces more NO and NO_x emissions. RO15 performs better than diesel on most occasions. It is significantly more fuel efficient and thermally efficient, along with producing slightly less NO and NO_x emissions and considerably less HC emissions. Other 15% blends do not differ noticeably from the performance of diesel. Increasing RME content in diesel/RME blends generally increases the performance of the fuel. Thrust and fuel efficiency are very similar in all RME blends, whereas the thermal efficiency increases along with slightly lower NO and NO_x emissions as the fraction of RME in the mixture is increased. The effectiveness of combustion also increases at higher TSFCs and hence engine speeds for fuels with a higher percentage of RME. JME blends seem to have both up and down sides to them. They produce much more NO and NO_x emissions at high engine speeds. However the combustion process is much more efficient at these speeds. The performance factors are generally the same for all JME blends and diesel and a significant jump in thermal efficiency occurs for pure JME, suggesting high levels of JME in the mixtures may produce more thermally efficient fuels.

Rapeseed methyl ester shows the best characteristics out of the pure fuels tested and the results suggest that high percentage RME-diesel blends would perform excellently. Most 15% blends do not make much difference in the performance of diesel apart from the 15% rapeseed oil blend which rises above the rest. If a higher percentage RO-diesel blend could be tested, this could potentially be the best candidate for a biofuel-diesel blend out of all fuels used herein. Emission characteristics of RME blends are superior to that of diesel, whereas JME blends produce more nitrogen oxides. The fact that most parameters tested with these biofuels and their diesel blends are either equal to or better than that of standard diesel shows promise for these types of fuels as fossil fuel alternatives.

CHAPTER 9
CONCLUSIONS AND FUTURE WORK

9.1 Introduction

The main findings and final remarks for the various parts of this investigation have been summarised in this chapter, concluding the individual investigations and connecting the findings to real world solutions and recommendations for future work. Section 9.2 includes the concluding remarks from the gas phase LIP in heated turbulent jets study. The investigation into the suitability of YAG:Dy and BAM for flame thermometry methods is discussed in Section 9.3. Section 9.4 includes the work looking into the dilution effects on soot in gaseous fuel flames. The investigation into biodiesel composition effects on soot is concluded in Section 9.5 and the gas turbine engine pilot study in Section 9.6.

9.2 Gas phase LIP in heated turbulent jets using YAG:Dy and BAM

Planar laser induced phosphorescence was used in conjunction with thermographic phosphors BAM and YAG:Dy to determine the temperature distribution of heated jets with different Reynolds numbers and at a range of temperatures. YAG:Dy conveyed no appreciable phosphorescence signal at 2.5 µm diameter when seeded within the gas flow, however larger 10.2 µm YAG:Dy particles did produce a high enough signal for gas phase temperature measurements. The 2.9 µm BAM particles produced a higher phosphorescence signal yield, compared with both 2.5 and 10.2 µm YAG:Dy particle diameters, therefore single shot results with high SNR were acquired using BAM, but not with YAG:Dy. Both phosphors could be used to express time averaged temperature distributions, due to an increase in signal to noise ratio that could be achieved by accumulating images.

The YAG:Dy and BAM phosphorescence signal strengths are shown to decrease with an increase in temperature and diminish around 1300 K and 1100 K respectively, where BAM only shows temperature sensitivity up to 875 K. The phosphorescence lifetimes at room temperature are shown to be approximately 1.1 ms for YAG:Dy and 2.5 µs for BAM.

The high emission intensity produced by BAM allowed for detailed jet temperature distributions to be made at various temperatures up to 850 K, displaying a large portion of the jet, up to 90 mm above the nozzle exit. The fact that BAM phosphorescence emission intensity is high at short gating times of around 1 µs means that it is capable of detecting the flow structure at this characteristic time scale in the jet. Raw images at 300 K show the intensity ratio is almost homogeneous despite phosphorescence signal inhomogeneity. Near nozzle time averaged images were produced for both of the phosphors, where the spatial temperature distributions are clearly defined and the characteristics of different jets were identified.

The precision and uncertainty of the experiment were investigated, where the standard deviation of the results at 300 K was 8.6 K (2.8 %), increasing up to 49.8 K

(5.9 %) at 850 K, showing a decrease in precision and increase in uncertainty with an increase in temperature. The largest calculated error for BAM was 3.1 % and for YAG:Dy 10.1 %, where the discrepancy is likely to be due to the larger sized YAG:Dy particles and hence, longer response times. BAM is suitable for turbulent flow situations, whereas YAG:Dy displays less sensitivity within the temperature range in this study and a slower response time to temperature changes.

9.3 Suitability of YAG:Dy and BAM for flame thermometry measurements

YAG:Dy and BAM were used to measure flame temperatures in conjunction with the gas phase laser induced phosphorescence technique. The results showed that the thermographic phosphor thermometry technique carried out in flames in this way, using the TPs YAG:Dy and BAM, may not be suitable for combustion temperature measurements. Due to the particular properties of the TPs used in this study, measurements of the high temperature regions of the flames were inaccurate. Thermocouple measurements were also carried out for a comparison, revealing that the lower temperature regions produced fairly accurate results, within approximately 40 K, which is less than 7.5 % at 600 K.

In order to improve on the results acquired in this study, a thermographic phosphor should be used that produces a higher phosphorescence intensity at flame temperatures, compared with YAG:Dy and BAM. Furthermore the temperature response time of the TP must be high enough to reach combustion temperatures within the residence time inside the flame. The diameter of the TPs should therefore be less than 3 µm. It is possible that other so called high temperature TPs would provide a more accurate temperature distribution in flames, compared with the phosphors used in this work. TPs including Y_2O_3:Eu, $LuPO_4$:Dy, Y_2O_2S:Sm and various YAG based phosphors are all good candidates (Bosze, et al., 2011; Feist & Heyes, 2000; Cates, et al., 2003; Heyes, 2009).

9.4 Dilution and hydrogen addition effects on soot emissions

Planar two colour laser induced incandescence (LII) was used to determine the soot volume fraction (SVF) distributions in propane laminar diffusion flames. The flames were diluted with nitrogen, carbon dioxide or hydrogen, as well as a combination of either hydrogen and nitrogen or hydrogen and carbon dioxide, in order to investigate how the SVF was influenced by the dilution effects of the gases added. The LII technique used was proven to be robust as it produced very similar SVF results for both wavelengths (415 and 632 nm). The maximum average error, out of all of the flames used in this study was determined to be 4.5 %, where the shot to shot fluctuations were taken into account over 50 single shot images for each flame height measurement in each flame.

As nitrogen was added to the propane diffusion flame the luminous envelope of the flame decreased in size, where the distance between the formation of the luminous envelope and the burner exit increased, reducing the luminous area and as a result, increased the size of the blue part of the flame. The SVF was also found to decrease as nitrogen was added, which was mainly due to inert and thermal dilution effects. The SVF was reduced to a greater extent with carbon dioxide dilution, due to the added chemical dilution effects due to the dissociation of CO_2 at high temperatures, increasing oxidising potential, as well as enhanced soot reduction due to thermal effects, compared with nitrogen. Adding hydrogen produced a negligible reduction in soot due to dilution effects. This could be due to different dilution effects having opposite effects on soot formation, causing negligible net soot production. The chemical effects of hydrogen were determined to be negligible due to propane already having a relatively large amount of hydrogen present. When using hydrogen combined with either carbon dioxide or nitrogen, SVF reduction seems to occur due to cumulative dilution effects of both diluents.

9.5 Biodiesel composition effects on soot and emissions

Planar two colour LII was also used to determine SVF distributions in biodiesel and diesel flames in order to relate the SVF to fuel composition. In order to accurately determine the individual fuel composition, gas chromatography (GC) was applied to the biodiesel fuels, identifying the major ester components. Biodiesels tested in this investigation were RME, FEE, CME, SME, TME and UCOME, where UCOME would not produce a flame in the wick burner due to its relatively high viscosity. The wick interfered with LII measurements in lower parts of the liquid fuel flames and therefore areas that matched in height with the wick were omitted from the analysis. Despite this, a wick burner was still considered to be superior for this type of study, compared with other types of burners, such as burners using a vaporiser chamber. A vaporiser may evaporate lighter fuel molecules more readily than heavier ones, leading to erroneous SVF results.

The oxygen content of diesel was increased by mixing varying amounts of oxygenate by weight. The SVF was shown to decrease with increasing amounts of oxygen content. RME-diesel blends were then mixed by weight and the oxygen percentage of each mixture was calculated. The SVF was shown to decrease by an increased amount, compared with the oxygenate mixtures, revealing that other changes in composition must be causing a further reduction. It was deduced that the replacement of aromatic content in the diesel, as RME percentage was increased, with olefins which make up almost all of the RME fuel, is likely to be the cause of the extra reduction in SVF. This is because olefins produce less soot than aromatics. Due to differences in composition, the SVF results showed that diesel was sootier than the biodiesels. The GC results also allowed the composition of the biodiesels to be compared with each other and the fuels could then be ranked in terms of sooting tendency, with respect to their composition. Fuels such as RME and SME were found to produce larger amounts of soot due to their high degree of unsaturation and higher percentage of longer chain methyl ester molecules. FEE was also found to be one of the sootiest biodiesels due to the fact that it contained ethyl esters instead of methyl esters, despite the fact that it was composed of a larger percentage of

saturated molecules. TME was determined as the second to least sooting biodiesel, due to containing a relatively low amount of unsaturated molecules, compared with RME and SME. Finally, CME was the least sooting biodiesel due to its high degree of shorter, more saturated methyl ester molecules.

The amount of soot produced by a particular fuel could be used a measure of its quality and therefore, shorter chain molecules, with a higher degree of saturation and oxygen percentage should be used. The FEE used in this study was modified to remove its omega three oils, of which most were longer, highly saturated molecules. This would have made the fuel produce less soot and if it was a methyl ester, would most likely have been placed as the second to least sooting fuel, after TME. Genetic modification of crops could also lead to a similar result, where highly unsaturated fuels could potentially become more saturated, thereby reducing their sooting tendency. Future work into biodiesels should be focused on shorter chain and highly saturated composition fuels, as these fuels would help reduce emissions in a better way than longer, unsaturated fuels.

9.6 Gas turbine engine pilot study

Gaseous emissions testing was carried out on an SR-30 gas turbine engine using diesel, biofuels and diesel-biofuel blends, in order to investigate the effects that biofuels had on engine performance parameters as well as emissions. The main conclusions drawn from the pilot study have already been discussed in the previous chapter, where it was found that generally, biofuels and biofuel-diesel blends compare well with diesel in both emissions and performance. The main aim of the study was to prove the effectiveness of biofuels in practical applications in order to link the fundamental knowledge gained from the main investigation to real life situations. Not only do biofuels generally produce less soot and gaseous emissions, compared with widely available commercial fuels, such as diesel, but they are also often equal or better in practical engine performance. This study demonstrates that present technology can cope with using biofuels in laboratory controlled conditions

and therefore the jump to using biofuels for conventional uses worldwide as a short term solution to climate change and fossil fuel shortages is possible.

References

Abián, M., Millera, A., Bilbao, R. & Alzueta, M., 2012. Experimental study on the effect of different CO2 concentrations on soot and gas products from ethylene thermal decomposition. *Fuel,* Volume 91, pp. 307 - 312.

Abram, C., Fond, B., Heyes, A. L. & Beyrau, F., 2013. High-speed planar thermometry and velocimetry using thermographic phosphor particles. *Applied Physics B,* Volume 111, pp. 155 - 160.

Ackman, R. G., 2005. Bailey's Industrial Oil and Fat Products 6th Edition. In: F. Shahidi, ed. *Speciality Oils and Oil Products.* s.l.:Wiley, p. 288.

Agarwal, A. K., 2007. Biofuels (alcohols and biodiesel) applications as fuels for internal combustion engines. *Progress in Energy and Combustion Science,* Volume 33, pp. 233 - 271.

Agrawal, A., Sreenivas, K. R. & Prasad, A. K., 2004. Velocity and temperature measurements in an axisymmetric turbulent jet with cloud-like off-source heating. *International Journal of Heat and Mass Transfer,* Volume 47, p. 1433–1444.

Aldén, M., Omrane, A., Richter, M. & Sarner, G., 2011. Thermographic phosphors for thermometry: A survey of combustion applications. *Progress in Energy and Combustion Science,* Volume 37, pp. 422 - 461.

Allison, S. W. & Gilles, G. T., 1997. Remote thermometry with thermographic phosphors: Instrumentation and applications. *Rev. Sci. Instrum.,* 68(7), pp. 2615 - 2650.

Analysis Automation Limited, 1990. *Instrument specification AAL model 443 NO/NOx chemiluminescent analyser.* s.l.:s.n.

Analysis Automation Limited, 1990. *Instrument specification AAL model 523 FID hydrocarbon analyser*. s.l.:s.n.

Andor Technology Limited, 1999. *A User's Guide To Andor ICCDs, Version 2B.* s.l.:s.n.

Axelbaum, R. L. & Law, C. K., 1990. Soot formation and inert addition in diffusion flames. *Twenty-Third Symposium (International) on Combustion,* pp. 1527-1523.

Basile, G. et al., 2002. Coagulation and Carbonisation processes in slightly sooting premixed flames. *Proceedings of the Combustion Institute, Vol 29,* pp. 2391 - 2397.

Bizarri, G. & Moine, B., 2005. On BaMgAl10O17:Eu2+ phosphor degradation mechanism: Thermal treatment effects. *Journal of Luminescence,* Volume 113, pp. 199 - 213.

Borjesson, P. & Tufvesson, L. M., 2011. Agricultural crop-based biofuels-resource efficiency and environmental performance including direct land use changes. *Journal of Cleaner Production,* pp. 108 - 120.

Bosze, E. J., Hirata, G. A. & McKittrick, J., 2011. An analysis of Y2O3:Eu3+ thin films forthermographic phosphor applications. *Journal of Luminescence*, Volume 131, pp. 41 - 48.

Bougie, B. et al., 2007. Soot particulate size characterization in a heavy-duty diesel engine for different engine loads by laser-induced incandescence. *Proceedings of the Combustion Institute*, Volume 31, pp. 685 - 691.

Brackmann, C., Nygren, J., Bai, X. & Li, Z., 2003. Laser-induced fluorescence of formaldehyde in combustion using third harmonic Nd:YAG laser excitation. *Spectrometer Acta Part A 59,* pp. 3347 - 3356.

Britaine, R. & Lutalado, N., 2010. Jatropha: A smallholder bioenergy crop. The potential for Pro-poor development. *Integrated crop management Vol. 8.*

Brubach, J., Patt, A. & Dreizler, A., 2006. Spray thermometry using thermographic phosphors. *Applied Physics B,* Volume 83, pp. 499 - 502.

Brubach, J., Pflitsch, C., Dreizler, A. & Atakan, B., 2013. On surface temperature measurements with thermographic phosphors: A review. *Progress in Energy and Combustion Science,* Volume 39, pp. 37 - 60.

Brundage, A. L. et al., 2011. Thermocouple Response in Fires, Part 1: Considerations in Flame Temperature Measurements by a Thermocouple. *Journal of Fire Sciences,* Volume 29, pp. 195 - 211.

Caslavsky, J. L. & Viechnicki, D. J., 1980. Melting behaviour and metastability of yttrium aluminium garnet (YAG) and YAlO3 determined by optical differential thermal analysis. *Journal of Materials Science,* Volume 15, pp. 1709 - 1718.

Cates, M. R., Allison, S. W., Jaiswal, S. L. & Beshears, D. L., 2003. *YAG:Dy and YAG:Tm Fluorescence To 1700 C.* Orlando, Florida, s.n.

Collis, D. C. & Williams, M. J., 1959. Two dimensional convection from heated wires at low reynolds numbers. *Journal of Fluid Mechanics,* 6(3), pp. 357 - 384.

Crosland, B. M., Johnson, M. R. & Thomson, K. A., 2011. Analysis of uncertainties in instaneous soot volume fraction measurements using two-dimensional, auto-compensating, laser-induced incandescence (2D-AC-LII). *Applied Physics B,* Volume 102, pp. 173 - 183.

Curran, H., Gaffuri, P., Pitz, W. & Westbrook, C., 1998. A Comprehensive Modeling Study of n-Heptane Oxidation. *Combustion and Flame,* 114(1 - 2), pp. 149 - 177.

D'Alessio, A. et al., 2000. On the relevance of surface growth in soot formation in premixed flames. *Proceedings of the Combustion Institute, Volume 28,* pp. 2547 - 2554.

D'Anna, A., 2009. Combustion formed nanoparticles. *Proceedings of the Combustion Institute,* pp. 593 - 613.

D'Anna, A. et al., 2009. Particle formation in opposed-flow diffusion flames of ethylene: An experimental and numerical study. *Proceedings of the Combustion Institute 32,* pp. 793 - 801.

D'Anna, A. & Kent, J. H., 2008. A model of Particulate and species formation applied to laminar, non-premixed flames for three aliphatic-hydrocarbon fuels. *Combustion and Flame 152,* pp. 573 - 587.

D'Anna, A. et al., 2005. Nano-organic carbon and soot particle measurements in a laminar ethylene diffusion flame. *Proceedings of the Combustion Institute,* Volume 30, pp. 1449-1456.

D'Anna, A. & Violi, A., 1998. A kinetic model for the formation of aromatic hydrocarbons in premixed laminar flames. *Twenty-Seventh Symposium (International) on Combustion/The Combustion Institute,* p. 425 – 433.

D'Anna, A., Violi, A., D'Alessio, A. & Sarofim, A. F., 2001. A reaction pathway for nanoparticle formation in rich premixed flames. *Combustion and Flame 127,* pp. 1995 - 2003.

De Iuliis, S. et al., 1998. Determination of the Soot Volume Fraction in an Ethylene Diffusion Flame by Multiwavelength Analysis of Soot Radiation. *Combustion and Flame,* Volume 115, pp. 253 - 261.

Dobbins, R. A. & Megaridis, C. M., 1987. Morphology of Flame-Generated Soot As Determined by Thermophoretic Sampling. *Langmuir*, 3(2), p. 254 – 259.

Dockery, D. W. et al., 1993. An association between air pollution and mortality in six U.S. cities. *The New England Journal of Medicine*, 329(24), pp. 1753 - 1759.

Eldridge, J. I., Bencic, T. J., Allison, S. W. & Beshears, D. L., 2004. Depth-Penetrating Temperature Measurements of Thermal Barrier Coatings Incorporating Thermographic Phosphors. *Journal of Thermal Spray Technology*, 13(1), pp. 44 - 50.

Feist, J. P. & Heyes, A. L., 2000. The characterization of Y2O2S:Sm powder as a thermographic phosphor for high temperature applications. *Meas. Sci. Technol.*, Volume 11, pp. 942 - 947.

Feist, J. P., Heyes, A. L. & Seedfelt, S., 2002. Thermographic phosphors for gas turbine instrumentation development and measurement uncertainties. *Proceedings of the 11th International Symposium on Applications of Laser Techniques to Fluid Mechanics*, p. 18.

Flagan, R. C. & Seinfeld, J. H., 1988. Fundamentals of air pollution engineering, Chapter 2. Combustion fundamentals. In: New Jersey: Prentice Hall, Inc., pp. 59 - 67.

Flower, W. L., 1985. Laser diagnostic techniques used to measure soot formation. *Applied Optics*, 24(8), p. 1101.

Fond, B. et al., 2012. Simultaneous temperature, mixture fraction and velocity imaging in turbulent flows using thermographic phosphor tracer particles. *Optics Express*, 20(20), pp. 22118 - 22133.

Fuhrmann, N., Brubach, J. & Dreizler, A., 2013. Phosphor Thermometry: A comparson of the luminescence lifetime and the intensity ratio approach. *Proceedings of the Combustion Institute,* Volume 34, pp. 3611 - 3618.

Fuhrmann, N. et al., 2012. Two-dimensional cycle-resolved exhaust valve temperature measurements in an optically accessible internal combustion engine using thermographic phosphors. *Applied Physics B,* Volume 106, pp. 945 - 951.

Garner, S., Sivaramakrishnan, R. & Brezinsky, K., 2009. The high-pressure pyrolysis of saturated and unsaturated C7 hydrocarbons. *Proceedings of the Combustion Institute,* Volume 32, pp. 461 - 467.

Ginnings, D. C. & Furukawa, G. T., 1953. Heat capacity standards for the range 14 to 1200 K. *J. Am. Chem. Soc.*, 75(3), pp. 522-527.

Glassman, I., 1988. Soot formation in combustion processes. *Twenty-Second Symposium (International) on Combustion,* pp. 295 - 311.

Glassman, I., 1996. *Combustion, 3rd edition.* s.l.:Elsevier.

Glassman, I., 1996. Environmental combustion considerations. In: *Combustion 3rd edition.* s.l.:Academic Press.

Glassman, I., 1998. Sooting laminar diffusion flames: Effect of dilution, additives, pressure and microgravity. *Twenty-Seventh Symposium (International) on Combustion/The Combustion Institute,* pp. 1589 - 1596.

Glassman, I. & Yaccarino, P., 1981. The temperature effect in sooting diffusion flames. *Eighteenth Symposium (International) on Combustion,* 18(1), pp. 1175 - 1183.

Goss, L. P., Smith, A. A. & Post, M. E., 1989. Surface thermometry by laser-induced fluorescence. *Rev. Sci. Instrum.,* 60(12), pp. 3702 - 3706.

Graboski, M. S. & McCormick, R. L., 1998. Combustion of fat and vegetable oil derived fuelsin diesel engines. *Progress in Energy Combustion Science, Vol. 24,* pp. 125 - 164.

Gulder, O. L., Snelling, D. R. & Sawchuk, R. A., 1996. Influence of hydrogen addition to fuel on temperature field and soot formation in diffusion flames. *Twenty-Sixth Symposium (International) on Combustion,* p. 2351–2358.

Habib, Z., Parthasarathy, R. & Gollahalli, S., 2010. Performance and emission characteristics of biofuel in a small-scale gas turbine engine.. *Applied energy 87,* pp. 1701 - 1709.

Hakka, M. H., Glaude, P.-A., Herbinet, O. & Battin-Leclerc, F., 2009. Experimental study of the oxidation of large surrogates for diesel and biodiesel fuels. *Combustion and Flame,* Volume 156, pp. 2129 - 2144.

Harrington, J. E. & C. Smyth, K., 1993. Laser induced fluorescence measurements of formaldehyde in a methane/air diffusion flame. *Chemical Physics Letters, Vol 202, No. 3 - 4,* pp. 196 - 202.

Hartzell, G. E., 1996. Overview of Combustion Toxicology. *Toxicology,* Volume 115, pp. 7 - 23.

Hasegawa, R. et al., 2007 a. Two-dimensional gas-phase temperature measurements using phosphor thermometry. *Applied Physics B,* Volume 88, pp. 291 - 296.

Hasegawa, R. et al., 2007 b. Two-Dimensional Temperature Measurements in Engine Combustion Using Phosphor Thermometry. *SAE Paper,* Volume Paper number 2007-01-1883, pp. 1797 - 1803.

Haynes, B. S. & Wagner, H. G., 1981. Soot formation. *Progress in Energy and Combustion Science,* Volume 7, pp. 229 - 273.

Heyes, A. L., 2009. On the design of phosphors for high-temperature thermometry. *Journal of Luminescence,* Volume 129, pp. 2004 - 2009.

Hoekman, S. K. et al., 2012. Review of biodiesel composition, properties, and specifications. *Renewable and Sustainable Energy Reviews,* Volume 16, pp. 143 - 169.

Hofeldt, D. L., 1993. Real-Time Soot Concentration Measurement Technique for Engine Exhaust Streams. *SAE Technical Paper 930079.*

Hofmann, M., Bessler, W. G., Schulz, C. & Jander, H., 2003. Laser-Induced Incandescence for Soot Diagnostics at High Pressures. *Applied Optics,* 42(12), pp. 2052 - 2062.

Jovicic, G., Zigan, L., Pfadler, S. & Leipertz, A., 2012. *Simultaneous Two-dimensional Temperature and Velocity Measurements in a Gas Flow Applying Thermographic Phosphors.* Lisbon, Portugal, s.n.

Justel, T., Bechtel, H., Mayr, W. & Wiechert, D. U., 2003. Blue emitting BaMgAl10O17:Eu with a blue body color. *Journal of Luminescence,* Volume 104, pp. 137 - 143.

Kennedy, I. M., 2007. The health effects of combustion-generated aerosols. *Proceedings of the Combustion Institute,* Volume 31, pp. 2757 - 2770.

Kim, H.-J.et al., 2004. Transesterification of vegetable oil to biodiesel using heterogeneous base catalyst. *Catalysis Today,* Volume 93 - 95, pp. 315 - 320.

Kim, K.-B., Koo, K.-W., Cho, T.-Y. & Chun, H.-G., 2003. Effect of heat treatment on photoluminescence behaviour of BaMgAl10O17:Eu phosphors. *Materials Chemistry and Physics,* Volume 80, pp. 682 - 689.

Knothe, G., Dunn, R. O. & Bagby, M. O., 1997. The use of vegetable oils and their derivatives as alternative diesel fuels. In: *Fuels and chemicals from biomass.* s.l.:American chemical society.

Kobayashi, Y., Furuhata, T., Amagai, K. & Arai, M., 2008. Soot precursor measurements in benzene and hexane diffusion flames. *Combustion and Flame,* Volume 154, pp. 346 - 355.

Koechner, W., 2006. Solid-state laser engineering, 6th edition. In: s.l.:Springer science and business media inc., p. 55.

Köhler, M. et al., 2011. Sooting turbulent jet flame: characterization and quantitative soot measurements. *Applied Physics B,* Volume 104, pp. 409 - 425.

Kohse-Höinghaus, K. et al., 2010. Biofuel combustion chemistry: from ethanol to biodiesel. *Angewandte Chemie International Edition,* 49(21), pp. 3572 - 3597.

Labecki, L. & Ganippa, L., 2012. Effects of injection parameters and EGR on combustion and emission characteristics of rapeseed oil and its blends in diesel engines. *Fuel,* Volume 98, pp. 15 - 28.

Labecki, L. et al., 2013. Effects of injection parameters and EGR on exhaust soot particle number-size distribution for diesel and RME fuels in HSDI engines. *Fuel,* Volume 112, pp. 224 - 235.

Ladommatos, N., Abdelhalim, S. M., Zhao, H. & Hu, Z., 1996. The Dilution, Chemical, and Thermal Effects of Exhaust Gas Recirculation on Diesel Engine Emissions - Part 2: Effects of Carbon Dioxide. *SAE Technical Paper 961167.*

Ladommatos, N., Rubenstein, P. & Bennett, P., 1996. Some effects of molecular structure of single hydrocarbons on sooting tendency. *Fuel,* 75(2), pp. 114 - 124.

Ladommatos, N. & Zhao, H., 1994. A Guide to Measurement of Flame Temperature and Soot Concentration in Diesel Engines Using the Two-Colour Method Part 2: Implementation. *SAE Technical Paper 941957.*

Ladommatos, N. & Zhao, H., 1994. A Guide to Measurement of Flame Temperature and Soot Concentration in Diesel Engines Using the Two-Colour Method Part I: Principles. *SAE Technical Paper 941956.*

Lahaye, J., Boehm, S., Chambrion, P. & Ehrburger, P., 1996. Influence of cerium oxide on the formation and oxidation of soot. *Combustion and Flame,* Volume 104, pp. 1996 - 2007.

Lai, J. Y., Lin, K. C. & Violi, A., 2011. Biodiesel combustion: Advances in chemical kinetic modeling. *Progress in Energy and Combustion Science,* Volume 37, pp. 1 - 14.

Law, C. K., 2007. Combustion at a crossroads: Status and prospects. *Proceedings of the Combustion Institute,* Volume 31, pp. 1 - 29.

Lawrence, M., Zhao, H. & Ganippa, L., 2013. Gas phase thermometry of hot turbulent jets using laser induced phosphorescence. *Optics Express,* 21(10), pp. 12260 - 12281.

Lemoine, F., Antoine, Y., Wolff, M. & Lebouche, M., 1999. Simultaneous temperature and 2D velocity measurements in a turbulent heated jet using combined laser-induced fluorescence and LDA. *Experiments in Fluids,* Volume 26, pp. 315-323.

Lerner, J. M., 2006. Imaging Spectrometer Fundamentals for Researchers in the Biosciences–A Tutorial. *Cytometry Part A,* Volume 69A, p. 712–734.

Lindén, J., Knappe, C., Richter, M. & Aldén, M., 2012. Precision in 2D temperature measurements using the thermographic phosphor BAM. *Measurement Science and Technology,* Volume 23.

Lindén, J. et al., 2009. Investigation of potential laser-induced heating effects when using thermographic phosphors for gas-phase thermometry. *Applied Physics B,* Volume 96, pp. 237 - 240.

Liu, F., Guo, H., Smallwood, G. J. & Gulder, O. L., 2001. The Chemical Effects of Carbon Dioxide as an Additive in an Ethylene Diffusion Flame: Implications for Soot and NOx Formation. *Combustion and Flame,* Volume 125, pp. 778 - 787.

Love, N. D., Parthasarathy, R. N. & Gollahalli, S. R., 2009. Rapid Characterization of Radiation and Pollutant Emissions of Biodiesel and Hydrocarbon Liquid Fuels. *Journal of Energy Resources Technology,* 131(1), pp. 1 - 9.

Marrero, T. R. & Mason, E. A., 1972. Gaseous diffusion coefficients. *J. Phys. Chem. Ref. Data,* 1(1).

Martin, M. & Eklund, M., 2011. Improving the environmental performance of biofuels with industrial symbiosis. *Biomass and Bioenergy,* pp. 1747 - 1755.

McEnally, C. S. & Pfefferle, L. D., 2004. Experimental study of fuel decomposition and hydrocarbon growth processes for cyclohexane and related compounds in nonpremixed flames. *Combustion and Flame,* Volume 136, pp. 155 - 167.

McEnally, C. S. & Pfefferle, L. D., 2005. Decomposition and hydrocarbon growth processes for hexenes in non-premixed flames. *Combustion and Flame,* Volume 143, pp. 246 - 263.

McEnally, C. S. & Pfefferle, L. D., 2005. Fuel decomposition and hydrocarbon growth processes for substituted cyclohexanes and for alkenes in nonpremixed flames. *Proceedings of the Combustion Institute,* Volume 30, pp. 1425 - 1432.

McEnally, C. S., Pfefferle, L. D., Atakan, B. & Kohse-Hoinghaus, K., 2006. Studies of aromatic hydrocarbon formation mechanisms in flames: Progress towards closing the gap. *Progress in Energy and Combustion Science,* Volume 32, pp. 247 - 294.

Melling, A., 1997. Tracer particles and seeding for particle image velocimetry. *Measurement Science and Technology,* Volume 8, pp. 1406 - 1416.

Menkiel, B. et al., 2012. Measurement of in-cylinder soot particles and their distribution in an optical HSDI diesel engine using time resolved laser induced incandescence (TR-LII). *Combustion and Flame 159,* Volume 159, pp. 2985 - 2998.

Merchan-Merchan, W., Sanmiguel, S. G. & McCollam, S., 2012. Analysis of soot particles derived from biodiesels and diesel fuel air-flames. *Fuel ,* Volume 102, p. 525 535.

Miller, J. A. & Melius, C. F., 1992. Kinetic and Thermodynamic Issues in the Formation of Aromatic Compounds in Flames of Aliphatic Fuels. *Combustion and Flame,* Volume 91, pp. 21-39.

Milliken, R. C., 1962. Non-equilibrium soot formation in premixed flames. *The Journal of Physical Chemistry,* 66(5), p. 794 – 799.

Naik, C. et al., 2011. Detailed chemical kinetic reaction mechanism for biodiesel components methyl stearate and methyl oleate. *Proceedings of the Combustion Institute,* Volume 33, pp. 383 - 389.

Nara, S. & Ibuki, S., 2006. Fundamentals of Luminescence. In: *Phosphor Handbook 2nd edition.* s.l.:Taylor and Francis Group.

Noel, B. W. et al., 1991. Evaluating thermographic phosphors in an operating turbine engine. *J. Eng. Gas Turbines Power,* 113(2), pp. 242 - 245.

Oberdörster, G., Oberdörster, E. & Oberdörster, J., 2005. Nanotoxicology: An Emerging Discipline Evolving from Studies of Ultrafine Particles. *Environmental Health Perspectives,* 113(7), pp. 823 - 839.

Ocean Optics, 1989 - 2012. *HG-1 Mercury Argon Calibration Source.* [Online] Available at: http://www.oceanoptics.com/Products/hg1.asp [Accessed 30 6 2011].

Olson, D. B. & Pickens, J. C., 1984. The Effects of Molecular Structure on Soot Formation, I. Soot Thresholds in Premixed Flames. *Combustion and Flame,* Volume 57, pp. 199 - 208.

Olson, D. B., Pickens, J. C. & Gill, R. J., 1985. The Effects of Molecular Structure on Soot Formation II. Diffusion Flames. *Combustion and Flame,* Volume 62, pp. 43 - 60.

Omrane, A., Juhlin, G., Ossler, F. & Aldén, M., 2004. Temperature measurements of single droplets by use of laser-induced phosphorescence. *Applied Optics,* 43(17), pp. 3523 - 3529.

Omrane, A. et al., 2003. Surface Temperature Measurement of Flame Spread Using Thermographic Phosphors. *Fire Safety Science,* Volume 7, pp. 141 - 152.

Omrane, A., Petersson, P., Aldén, M. & Linne, M. A., 2008. Simultaneous 2D flow velocity and gas temperature measurements using thermographic phosphors. *Applied Physics B,* Volume 92, pp. 99 - 102.

Omrane, A., Sarner, G. & Aldén, M., 2004. 2D-temperature imaging if single droplets and sprays using thermographic phosphors. *Applied Physics B,* Volume 79, pp. 431 - 434.

Osunsanya, T., Prescott, G. & Seaton, A., 2001. Acute respiratory effects of particles: mass or number?. *Occupational and Environmental Medicine,* Volume 58, pp. 154 - 159.

Ozawa, L., 2007. Luminescent Properties Generated in Phosphors Particles. In: *Cathodeluminescence and Photoluminescence Theories and Practical Applications.* s.l.:Taylor and Francis Group.

Palmer, H. B. a. C. C. F., 1965. The formation of carbon from carbon gases. In: *The chemistry and physics of carbon Vol 1*. New York: Marcel Dekker, pp. 265 -325.

Pandey, P., Pundir, B. & Panigrahi, P., 2007. Hydrogen addition to acetylene–air laminar diffusion flames: Studies on soot formation under different flow arrangements. *Combustion and Flame,* Volume 148, pp. 249 - 262.

Penner, S. S. & Berlad, A. L., 1995. Fundamental combustion research in support of industrial applications. *Energy,* 20(4), pp. 311 - 324.

Pitts, W. M. et al., 2002. Temperature uncertainties for bare-bead and aspirated thermocouple measurements in fire environments. *Proceedings. ASTM STP 1427,* pp. 3 - 15.

Pitz, W. J. & Mueller, C. J., 2011. Recent Progress in the Development of Diesel Surrogate Fuels. *Progress in Energy and Combustion Science,* 37(3), pp. 330 - 350.

Pringsham, P., 1949. Introduction. In: *Fluorescence and Phosphorescence.* s.l.:Interscience Publishers.

Rabé, E. L. M., 2006. *Jatropha oil in compression ignition engines, effects on the engine, environment and Tanzania a supplying country,* s.l.: s.n.

Raju, G. S. R. et al., 2010. Sintering temperature effect and luminescent properties of Dy3+:YAG nanophosphor. *Journal of Optoelectronics and Advanced Materials,* 12(6), pp. 1273 - 1278.

Ravichandran, D., Roy, R. & White, W. B. E. S., 1997. Synthesis and characterisation of sol-gel dervied hexa-aluminate phosphors. *Journal of Materials Research,* 12(3), pp. 819 - 824.

Richter, H. & Howard, J. B., 2000. Formation of polycyclic aromatic hydrocarbons and their growth to soot—a review of chemical reaction pathways. *Progress in Energy and Combustion Science,* Volume 26, pp. 565 - 608.

Ronda, C. R., 1997. Recent achievements in research on phosphors for lamps and displays. *Journal of Luminescence,* Volume 72 - 74, pp. 49 - 54.

Rothamer, D. A. & Jordan, J., 2012. Planar imaging thermometry in gaseous flows using upconversion excitation of thermographic phosphors. *Applied Physics B,* Volume 106, pp. 435 - 444.

Sarner, G., Richter, M. & Aldén, M., 2008. Two-dimensional thermometry using temperature-induced line shifts of ZnO:Zn and ZnO:Ga fluorescence. *Optics Letters,* 33(12), pp. 1327 - 1329.

Sgro, L. A. et al., 2003. Detection of Combustion Formed Nanoparticles. *Chemosphere 51,* pp. 1079 - 1090.

Shafiee, S. & Topai, E., 2009. When will fossil fuels be diminished?. *Energy Policy 37,* pp. 181 - 189.

Shih, H.-Y. & Hsu, J.-R., 2013. Dilution effects analysis of opposed-jet H2/CO syngas diffusion flames. *Combustion Theory and Modelling,* 17(3), p. 543 – 562.

Skinner, S. J. et al., 2009. YAG:YSZ composites as potential thermographic phosphors for high temperature sensor applications. *Sensors and Actuators B: Chemical,* Volume 136, pp. 52 - 59.

Snelling, D. L. F. S. G. G. Ö., 2000. Evaluation of the nanoscale heat and mass transfer model of the laser-induced incandescence process for excitation intensity prediction. *Proceedings of the 34th National Heat Transfer Conference,* pp. NHTC2000-12132.

Snelling, D. R., Liu, F., Smallwood, G. J. & Gülder, Ö. L., 2004. Determination of the soot absorption function and thermal accommodation coefficient using low-fluence LII in a laminar coflow ethylene diffusion flame. *Combustion and Flame,* Volume 136, pp. 180 - 190.

Snelling, D. R. et al., 2005. A calibration-independent laser-induced incandescence technique for soot measurement by detecting absolute light intensity. *Applie Optics,* 44(31), pp. 6773 - 6785.

Someya, S., Yoshida, S., Li, Y. & Okamoto, K., 2009. Combined measurement of velocity and temperature distributions in oil based on the luminescent lifetimes of seeded particles. *Measurement Science and Techonlogy,* Volume 20.

Tobin, K. W. et al., 1990. High temperature phosphor thermometry of rotating turbine blades. *AAIA Journal,* 28(8), pp. 1485 - 1490.

Tran, N. T., You, J. P. & Shi, F. G., 2009. Effect of Phosphor Particle Size on Luminous Efficacy of Phosphor-Converted White LED. *Journal of Lightwave Technology,* 27(22), pp. 5145 - 5150.

Tree, D. R. & Svensson, K. I., 2007. Soot processes in compression ignition engines. *Progress in Energy and Combustion Science,* Volume 33, pp. 272 - 309.

Turbine Technologies, Ltd., 2006. *Minilab Gas turbine power system Operator's manual, Model ML-409.* s.l.:s.n.

Turbine Technologies, Ltd., 2006. *Minilab Gas turbine power system, Sample lab experiment procedure.* s.l.:s.n.

Turbine Technologies, Ltd, 2006. *Gas turbine power system SR-30.* [Online] Available at: www.turbinetechologies.com [Accessed March 2011].

Valeur, B., 2001. Characteristics of fluorescence emission. In: *Molecular Fluorescence Principles and Applications.* s.l.:Wiley - VCH.

Van Gerpen, J., 2005. Biodiesel processing and production. *Fuel Processing Technology,* Volume 86, pp. 1097 - 1107.

van Lipzig, J. P. J. et al., 2012. Gas phase thermometry in a high pressure cell using BaMgAl10O17:Eu as a thermographic phosphor. *submitted to Applied Physics B,* Volume (in revision).

Vander Wal, R. L., Jensen, K. A. & Choi, M. Y., 1997. Simultaneous laser-induced emission of soot and polycyclic aromatic hydrocarbons with a gas-jet diffusion flame. *Combustion and Flame 109,* pp. 399 - 414.

Wade, S. A., Collins, S. F. & Baxter, G. W., 2003. Fluorescence intensity ratio technique for optical fiber point temperature sensing. *Journal of Applied Physics,* Volume 94, pp. 4743 - 4756.

Wal, V. & L., R., 1996. Laser-induced incandescence: detection issues. *Applied Optics,* 35(33), pp. 6548 - 6559.

Wal, V., L., R. & Jensen, K. A., 1998. Laser-induced incandescence: excitation intensity. *Applied optics,* 37(9), pp. 1607 - 1616.

Westbrook, C., Pitz, W., Sarathy, S. & Mehl, M., 2013. Detailed chemical kinetic modeling of the effects of C=C double bonds on the ignition of biodiesel fuels. *Proceedings of the Combustion Institute,* Volume 34, pp. 3049 - 3056.

Westmoreland, P. R., Dean, A. M., Howard, J. B. & Longwell, J. P., 1989. Forming Benzene in Flames by Chemically Activated Isomerisation. *J. Phys. Chem.,* Volume 93, pp. 8171 - 8180.

Will, S., Schraml, S. & Leipertz, A., 1995. Two-dimensional soot-particle sizing by time-resolved laser-induced incandescence. *Optics Letters,* 20(22), pp. 2342 - 2344.

Will, S., Schraml, S. & Leipertz, A., 1996. Comprehensive two-dimensional soot diagnostics based on laser induced incandescence (LII). *Twenty-Sixth Symposium (International) on Combustion,* p. 2277 – 2284.

Yen, W. M., Shionoya, S. & Yamamoto, H., 2007. *Phosphor Handbook Second Edition.* s.l.:CRC Press/Taylor and Francis.

Yu, M. et al., 2010. Survivability of thermographic phosphors (YAG:Dy) in a combustion environment. *Measurement Science and Techonlogy,* Volume 21.

Zhao, H. & Ladommatos, N., 1998. Optical diagnostics for soot and temperature measurement in diesel engines. *Progress in Energy and Combustion Science,* Volume 24, pp. 221 - 255.